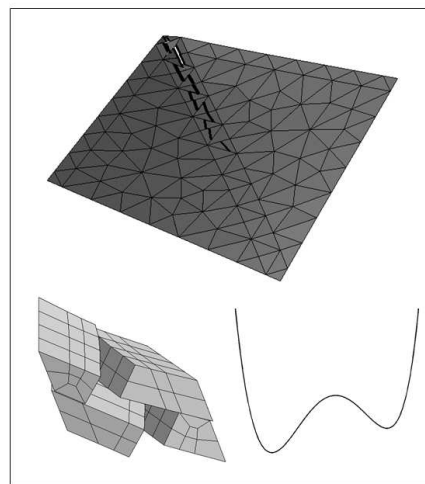
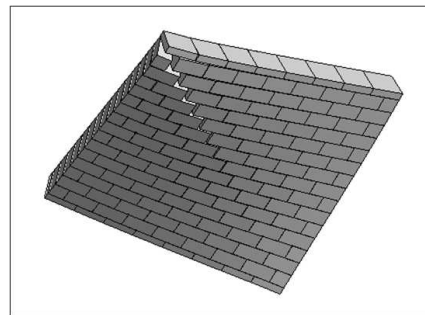


# Multi-scale modelling of shell failure for periodic quasi-brittle materials



*Benoît Mercatoris*

PhD director: Prof. T.J. Massart

PhD co-director: Prof. Ph. Bouillard

Original dissertation presented for the obtaining  
of the title of Doctor in Engineering Sciences.

*To Audrey*

# Contents

<b>1</b>	<b>Introduction</b>	<b>1</b>
1.1	Motivation of the research . . . . .	1
1.2	Methodology . . . . .	2
1.3	Outline . . . . .	2
<b>2</b>	<b>Multi-scale methods for the failure of heterogeneous materials</b>	<b>4</b>
2.1	Characterisation of masonry failure . . . . .	4
2.2	Closed-form models for the non-linear behaviour of masonry . . . . .	5
2.3	Coarse graining methodologies for the failure of materials . . . . .	6
2.3.1	Non-linear behaviour of heterogeneous materials . . . . .	6
2.3.2	Computational modelling of damage localisation . . . . .	6
2.3.3	Methods for upscaling the behaviour of heterogeneous materials . . . . .	8
2.4	Adopted strategy and originality of the work . . . . .	11
<b>3</b>	<b>Embedded strong discontinuity in shell formulation</b>	<b>13</b>
3.1	Introduction . . . . .	13
3.2	Shell formulation . . . . .	13
3.2.1	Reissner-Mindlin kinematics and equilibrium equations . . . . .	13
3.2.2	Enhanced assumed strain for shear locking avoidance . . . . .	15
3.3	Embedded discontinuities for the modelling of localised failure . . . . .	17
3.3.1	Modelling of shell failure with strong discontinuities . . . . .	17
3.3.2	Shell finite elements with embedded strong discontinuities . . . . .	19
<b>4</b>	<b>Multi-scale detection of failure in thin shells using computational homogenisation</b>	<b>25</b>
4.1	Introduction . . . . .	25
4.2	Masonry homogenisation . . . . .	27
4.2.1	Scales of interest for masonry mechanical behaviour . . . . .	27
4.2.2	Computational homogenisation of thin masonry shell properties . . . . .	28
4.3	Simplified mesoscopic constitutive setting . . . . .	33
4.4	Failure detection in thin shell formulations . . . . .	35
4.5	Macroscopic localisation analysis . . . . .	36
4.5.1	Bed joint failure . . . . .	37
4.5.2	Stair-case failure . . . . .	40
4.6	Discussion . . . . .	43
4.6.1	Influence of mesoscopic material properties . . . . .	43
4.6.2	Influence of the loading modes . . . . .	45
4.6.3	Influence of the RVE size . . . . .	47
4.6.4	Incorporation in structural computations . . . . .	49

4.7	Conclusions . . . . .	50
<b>5</b>	<b>Assessment of periodic homogenisation computational schemes for structural failure</b>	<b>51</b>
5.1	Introduction . . . . .	51
5.2	Simplified fine-scale constitutive setting for masonry . . . . .	53
5.3	Homogenisation-based upscaling framework for failure . . . . .	54
5.3.1	Periodic homogenisation of masonry behaviour . . . . .	54
5.3.2	Principles for upscaling the failure behaviour of periodic materials .	56
5.3.3	Incorporation of a strong discontinuity at coarse scale . . . . .	57
5.3.4	Upscaling localising behaviour towards coarse-scale discontinuities .	58
5.4	Comparison of multi-scale and fine-scale results on structural computations	60
5.4.1	Confined shearing of a full masonry wall . . . . .	60
5.4.2	Confined shearing of a masonry wall with an opening . . . . .	68
5.4.3	Discussion . . . . .	73
5.5	Conclusions . . . . .	76
<b>6</b>	<b>A coupled two-scale computational scheme for the failure of periodic thin shells</b>	<b>77</b>
6.1	Introduction . . . . .	77
6.2	Localised shell failure with embedded strong discontinuity . . . . .	81
6.2.1	Shell formulation . . . . .	81
6.2.2	Embedded strong discontinuity in shell formulation . . . . .	83
6.3	Non-linear computational homogenisation of thin shell properties . . . . .	85
6.3.1	Averaging relations for Kirchhoff-Love shell kinematics . . . . .	85
6.3.2	Homogenisation with periodic boundary conditions . . . . .	86
6.3.3	Control system of the mesoscopic boundary value problem . . . . .	86
6.4	Homogenisation-based failure detection in thin shells . . . . .	88
6.5	Homogenisation-based upscaling framework for shell localisation . . . . .	89
6.5.1	Localisation-enhanced two-scaled scheme for thin shells . . . . .	89
6.5.2	Computational aspect . . . . .	92
6.6	Comparison of the coupled two-scale scheme results with direct fine-scale simulations . . . . .	94
6.6.1	Three-dimensional fine-scale constitutive model for masonry cracking	95
6.6.2	Bed joint flexural failure in out-of-plane loaded masonry shell . . .	97
6.6.3	Stair-case flexural failure in out-of-plane loaded masonry shell . . .	100
6.6.4	Discussion . . . . .	104
6.7	Conclusions . . . . .	106
<b>7</b>	<b>Conclusions and perspectives</b>	<b>109</b>
	<b>Bibliography</b>	<b>113</b>
	<b>Summary</b>	<b>122</b>
	<b>Acknowledgements - Remerciements</b>	<b>124</b>

# Chapter 1

## Introduction

### 1.1 Motivation of the research

Masonry is a material which has been used extensively for building in history. Most of historical masonry structures which still exist nowadays present the occurrence of cracks which may significantly affect their load bearing capacity. In the context of restoration, it is therefore crucial to be able to estimate the residual strength in order to assess the safety of buildings. As a consequence of its complex structure, masonry presents preferential damage orientations which are complex to incorporate in structural computations. Furthermore, masonry structures are generally subjected to complex loading processes including both in-plane and out-of-plane loads which considerably influence the potential failure mechanisms. As a consequence, both the membrane and the flexural behaviours of masonry walls have to be taken into account for a proper estimation of the structural stability.

Numerical models are widely used in the literature to model the quasi-brittle material behaviour of the masonry material. Two methodologies may be considered based on the scale of interest. For large-scale structures, masonry can be considered as an equivalent homogeneous material. The macroscopic scale material behaviour is governed by phenomenological laws including a set of parameters which characterises the average behaviour of the material. These parameters need to be identified through experimental tests. For the case of masonry, this material law identification can become costly due to the complexity of its behaviour particularly when cracks appear. The existing macroscopic models are consequently restricted to particular assumptions. In addition, it is observed experimentally that cracking of masonry most often results from localisation of damage in narrow zones at the structural scale. Advanced numerical techniques are necessary to properly model this localised behaviour which increases significantly the complexity of the macroscopic models. Another methodology based on a detailed mesoscopic description can be considered to estimate the strength of masonry and its behaviour with failure. This approach uses separate descriptions for each constituent of the mesostructure, namely the bricks and the mortar joints, considering masonry as a heterogeneous material. This is motivated by the fact that the behaviour of each constituent is a priori easier to identify than the global structural response. These mesoscopic models are therefore more accurate since all the heterogeneities are represented, but they can rapidly become unaffordable in terms of computational cost for the case of large-scale three-dimensional structures.

In order to keep the accuracy of the mesoscopic modelling with more affordable computational effort for large-scale structures, a multi-scale approach using computational

homogenisation is developed to bridge the mesoscopic and macroscopic scales for the representation of quasi-brittle structural failure. The main idea of this approach is to extract a coarse-scale constitutive material response from computations performed on a sample of the mesostructure. A fine-scale model is used to represent the sample. Computational homogenisation approaches have extensively been discussed in the last decades but remain rather unexplored for the case of flexural behaviour with localised failure. The development of a coupled two-scale computational framework for masonry shell failure would therefore constitute a major step forward in the characterisation of masonry and more generally in the multi-scale approaches.

## 1.2 Methodology

A multi-scale approach is developed here for the structural analysis of planar running bond masonry walls subjected to in-plane and out-of-plane loadings with a specific treatment including localisation of cracking. A closed-form constitutive law for such a shell behaviour would be complex to postulate and identify. A multi-scale approach allows to postulate the material laws at the scale of the constituents, which are a priori more straightforward to identify. A periodic non-linear computational homogenisation method is used to capture the local quasi-brittle material behaviour of masonry thin shells. Based on the periodicity of the mesostructure, a representative volume element (RVE) can be defined and modelled by using mesoscopic closed-form material laws. At the structural scale, the localisation of damage is represented by means of fine-scale informed cohesive zones incorporated in the macroscopic shell description. These cohesive zones are represented by a local enrichment of the kinematics based on embedded strong discontinuities representing in an average sense the fine-scale crack openings. In the context of multi-scale modelling, both the appearance and the material behaviour of these cohesive zones have to be driven by the mesostructural response. A new methodology is proposed to upscale the material information of the mesostructural samples towards the macroscopic cracking representation. A generalised localisation criterion is used to detect the occurrence of macroscopic localisation in thin shell descriptions and to determine its orientation. This detection criterion is based on the macroscopic homogenised tangent stiffness extracted from the response of the RVE. The material behaviour of the discontinuity which represents the structural localisation is extracted from a further damaging sample, denoted as Localising Volume Element (LVE), by means of an enhanced upscaling procedure based on an approximate energy consistency requirement. The enhanced scale transition relations are firstly developed for the in-plane case and are then extended to the out-of-plane case. The complete multi-scale scheme is validated against full fine-scale computations (direct fine-scale simulations) in order to assess the robustness of the proposed approach.

## 1.3 Outline

The dissertation is organised as follows. A brief review of methodologies for upscaling the behaviour of heterogeneous materials is presented in Chapter 2. A characterisation of the masonry behaviour is first given, based on experimental results available in the literature, in order to highlight the complex non-linear quasi-brittle behaviour of masonry structures in relation with the corresponding failure mechanisms. A brief state of the art of existing phenomenological models for masonry is also presented. Coarse-graining

methodologies for the non-localised and localised behaviour of heterogeneous materials are then discussed. Both the in-plane and shell descriptions are considered. Different numerical techniques developed in the past two decades to handle localisation at the structural scale for in-plane and shell descriptions are also reviewed. The multi-scale approach proposed in this dissertation is then motivated by this literature survey, showing that the topic of coarse-graining failure started to emerge for in-plane descriptions recently, but was not extensively explored for the out-of-plane behaviour up to now.

The engineering shell description used in this dissertation is recalled in Chapter 3. An embedded strong discontinuity approach used to represent the shell failure and taken from the literature is also outlined in order to give the mathematical tools and notations used in the sequel. Chapter 4 is devoted to the definition of a homogenisation-based detection criterion of failure in planar masonry thin shells. The non-linear computational homogenisation scheme is developed for the non-localised behaviour of masonry thin shells and the fine-scale modelling used at the RVE level is presented. A localisation analysis is proposed to numerically determine the average orientation of the structural localisation and is validated against RVE computations.

The nested multi-scale computational scheme for quasi-brittle structural failure is developed in Chapter 5 for in-plane problems. The principles for upscaling the failure behaviour of periodic materials are presented. This approach is based on an approximate energy consistency argument in order to objectively upscale the total energy dissipation, based on the assumption of a single period failure pattern. The results obtained from this multi-scale framework for the confined shearing of a masonry wall are compared with those of a complete fine-scale modelling of the wall for which all the heterogeneities are discretised using the same fine-scale laws. The assumptions of the multi-scale approach, namely the periodicity and the scale separation, are challenged in order to estimate their impact on the results. The multi-scale scheme is extended to the case of thin shell failure in Chapter 6. This framework is again validated against full fine-scale computations for different failure mechanisms. Finally, Chapter 7 concludes this dissertation and identifies different perspectives for future developments.

Note that this dissertation is based on the compilation of three papers. The two first papers (Chapters 4 and 5) were published in international journals, while the third paper (Chapter 6) has been submitted for publication. Since each paper needs to be self-contained, this dissertation may contain repetitions, especially in Chapters 5 and 6.

# Chapter 2

## Multi-scale methods for the failure of heterogeneous materials

### 2.1 Characterisation of masonry failure

Masonry is a textured heterogeneous material composed of an arrangement of bricks and mortar joints. For the characterisation of its mechanical behaviour, two scales of interest may be identified, namely the structural or macroscopic scale, on the order of meters, and the mesoscopic scale, on the order of centimeters. The macroscopic scale is the typical size of the masonry structure in which the external loads are defined and the mesoscopic scale represents the characteristic size of the bricks and the mortar joints.

In the past, experimental tests were carried out on planar masonry walls in order to characterise the non-linear mesoscopic and macroscopic behaviour of the composite material both for in-plane and out-of-plane loadings. Since the mortar joints are weaker than the bricks, cracking of masonry structure is mainly concentrated in the mortar joints. For the mesoscopic failure behaviour, a series of deformation controlled tests was performed on a single mortar joint linking two bricks in van der Pluijm (1999) to characterise the tensile and shearing failure of mortar joints and mortar-brick interfaces. Bending tests were also carried out on a single mortar joint specimen of masonry in order to estimate the flexural fracture energy. The low values of fracture energy extracted from these tests indicate a quasi-brittle fracture behaviour of the mortar joints.

In the context of structural characterisation, the periodic stacking of the bricks results in an initial anisotropy of the material. In the case of running bond masonry for instance, the material behaviour is orthotropic since the axes of symmetry in the material structure are perpendicular. Due to the periodic arrangement, preferential cracking orientations can be observed leading to another type of anisotropy induced by the cracking and strongly dependent on the loading mode. For instance, a wall presenting a bed joint crack pattern keeps (modified) orthotropic properties whereas a stair-case crack pattern leads to a more complex form of anisotropy. These crack patterns were reproduced in experimental tests carried out on small planar walls subjected to in-plane loadings in Page (1981, 1983), Dhanasekar et al. (1985) and to out-of-plane loadings in van der Pluijm (1999). For the in-plane case, macroscopic failure envelopes for proportional uniform biaxial loading of running bond masonry were established in Page (1981, 1983), Dhanasekar et al. (1985) for different orientations of the applied principal stresses with respect to the orthotropy axes. It was shown that the shape of the failure envelopes changes with the loading direction. Using such experimental results obtained for proportional loading directly for structural

computations is a strong assumption due to stress redistributions caused by cracking and related damage evolutions.

For the characterisation of the masonry bending behaviour, experimental tests were carried out in van der Pluijm (1999) until the load bearing capacity was reached. Small masonry walls were tested under four-point bending loading in such a way that the critical cross-section is tested in pure bending in order to characterise the flexural behaviour. Different bending directions with respect to the bed joint direction were considered. It was shown that the misalignment between the bending direction and the bed joint direction can lead to complex stiffness evolutions and stress redistributions since the preferential cracking orientation is not necessarily parallel to the loading direction. Note that non-linear stress redistributions already occur prior to the peak load due to evolving damage.

In these experimental results, localisation of damage was observed at the structural scale in narrow zones on the order of joint thickness. The macroscopic failure behaviour is however strongly related to the mesostructure since damage occurs and evolves mainly in the mortar joints leading to stress redistributions at the structural scale. The size and the orientation of this localisation phenomenon has to be captured properly to determine the structural failure modes and the associated energy dissipation.

## 2.2 Closed-form models for the non-linear behaviour of masonry

Inspired by the experimental work of Page (1981, 1983), Dhanasekar et al. (1985), macroscopic phenomenological models were elaborated to represent the non-linear behaviour of in-plane loaded masonry structures. A plane stress model using non-associated plasticity laws was proposed in Lourenço et al. (1997). In order to characterise the orthotropic behaviour of masonry, this model includes a tensile fracture energy and a compressive fracture energy, which are different for each material axis. In the same spirit, an orthotropic damage model accounting for stiffness degradation and including four independent internal damage parameters, one in tension and one in compression for each of the two material axes, was developed in Berto et al. (2002) to consider the damage-induced anisotropy of masonry. A model including both plasticity effects and stiffness degradation was proposed in Papa and Nappi (1997). Note that these models all assume that the failure envelopes obtained experimentally under proportional loadings remain valid for the case of non proportional loadings and therefore take into account in an approximate way the stress redistributions due to stiffness evolutions, which may lead to considerable path dependency effects. For the out-of-plane loading case, the orthotropic two-dimensional continuum model proposed in Lourenço et al. (1997) was used in layered shell structures in Lourenço (2000). This model based on plasticity concept includes softening behaviour and independent fracture energies along each material axis.

All these phenomenological models are based on the formulation of closed-form constitutive laws, and incorporate parameters to be identified experimentally. In the context of the non-linear behaviour of orthotropic composite such as masonry, the representation of full damage-induced anisotropy by means of closed-form constitutive laws however remains complex and leads to difficult parameter identification procedures. In addition, the case of out-of-plane loaded masonry structures requires even more complex closed-form laws since other aspects of the behaviour such as membrane-flexural couplings have to be taken into consideration.

This motivates the use of multi-scale approaches allowing to postulate closed-form constitutive laws at the scale of the constituents, and for which the material parameters are a priori more straightforward to identify. The macroscopic anisotropy evolution effects are naturally deduced from the mesostructure by using homogenisation techniques. Furthermore, the representation of damage localisation requires the use of a regularisation technique which, in the context of multi-scale approaches, has to be mesoscopically motivated since all the material information is postulated at the mesoscopic scale.

## 2.3 Coarse graining methodologies for the failure of materials

### 2.3.1 Non-linear behaviour of heterogeneous materials

In the last decades, considerable progress has been achieved in the field of the modelling of the non-linear mechanical behaviour of heterogeneous materials. In this context, multi-scale methods based among other approaches on homogenisation techniques have been the topic of many contributions and are still a subject of intensive research nowadays, see Geers et al. (2009). The main goal of these methods is to bridge the different physical phenomena taking place at different scales in order to more accurately take into account the effect of heterogeneities on the global material response. This is important for the non-linear modelling of heterogeneous materials for which phenomena occurring at very different scales strongly influence the global behaviour. In parallel to this research domain, the modelling of deformation localisation phenomena leading to failure has been widely considered in order to resolve highly non-linear problems resulting from crack propagation and softening material behaviour.

In certain classes of materials, the modelling of localisation physically calls for multi-scale representations since the structural or coarse-scale localisation generally originates from physical phenomena which appear at finer scales, and since closed-form macroscopic laws are then difficult to formulate. The consideration of multi-scale methods in up-scaling microstructural material behaviour toward structural localised material response only started to emerge recently in the literature, see for instance Massart et al. (2007a), Belytschko et al. (2008), Belytschko and Song (2009).

Both concepts of damage localisation and coarse graining have extensively but almost separately been discussed in the literature in the case of quasi-brittle material behaviour, and were mostly restricted to two-dimensional problems. Complex heterogeneous materials are however more and more met in shell-like structures such as, for instance, laminated composite, honeycomb-type sandwich in mechanical engineering or masonry structure in civil engineering. As a consequence, some work has been done in the literature in order to extend multi-scale approaches and localisation modelling to shell formulations.

### 2.3.2 Computational modelling of damage localisation

In the two last decades, different approaches have been considered to model localisation of damage either with non-local models Pijaudier-Cabot and Bazant (1988), Peerlings et al. (1996), or with cohesive zone models Xu and Needleman (1994), Lourenço (1996), Sluys and Berends (1998), de Borst (2003). Motivated by the appearance of high strain gradients in narrow zones and crack openings, the concept of discontinuity incorporation

within classical continuum descriptions has been widely used. A brief overview of this concept is given now for plane and shell descriptions. Initially, embedded discontinuities were used by introducing jumps either into strain fields, leading to weak discontinuities as in Ortiz et al. (1987), Belytschko et al. (1988); or into displacement fields leading to a strong discontinuity approach, see Simo et al. (1993), Lofti and Shing (1995), Oliver (1996a,b), Armero and Garikipati (1996), Armero (1999), Wells and Sluys (2000). Both approaches were discussed in a unified framework in Jirásek (2000). Later, the so-called extended finite element method (X-FEM) based on the partition unity concept was presented in Moës et al. (1999), Belytschko and Black (1999), Belytschko et al. (2001), Wells and Sluys (2001); allowing for continuous crack path and crack kinematics, in contrast with the embedded discontinuity approach, which uses mainly element-based enrichments. The partition unity concept was used to introduce stress free cracks in the context of linear elastic fracture mechanics in Moës et al. (1999) as well as cohesive laws with arbitrary crack paths without remeshing in Wells and Sluys (2001). A recent extensive review of the X-FEM methodology is available in Belytschko et al. (2009).

The two aforementioned approaches (embedded discontinuity and X-FEM) have been extended for through-thickness cracks and delamination of plates and shells in the last decade. In the context of through-thickness cracks, the extended finite element method was firstly adapted for the modelling of cracks in Reissner-Mindlin plates in Dolbow et al. (2000), accounting for a proper representation of the stress intensity factors (i.e. without crack growth). The X-FEM methodology was also adapted to the continuum-based shell formulation, see Areias and Belytschko (2005). A difficulty encountered in this context was the consideration of specific cohesive laws for the transverse shear stress, a problem which is not met in thin shell considerations. A meshfree Kirchhoff-Love formulation was proposed recently in Rabczuk et al. (2007) resulting in no discretisation of the director field, and allowing a straightforward implementation. Similarly to an in-plane approach presented in Hansbo and Hansbo (2004), Mergheim et al. (2005), the X-FEM methodology was reinterpreted in Areias et al. (2006). The discontinuity is then represented by two overlapping elements using a pair of distinct deformation mapping for the displacement and director fields. This concept was also applied in Cirak et al. (2005) for the dynamic fracture and fragmentation of viscoplastic aluminium shells. In the context of delamination of multi-layered composite structures, some approaches were proposed such as an extension of the X-FEM methodology developed in Remmers et al. (2003) for solid-like shell formulations in which delamination crack can occur at an arbitrary position in the thickness. In addition, the X-FEM methodology was used recently for quasi-static crack propagation of thin shells taking into account softening, adhesion and contact behaviour by means of closed-form macroscopic cohesive laws, see Areias and Rabczuk (2008); and for dynamic quasi-brittle fracture of thin shells subjected to impulse loads, see Song and Belytschko (2009). Although the X-FEM methodology seems to prevail in the modelling of crack propagation, the embedded discontinuity method still has drawn interest in the past years at least for two-dimensional applications. The two-dimensional strong embedded discontinuity approach proposed in Armero (1999) was extended to the Euler-Bernoulli beam kinematics in Armero and Ehrlich (2006b) and the Reissner-Mindlin plate kinematics in Armero and Ehrlich (2006a). Another approach based on a strong embedded discontinuity formulation was presented for a continuum-based shell formulation in Larsson (2004) in order to analyse delamination of laminated composite structures with damage-plastic coupling.

### 2.3.3 Methods for upscaling the behaviour of heterogeneous materials

In the field of multi-scale frameworks for heterogeneous materials, different techniques have been developed in the past decades. Three techniques have emerged due to the increase of available computational power for two-dimensional and three-dimensional problems; namely the asymptotic homogenisation theory, the substructuring method, and the computational homogenisation method. These techniques are briefly reviewed, the focusing on last progress achieved for the case of heterogeneous shells on one hand and the consideration of size effects to properly represent structural localisation on the other hand. The asymptotic homogenisation theory, proposed in Bensoussan et al. (1978), Sanchez-Palencia (1980) and presented for two-dimensional problems in Suquet (1987) is based on the assumption of a periodic microstructure and is still widely used for composite materials, see the recent extensive review in Kalamkarov et al. (2009). This theory is based on the asymptotic expansion of the macroscopic variables in powers of a scale ratio characterising the scale of the periodic heterogeneities. This ratio is assumed to be very small according to the scale separation principle which allows the definition of a representative volume element (RVE) of the microstructure. Using the asymptotic expansion, a boundary value problem can be defined on the RVE for each order under consideration, see Peerlings and Fleck (2004). Note that each of these corresponding boundary value problems needs to be solved numerically. The first-order asymptotic homogenisation rigorously gives the same solution as the computational homogenisation approach with periodic boundary conditions, even though the respective boundary value problems defined at the microstructural level are different. For thin structures, an additional scale ratio is considered to characterise the small thickness, with respect to the Kirchhoff-Love assumption. Note that the properties of a homogenised shell structure depend on the ratio between both the characteristic length scales, see Cartraud and Messenger (2006) for the similar case of beam-like structures.

One of the most common applications of this approach in the field of engineering mechanics is the determination of the elastic coefficients, see for instance Challagulla et al. (2008) for the case of composite shell structures with orthotropic reinforcements. Asymptotic homogenisation techniques were also applied for the case of periodic running bond masonry walls subjected to out-of-plane loading. Such Kirchhoff-Love and Reissner-Mindlin shell descriptions were developed respectively in Cecchi and Sab (2002b) and Cecchi and Sab (2004) to characterise the elastic masonry behaviour. In both models, rigid bricks connected by elastic interfaces were considered. The influence of bricks elasticity was later presented in Cecchi and Sab (2007). In addition to engineering mechanics, the asymptotic homogenisation is still applied for shell structures in various disciplines as for instance the identification of elastic-electrical couplings of composite shell structures incorporating piezoelectric materials, see Ghergu et al. (2005), Kalamkarov et al. (2007), and the computation of magnetic field mitigation produced by ferromagnetic grid shell shields, see Bottauscio et al. (2007, 2008).

The extension of the asymptotic homogenisation approach to non-linear problem is not straightforward. Asymptotic homogenisation techniques were combined with limit analysis concepts and optimisation techniques in order to compute ultimate strength properties of structures and determine their failure mechanism. For the case of out-of-plane loaded masonry walls, a kinematic limit analysis method was combined with a homogenised description under both Kirchhoff-Love and Reissner-Mindlin assumptions, see Milani et al.

(2006c), Cecchi et al. (2007), to find an upper bound approximation of the masonry failure surface in the space of the generalised stresses, see also Cecchi and Milani (2008). In spite of the quasi-brittle and frictional behaviour of mortar joints in masonry which requires non-associated flow rule, perfect plasticity assumption and associated flow rule are used in this context. A limit analysis approach based on a homogenisation procedure accounting for the strength domain of any shell failure mechanism was developed recently in Milani et al. (2008) for the structural analysis of curved masonry shells such as arches, vaults and domes. In this approach, a curved unit cell is considered to represent the microstructure and generalised cylindrical hinges are incorporated at the interfaces of shell elements to represent structurally the plastic dissipation occurring at the microstructural scale. A kinematic and static limit analysis scheme was also combined with an asymptotic expansion method to determine the overall homogenised Kirchhoff-Love strength domain of a rigid perfectly plastic periodic multi-layered plate, see Dallot and Sab (2008a,b) for an extension towards thick plates.

The limit analysis methods effectively predict the load bearing capacity and the associated failure modes. These methods however are not able to represent the evolution of stable cracks, i.e. the service states far below the ultimate load capacity. In order to track the complete non-linear force-displacement response of heterogeneous shells and still overcome the costly and cumbersome identification of closed-form models, complementary computational multi-scale techniques were set up based on substructuring and computational homogenisation methods. These concepts were also motivated by the fact that the extension of multi-scale methods based on asymptotic expansion to geometrically non-linear problems remains difficult, see Fish and Fan (2008). In the case where the characteristic length scale of the microstructure is not small enough to satisfy the scale separation principle, substructuring models which bear similarities with domain decomposition methods have been proposed for two-dimensional problems. In this approach the structure is decomposed in non-overlapping subdomains which are related to finite-sized parts of the microstructure, see Ibrahimbegovic and Markovic (2003), Markovic and Ibrahimbegovic (2004) for instance. A localised Lagrange multiplier method is used in order to connect the finite element mesh of each considered subdomain to the macroscopic finite element mesh playing the role of frame. A similar approach was applied more recently for the in-plane non-linear behaviour of large masonry structures in Brasile et al. (2007a,b). The concept of structural decomposition was also exploited for damage assessment in two-dimensional random particle reinforced porous composites. In this field, an adaptative multi-level model was proposed in Ghosh et al. (2001) combining an asymptotic homogenisation procedure with a microstructural representation based on a network of single-inclusion multi-sided convex cells, called Voronoi cells, see Moorthy and Ghosh (1998). This cell model, based on a hybrid stress-based finite element formulation, allows one to account for the inclusion dispersion. As an application, this approach was recently enhanced for the modelling of damage-induced anisotropy in ductile cast alloys such as aluminium and metal matrix composites, see Ghosh et al. (2009). In this case, a non-local constitutive law is used at the macroscopic level to incorporate a characteristic length scale avoiding mesh dependency. In these multi-level methods, the macroscopic constitutive law is assumed and calibrated by means of the homogenisation of evolving microstructural variables. However, the concept of substructuring models seem to be not widely extended to shell formulation.

Based on the scale separation assumption, the computational homogenisation approach allows to numerically compute the average non-linear behaviour of a heteroge-

neous microstructure by means of averaging theorems and a boundary value problem on a RVE, see Smit et al. (1998), Feyel and Chaboche (2000), Kouznetsova et al. (2001) and also Geers et al. (2009) for a state of the art of recent trends and challenges of this approach. In the field of engineering mechanics, the computational homogenisation approach was extended recently for structured thin sheets using the homogenisation of a through-thickness RVE based on a second-order strategy, see Geers et al. (2007), Coenen et al. (2008). However, the thick shell case still raises questions concerning the transverse shear upscaling and is the topic of current research work. As a special case, a periodic homogenisation procedure presented in Mistler et al. (2007) for the case of elastic Kirchhoff-Love masonry shells may be adapted for non-linear material response, as will be shown in the sequel. Computational homogenisation procedures generally consider the same physical space at the different scales. A recent approach proposed in Grytz and Meschke (2008) generalises computational homogenisation to the formulation of continua in curvilinear coordinates by introducing a proper physical reference coordinates at each scale. This requires the definition of transition operators which account for the transformations between the different physical coordinate systems. This approach is adapted to the non-linear continuum-based shell formulation considering appropriate shell assumptions and applied to the biomechanical multi-scale modelling of shell-like soft tissues, see Grytz and Meschke (2008).

In order to reduce the typical high computational cost of direct computational homogenisation procedures with a certain compromise on the solution accuracy, transformation field analysis initially proposed in Dvorak (1992) was presented for deriving the non-linear behaviour of plastic and damaging composite. This approach is based on the decomposition of each constituent of the microstructure into subdomains in which uniform inelastic strain fields are assumed, leading to off-line homogenisation. This concept was applied recently for the case of in-plane loaded masonry walls in Sacco (2009). In order to evaluate the inelastic behaviour of heterogeneous shells, an asymptotic homogenisation procedure was also recently coupled to an eigendeformation-based model reduction which generalises transformation field analysis to account for interface debonding within the microstructure, see Oskay and Fish (2007, 2008).

Two multi-scale frameworks for the non-linear analysis of periodic heterogeneous plates were presented using continuum damage mechanics. A two-fold multi-scale enrichment methodology was proposed recently in Oskay (2009) for the inelastic analysis of heterogeneous plate structures. The enrichment strategy consists of a strain enrichment using the asymptotic homogenisation theory and based on non-local developments, and a displacement enrichment using a partition of unity method. The latter allows one to consider cases in which the scale separation assumption does not hold, see also Fish and Yuan (2005). This method is combined with an eigendeformation-based model reduction in order to avoid high computational cost for non-linear analysis of large structure by compromising on the solution accuracy, see Oskay and Fish (2007, 2008). The applicability of this model however remains restricted to the analysis of very thin structures where the Kirchhoff-Love assumptions are valid at the structural scale. Another multi-scale framework based on an asymptotic homogenisation procedure was developed for the analysis of failure of thin heterogeneous plates, see Oskay and Ghanshyam (2009). In this approach, macroscopic inelastic and damage fields are linked to microscopic inelastic and damage fields by means of weighted averaging relations using the eigendeformation concept. A viscous regularisation is used at the structural scale to avoid mesh sensitivity but does not allow to represent damage localisation at the structural scale. Both these models,

Oskay (2009), Oskay and Ghanshyam (2009) have been verified against a full fine-scale model where all the heterogeneities are represented.

Some above-mentioned multi-scale models are based on non-local descriptions at the structural scale such as Ghosh et al. (2009) for in-plane problems and Oskay and Ghanshyam (2009) for the case of thin structures. These models allow to consider structural strain localisation bands to some extent by means of relatively fine mesh and leading to remeshing in the case of propagating failure. Another damage model based on a description of the energy dissipation associated with failure was proposed recently in Dascalu et al. (2008). This continuum model incorporating an internal length parameter deduced from the microstructure is coupled with the asymptotic homogenisation method to describe size effects, material softening and damage-induced anisotropy in brittle heterogeneous material. In the context of computational homogenisation, a second-order approach was proposed in Kouznetsova et al. (2004) incorporating in the macroscopic continuum a length scale defined by the size of the RVE. In this enhanced homogenisation procedure linear variations of the average strain field can be considered over the RVE allowing to account for moderate size effects. An alternative computational homogenisation approach based on a coupling between the structural finite element size and the RVE size similar to substructuring approaches was proposed in Gitman et al. (2008) to account for the softening response of quasi-brittle materials with no dependency on the discretisation size.

It is now well known to be crucial in such multi-scale frameworks to properly treat the localisation phenomenon at each scale under consideration in order to keep a well-posed description for a complete softening analysis of problems involving damage and fracture. In this spirit and inspired by progress made in the development of embedded localisation models, continuous-discontinuous scale transitions started to emerge in the literature. A first approach based on this concept was developed in Massart et al. (2007a) for damage in in-plane loaded masonry wall, see also Massart et al. (2007b). A twofold first-order computational homogenisation scheme is presented to account for the behaviour of damaging and unloading material. This procedure relies on the definition of a localisation band using strain discontinuities driven by an evolving damaging unit cell. The detection of localisation bands is based on the macroscopic homogenised tangent stiffness leading to a physically based description of preferential damage orientations. A methodology based on a condition of increasing energy dissipation is also presented to treat microstructural snap-backs. Another multi-scale approach was recently coupled to the extended finite element method. This approach consists in feeding the behaviour of structural scale equivalent displacement discontinuities with information extracted from the aggregation of all microstructural material instabilities present in a unit cell, see Belytschko et al. (2008), Belytschko and Song (2009).

## 2.4 Adopted strategy and originality of the work

The macroscopic behaviour of textured heterogeneous materials such as masonry is not obvious to capture. Complex behaviours such as damage-induced anisotropy leading to stress redistributions can be observed in experimental results for in-plane and out-of-plane loading processes as discussed in Section 2.1. The modelling of such a macroscopic behaviour through closed-form relations may be cumbersome to identify due to a large number of material parameters, see Section 2.2; and even complex to formulate from a mathematical point of view.

A multi-scale approach can therefore offer an attractive and flexible solution in the characterisation of heterogeneous materials. In the context of non-linear behaviour, the computational homogenisation method is at present the most versatile approach. The principle of this method is to extract the macroscopic quantities from mesoscopic computational analyses which are nested in the structural computations. This allows to avoid the formulation of closed-form macroscopic constitutive laws and therefore allows one to consider complex mesostructures, which may evolve during the loading process.

For the numerical treatment of damage localisation, different techniques were briefly reviewed in Section 2.3.2. In the case of masonry, the structural localisation can be treated by discontinuities since the size of the localisation zone is usually smaller than the RVE size. The embedded strong discontinuity approach proposed in Armero (1999), Armero and Ehrlich (2006a) will be used here to represent the collective behaviour of fine-scale cracks using average cohesive zones including mixed cracking modes and presenting evolving orientation related to fine-scale damage evolutions.

As shown in Section 2.3, coarse graining methodologies for the failure of quasi-brittle heterogeneous materials have started to emerge for in-plane problems but remain largely unexplored for shell descriptions. This dissertation proposes a new periodic homogenisation-based multi-scale approach for quasi-brittle thin shell failure. A first originality of this research work is the definition and analysis of a criterion based on the homogenisation of a fine-scale modelling to detect localisation in a shell description and determine its evolving orientation. Secondly, an enhanced continuous-discontinuous homogenisation method incorporating strong embedded discontinuities driven by the damaging mesostructure is proposed for the case of in-plane loaded structures. Finally, this continuous-discontinuous homogenisation scheme is extended to a shell description in order to model the localised behaviour of out-of-plane loaded structures. These multi-scale approaches for failure are applied on masonry walls and verified against three-dimensional full fine-scale computations in which all the bricks and the joints are discretised.

# Chapter 3

## Embedded strong discontinuity in shell formulation

### 3.1 Introduction

This chapter presents the mathematical tools and notations used in the sequel to treat the damage localisation at the structural scale. These tools are taken from the literature and recalled here for the readability of the dissertation. First, the Reissner-Mindlin engineering shell formulation is presented for a non-linear material behaviour. The equilibrium equations are given and an enhanced assumed strain method proposed in Batoz and Lardeur (1989), Batoz and Dhatt (1990) to avoid transverse shear-locking for linear problems is extended here to the material non-linearities. Secondly, the embedded strong discontinuity approach proposed in Armero (1999), Armero and Ehrlich (2006a) is presented for the modelling of localised shell failure. This method is based on an element enhancement using displacement discontinuities to represent the cracks. Additional local equilibrium equations are introduced to couple the crack behaviour to the global shell equilibrium. Details are given about the numerical implementation.

### 3.2 Shell formulation

#### 3.2.1 Reissner-Mindlin kinematics and equilibrium equations

The domain of the global problem of interest is a flat shell represented by its reference plane  $\Omega$  and its contour  $\partial\Omega$ . The classical Reissner-Mindlin kinematics is considered in the infinitesimal strains range using the engineering or generalised displacements, namely the in-plane displacement vector  $\vec{v}$ , the rotation vector  $\vec{\vartheta}$  and the transverse deflection  $w$ . The Reissner-Mindlin kinematics is based on the assumptions that (i) the ‘normals to the undeformed reference surface remain straight but not necessarily normal to the deformed reference surface’, (ii) the thickness remains constant, and (iii) the normal stress in the thickness direction vanishes. Using the first two assumptions, the in-plane and out-of-plane displacements of any material point  $P$  in the thickness of the shell can be expressed as

$$\begin{cases} \vec{v}_P &= \vec{v}(x, y) + z\vec{\beta}(x, y) \\ w_P &= w(x, y) \end{cases} \quad (3.1)$$

where  $x, y$  are the in-plane Cartesian coordinates and  $z$  is the out-of-plane or thickness coordinate. Note that the vector  $\vec{\beta}$  is linked to the rotations around the in-plane axes by

$\vec{\beta} = \vec{\vartheta} \times \vec{e}_z$  with  $\vec{e}_z$  the unit vector in  $z$ -direction.

In this context, the generalised strain measures are the membrane strain tensor  $\mathbf{E}$ , the curvature tensor  $\boldsymbol{\chi}$  and the transverse shear vector  $\vec{\gamma}$  defined as

$$\begin{cases} \mathbf{E} &= (\vec{\nabla} \vec{v})^{\text{sym}} \\ \boldsymbol{\chi} &= (\vec{\nabla} \vec{\beta})^{\text{sym}} \\ \vec{\gamma} &= \vec{\nabla} w + \vec{\beta} \end{cases} \quad \text{with } \vec{\beta} = \vec{\vartheta} \times \vec{e}_z \quad (3.2)$$

where  $\vec{\nabla}$  is the gradient operator vector with respect to the in-plane coordinates. The stress resultants significant to the shell formulation are work conjugate to the generalised strain measures (3.2) and denoted by  $\mathbf{N}$  for the membrane force tensor,  $\mathbf{M}$  for the bending moment tensor and  $\vec{T}$  for the transverse shear force vector. These stress measures are given by the integration of the tridimensional stresses along the thickness which reads in subscript notation

$$\begin{cases} N_{\alpha\beta} &= \int_t \sigma_{\alpha\beta} dz \\ M_{\alpha\beta} &= \int_t \sigma_{\alpha\beta} z dz \\ T_\alpha &= \int_t \sigma_{\alpha 3} dz \end{cases} \quad (3.3)$$

where Greek subscripts vary from 1 to 2 only and correspond to the in-plane components. The subscript 3 corresponds to the out-of-plane component. The sign convention of all the stress components is shown in Figure 3.1.

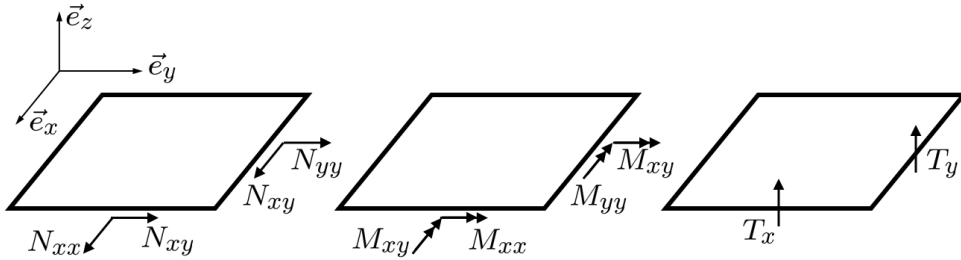


Figure 3.1: Sign convention of Reissner-Mindlin generalised stress components.

Using these generalised stress measures, the equilibrium equations at a point of the reference surface can be written as follows

$$\begin{cases} \vec{\nabla} \cdot \mathbf{N} + \vec{F} = \vec{0} \\ \vec{\nabla} \cdot \vec{T} + p = 0 \\ \vec{\nabla} \cdot \mathbf{M} - \vec{T} + \vec{m} = \vec{0} \end{cases} \quad (3.4)$$

where  $\vec{F}$  and  $\vec{m}$  are the thickness integration of respectively the in-plane body forces and the torques of these forces. The scalar  $p$  represents the external out-of-plane pressure applied on the shell reference surface. The first two equations in (3.4) corresponds respectively to the in-plane and out-of-plane translation equilibrium and the third equation in (3.4) imposes rotation equilibrium.

In order to be resolved by a finite element scheme, this equilibrium problem can be expressed in a weak form by the variational statement

$$\int_{\Omega} (\mathbf{N} : \delta \mathbf{E} + \mathbf{M} : \delta \boldsymbol{\chi} + \vec{T} \cdot \delta \vec{\gamma}) d\Omega = \int_{\Omega} \delta w_s^{\text{ext}} d\Omega + \int_{\partial\Omega} \delta w_c^{\text{ext}} d\Gamma \quad (3.5)$$

for all admissible variations  $\delta\vec{u}$ ,  $\delta\vec{\vartheta}$  and  $\delta w$ , and where  $\delta w_s^{\text{ext}}$  and  $\delta w_c^{\text{ext}}$  represent the variation of the external work density of applied forces and torques, respectively per unit area and per unit length.

Accounting for material non-linearities, the constitutive law linking the generalised stresses to the generalised strains has to be introduced in its linearised form to close the shell formulation

$$\begin{cases} \delta\mathbf{N} = {}^4\mathbf{L}_{mm} : \delta\mathbf{E} + {}^4\mathbf{L}_{mf} : \delta\boldsymbol{\chi} + {}^3\mathbf{L}_{ms} \cdot \delta\vec{\gamma} \\ \delta\mathbf{M} = {}^4\mathbf{L}_{fm} : \delta\mathbf{E} + {}^4\mathbf{L}_{ff} : \delta\boldsymbol{\chi} + {}^3\mathbf{L}_{fs} \cdot \delta\vec{\gamma} \\ \delta\vec{T} = {}^3\mathbf{L}_{sm} : \delta\mathbf{E} + {}^3\mathbf{L}_{sf} : \delta\boldsymbol{\chi} + {}^2\mathbf{L}_{ss} \cdot \delta\vec{\gamma} \end{cases} \quad (3.6)$$

where the nine tensors  $\mathbf{L}_{ab}$  (with  $a, b = [m, f, s]$ ) are the material tangents governing the membrane ( $m$ ), flexural ( $f$ ) and shearing ( $s$ ) material behaviours and the couplings between each other.

In the sequel, especially for the finite element discretisation, the developments will be expressed in a compact matrix form in order to keep the generality and focus on the physical meaning of the equations. For the Reissner-Mindlin shell formulation sketched above, the following matrices are considered

$$\{q\} = \{v_x v_y \vartheta_x \vartheta_y w\}^T \quad (3.7)$$

$$\{E\} = \{E_{xx} E_{yy} E_{xy} \chi_{xx} \chi_{yy} \chi_{xy} \gamma_x \gamma_y\}^T \quad (3.8)$$

$$\{\Sigma\} = \{N_{xx} N_{yy} N_{xy} M_{xx} M_{yy} M_{xy} T_x T_y\}^T \quad (3.9)$$

$$(3.6) \longrightarrow \{\delta\Sigma\} = [L]\{\delta E\} \quad (3.10)$$

### 3.2.2 Enhanced assumed strain for shear locking avoidance

It is now well known that the discretisation of the transverse shear strain directly from the kinematics definition (3.1) leads to the shear locking problem. In this work, the Discrete Shear Triangle (DST) finite element formulation proposed by Batoz and Dhett (1990) has been implemented to overcome the locking problem. Note that the DST finite element was formulated in Batoz and Dhett (1990) for the linear elastic case. This formulation is here extended in order to take into account material non-linearities in the infinitesimal range.

In the DST formulation, the independent representation  $\vec{\gamma}$  of the transverse shear is based on the rotation equilibrium equation (3.4) with the absence of surface torques and the decoupling of the shear behaviour with the membrane and flexural behaviours, i.e.  ${}^3\mathbf{L}_{ms} = {}^3\mathbf{L}_{sm} = {}^3\mathbf{L}_{fs} = {}^3\mathbf{L}_{sf} = {}^3\mathbf{0}$ .

$$\delta\vec{\gamma} = {}^2\mathbf{L}_{ss}^{-1} \cdot \delta\vec{T} \quad (3.11)$$

$$\vec{T} = \vec{\nabla} \cdot \mathbf{M} \quad (3.12)$$

$$\delta\mathbf{M} = {}^4\mathbf{L}_{fm} : \delta\mathbf{E} + {}^4\mathbf{L}_{ff} : \delta\boldsymbol{\chi} \quad (3.13)$$

In the linear elastic case, the material laws (3.6) are expressed in terms of the total values of stress and strain variables, and can therefore be directly substituted in the rotation equilibrium equation so that

$$\vec{\gamma} = {}^2\mathbf{L}_{ss}^{-1} \cdot \underbrace{\left( \vec{\nabla} \cdot \left( {}^4\mathbf{L}_{fm} : \mathbf{E} + {}^4\mathbf{L}_{ff} : \boldsymbol{\chi} \right) \right)}_{=\vec{T}} \quad (3.14)$$

This relation allows to define the assumed transverse shear strain in particular as a function of the rotation field through the definition of the curvature tensor, see Batoz and Lardeur (1989), Batoz and Dhatt (1990). In the case of material non-linearities, the total stress values used in the rotation equilibrium are not explicitly given by the material laws (3.6), as these laws are expressed in their linearised form. As a consequence, a first-order approximation is assumed to estimate the total stress values needed to represent the assumed transverse shear strain. In the context of an incremental iterative Newton-Raphson resolution scheme, as the total stress values at the iteration (i) of a given incremental step have to be evaluated from the last physical state, and not from the previous iteration, the material tangents computed at the last converged state are considered in the first-order development

$$\mathbf{M}^{(i)} \approx \mathbf{M}^{(0)} + {}^4\mathbf{L}_{\text{fm}}^{(0)} : \Delta \mathbf{E}^{(i)} + {}^4\mathbf{L}_{\text{ff}}^{(0)} : \Delta \boldsymbol{\chi}^{(i)} \quad (3.15)$$

$$\vec{T}^{(i)} \approx \vec{T}^{(0)} + {}^2\mathbf{L}_{\text{ss}}^{(0)} \cdot \Delta \vec{\gamma}^{(i)} \quad (3.16)$$

where the iteration (0) of the current incremental step corresponds to the last converged step. In Equations (3.15) and (3.16), the symbol  $\Delta$  represents the incremental variation of a variable from the last converged state to the current iteration. Substituting (3.15) into (3.12) with the curvature definition (3.2), and neglecting the membrane effects and spatial variations of the material tangents, the assumed transverse shear strain can be extracted from (3.16) and given in the infinitesimal range by

$$\Delta \vec{\gamma}^{(i)} = ({}^2\mathbf{L}_{\text{ss}}^{(0)})^{-1} \cdot \left( {}^4\mathbf{L}_{\text{ff}}^{(0)} : \vec{\nabla} \left( \vec{\nabla} \Delta \vec{\beta}^{(i)} \right)^{\text{sym}} \right) \quad (3.17)$$

Equation (3.17) shows that the interpolation of the assumed transverse shear strain needs at least a quadratic interpolation of the rotation field due to the second derivative. As a consequence, a set of incomplete quadratic shape functions can be introduced to interpolate the rotation field, see Batoz and Dhatt (1990). Considering a local axis system for each side of the element, with s-axis and n-axis respectively tangent and normal to the side, the component  $\beta_s$  is interpolated quadratically along each side whereas the component  $\beta_n$  remains linear. This interpolation introduces one additional degree of freedom  $\alpha_J$  at the middle of each side of the considered element, which leads in a matrix form to

$$\{\beta\} = \sum_{I=1}^{n_n} \mathcal{N}^I \{\beta_I\} + \sum_{J=1}^{n_{\text{side}}} \{\mathcal{P}^J\} \alpha_J \quad (3.18)$$

where  $\mathcal{N}^I$  is a set of linear shape functions and  $\{\mathcal{P}^J\}$  contains only quadratic terms. Substituting the discretisation (3.18) into (3.17), the assumed transverse shear can be interpolated only as a function of the additional parameters  $\{\alpha\}$

$$\{\Delta \vec{\gamma}\} = [B_{s\alpha}] \{\Delta \alpha\} \quad (3.19)$$

Note that the assumed shear strain operator  $[B_{s\alpha}]$  is implicitly a function of the material tangent matrices  $[L_{\text{ss}}]$  and  $[L_{\text{ff}}]$  as shown in (3.17).

In order to eliminate the additional parameters  $\{\alpha\}$ , different conditions can be prescribed by means of either a discrete collocation, see Batoz and Lardeur (1989) or an integral form, see Batoz and Dhatt (1990). In the sequel, the following integral form will be considered

$$\int_{\text{side}} (\gamma_s - \bar{\gamma}_s) ds = 0 \quad \Rightarrow \quad \int_{\text{side}} (\nabla_s w + \beta_s - \bar{\gamma}_s) ds = 0 \quad (3.20)$$

which allows to relate the additional parameters to the classical degrees of freedom, see Batoz and Dhett (1990) for detailed developments in the linear elastic case.

$$\{\Delta\alpha\} = [A_n]\{\Delta q\} \quad (3.21)$$

The discretisation of the membrane strain and curvature fields can be obtained by the derivation of the interpolated displacement fields. Considering a 3-noded shell finite element, a classical linear interpolation is used for the in-plane displacement field  $\vec{v}$ . This choice leads to a constant membrane strains tensor over each element. This motivates the fact that the membrane effects have been neglected in the independent representation of the transverse shear strain since (3.17) is based on the derivation of the Equation (3.15). For the curvature field, the quadratic interpolation (3.18) is derived. Consequently, the generalised strain incremental variation reads in the infinitesimal range

$$\begin{aligned} \begin{Bmatrix} \Delta E \\ \Delta\chi \\ \Delta\bar{\gamma} \end{Bmatrix} &= \begin{bmatrix} B_m & 0 & 0 & 0 \\ 0 & B_{t\theta} & 0 & B_{r\alpha} \\ 0 & 0 & 0 & B_{s\alpha} \end{bmatrix} \begin{Bmatrix} \Delta v \\ \Delta\vartheta \\ \Delta w \\ \Delta\alpha \end{Bmatrix} \\ \Rightarrow \{\Delta E\} &= [B_q \ B_\alpha] \begin{Bmatrix} \Delta q \\ \Delta\alpha \end{Bmatrix} \end{aligned} \quad (3.22)$$

Eliminating the additional parameters variations  $\{\Delta\alpha\}$  in (3.22) by (3.21), the discretised strain fields can be expressed as a function of the nodal degrees of freedom only

$$\{\Delta E\} = ([B_q] + [B_\alpha][A_n])\{\Delta q\} \Rightarrow \{\Delta E\} = [\bar{B}]\{\Delta q\} \quad (3.23)$$

where the operator  $[\bar{B}]$  depends on the material tangents because of the assumed transverse shear strain (3.17). This dependence is required for a proper convergence of the computation scheme.

### 3.3 Embedded discontinuities for the modelling of localised failure

#### 3.3.1 Modelling of shell failure with strong discontinuities

The formulation of a continuum model capturing the localised dissipation observed in failure of shells is presented in this Section.

The global mechanical problem of interest here has been presented in Section 3.2. A flat shell of domain  $\Omega$  is then considered with the Reissner-Mindlin kinematics assumptions. In order to characterise the localised dissipative mechanisms, singular displacement fields are introduced in a local neighbourhood  $\Omega_d \subset \Omega$  of a global material point  $\vec{x}$  where a localised failure mechanism has been detected along a curve  $\Gamma_d \subset \Omega_d$ . The main idea of this kinematics enrichment is to incorporate the associated dissipative effects driven by a local closed-form cohesive law into the global problem (3.5) as the size of this neighbourhood vanishes, see Armero (1999, 2001), Armero and Ehrlich (2006a). For this purpose, the generalised displacement fields in  $\Omega_d$  ( $\vec{v}_\mu, \vec{\vartheta}_\mu, w_\mu$ ) are given by the enrichment of the classical regular generalised displacement fields ( $\vec{v}, \vec{\vartheta}, w$ ) by a discontinuous part according to

$$\begin{cases} \vec{v}_\mu &= \vec{v} + [[\vec{v}_\mu]]\Psi_v \\ \vec{\vartheta}_\mu &= \vec{\vartheta} + [[\vec{\vartheta}_\mu]]\Psi_\vartheta \\ w_\mu &= w + [[w_\mu]]\Psi_w \end{cases} \quad (3.24)$$

where the three local functions  $\Psi_v$ ,  $\Psi_\vartheta$  and  $\Psi_w$  exhibit a unit jump ( $[[\Psi]] = 1$ ) along the curve  $\Gamma_d$ . The discontinuous fields added to the regular fields in (3.24) are expressed in terms of the jumps  $[[\vec{v}_\mu]]$ ,  $[[\vec{\vartheta}_\mu]]$  and  $[[w_\mu]]$  of the in-plane displacement vector, rotation vector and transverse deflection, respectively. Using the classical Reissner-Mindlin theory, the enhanced generalised strain measures in the local neighbourhood are defined by

$$\begin{cases} \mathbf{E}_\mu &= \mathbf{E}(\vec{v}) + \tilde{\mathbf{E}}([[ \vec{v}_\mu ]]) + ([[ \vec{v}_\mu ]] \vec{n})^{\text{sym}} \delta_{\Gamma_d} \\ \boldsymbol{\chi}_\mu &= \boldsymbol{\chi}(\vec{\beta}) + \tilde{\boldsymbol{\chi}}([[ \vec{\vartheta}_\mu ]]) + ([[ \vec{\vartheta}_\mu ]] \vec{n})^{\text{sym}} \delta_{\Gamma_d} \\ \vec{\gamma}_\mu &= \vec{\gamma}(\vec{\vartheta}, w) + \tilde{\vec{\gamma}}([[ \vec{\vartheta}_\mu ]], [[ w_\mu ]]) + [[ w_\mu ]] \vec{n} \delta_{\Gamma_d} \end{cases} \quad (3.25)$$

where  $\vec{n}$  is the unit normal to the curve  $\Gamma_d$  and  $\delta_{\Gamma_d}$  is the Dirac function centred on  $\Gamma_d$ . The first two terms of the right hand side of Equations (3.25) represent the regular part of the generalised strain measures in the bulk part of the neighbourhood ( $\Omega_d \setminus \Gamma_d$ ).

The determination of the new fields  $\vec{v}_\mu$ ,  $\vec{\vartheta}_\mu$  and  $w_\mu$  defined along  $\Gamma_d$  requires the consideration of an additional equation to connect these local fields with the global problem (3.5) in  $\Omega_d$ . The physical meaning of the additional fields as being the jumps of the local generalised displacements points directly to the consideration of the weak form of the local equilibrium equation along  $\Gamma_d$

$$\int_{\Gamma_d} \left[ \delta [[ \vec{v}_\mu ]] \cdot (\vec{N}_d - \mathbf{N} \cdot \vec{n}) + \delta [[ \vec{\vartheta}_\mu ]] \cdot (\vec{M}_d - \vec{e}_z \times (\mathbf{M} \cdot \vec{n})) + \delta [[ w_\mu ]] (T_d - \vec{T} \cdot \vec{n}) \right] d\Gamma = 0 \quad (3.26)$$

for all variations  $\delta [[ \vec{v}_\mu ]]$ ,  $\delta [[ \vec{\vartheta}_\mu ]]$  and  $\delta [[ w_\mu ]]$  in  $\Gamma_d$ . Equation (3.26) rules, under a weak form, the continuity of the generalised tractions along the discontinuity curve and allows to define the membrane force vector  $\vec{N}_d$ , the bending moment vector  $\vec{M}_d$  and the transverse force scalar  $T_d$  across the discontinuity in terms of the corresponding generalised stresses  $\mathbf{N}$ ,  $\mathbf{M}$ , and  $\vec{T}$  in the bulk  $\Omega_d \setminus \Gamma_d$  and their projection on the discontinuity curve  $\Gamma_d$ . Note that the bending moment vector  $\vec{M}_d$  is work conjugate to the rotation jump vector  $[[ \vec{\vartheta}_\mu ]]$ , and not to  $[[ \vec{\beta}_\mu ]]$ . As a consequence, the components of the vector  $\vec{M}_d$  correspond to the couples along the reference axes. Following this convention, the bending moment tensor  $\mathbf{M}$  has to be properly projected on the discontinuity line by  $\vec{e}_z \times (\mathbf{M} \cdot \vec{n})$  as used in Equation (3.26) in order to make the projection of  $\mathbf{M}$  correspond to the vector  $\vec{M}_d$ .

As a material response is used to link the bulk strains to the bulk stresses in the global problem, a constitutive law needs to be defined in the local neighbourhood to close the formulation. This law characterises the cohesive behaviour of the discontinuity by relating the generalised stresses across the discontinuity to the generalised displacement jumps

$$\begin{cases} \delta \vec{N}_d &= {}^2\mathbf{C}_{mm}^d \cdot \delta [[ \vec{v}_\mu ]] + {}^2\mathbf{C}_{mf}^d \cdot \delta [[ \vec{\vartheta}_\mu ]] + {}^1\mathbf{C}_{ms}^d \delta [[ w_\mu ]] \\ \delta \vec{M}_d &= {}^2\mathbf{C}_{fm}^d \cdot \delta [[ \vec{v}_\mu ]] + {}^2\mathbf{C}_{ff}^d \cdot \delta [[ \vec{\vartheta}_\mu ]] + {}^1\mathbf{C}_{fs}^d \delta [[ w_\mu ]] \\ \delta T_d &= {}^1\mathbf{C}_{sm}^d \cdot \delta [[ \vec{v}_\mu ]] + {}^1\mathbf{C}_{sf}^d \cdot \delta [[ \vec{\vartheta}_\mu ]] + {}^0\mathbf{C}_{ss}^d \delta [[ w_\mu ]] \end{cases} \quad (3.27)$$

where the tensors  $\mathbf{C}_{ab}^d$  (with  $a, b = [m, f, s]$ ) are the material tangents of the discontinuity incorporating potential inelastic effects as needed for the particular material under consideration.

Note again that the interest of the formulation presented here lies in the local character of Equation (3.26) in contrast with the global Equation (3.5), and the fact that its solution defines the local enriched displacement fields as functions of the global displacement fields allowing the elimination of these local fields in the global problem, see Armero

(1999, 2001). Therefore, the existence of solutions of Equation (3.26) can be obtained by considering the limit of a vanishing local neighbourhood in the sense that

$$h_d = \frac{\text{measure}(\Omega_d)}{\text{measure}(\Gamma_d)} \longrightarrow 0 \quad (3.28)$$

for a fixed global domain  $\Omega$ . As discussed in Armero (2001), the resulting problem can be shown to have a solution incorporating the dissipative effects of the local cohesive law in the global problem whose solution represents the main purpose in all these considerations.

### 3.3.2 Shell finite elements with embedded strong discontinuities

The finite element setting corresponding to the above continuum framework of strong discontinuities is discussed in this Section. For the sake of clarity and generality, the following developments are presented in a compact matrix format.

#### Global finite element problem

In the continuum approach presented in the previous Section, the global boundary value problem (3.5) can be approximated numerically by the standard finite element discretisation. The domain  $\Omega$  is discretised with a mesh of elements  $\Omega_e^h$ . The global generalised displacements can be interpolated through a standard set of shape functions. The generalised strain measures can be expressed in terms of the nodal displacements and rotations

$$\{\varepsilon^h\} = [\bar{B}]\{q\} \quad (3.29)$$

where  $[\bar{B}]$  is the generic strain operator. This operator defines the appropriate assumed strain formulation for the bulk response in order, for instance, to avoid shear-locking in Reissner-Mindlin formulation as shown in Section 3.2. The global problem (3.5) can therefore be discretised as

$$\{R\} = \{f_{ext}\} - \mathbf{A} \left( \int_{\Omega_e^h} [\bar{B}]^T \{\sigma\} d\Omega \right) = \{0\} \quad (3.30)$$

by introducing the standard assembly operator  $\mathbf{A}$  of all the elements of the mesh  $\Omega^h$ .

#### Embedded strong discontinuities as element enhancements

In order to keep the continuum aspect of the classical finite element framework, the discontinuities have been embedded in a local neighbourhood  $\Omega_d$  vanishing in the limit. In the discrete approach, this neighbourhood can be identified as a finite element  $\Omega_e^h$  where a discontinuity has been detected by an appropriate criterion. In this context, note that the limit relation (3.28) corresponds to the fundamental notion of mesh refinement. In order to discretise the discontinuity, a straight segment  $\Gamma_e^h$ , named the discontinuity line, is considered through a given element  $\Omega_e^h$  for the shell problem of interest here.

A local interpolation of the displacement jump fields introduced in Equation (3.24) is considered

$$\{[q_e^h]\} = [J]\{\xi\} \quad (3.31)$$

in terms of a set of local element parameter  $\{\xi\}$  and associated jump interpolation functions  $[J]$  along  $\Gamma_e^h$ . The degree of these jump interpolation functions can be a priori

chosen. For the case of plane kinematics, this approach has been first developed with constant jumps along the discontinuity line, see Armero (1999), and recently extended to linear jump interpolations in order to avoid stress locking in more complex failure mode, see Linder and Armero (2007). For the case of plate or shell kinematics, as the transverse deflection is related to the rotation through the transverse shear strain definition, the transverse deflection jump  $[[w_e^h]]$  has to be interpolated as a function of the rotation jump parameters, see Armero and Ehrlich (2006a). This requires the introduction of an articulation point located at position  $\vec{x}_{\Gamma_e^h}$  which is the centre of the rotation jump. The position of this point can be a priori chosen along the discontinuity line. For the sequel, a constant interpolation will be considered for the membrane and rotation jumps and the discontinuity line will be introduced at the geometrical centre of the element. The transverse deflection jump will therefore be a linear function of the rotation jump, as shown in Equation (3.32). The constant term  $\xi_w$  corresponds to the transverse deflection jump at the articulation point, see Figure 3.2.

$$\begin{cases} [[\vec{v}_e^h]] &= \vec{\xi}_v \\ [[\vec{\vartheta}_e^h]] &= \vec{\xi}_\vartheta \\ [[w_e^h]] &= \xi_w - (\vec{x} - \vec{x}_{\Gamma_e^h}) \cdot \vec{\xi}_\beta \\ &= \xi_w + \vec{\xi}_\vartheta \cdot [(\vec{x} - \vec{x}_{\Gamma_e^h}) \times \vec{e}_z] \\ &= \xi_w + (y - y_{\Gamma_e^h})\xi_{\vartheta_x} - (x - x_{\Gamma_e^h})\xi_{\vartheta_y} \end{cases} \quad (3.32)$$

$$\Rightarrow [J] = \begin{bmatrix} 1 & 0 & 0 & 0 & 0 \\ 0 & 1 & 0 & 0 & 0 \\ 0 & 0 & 1 & 0 & 0 \\ 0 & 0 & 0 & 1 & 0 \\ 0 & 0 & (y - y_{\Gamma_e^h}) & -(x - x_{\Gamma_e^h}) & 1 \end{bmatrix} \quad (3.33)$$

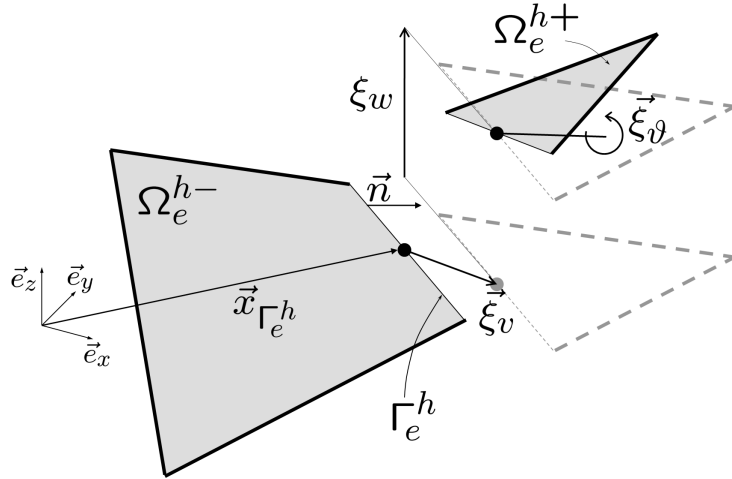


Figure 3.2: Embedded strong discontinuity for a shell element.

Due to the new five element parameters  $\{\xi\} = \{\xi_{v_x}, \xi_{v_y}, \xi_{\vartheta_x}, \xi_{\vartheta_y}, \xi_w\}^T$ , the discretisation of the regular part of the generalised strain measures introduced in Equation (3.25) takes the form

$$\{\varepsilon^h\} = [\bar{B}]\{q\} + [G_{(c)}]\{\xi\} \quad (3.34)$$

where  $[G_{(c)}]$  is a linear strain operator, named compatibility operator, incorporating the jump effects into the bulk strains, see Armero (1999), Jirásek (2000).

Before defining a general procedure to determine the compatibility operator  $[G_{(c)}]$ , the simple case of a unidimensional bar element is considered to interpret the influence of this operator and the effect of the jump on the bulk deformation, see Figure 3.3. Without localisation, the infinitesimal elongation of the bar is simply given by the ratio between the relative displacement and the bar length, see Figure 3.3 (b). Upon localisation, Figure 3.3 (c) shows that the elongation of the bulk is smaller by considering the same total relative displacement. Indeed, this bulk elongation is given by the ratio between the effective relative displacement  $(u - \xi)$  and the bar length. In this simple example, it clearly appears that the enhanced compatibility operator is equal to the opposite of the classical strain operator. The new enhanced operator therefore allows to reduce the bulk strain during the deformation localisation process. Once the deformation is completely localised, which corresponds to a fully softened state, the strain bulk vanishes and the total relative displacement is entirely given by the jump, see Figure 3.3 (d).

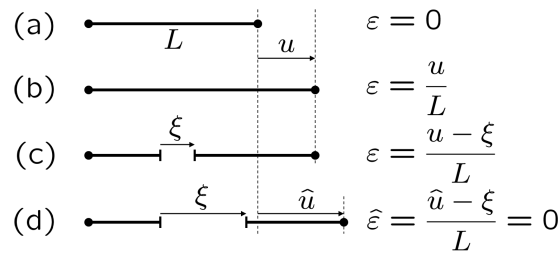


Figure 3.3: Interpretation of the compatibility operator  $[G_{(c)}]$  in the case of a bar element: (a) undeformed configuration, (b) deformed configuration without localisation, (c) deformed configuration with localisation, (d) fully softened state.

In a general way, the determination of the compatibility operator  $[G_{(c)}]$  relies on the design of stress locking-free finite elements. In other words, the kinematics of a fully softened discontinuity has to be correctly resolved without any spurious transfer of stresses across the discontinuity. This state is referred to as the discontinuity mode, see Armero and Ehrlich (2006a). This corresponds to no traction along the discontinuity line with no stress resultants, and consequently vanishing strain measures, in the bulk of the element

$$\{\hat{\varepsilon}^h\} = [\bar{B}]\{\hat{q}\} + [G_{(c)}]\{\xi\} = \{0\} \quad \forall \{\xi\} \quad (3.35)$$

The displacements of a node  $I$  of an element presenting a discontinuity mode can easily be expressed in terms of the jump parameters and a rigid displacement for the sake of generality

$$\{\hat{q}_I\} = \{q_{\text{rigid}}\} + \mathcal{H}_{\Gamma_e^h}[J^I]\{\xi\} \quad (3.36)$$

where  $\mathcal{H}_{\Gamma_e^h}$  is the Heaviside function centred on the discontinuity line  $\Gamma_e^h$ . This line subdivides the element into both domains  $\Omega_e^{h-}$  and  $\Omega_e^{h+}$ , see Figure 3.2, in which the Heaviside function takes the values 0 and 1, respectively. Substituting (3.36) in (3.35), it can be shown that the compatibility operator is given by

$$[G_{(c)}] = - \sum_{I \in \Omega_e^{h+}} [\bar{B}^I][J^I] \quad (3.37)$$

where only the contribution of the nodes belonging to the domain  $\Omega_e^{h+}$  is taken into account.

### Local discrete equilibrium equations along the discontinuity

As presented in Section 3.3.1 for the continuum framework, the enrichment of the displacement fields by additional jump fields leads to the definition of an additional set of Equations (3.26) which corresponds to the stress continuity condition across the discontinuity line. In their discrete version, these local equations can be expressed in a compact matrix form as follows

$$\int_{\Gamma_e^h} \{\delta[q_e^h]\}^T (\{\sigma_d\} - \{\sigma_n\}) d\Gamma = 0 \quad \forall \{\delta[q_e^h]\} \quad (3.38)$$

where the column vector  $\{\sigma_d\}$  collects the stress resultants of the discontinuity and  $\{\sigma_n\}$  is the column vector collecting the projections of the stress resultants on the discontinuity line of normal  $\vec{n}$  with  $\{\sigma_n\} = [n]\{\sigma\}$  where  $[n]$  is a projection matrix based on the components of the unit normal vector  $\vec{n}$ , see Equation (3.39).

$$\begin{pmatrix} N_{n_x} \\ N_{n_y} \\ M_{n_x} \\ M_{n_y} \\ T_n \end{pmatrix} = \begin{bmatrix} n_x & 0 & n_y & 0 & 0 & 0 & 0 & 0 \\ 0 & n_y & n_x & 0 & 0 & 0 & 0 & 0 \\ 0 & 0 & 0 & 0 & -n_y & -n_x & 0 & 0 \\ 0 & 0 & 0 & n_x & 0 & n_y & 0 & 0 \\ 0 & 0 & 0 & 0 & 0 & 0 & n_x & n_y \end{bmatrix} \begin{pmatrix} N_{xx} \\ N_{yy} \\ N_{xy} \\ M_{xx} \\ M_{yy} \\ M_{xy} \\ T_x \\ T_y \end{pmatrix} \quad (3.39)$$

Substituting the jump discretisation (3.31) into (3.38), the stress continuity condition reads

$$\int_{\Gamma_e^h} [J]^T \{\sigma_d\} d\Gamma - \int_{\Gamma_e^h} [J]^T [n] \{\sigma\} d\Gamma = \{0\} \quad (3.40)$$

As the generalised bulk stresses  $\{\sigma\}$  are defined naturally in the bulk and, in particular, are known at the quadrature points used in the evaluation of the integral in (3.30), a projection scheme has to be defined in order to integrate the bulk stresses along the discontinuity line. For this reason, a new operator  $[G_{(e)}]$ , named equilibrium operator, is introduced to approximate the local discrete equilibrium, see Armero (1999), Jirásek (2000), Armero and Ehrlich (2006a), which then reads

$$\int_{\Omega_e^h} [G_{(e)}]^T \{\sigma\} d\Omega + \int_{\Gamma_e^h} [J]^T \{\sigma_d\} d\Gamma = \{0\} \quad (3.41)$$

Based on this consideration, the equilibrium operator, a priori different from the compatibility operator  $[G_{(c)}]$ , has to satisfy the following conditions

$$\int_{\Omega_e^h} [G_{(e)}]^T \{\sigma\} d\Omega = - \int_{\Gamma_e^h} [J]^T [n] \{\sigma\} d\Gamma + l_{\Gamma_e^h} o(h_e^{p+1}) \quad (3.42)$$

where  $h_e$  is the ratio between the element area and the discontinuity length. It is recalled that the dissipative effects driven by the local closed-form cohesive law are incorporated into the global problem by considering the limit of a vanishing local neighbourhood (3.28), which corresponds to the limit of refining meshes ( $h_e \rightarrow 0$ ), see Armero (1999, 2001), Armero and Ehrlich (2006a). As the purpose of the equilibrium operator is to project the bulk stresses on the discontinuity line, this is assumed to be expressed by the form

$[G_{(e)}]^T = -1/h_e[F(x, y)]^T[n]$ . The matrix function  $[F(x, y)]$  can be determined in such a way that the condition (3.42) is exactly satisfied, with no higher order terms, for complete polynomials of order up to  $p$

$$\frac{1}{h_e} \int_{\Omega_e^h} [F(x, y)]^T x^k y^l d\Omega = \int_{\Gamma_e^h} [J]^T x^k y^l d\Gamma \quad (3.43)$$

for all  $k, l = \{0, 1, \dots, p\}$  with  $k + l \leq p$ , see Armero and Ehrlich (2006a) for detailed developments.

Considering linear spatial variations of the stress fields on the elements, the approximation order can be restricted to  $p = 1$ . As a consequence, the matrix function  $[F]$  is a set of complete linear polynomials such that  $F_{ij} = a_{ij} + b_{ij}x + c_{ij}y$  with  $i, j = \{1, 2, \dots, 5\}$ . After straightforward manipulations, it can be show that the coefficients of the functions  $F_{ij}$  are given by

$$\begin{Bmatrix} a_{ij} \\ b_{ij} \\ c_{ij} \end{Bmatrix} = h_e \left( \int_{\Omega_e^h} \begin{bmatrix} 1 & x & y \\ x & x^2 & xy \\ x & xy & y^2 \end{bmatrix} d\Omega \right)^{-1} \left( \int_{\Gamma_e^h} J_{ij} \begin{Bmatrix} 1 \\ x \\ y \end{Bmatrix} d\Gamma \right) \quad (3.44)$$

$$\text{with } i, j = \{1, 2, \dots, 5\}$$

Note that in the case of constant stress fields on the elements ( $p = 0$ ) and an articulation point at the middle of the discontinuity line, the functions  $F_{ij}$  are strongly simplified leading to

$$F_{ij} = \begin{cases} J_{ij} & \text{for constant } J_{ij} \\ 0 & \text{for linear } J_{ij} \end{cases} \quad \text{with } i, j = \{1, 2, \dots, 5\} \quad (3.45)$$

In this particular case, the coupling between the rotation jumps and the deflection jumps, due to the non-diagonal terms of jump interpolation matrix  $[J]$  (see Equation (3.33)) vanishes in the stress continuity condition.

Note also that the equilibrium operator is completely determined by knowing the geometry of the element and the position of the discontinuity line. Moreover, these local equations identify weakly the driving stress of the discontinuity which are linked to the jump parameters through the considered cohesive law governing the response of the discontinuity.

## Numerical implementation

In this Section, the numerical implementation of the finite element method described above is outlined. This leads to the resolution of the discrete global equilibrium (3.30) together with the discrete enhanced local equilibrium (3.41). For the sake of clarity, the following development is considered at the element level. The global problem may be constructed by using a classical assembly scheme. The element equilibrium equations can therefore be rewritten by introducing the internal forces  $\{f_{e,q}^{\text{int}}\}$  and  $\{f_{e,\xi}^{\text{int}}\}$  corresponding to the displacement and jump degrees of freedom, respectively.

$$\{f_{e,q}^{\text{int}}\} = \int_{\Omega_e^h} [\bar{B}]^T \{\sigma\} d\Omega \quad (3.46a)$$

$$\{f_{e,\xi}^{\text{int}}\} = \int_{\Omega_e^h} [G_{(e)}]^T \{\sigma\} d\Omega + \int_{\Gamma_e^h} [J]^T \{\sigma_d\} d\Gamma \quad (3.46b)$$

Note that  $\{f_{e,\xi}^{\text{int}}\}$  does not represent internal forces in the physical sense, but has to be considered as a residual associated to the equilibrium along the discontinuity. A classical incremental iterative Newton-Raphson procedure can be used to solve this system of equations. For this purpose, the equilibrium equations are linearised as followed

$$[K_{e,qq}]^{(i-1)}\{\delta q\}^{(i)} + [K_{e,q\xi}]^{(i-1)}\{\delta\xi\}^{(i)} = \{f^{\text{ext}}\} - \{f_{e,q}^{\text{int}}\}^{(i-1)} \quad (3.47a)$$

$$[K_{e,\xi q}]^{(i-1)}\{\delta q\}^{(i)} + [K_{e,\xi\xi}]^{(i-1)}\{\delta\xi\}^{(i)} = \{0\} - \{f_{e,\xi}^{\text{int}}\}^{(i-1)} \quad (3.47b)$$

for the iterative increments of the displacement and jump degrees of freedom at iteration  $(i)$ . The stiffness matrices are given by

$$[K_{e,qq}] = \int_{\Omega_e^h} [\bar{B}]^T [L] [\bar{B}] \, d\Omega \quad (3.48a)$$

$$[K_{e,q\xi}] = \int_{\Omega_e^h} [\bar{B}]^T [L] [G_{(c)}] \, d\Omega \quad (3.48b)$$

$$[K_{e,\xi q}] = \int_{\Omega_e^h} [G_{(e)}]^T [L] [\bar{B}] \, d\Omega \quad (3.48c)$$

$$[K_{e,\xi\xi}] = \int_{\Omega_e^h} [G_{(e)}]^T [L] [G_{(c)}] \, d\Omega + \int_{\Gamma_e^h} [J]^T [C_d] [J] \, d\Gamma \quad (3.48d)$$

where  $[L]$  and  $[C_d]$  are the material tangent matrices of, respectively, the bulk response in  $\Omega_e^h \setminus \Gamma_e^h$  and the cohesive law introduced along  $\Gamma_e^h$  defined by the consistent linearisations

$$\{\delta\sigma\} = [L]\{\delta\varepsilon\} \quad (3.49a)$$

$$\{\delta\sigma_d\} = [C_d]\{\delta[[q_e]]\} \quad (3.49b)$$

As the compatibility and equilibrium operators  $[G_{(c)}]$  and  $[G_{(e)}]$  are a priori different, the complete stiffness matrix introduced in Equations (3.47) is not symmetric. Note that the stiffness matrices and the internal forces in (3.47) are evaluated at the last iteration  $(i-1)$ . One Gauss quadrature point over the element and along the discontinuity line will be used to evaluate the integrals in (3.48).

Note also that the second set of equations in (3.47) holds independently for each element  $\Omega_e^h$  where a discontinuity has been introduced, consequently no assembling is required for the secondary degrees of freedom associated with the jumps along the discontinuity and the iterative increments of the local degrees of freedom  $\{\delta\xi\}$  can be statically condensed and only the global solution of a system of equations on the iterative increments of the displacement degrees of freedom is required. The final condensed system of equation reads then

$$[K_{e,qq}^*]^{(i-1)}\{\delta q\}^{(i)} = \{f^{\text{ext}}\} - \{f_{e,q}^{\text{int}*}\}^{(i-1)}$$

with 
$$\begin{cases} [K_{e,qq}^*]^{(i-1)} = [K_{e,qq}]^{(i-1)} - [K_{e,q\xi}]^{(i-1)} ([K_{e,\xi\xi}]^{(i-1)})^{-1} [K_{e,\xi q}]^{(i-1)} \\ \{f_{e,q}^{\text{int}*}\}^{(i-1)} = \{f_{e,q}^{\text{int}}\}^{(i-1)} - [K_{e,q\xi}]^{(i-1)} ([K_{e,\xi\xi}]^{(i-1)})^{-1} \{f_{e,\xi}^{\text{int}}\}^{(i-1)} \end{cases} \quad (3.50)$$

and the iterative increments of the jump parameters can be recovered at the element level by

$$\{\delta\xi\}^{(i)} = - ([K_{e,\xi\xi}]^{(i-1)})^{-1} (\{f_{e,\xi}^{\text{int}}\}^{(i-1)} + [K_{e,\xi q}]^{(i-1)}\{\delta q\}^{(i)}) \quad (3.51)$$

# Chapter 4

## Multi-scale detection of failure in planar masonry thin shells using computational homogenisation

This Chapter presents a computational homogenisation-based technique for localisation detection in planar masonry shells. A computational homogenisation procedure is used for the in-plane and the out-of-plane behaviour of masonry walls taking the periodicity of the material into account. The quasi-brittle nature of the masonry constituents results in initial and damage-induced (evolving) anisotropy properties with localisation of damage at both the structural and fine scales. Using a closed-form damage model at the mesoscopic scale, it is shown that a structural scale localisation criterion based on the acoustic tensor adapted to shell kinematics allows to detect the structural scale localisation. This detection identifies average preferential cracking orientations consistent with the stacking mode of masonry for both in-plane and out-of-plane failure. This approach is illustrated by examples of bed joint and stair-case failure, and its subsequent integration in multi-scale nested computational schemes is discussed.

### 4.1 Introduction

The formulation of macroscopic constitutive laws for the behaviour of masonry is a complex task, due to its strongly heterogeneous microstructure which considerably influences its overall mechanical behaviour. Because of the quasi-brittle nature of its constituents, this results in initial and damage-induced (evolving) anisotropic properties, accompanied with localisation of damage at both the structural and constituents scales.

Closed-form laws have therefore been developed for equivalent two-dimensional or three-dimensional media for elastic and cracking behaviour. Some of these formulations only take into account the low or vanishing tensile strength of the material without explicitly accounting for its specific material symmetries, see Cuomo and Ventura (2000), Pietruszczak and Ushaksaraei (2003). Other models were therefore developed to account for the initial and/or induced anisotropy for damaging laws, see Papa and Nappi (1997),

---

This Chapter is based on: B.C.N. Mercatoris, P. Bouillard and T.J. Massart, Multi-scale detection of failure in planar masonry thin shells using computational homogenisation, *Engineering Fracture Mechanics*, 76(4), 479–499, 2009.

Berto et al. (2002), plastic behaviour, see Lourenço et al. (1997), or time-dependent behaviour, see van Zijl et al. (2001). Some of these models were later used in the modelling of plate failure, as performed in Lourenço (2000), where plane stress constitutive models were integrated across the thickness of plates.

The use of such models in the cracking regime is however impeded by their costly and cumbersome identification. As a complementary approach to closed-form constitutive relations, multi-scale computational strategies started to emerge as alternative options, transferring most of the cost to the computational effort rather than to experimental identification. Their aim is to deduce a homogenised response at the structural scale from a representative volume element (RVE), based on constituents properties and averaging theorems.

These approaches were first proposed for the elastic behaviour of masonry, starting with Pande et al. (1989). The periodic nature of the material has been further exploited in Anthoine (1995), and has led to parametric studies, see Cecchi and Sab (2002a), and to the study of particular assumptions related to the deformability of units, see Cecchi and Di Marco (2000), Cecchi and Rizzi (2001). New averaging schemes have been developed recently, based on polynomial stress expansions combined with homogenisation concepts in Zucchini and Lourenço (2002). The homogenisation principles were also extended towards elastic plate models for out-of-plane loading. Several homogenisation techniques based on different assumptions were therefore proposed. A Kirchhoff-Love shell model was developed to characterise the elastic masonry behaviour by means of an asymptotic homogenisation method, see Cecchi and Sab (2002b). In order to enhance this model, shear effects were added leading to the identification of a Reissner-Mindlin homogenised model, compared with a discrete three-dimensional model and the aforementioned Kirchhoff-Love model, see Cecchi and Sab (2004). In both models, the case of rigid bricks connected by elastic interfaces which represent the mortar joints is considered. Another elastic Reissner-Mindlin shell model was proposed in Cecchi and Sab (2007) where both elastic bricks and elastic mortar joints are considered. A periodic homogenisation scheme has also been developed recently in Mistler et al. (2007) to derive elastic Kirchhoff-Love shell stiffness properties of running bond masonry. Note that this scheme may be adapted for non-linear material response as will be illustrated below, and may be considered as a special case of a more general computational homogenisation scheme based on a second-order solution strategy proposed in Geers et al. (2007) for structured thin sheets.

Homogenisation techniques were also defined to investigate the average material behaviour of masonry in the non-linear range. An analytical approach to the ultimate strength of masonry was proposed in De Buhan and De Felice (1997). Specific loading paths were considered in Pegon and Anthoine (1997), Anthoine (1997); later complemented by investigations with an emphasis on damage-induced anisotropy in Massart et al. (2004), or on failure locus identification in Massart et al. (2005b).

Their incorporation into structural computations have subsequently been proposed. For in-plane loaded structures, homogenised descriptions were combined with limit analysis concepts and optimisation techniques, to compute ultimate strength properties both for material characterisation, see Milani et al. (2006a), and for structural computations, see Milani et al. (2006b). As extensions to the non-linear behaviour, two limit analysis approaches were developed in order to derive the failure surfaces of out-of-plane loaded running bond masonry walls using optimisation procedures. First, a limit analysis was combined with a homogenisation technique under the assumptions of perfect plasticity and associated flow rule for both the bricks and the mortar joints, see Milani et al. (2006c).

The case of rigid bricks connected by mortar joints reduced to interfaces with rigid-plastic behaviour was considered in a limit analysis approach for the Reissner-Mindlin shell kinematics in order to estimate the influence of joint shear strength on the collapse load, see Cecchi et al. (2007).

Another complementary approach consists in using multi-scale computational approaches of the FE<sup>2</sup> type as proposed in Feyel and Chaboche (2000), Smit et al. (1998). A first step in this respect has been proposed in Luciano and Sacco (1997, 1998) where off-line periodic homogenisation was used in combination with a binary damage model, assuming perfectly brittle joints, but without any structural scale localisation treatment. It is now well known to be crucial in such a multi-scale computational framework to detect and treat the localisation of damage at both the structural and fine scales in order to keep a well-posed problem. In order to build a consistent multi-scale framework, the detection of localisation at the structural scale has then to be based on the homogenised response of the microstructure. Such an extension has been proposed recently in Massart et al. (2007a) for in-plane loaded structures. The extension of the required structural scale localisation detection procedure based on masonry shell homogenisation is the objective of this contribution. It will be shown how the out-of-plane computational homogenisation approach proposed in Mistler et al. (2007), but used here with masonry constituents non-linear properties, coupled to a localisation criterion adapted to shell kinematics, allows to identify localisation orientations strongly related to the preferential damage patterns of masonry.

The Chapter is structured as follows. The computational homogenisation for in-plane and out-of-plane behaviours proposed in Mistler et al. (2007) is first briefly recalled in Section 4.2. A simple scalar damage model with interface elements used for the joints at the fine scale is formulated in Section 4.3. Based on a procedure defined in Section 4.4 to detect localisation and to identify average localisation orientations in shells at the structural scale, it is shown in Section 4.5 that the combination of these tools allows to detect structural localisation orientations consistent with fine-scale damage patterns when both in-plane and out-of-plane loading patterns are considered. Finally, a discussion of the proposed localisation analysis is given in Section 4.6, before the conclusions and prospects, given in Section 4.7.

## 4.2 Masonry homogenisation

### 4.2.1 Scales of interest for masonry mechanical behaviour

As in any heterogeneous material, several scales of interest can be identified in masonry structures. First, the structural or macroscopic scale is used to define complete masonry structures and their external loads and boundary conditions. When postulated at this scale, the constitutive law links the average strain and stress fields. At the lower or mesoscopic scale based on the size of the basic constituents of masonry, namely bricks and mortar joints, the heterogeneous nature of the material appears. Some of the effects observed at the macroscopic scale, such as damage-induced anisotropy, are mainly governed by damage growth taking place at the mesoscopic scale, together with the stacking mode characterising the mesostructure. Postulating and identifying macroscopic laws accounting for such effects may be difficult, especially when flexural behaviour of shells is considered. Using plane stress closed-form laws integrated across the thickness of shells may be considered as a viable option in certain cases, see Lourenço (2000), but raises

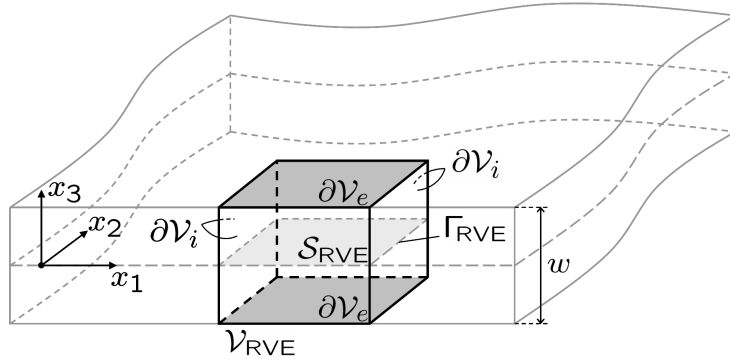


Figure 4.1: Through-thickness RVE for shells.

questions in terms of accuracy of the thickness integration when damage localisation is appearing. Therefore, the use of through-thickness homogenisation of three-dimensional RVEs may be helpful in characterising and identifying constitutive laws linking shell kinematical quantities to membrane forces and bending moments.

#### 4.2.2 Computational homogenisation of thin masonry shell properties

The purpose of a computational homogenisation procedure is to obtain numerically the average macroscopic response of a heterogeneous material from the underlying mesostructure of the material and the behaviour of its constituents. It is based on the solution of a mesostructural problem on the RVE relying on averaging theorems. This approach uses the fundamental assumption that the material configuration is macroscopically homogeneous, but microscopically heterogeneous, see Kouznetsova et al. (2001). This principle is known as the separation of scales. For the case of masonry walls, the characteristic length of the structure is considered to be much larger than the RVE one.

##### Shell kinematics and averaging relations

A through-thickness RVE for shells is depicted in Figure 4.1 where  $\mathcal{V}_{\text{RVE}}$  is the volume of the RVE,  $\mathcal{S}_{\text{RVE}}$  is the reference surface,  $\Gamma_{\text{RVE}}$  is the contour of the reference surface,  $\partial\mathcal{V}_e$  consists of the two external faces,  $\partial\mathcal{V}_i$  consists of the four lateral internal faces, and  $w$  is the shell thickness. The averaging theorems linking the coarse (macro) scale and the fine (meso) scale quantities have to be verified for the strain, the stress and the work variations. If the macroscopic description is based on the Kirchhoff-Love shell kinematics, it is postulated that the macroscopic membrane strain tensor  $\mathbf{E}$  is the average of the local membrane strain tensor over the reference surface  $\mathcal{S}_{\text{RVE}}$ , see Equation 4.1a. The macroscopic curvature tensor  $\boldsymbol{\chi}$  is assumed to be the surface average of the local curvature tensor over  $\mathcal{S}_{\text{RVE}}$ , see Equation 4.1b. Note that the Reissner-Mindlin shell kinematics is not used in this first study. The introduction of the transverse shear effects in a shell computational homogenisation procedure based on a 3D through-thickness RVE still raises questions as shown in Geers et al. (2007). In the following developments, Greek subscripts vary from 1 to 2 only and correspond to the in-plane components. The subscript 3 corresponds to the out-of-plane component, see Figure 4.1.

$$E_{\alpha\beta} = \frac{1}{\mathcal{S}_{\text{RVE}}} \int_{\mathcal{S}_{\text{RVE}}} (u_{\alpha,\beta})^{\text{sym}} d\mathcal{S}_{\text{RVE}} \quad (4.1a)$$

$$\chi_{\alpha\beta} = \frac{-1}{\mathcal{S}_{\text{RVE}}} \int_{\mathcal{S}_{\text{RVE}}} u_{3,\alpha\beta} d\mathcal{S}_{\text{RVE}} \quad (4.1b)$$

Using the divergence theorem to express these strain measures in terms of RVE boundary quantities, relations (4.1) lead respectively to

$$E_{\alpha\beta} = \frac{1}{\mathcal{S}_{\text{RVE}}} \oint_{\Gamma_{\text{RVE}}} (u_{\alpha} n_{\beta})^{\text{sym}} d\Gamma_{\text{RVE}} \quad (4.2a)$$

$$\chi_{\alpha\beta} = \frac{-1}{\mathcal{S}_{\text{RVE}}} \oint_{\Gamma_{\text{RVE}}} (u_{3,\alpha} n_{\beta})^{\text{sym}} d\Gamma_{\text{RVE}} \quad (4.2b)$$

where  $\vec{n}$  is the outer normal to  $\Gamma_{\text{RVE}}$ .

In a computational homogenisation technique, the energy consistency is classically assumed, and expressed by

$$N_{\alpha\beta} \delta E_{\alpha\beta} + M_{\alpha\beta} \delta \chi_{\alpha\beta} = \frac{1}{\mathcal{S}_{\text{RVE}}} \int_{\mathcal{V}_{\text{RVE}}} \sigma_{ij} \delta \varepsilon_{ij} dV_{\text{RVE}} \quad (4.3)$$

where  $\boldsymbol{\varepsilon}$ , or  $\varepsilon_{ij} = (u_{i,j})^{\text{sym}}$  is the (local) mesostructural infinitesimal strain tensor work conjugate to the mesoscopic stress field  $\boldsymbol{\sigma}$ , and  $\mathbf{N}$  and  $\mathbf{M}$  are respectively the macroscopic membrane force and bending moment tensors. Equation (4.3) enforces that the macroscopic work density variation is equal to the volume integral of the mesoscopic work density variation performed on the RVE divided by the reference surface.

The right hand side of Equation (4.3) can be integrated by parts after introducing the definition of the mesostructural infinitesimal strain tensor. Applying then the divergence theorem with the fact that the mesoscopic stress field  $\boldsymbol{\sigma}$  is divergence-free (absence of body forces) and that no surface forces are applied on  $\partial\mathcal{V}_e$ , it can be shown that the macroscopic work density variation depends on the work variation of the traction  $t_i = \sigma_{ij} n_j$  on  $\partial\mathcal{V}_i$ . Therefore, the energy consistency (4.3) leads to

$$N_{\alpha\beta} \delta E_{\alpha\beta} + M_{\alpha\beta} \delta \chi_{\alpha\beta} = \frac{1}{\mathcal{S}_{\text{RVE}}} \int_{\partial\mathcal{V}_i} t_i \delta u_i d\partial\mathcal{V}_i \quad (4.4)$$

The satisfaction of both averaging relations (4.1) and (4.3) for given boundary conditions on the RVE leads to the satisfaction of the averaging theorem for the stress measures and allows to relate the macroscopic membrane force tensor  $\mathbf{N}$  and the macroscopic bending moment tensor  $\mathbf{M}$  to the mesoscopic statically admissible stress field  $\boldsymbol{\sigma}$  on the surface of the RVE.

## Homogenisation with periodic boundary conditions

In this Chapter, the failure detection will be achieved assuming perfect periodicity of the masonry mesostructure. A natural strategy is then to prescribe periodic boundary conditions on the RVE, see Mistler et al. (2007), Kouznetsova et al. (2001). Assuming that the rigid body translations and rotations of the RVE vanish, it can be shown that the kinematically admissible displacement field is strain-periodic and given by

$$u_{\alpha} = E_{\alpha\beta} x_{\beta} + \chi_{\alpha\beta} x_{\beta} x_3 + u_{\alpha}^p \quad (4.5a)$$

$$u_3 = -\frac{1}{2} \chi_{\alpha\beta} x_{\alpha} x_{\beta} + u_3^p \quad (4.5b)$$

where  $\vec{u}^p(\vec{x})$  is a periodic displacement fluctuation field, i.e. taking equal values on any two boundary points on the internal faces related by the periodicity relation, which accounts for the heterogeneity inside the RVE, see Anthoine (1995). This condition reads

$$u_i^p(x_j + V_j^\alpha) = u_i^p(x_j) \quad (4.6)$$

where  $\vec{V}^1$  and  $\vec{V}^2$  are the two vectors which allow to recompose an entire wall based on the RVE using the periodicity assumption, see Figure 4.2. Furthermore, it can be shown that the displacement field defined by relations (4.5) satisfies averaging theorem (4.2) for the strain measures.

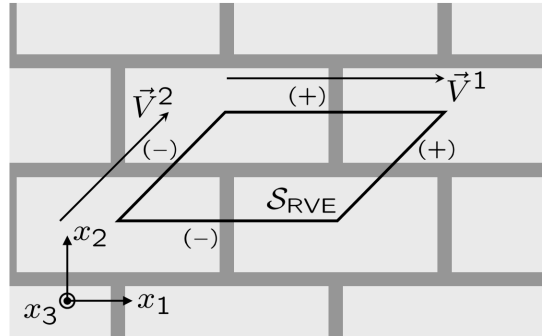


Figure 4.2: In-plane periodicity of running bond masonry, see Anthoine (1995).

Considering the internal boundaries of the RVE, and eliminating the periodic fluctuation  $\vec{u}^p$  based on the periodicity argument, Equations (4.5) and (4.6) lead to the following expressions

$$u_\alpha^+ - u_\alpha^- = (E_{\alpha\beta} + x_3\chi_{\alpha\beta})(x_\beta^+ - x_\beta^-) \quad (4.7a)$$

$$u_3^+ - u_3^- = -\frac{1}{2}\chi_{\alpha\beta}(x_\alpha^+x_\beta^+ - x_\alpha^-x_\beta^-) \quad (4.7b)$$

which involve only the relative displacements and positions between any pair of boundary points related by periodicity. The superscripts + and - refer to the opposite parts of the internal surface of the RVE which are defined such that  $\vec{n}^+ = -\vec{n}^-$  at corresponding points, see Figure 4.2 for the case of running bond masonry.

### Control system for running bond masonry unit cell

Running bond masonry exhibits a two-dimensional orthotropic heterogeneous structure with a periodic stacking of constituents along two directions in its own plane. Due to this periodicity, its mesostructure can be defined by a representative volume element (RVE). Different RVE choices can be made depending on the type of behaviour to represent. For non-linear behaviour of such a material, a unit cell, i.e. a single period RVE, can be used as in Pegon and Anthoine (1997), Massart et al. (2004, 2005b). For the sake of simplicity, a parallelepipedic through-thickness portion of masonry sketched in Figure 4.3 is used as in Mistler et al. (2007).

In the case of infinitesimal deformation, the strains defined in the Kirchhoff-Love kinematics are given by six independent scalar quantities. The deformation state of a material point can therefore be fully prescribed using six controlling degrees of freedom if the periodic conditions are enforced. The macroscopic membrane deformations are

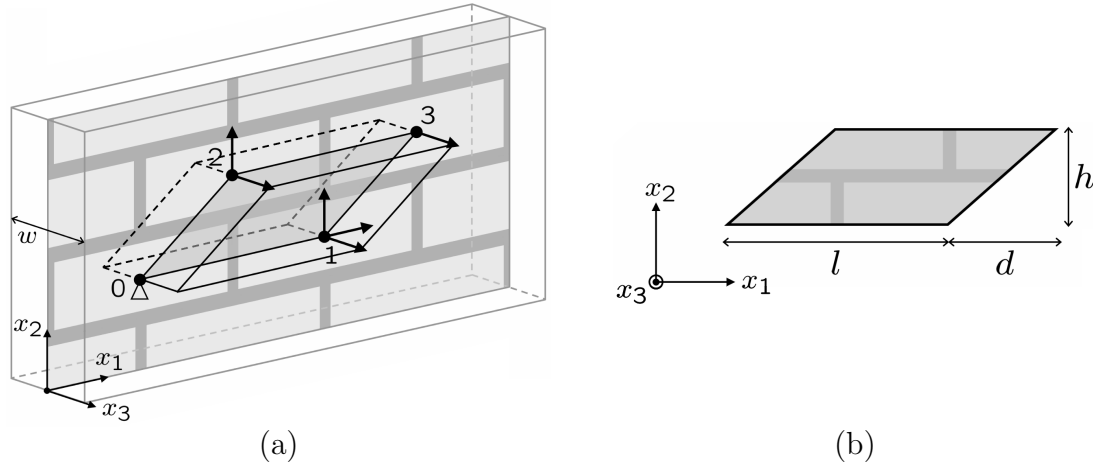


Figure 4.3: Through-thickness RVE for running bond masonry, see Mistler et al. (2007): controlling degrees of freedom of the deformations (a) and in-plane dimensions (b).

prescribed using three reference plane displacement components, while the macroscopic curvatures are fixed by three out-of-plane displacement components. These controlling degrees of freedom are chosen among the ones of three corner points on the reference surface of the RVE as proposed in Mistler et al. (2007). The degrees of freedom of the fourth corner point (0 in Figure 4.3) are set to zero to prevent any RVE rigid body translation. Based on this choice and using Equations (4.7) for these points, the relations linking the controlling displacements to the average strains read

$$u_1^1 = lE_{11} \quad (4.8a)$$

$$u_2^1 = lE_{12} \quad (4.8b)$$

$$u_2^2 = dE_{12} + hE_{22} \quad (4.8c)$$

$$u_3^1 = -\frac{l^2}{2}\chi_{11} \quad (4.8d)$$

$$u_3^2 = -\frac{d^2}{2}\chi_{11} - hd\chi_{12} - \frac{h^2}{2}\chi_{22} \quad (4.8e)$$

$$u_3^3 = -\frac{(l+d)^2}{2}\chi_{11} - h(l+d)\chi_{12} - \frac{h^2}{2}\chi_{22} \quad (4.8f)$$

where  $l$ ,  $d$  and  $h$  are defined in Figure 4.3, and  $x_j^i$  is the  $j^{\text{th}}$  component of the vector  $\bar{x}$  associated to the controlling point  $i$ , see Mistler et al. (2007).

These relations can be recast in a matrix form given by

$$\{u_{\text{ctl}}\} = [D_u]^{-1}\{E_{\text{KL}}\} \quad (4.9)$$

where  $\{u_{\text{ctl}}\}$  is a column vector of the six controlling degrees of freedom,  $\{E_{\text{KL}}\}$  is a column vector of the Kirchhoff-Love generalised (membrane and curvature) strains, and  $[D_u]$  is a matrix which depends on the in-plane dimensions of the RVE. Relations (4.7) for all the other points of the internal boundary are used to enforce the periodicity condition as a boundary condition for the mesostructural problem. These relations can be rearranged by eliminating the average generalised strain components with Equations (4.8). Consequently, the relative displacements between points of homologous boundaries are related to the controlling degrees of freedom, see Mistler et al. (2007). Each of these tying relations is associated with tying forces at the pair of considered boundary points

related by periodicity and at the involved controlling points. Since the tying forces of any homogeneous constraint relation should not bring any contribution to the work variation performed on the RVE, it is possible to show that the tying forces between boundary points are anti-periodic and that both the tying forces at the controlling points and at the boundary points are linked to each other. Similar developments have been performed for the case of plane computational homogenisation in Geers (2005).

Substituting the strain-periodic displacement field (4.5) into (4.4), considering that the contribution of the periodic fluctuations  $\vec{u}^p$  to the work variation vanishes due to the anti-periodicity of the tying forces between related boundary points, and using the fact that the periodic fluctuations vanish at the controlling points, the energy consistency leads to

$$N_{\alpha\beta} = \frac{1}{\mathcal{S}_{\text{RVE}}} \int_{\partial\mathcal{V}_i} (t_\alpha x_\beta)^{\text{sym}} \, d\partial\mathcal{V}_i \quad (4.10a)$$

$$M_{\alpha\beta} = \frac{1}{\mathcal{S}_{\text{RVE}}} \int_{\partial\mathcal{V}_i} \left[ (t_\alpha x_\beta)^{\text{sym}} x_3 - \frac{1}{2} t_3 x_\alpha x_\beta \right] \, d\partial\mathcal{V}_i \quad (4.10b)$$

The traction vector  $\vec{t}$  considered in relations (4.10) represents all the forces acting in a point of the boundary  $\partial\mathcal{V}_i$ , i.e. (i) the controlling forces  $\vec{f}$  which are conjugated to the controlling degrees of freedom and represent the action of the neighbouring cells, (ii) the tying forces at the pair of considered boundary points related by periodicity, and (iii) the tying forces at the controlling points. For the case of the membrane force tensor (4.10a), it can be shown that the contribution of the tying forces at the boundary points cancels a part of the contribution of the tying forces at the controlling points considering the anti-periodicity of the former and the link between both. The remaining contribution of the tying forces is eliminated by taking the symmetric part of the tensor  $t_\alpha x_\beta$ . Consequently, only the contribution of the in-plane controlling forces does not vanish, see developments in Geers (2005) for the case of planar computational homogenisation. All these considerations lead to

$$N_{11} = \frac{1}{h} f_1^1 \quad (4.11a)$$

$$N_{22} = \frac{1}{l} f_2^2 \quad (4.11b)$$

$$N_{12} = \frac{1}{2h} f_2^1 + \frac{d}{2lh} f_2^2 \quad (4.11c)$$

For the bending moment tensor (4.10b), the first term containing the in-plane projection of the traction vector  $t_\alpha$  only depends on the anti-periodic tying forces at boundary points since the thickness coordinate of all the controlling points is zero. In the second term which depends on the out-of-plane traction  $t_3$ , the contribution of the tying forces at boundary points cancels the out-of-plane part of the contribution of the tying forces at the controlling points considering the anti-periodicity of the former and the link between both. The remaining in-plane contribution of the tying forces cancels the first term. Consequently, only the contribution of the out-of-plane controlling forces does not vanish,

which leads to

$$M_{11} = -\frac{l}{2h}f_3^1 - \frac{d^2}{2lh}f_3^2 - \frac{(l+d)^2}{2lh}f_3^3 \quad (4.12a)$$

$$M_{22} = -\frac{h}{2l}f_3^2 - \frac{h}{2l}f_3^3 \quad (4.12b)$$

$$M_{12} = -\frac{d}{2l}f_3^2 - \frac{l+d}{2l}f_3^3 \quad (4.12c)$$

Relations (4.11) and (4.12) can be recast in a matrix form given by

$$\{\Sigma_{\text{KL}}\} = [D_f]\{f_{\text{ctl}}\} \quad (4.13)$$

where  $\{f_{\text{ctl}}\}$  is a column vector of the six controlling forces,  $\{\Sigma_{\text{KL}}\}$  is a column vector of the Kirchhoff-Love generalised stresses, and  $[D_f]$  is a matrix which depends on the in-plane dimensions of the RVE.

Based on Equations (4.8), any average deformation path can be prescribed. The related mesostructural boundary value problem is completely defined from the controlling degrees of freedom and the periodicity tyings, and can be solved using a classical finite element method scheme, provided mesostructural constitutive laws are postulated. This type of control is classically used in multi-scale nested scheme using displacement-based finite element schemes, see Massart et al. (2007a), Kouznetsova et al. (2001).

Note that a mesostructural boundary value problem can be formulated using either an average strain control, relations (4.7) and (4.8), or an average stress control, relations (4.7), (4.11) and (4.12). In Section 4.5, the macroscopic localisation detection for masonry shells will be illustrated for proportionally loaded RVEs based on an average (generalised) stress control.

Note also that this Kirchhoff-Love shell computation homogenisation scheme can be connected to the general second-order solid-solid computational homogenisation framework developed in Kouznetsova et al. (2002), since shell model can be interpreted as a second-gradient continuum. Such a link was established for the Reissner-Mindlin case by introducing the shell kinematical assumptions in the macroscopic second-gradient continuum, see Geers et al. (2007) for detailed developments.

### 4.3 Simplified mesoscopic constitutive setting

To close the formulation of the homogenisation mesostructural boundary value problem, three-dimensional constitutive laws have to be postulated for the constituents. In the case of masonry walls, the material responses of both the brick and the mortar joint, and brick-joint interface are formulated using closed-form laws. Since the mortar joints are much weaker than the brick material, the failure behaviour of the latter is not considered in this first study and the brick is assumed elastic. The combined behaviour of the brick-joint interface and of the mortar is modelled by an initially elastic planar interface element, for which both the normal and tangential stiffnesses ( $k_n$ ,  $k_t$ ) can be related to the elastic behaviour of mortar, see Lourenço and Rots (1997). In order to model the failure of the joint, a classical Mohr-Coulomb type strength criterion is used with a linear compression cap for the sake of simplicity, as depicted in Figure 4.4, see van Zijl (2000). The parameters  $f_t$  and  $f_c$  are respectively the tensile and compressive Mode-I strength of the mortar or mortar-brick interfaces,  $c$  is the cohesion,  $\varphi$  is the friction angle, and  $\vartheta$  is the angle which defines the linear compression cap.

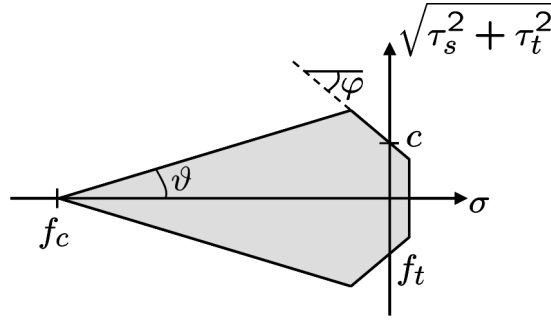


Figure 4.4: Mohr-Coulomb criterion for the mortar joint/mortar-brick interface.

A scalar damage model with an exponential evolution law is considered. The traction-separation law which links the traction vector  $\vec{t}$  across the interface to the relative displacement vector  $\vec{\delta}$  is given by

$$t_i = (1 - D) H_{ij} \delta_j \quad (4.14)$$

where  $D$  is the scalar damage variable growing from zero (virgin material) to one (complete failure) and  $\mathbf{H}$  is an elastic stiffness second order tensor which depends on the elastic stiffnesses  $k_n$  and  $k_t$ . Note that (4.14) implies that no stiffness recovery is taken into account upon crack closure.

The damage evolution law of the mortar joint is given by

$$D(\kappa) = 1 - \frac{f_t}{k_n \kappa} e^{-\frac{f_t}{G_f} (\kappa - \frac{f_t}{k_n})} \quad \text{for } \kappa \geq \frac{f_t}{k_n} \quad (4.15)$$

where  $G_f$  is the Mode-I fracture energy, see van der Pluijm (1999). Since the considered interface is three-dimensional and since the damage criterion has to take into account the different behaviours in tension and compression, the damage-driving parameter  $\kappa$  is taken as the most critical value of an equivalent relative displacement defined by

$$\delta_{eq} = \max \left\{ \begin{array}{l} \frac{f_t}{c} \tan \varphi \delta_n + \frac{f_t}{c} \frac{k_t}{k_n} \sqrt{\delta_s^2 + \delta_t^2} \\ \delta_n \\ -\frac{f_t}{f_c} \delta_n + \frac{f_t}{f_c} \frac{k_t}{k_n} \frac{1}{\tan \vartheta} \sqrt{\delta_s^2 + \delta_t^2} \end{array} \right\} \quad (4.16)$$

where  $\delta_n$  and  $\sqrt{\delta_s^2 + \delta_t^2}$  are the normal and tangential relative displacements, respectively. Note that relations (4.14) to (4.16) were postulated for the sake of simplicity and to illustrate the multi-scale detection of localisation and its correspondence with mesostructural geometrical features. The sequel of the procedure remains independent from the laws postulated for the constituents. In particular, more complex mortar formulations including anisotropic damage effects between mode I and mode II in terms of energy dissipation, see Lourenço and Rots (1997), or incorporating plastic dilatancy, see van Zijl (2004), could be used as well. A brick damage model could also be used for instance in order to extend the detection procedure to additional failure modes involving brick failure, see Massart et al. (2005b), Lourenço and Rots (1997) for the case of in-plane problems.

## 4.4 Failure detection in thin shell formulations

Failure in masonry shells is accompanied by the localisation of deformation and of degradation. Any localisation enhancement by means of discrete failure zones at the structural scale to represent failure as performed in Massart et al. (2007a) for planar cases would require a criterion to detect localisation and to determine its orientation. In the same spirit, the definition of computational homogenisation-based failure should also take into account structural scale localisation detection.

However, in a computational homogenisation procedure, the macroscopic material response is not postulated a priori but rather computed from the material laws introduced at the level of the mesostructural RVE. The detection and orientation of macroscopic localisation should then be based on the computationally homogenised quantities, the only available information related to the average material behaviour.

For the Kirchhoff-Love description assumed at the structural scale, a closed-form structural material law is not readily available. Nevertheless, the link between generalised stresses and strains variations can be obtained from the homogenised tangent stiffness defined as

$$\begin{cases} \delta N_{\alpha\beta} &= {}^4L_{\alpha\beta\delta\gamma}^{\text{mm}} \delta E_{\delta\gamma} + {}^4L_{\alpha\beta\delta\gamma}^{\text{mb}} \delta \chi_{\delta\gamma} \\ \delta M_{\alpha\beta} &= {}^4L_{\alpha\beta\delta\gamma}^{\text{bm}} \delta E_{\delta\gamma} + {}^4L_{\alpha\beta\delta\gamma}^{\text{bb}} \delta \chi_{\delta\gamma} \end{cases} \quad (4.17)$$

where the superscripts m and b stand for ‘membrane’ and ‘bending’. Note that the both tensors  ${}^4L^{\text{mb}}$  and  ${}^4L^{\text{bm}}$  do not vanish in a general context, which allows to take into account potential membrane-flexural couplings. As will be shown in Section 4.5.1, masonry flexural behaviour presents this type of couplings due to the different tensile and compressive strengths of the damaging joints. Relation (4.17) can be expressed in a more compact matrix form which reads

$$\{\delta \Sigma_{\text{KL}}\} = [L]\{\delta E_{\text{KL}}\} \quad (4.18)$$

where  $\{\Sigma_{\text{KL}}\}$  and  $\{E_{\text{KL}}\}$  are column vectors of the Kirchhoff-Love generalised stresses and strains, respectively. In the case of the computational homogenisation method presented in Section 4.2.2, the total RVE stiffness relation of the mesostructural boundary value problem can be partitioned into dependent, independent and control degrees of freedom. After eliminating the dependent degrees of freedom, due to the periodic boundary conditions, the residual forces corresponding to the independent degrees of freedom vanish as the mesostructural equilibrium is reached. As a result, the RVE mesostructural stiffness relation can be condensed in the 6x6 stiffness relation  $\{\delta f_{\text{ctl}}\} = [K^*]\{\delta u_{\text{ctl}}\}$ . Numerical details of this condensation can be found in Kouznetsova et al. (2001). The macroscopic tangent material stiffness  $[L]$  can therefore be computed by substituting the variation of Equations (4.9) and (4.13) in the RVE mesostructural stiffness relation condensed at the controlling degrees of freedom, which leads to

$$[L] = [D_f][K^*][D_u]^{-1} \quad (4.19)$$

The procedure proposed in Massart et al. (2007a) for in-plane loading to detect localisation and its orientation in the context of multi-scale computations can be extended to shell kinematics based on Makowski and Stumpf (1998). Similarly to the works of Rice (1976), Rice and Rudnicki (1980), the conditions of appearance of a uniform localisation zone in which damage is growing and localising can be treated as a material bifurcation or loss of uniqueness problem. Such an analysis identifies the conditions under which

more than one solution to the equilibrium problem exist. Equilibrium requires the stress quantities at the interface between the localising zone ( $l$ ) and its surrounding material ( $s$ ) to be continuous and can be extended to shell kinematics. At the structural scale, for the shell continuum, this reads

$$\begin{cases} n_\beta \left( \delta N_{\alpha\beta}^{(l)} - \delta N_{\alpha\beta}^{(s)} \right) = 0 \\ n_\beta \left( \delta M_{\alpha\beta}^{(l)} - \delta M_{\alpha\beta}^{(s)} \right) = 0 \end{cases} \quad (4.20)$$

where  $\vec{n}$  is the normal to the localising zone. Assuming the continuity of the displacement field across the localising zone, the generalised strain jumps have the form

$$\begin{cases} \delta E_{\alpha\beta}^{(l)} - \delta E_{\alpha\beta}^{(s)} = \frac{1}{2} (\delta m_\alpha^E n_\beta + n_\alpha \delta m_\beta^E) \\ \delta \chi_{\alpha\beta}^{(l)} - \delta \chi_{\alpha\beta}^{(s)} = \frac{1}{2} (\delta m_\alpha^x n_\beta + n_\alpha \delta m_\beta^x) \end{cases} \quad (4.21)$$

where  $\vec{m}^E$  and  $\vec{m}^x$  are the strain jump modes, which vanish in the initial, homogeneous situation, and must become nonzero for a bifurcated state to exist.

Equations (4.17) and (4.21) can now be introduced in Equations (4.20). Using the classical linear comparison solid which consists in assuming that the same tangent material stiffnesses  ${}^4\mathbf{L}^{ij}$  is valid on both sides of the surface separating the localising zone and its surrounding material, and taking into account the right minor symmetry of the tensors  ${}^4\mathbf{L}^{ij}$ , the traction continuity requirement becomes

$$\begin{bmatrix} \left( n_\alpha {}^4L_{\alpha\beta\delta\gamma}^{mm} n_\gamma \right) & \left( n_\alpha {}^4L_{\alpha\beta\delta\gamma}^{mb} n_\gamma \right) \\ \left( n_\alpha {}^4L_{\alpha\beta\delta\gamma}^{bm} n_\gamma \right) & \left( n_\alpha {}^4L_{\alpha\beta\delta\gamma}^{bb} n_\gamma \right) \end{bmatrix} \begin{Bmatrix} m_\delta^E \\ m_\delta^x \end{Bmatrix} = 0 \quad (4.22)$$

This system of equations admits a non trivial solution only if

$$\det(A_{\beta\delta}(\vec{n})) = \det \left( \begin{bmatrix} \left( n_\alpha {}^4L_{\alpha\beta\delta\gamma}^{mm} n_\gamma \right) & \left( n_\alpha {}^4L_{\alpha\beta\delta\gamma}^{mb} n_\gamma \right) \\ \left( n_\alpha {}^4L_{\alpha\beta\delta\gamma}^{bm} n_\gamma \right) & \left( n_\alpha {}^4L_{\alpha\beta\delta\gamma}^{bb} n_\gamma \right) \end{bmatrix} \right) = 0 \quad (4.23)$$

for some direction  $\vec{n}$ , where  $\mathbf{A}(\vec{n})$  is the acoustic tensor generalised to the Kirchhoff-Love shell theory.

## 4.5 Macroscopic localisation analysis

The shell localisation detection discussed above is now illustrated by means of computations performed on a unit cell. Using the presented homogenisation method with such a RVE, only single period crack patterns can be taken into account. The cell is subjected to stress-controlled proportional loading paths including flexural effects, for which the average failure detection and orientation are analysed. The case of bed joint out-of-plane failure mode and two cases of stair-case out-of-plane failure modes with different mesostructures (geometrical aspect ratios of the unit) are considered. The symmetric mode of one of the stair-case out-of-plane cracks is also considered. An average (macroscopic) out-of-plane failure direction can be identified for each of the typical mesostructural damage patterns, purely based on geometrical arguments. The loading of the unit cell is controlled by applying a bending moment leading to the considered out-of-plane failure mode. The path-following techniques proposed in Geers (1999a,b) are used in

computations to enable the tracing of snap-through and snap-back responses which may appear when localisation of damage occurs in thin zones with respect to the problem size. Relations (4.8), (4.11) and (4.12) are used to link respectively the average generalised strains and stresses to the control displacements and forces at the controlling points of the unit cell. The brick and mortar joint material parameters used in computations are respectively presented in the Table 4.1, see van Zijl (2000).

The dimensions of the considered unit cell are  $l = 200$  mm,  $d = l/2 = 100$  mm,  $h = 100$  mm and  $w = 100$  mm. The brick is meshed by using 20-noded quadratic volume finite elements with  $3 \times 3 \times 3$  Gauss integration points. The interfaces corresponding to mortar joints are meshed using 16-noded quadratic planar interface finite elements with  $3 \times 3$  Lobatto quadrature points. Six finite elements are used across the thickness and the in-plane discretisation is shown in Figure 4.5. Note that a rather coarse in-plane discretisation is chosen to challenge the results obtained with respect to the computational efficiency. The chosen three-dimensional mesh results in 3342 degrees of freedom for the mesostructural problem.

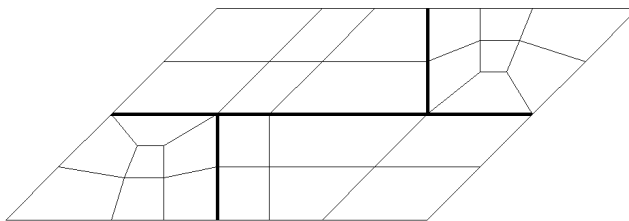


Figure 4.5: In-plane finite element mesh of the unit cell with the joints in bold line.

#### 4.5.1 Bed joint failure

For the first loading case, the loading of the cell is controlled by applying a bending moment  $M_{22}$  where the  $x_2$ -axis is perpendicular to the bed joint. A mode-I flexural failure in the bed joint is observed, which leads to an average out-of-plane failure orientation defined by its normal oriented at  $-90^\circ$  from the bed joint, see Figure 4.6. The load-curvature response depicted in Figure 4.7 represents the variation of the load factor as a function of the curvature  $\chi_{22}$ . The state corresponding to each point denoted by a capital letter on this curve is analysed below together with the localisation criterion (4.23). The joint damage distribution for each state is depicted in Figure 4.8 together with the corresponding acoustic tensor determinant spectrum as a function of the normal orientation  $\Theta$ , and with the deformed shape of the unit cell. During the first phase of the loading (Figure 4.8, state A), damage is initiating in the tension part of the bed joint and the acoustic tensor determinant already presents a minimum at  $\Theta = 90^\circ$ . Note that the

Table 4.1: Brick (a) and mortar/mortar-brick interface (b) material parameters, see van Zijl (2000).

	$E$ (MPa)	$\nu$	$k_n$ ( $\frac{\text{MPa}}{\text{mm}}$ )	$k_t$ ( $\frac{\text{MPa}}{\text{mm}}$ )	$f_t$ (MPa)	$G_f$ ( $\frac{\text{mJ}}{\text{mm}^2}$ )	$c$ (MPa)	$\varphi$ ( $^\circ$ )	$f_c$ (MPa)	$\vartheta$ ( $^\circ$ )
(a)	16700	0.15	-	-	-	-	-	-	-	-
(b)	-	-	438	182	0.2	0.005	0.28	36	3.0	45

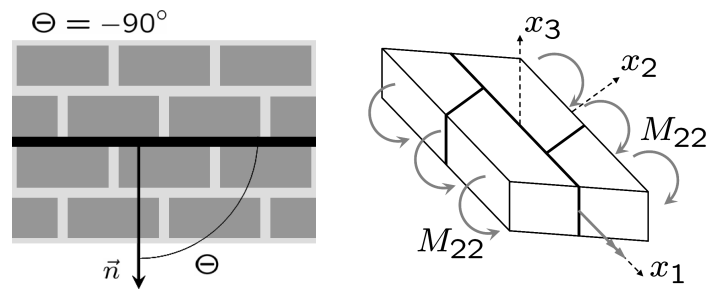


Figure 4.6: Average out-of-plane failure orientation defined by the normal  $\vec{n}$  for the bed joint failure pattern (left) and the loading mode of the unit cell (right).

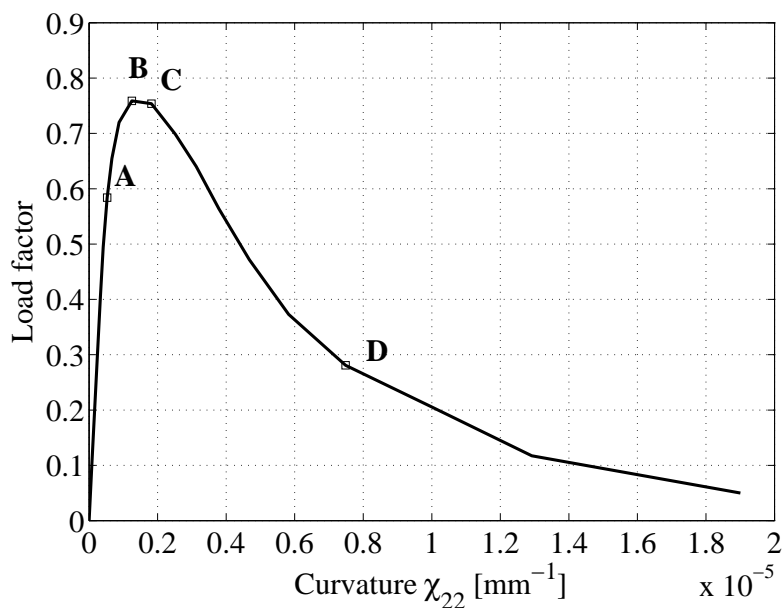


Figure 4.7: Load-curvature response under the bending moment  $M_{22}$  (see Figure 4.6). The unit load factor corresponds to  $M_{22} = 0.8$  kN.

presence of minima and maxima in the initial stages of loading can be understood from the initial anisotropy of the medium. The minimum at  $\Theta = 90^\circ$  indeed matches the orientation perpendicular to the bed joint, for which the elastic (undamaged) flexural stiffness is minimum. As illustrated for state B (peak of the response), damage further spreads over half of the bed joint. At the next step (point C), the acoustic tensor determinant becomes negative for a certain orientation range. However, it presents a negative local maximum at  $\Theta = 90^\circ$  which exactly matches the average orientation of the out-of-plane bed joint failure. Further in the softening range (Figure 4.8, state D), the bed joint is nearly completely damaged and the negative local maximum of the acoustic tensor determinant remains at the same orientation. Note that for planar cases all the orientations for which a negative acoustic tensor determinant is found could be considered for localisation when a discontinuous bifurcation is assumed, see Rice and Rudnicki (1980). It is however noted that the real average orientation observed in the unit cell exactly matches the local maximum present in the negative range.

As already pointed out in Section 4.4, note also that even for such a simple case with pure flexural loading, the different tensile and compressive strengths of the damaging joints inside the cell imply the appearance of membrane-flexural couplings which have

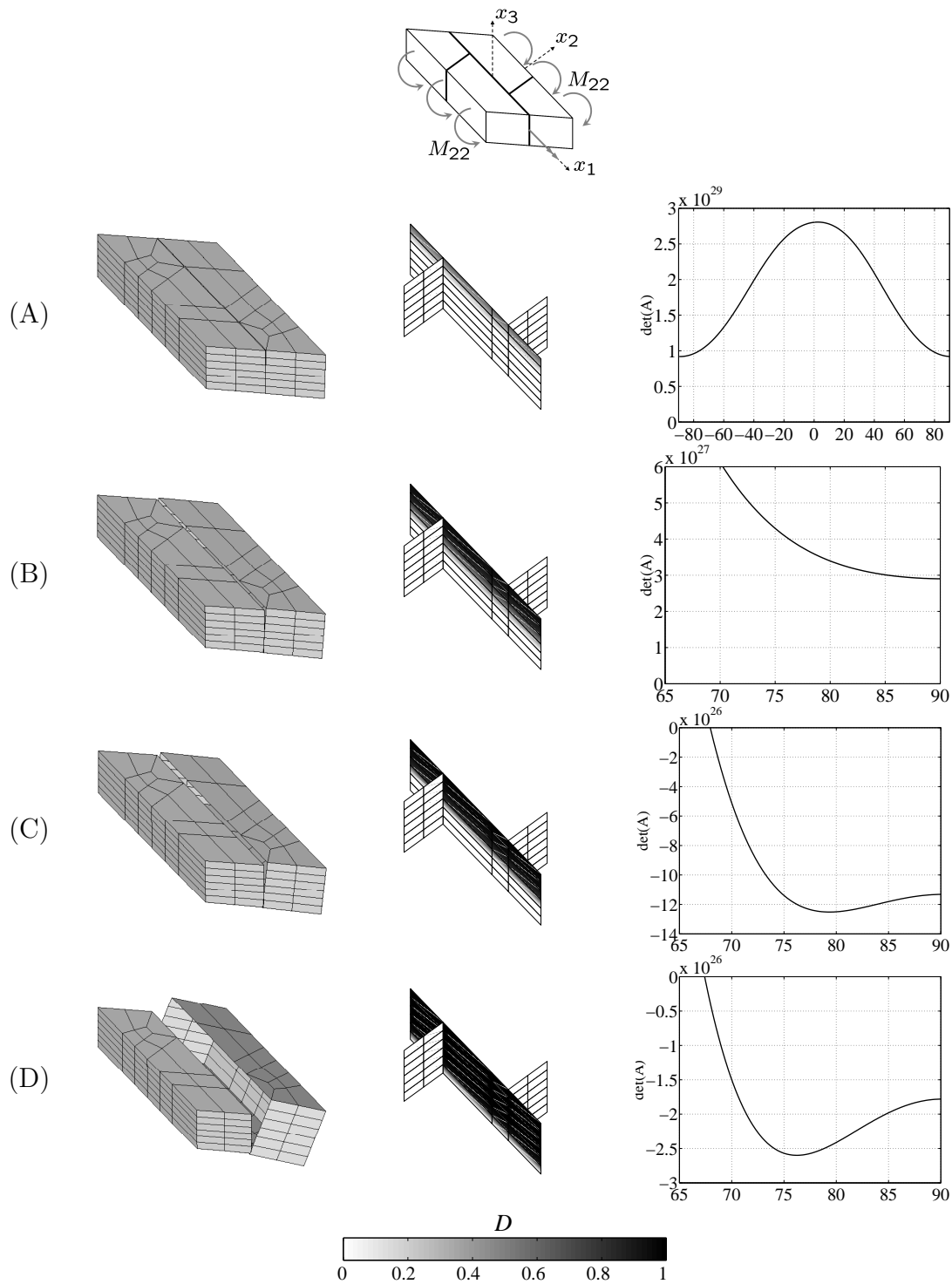


Figure 4.8: Out-of-plane bed joint failure under the bending moment  $M_{22}$  (see Figure 4.7, states A to D): deformed shape of the unit cell (the displacements are magnified by a factor of 500) (left), joint damage distribution (centre) and related acoustic tensor determinant spectrum as a function of the normal orientation  $\Theta$  ( $^\circ$ ) (right).

to be incorporated in the homogenisation procedure and in the localisation analysis. An analysis of the acoustic tensor based on the pure flexural part of the tangent stiffness does not allow a proper detection of the structural scale loss of uniqueness. This is illustrated by Figure 4.9 showing the presence of a non null average opening (in-plane  $E_{22}$  component),

and by the fact that the acoustic tensor associated to  ${}^4\mathbf{L}^{bb}$  does not exhibit a negative character for the correct orientation. The localisation and failure orientation analysis has to be based on the tangent stiffness of the material point, and cannot take into account the stress state only.

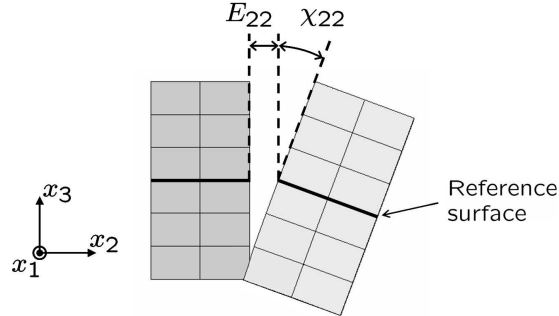


Figure 4.9: Membrane-flexural coupling for the case of the out-of-plane bed joint failure mode: deformed shape of the unit cell (the displacements are magnified by a factor of 500) in the softening regime, see state D in Figure 4.6.

## 4.5.2 Stair-case failure

As a second illustrative case, the analysis of a stair-case flexural failure mode, with two different geometrical shape factors of the unit cell corresponding to different brick aspect ratios, is considered. The shape factor is given by the ratio between the length and the height of the cell. First, the out-of-plane stair-case failure mode is studied for a brick shape factor equal to 0.5 which leads to an average stair-case crack normal orientation of  $-45^\circ$ , see Figure 4.10. The loading of the cell is controlled by a bending moment  $M_{vv}$  where  $v$  is an axis at  $60^\circ$  from the  $x_2$ -axis, see Figure 4.10. The numerical results for this case

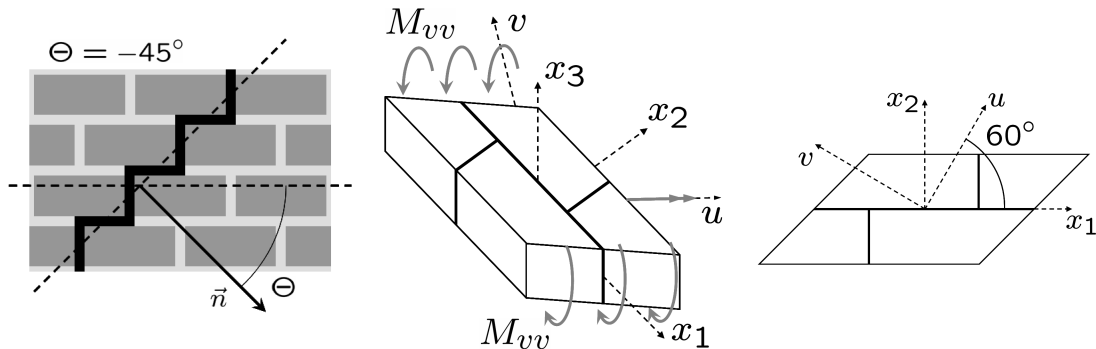


Figure 4.10: Average out-of-plane failure orientation defined by the normal  $\vec{n}$  for the stair-case failure pattern with a brick shape factor of 0.5 (left) and the loading mode applied on the unit cell (centre and right).

are shown in Figure 4.11 and 4.12. The evolution of the damage distribution, Figure 4.12 (left), for states A to D, matches the appearance of the out-of-plane stair-case failure. In state B, a stair-case cracking pattern can clearly be identified. No localisation orientation is identified yet from the acoustic tensor which is still positive-definite, but one can clearly see that the decrease of its determinant is more pronounced for orientations between  $-90^\circ$  and  $0^\circ$ . In state C, the stair-case crack pattern is even more pronounced. The potential

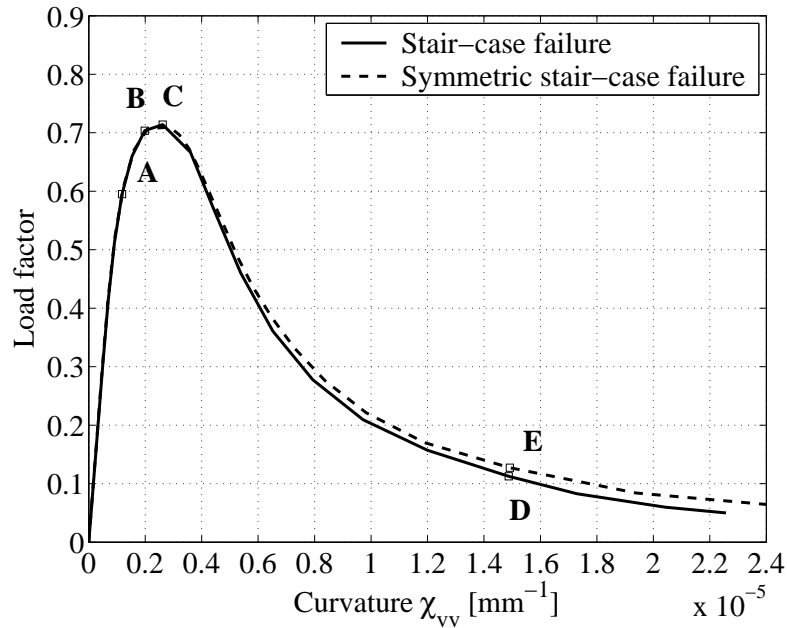


Figure 4.11: Load-curvature responses under the bending moment  $M_{vv}$  where  $v$  is an axis at  $60^\circ$  from the  $x_2$ -axis (solid line) (see Figure 4.10), and the symmetric bending moment where the axis  $v$  is an axis at  $-60^\circ$  from the  $x_2$ -axis (dashed-line). The unit load factor corresponds to  $M_{vv} = 1.7$  kN.

bifurcation has appeared for orientations between  $-55.8^\circ$  and  $-21.8^\circ$  (negative values of the acoustic tensor determinant). A minimum is found for the orientation of  $-38.5^\circ$  and the negative range of the determinant is approximately centered on this orientation. Finally, further in the softening regime (state D), the stair-case crack is fully developed, and a local maximum is found in the negative range at an orientation of  $-44.9^\circ$ . Note that the fact that the extremum is not at  $-45^\circ$  in state C and the slight imprecision in state D can be attributed to the quite coarse in-plane discretisation adopted here. This can be also understood from pattern C, where a slightly non-symmetric damage pattern can be seen in the bed joint due to the rather coarse discretisation used.

Furthermore, the symmetric stair-case failure mode with an average normal orientation of  $45^\circ$  can also be studied despite the use of a skew parallelepipedic cell. In this case, the loading of the cell is controlled by a bending moment  $M_{vv}$  where  $v$  is now an axis at  $-60^\circ$  from the  $x_2$ -axis. The numerical results are shown in Figure 4.11 and 4.13. In state E (Figure 4.13), the potential bifurcation has appeared for orientations between  $24.9^\circ$  and  $64.7^\circ$  and a negative local maximum is found at a normal orientation of  $44.6^\circ$ . The slight difference in the softening regime between both the stair-case failure mode responses depicted in Figure 4.11 and the slight imprecision in state E can be also understood from the non-symmetric coarse in-plane discretisation used in the bed joint.

For the sake of completeness, the out-of-plane stair-case failure is investigated for a second brick shape factor equal to 0.25 which leads to an a priori geometrical stair-case crack normal at an orientation of  $-63.44^\circ$ , see Figure 4.14. The loading of the unit cell is again controlled by a bending moment  $M_{vv}$  where  $v$  is an axis at  $60^\circ$  from the  $x_2$ -axis. The final situation in the softening regime is depicted in Figure 4.15. Similarly to the previous case, the determinant of the acoustic tensor has a local maximum in the negative range near the orientation corresponding to the stair-case for  $-64.2^\circ$ , a value which differs by less

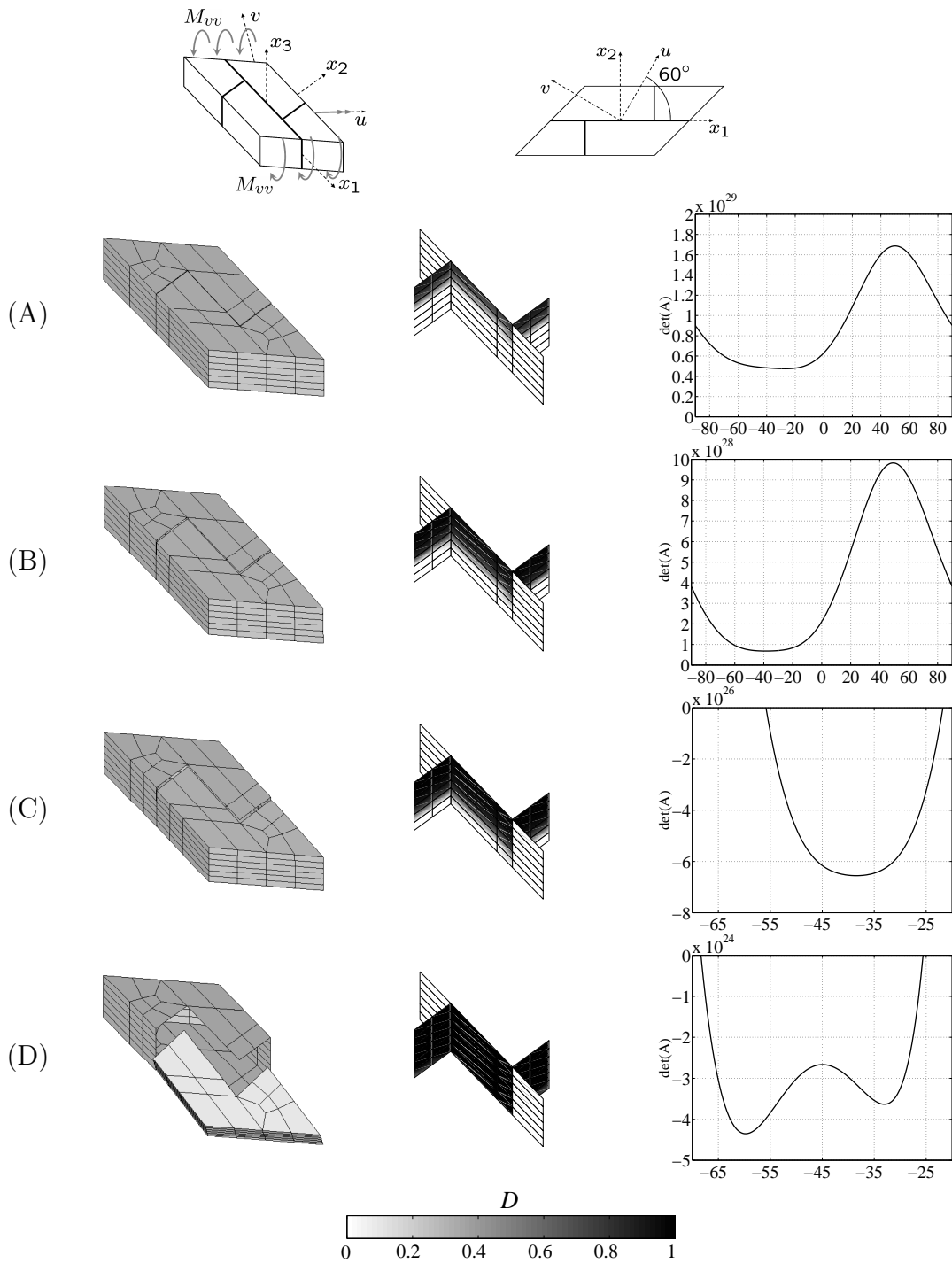


Figure 4.12: Out-of-plane stair-case failure with a brick shape factor of 0.5 under the bending moment  $M_{vv}$  where  $v$  is an axis at  $60^\circ$  from the  $x_2$ -axis (see Figure 4.11, states A to D): deformed shape of the unit cell (the displacements are magnified by a factor of 200) (left), joint damage distribution (centre) and related acoustic tensor determinant spectrum as a function of the normal orientation  $\Theta$  ( $^\circ$ ) (right).

than  $1^\circ$  from the a priori determined geometrical average orientation of the out-of-plane failure. Again, this slight difference is attributed to non uniform damage distribution in the stair-case crack, partially due to the coarse in-plane discretisation.

As a result, the proposed approach coupling shell computational homogenisation with

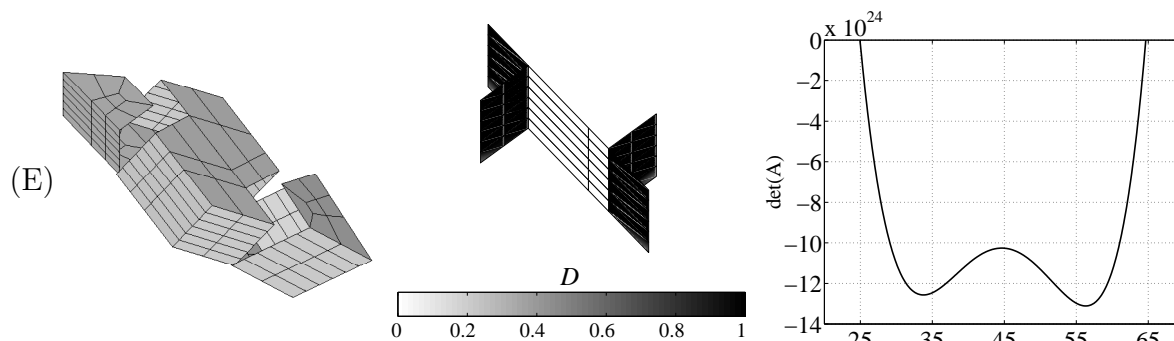


Figure 4.13: Out-of-plane symmetric stair-case failure with a brick shape factor of 0.5 under a bending moment  $M_{vv}$  where  $v$  is an axis at  $-60^\circ$  from the  $x_2$ -axis (see Figure 4.11, state E): deformed shape of the unit cell (the displacements are magnified by a factor of 200) (left), joint damage distribution (centre) and related acoustic tensor determinant spectrum as a function of the normal orientation  $\Theta$  ( $^\circ$ ) (right).

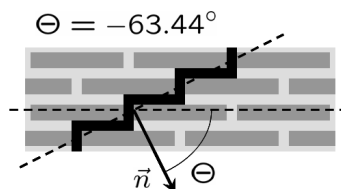


Figure 4.14: Average out-of-plane failure orientation defined by the normal  $\vec{n}$  for the stair-case failure pattern with a brick shape factor of 0.25.

macroscopic localisation detection allows the proper structural scale localisation tracking, even with rather coarse in-plane discretisation. It is emphasized that this methodology remains independent from the postulated material laws; i.e. the incorporation of any improved mesoscopic law for joint failure, see Lourenço and Rots (1997), would not affect the way macroscopic localisation is detected. Any change in the mesostructural features would be naturally accounted for, in the limit of the homogenisation procedure accuracy.

## 4.6 Discussion

In this Section, results of computations are shown in order to discuss the robustness of the proposed structural scale localisation detection procedure. First, the influence of the mesoscopic material properties on the obtained failure modes is discussed, motivated by the large scattering observed in masonry experimental programs, see van der Pluijm (1999). The influence of the loading modes and of the RVE size is also emphasized. Finally, the incorporation of the proposed localisation detection procedure in nested multi-level structural computations is briefly discussed.

### 4.6.1 Influence of mesoscopic material properties

In Section 4.5, both bed joint and stair-case out-of-plane failure modes are investigated by applying a bending moment  $M_{vv}$  where  $v$  is an axis at respectively  $0^\circ$  and  $60^\circ$  from the  $x_2$ -axis. In both cases, damaged joints correspond to preferential patterns associated to the masonry stacking mode. In order to analyse the influence of the constituent properties

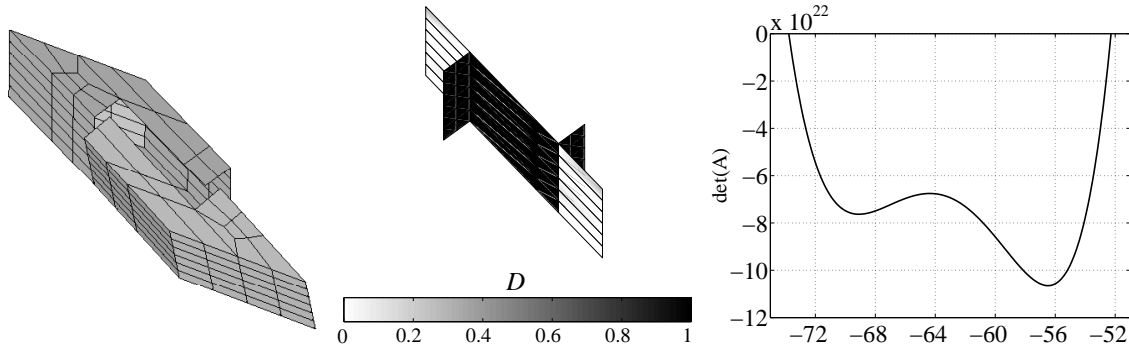


Figure 4.15: Out-of-plane stair-case failure with a brick shape factor of 0.25 under a bending moment  $M_{vv}$  where  $v$  is an axis at  $60^\circ$  from the  $x_2$ -axis: deformed shape of the unit cell (the displacements are magnified by a factor of 50) (left), joint damage distribution (centre) and related acoustic tensor determinant spectrum as a function of the normal orientation  $\Theta(^\circ)$  (right) at the end of the softening tail.

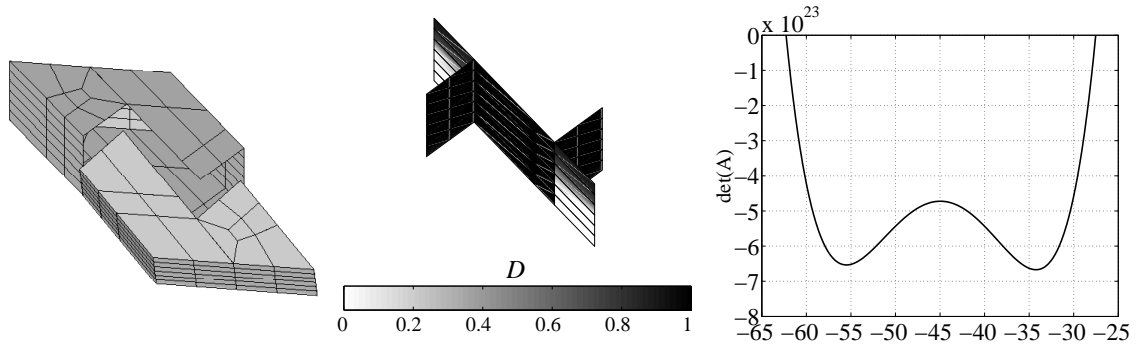


Figure 4.16: Out-of-plane stair-case failure with a brick shape factor of 0.5 under a bending moment  $M_{vv}$  where  $v$  is an axis at  $45^\circ$  from the  $x_2$ -axis: deformed shape of the unit cell (the displacements are magnified by a factor of 100) (left), joint damage distribution (centre) and related acoustic tensor determinant spectrum as a function of the normal orientation  $\Theta(^\circ)$  (right) at the end of the softening tail.

on the failure mode, a bending moment  $M_{vv}$  where  $v$  is now an axis at  $45^\circ$  from the  $x_2$ -axis is applied on the cell. The same material properties as in Section 4.5 are used, see Table 4.1. The brick shape factor is equal to 0.5 which leads to an average stair-case crack normal orientation of  $-45^\circ$ . The final situation in the softening regime is depicted in Figure 4.16. In contrast with the cases analysed in Section 4.5, all the joints are here partially or fully damaged, with a competition between both the bed joint and stair-case failure modes. It is shown in Figure 4.16 that the stair-case pattern is more damaged than the bed joint pattern and that the corresponding local maximum of the related acoustic tensor determinant is found in the negative range at the average stair-case crack normal orientation of  $-45^\circ$ .

In order to show that a slight variation of the mesoscopic material properties can affect the failure mode, the same computation is performed successively with a 10% decrease of the joint interface tensile Mode-I strength  $f_t$  and a 10% increase of the joint interface cohesion  $c$ . The numerical results are respectively shown in Figure 4.17 and 4.18. For both these cases, the 10% material parameter variation leads to a change of failure mode towards bed joint failure. This transition is caused by the fact that a decrease of the tensile Mode-I strength renders more critical the out-of-plane bed joint failure

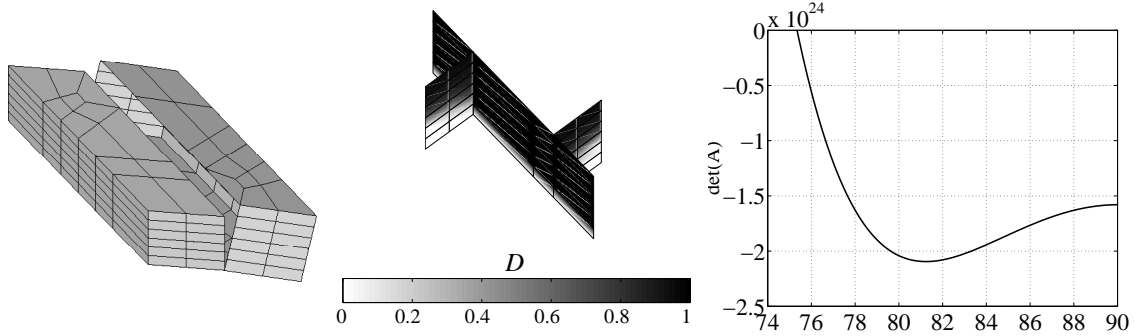


Figure 4.17: Out-of-plane bed joint failure with a 10% decrease of the mortar tensile Mode-I strength under a bending moment  $M_{vv}$  where  $v$  is an axis at  $45^\circ$  from the  $x_2$ -axis: deformed shape of the unit cell (the displacements are magnified by a factor of 100) (left), joint damage distribution (centre) and related acoustic tensor determinant spectrum as a function of the normal orientation  $\Theta(^\circ)$  (right) at the end of the softening tail.

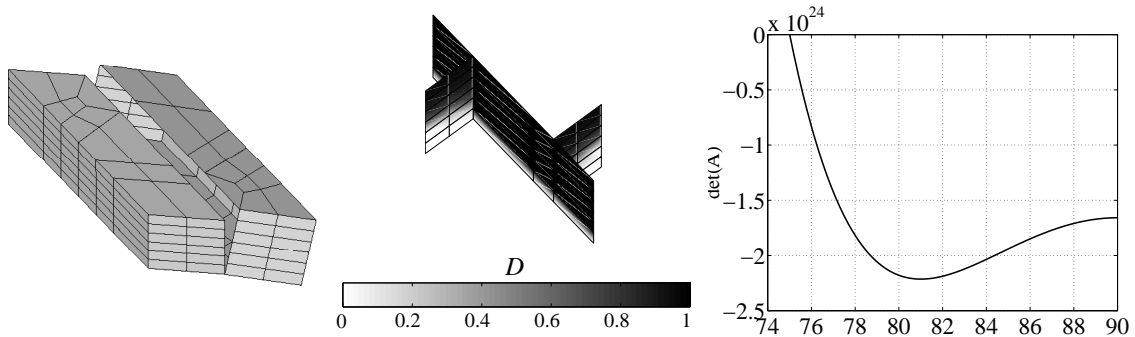


Figure 4.18: Out-of-plane bed joint failure with a 10% increase of the mortar cohesion under a bending moment  $M_{vv}$  where  $v$  is an axis at  $45^\circ$  from the  $x_2$ -axis: deformed shape of the unit cell (the displacements are magnified by a factor of 100) (left), joint damage distribution (centre) and related acoustic tensor determinant spectrum as a function of the normal orientation  $\Theta(^\circ)$  (right) at the end of the softening tail.

mode and that an increase of the cohesion leads to a less critical out-of-plane stair-case failure mode. The load-curvature responses of the three computations are depicted in Figure 4.19. Despite of the change of failure mode, it is shown that the carrying load capacity is only slightly affected. Note however that the change of failure mode may lead to strong modifications in terms of stress redistributions when introduced into structural computations. The post-peak curves are furthermore difficult to interpret due to the fact that only one component of the tensorial stiffness relation is depicted and that the localisation orientations are not the same. Moreover, the homogenised response of a localising unit cell cannot be used directly at the structural scale without taking into account a macroscopic localisation size due to the fact that the cell is associated to a macroscopic material point (see Section 4.6.3).

## 4.6.2 Influence of the loading modes

As mentioned in Section 4.4, an acoustic tensor-based detection criterion was used in Massart et al. (2007a) for in-plane descriptions with different mesoscopic models (gradient damage). An in-plane stair-case failure mode and its orientation was detected by this criterion when applying a bed joint compression  $N_{22}$  combined with in-plane shear  $N_{12}$  of

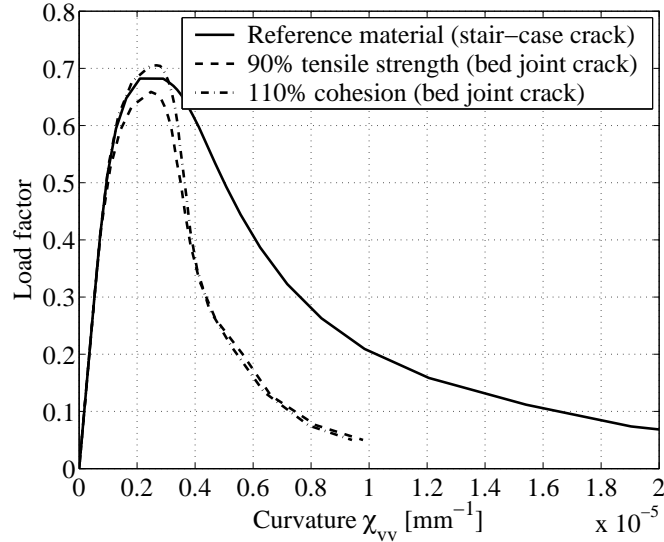


Figure 4.19: Load - curvature responses under a bending moment  $M_{vv}$  where  $v$  is an axis at  $45^\circ$  from the  $x_2$ -axis with reference material (solid line), 10% decrease of the mortar tensile Mode-I strength (dashed line), and 10% increase of the mortar cohesion (dash-dot line). The unit load factor corresponds to a bending moment of 1.7 kN.

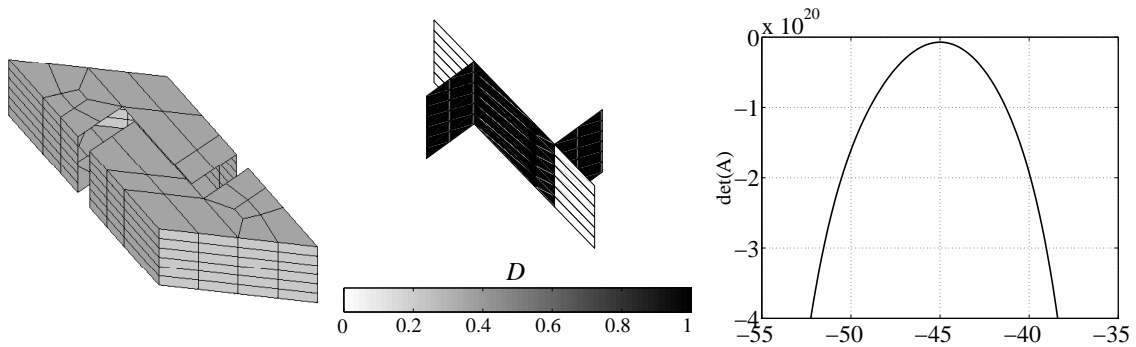


Figure 4.20: In-plane stair-case failure with a brick shape factor of 0.5 under a bed joint compression  $N_{22}$  combined with in-plane shear  $N_{12}$  of the same order of magnitude: deformed shape of the unit cell (the displacements are magnified by a factor of 10) (left), joint damage distribution (centre) and related acoustic tensor determinant spectrum as a function of the normal orientation  $\Theta$  ( $^\circ$ ) (right) at the end of the softening tail.

the same order of magnitude. The same failure mode can be detected here by using the criterion extended to Kirchhoff-Love shell formulation for the same loading case. Note that this computation is performed with the same material characteristics as in Section 4.5 except for the Mode-I fracture energy  $G_f$  which is taken 10 times larger to avoid a snap-back response which is more likely to appear for in-plane loading modes. Indeed, even though such a response can be traced using continuation methods, a snap-back response is accompanied with the recovery of a positive-definite tangent stiffness. As a result, the detection procedure cannot be applied anymore in snap-back regimes. The numerical results for this in-plane loading case are depicted in Figure 4.20 for the final situation in the softening regime. The potential bifurcation has appeared for orientations between  $-77.1^\circ$  and  $15.2^\circ$  (negative values of the related acoustic tensor determinant) with two local minima at  $-72.2^\circ$  and  $4.5^\circ$ , and a local maximum at the stair-case normal orientation

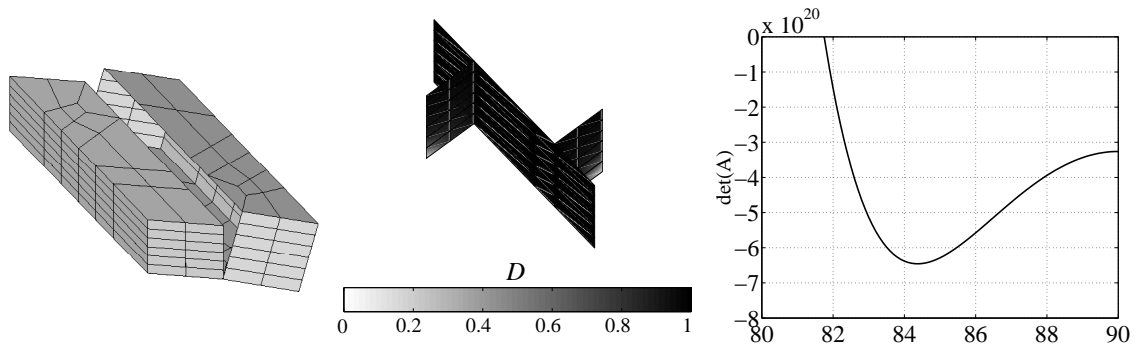


Figure 4.21: Out-of-plane bed joint failure under a bed joint compression  $N_{22}$  combined with in-plane shear  $N_{12}$  of the same order of magnitude and a bending moment  $M_{22}$ : deformed shape of the unit cell (the displacements are magnified by a factor of 10) (left), joint damage distribution (centre) and related acoustic tensor determinant spectrum as a function of the normal orientation  $\Theta(^{\circ})$  (right) at the end of the softening tail. The loading is along the stress path  $N_{22} = N_{12} = -25$  kN/m and  $M_{22} = 1.8$  kN

of  $-45^{\circ}$ , which shows again that the detection procedure works properly.

In order to show the influence of the loading on the obtained failure mode, a bending moment  $M_{22}$  is added to the bed joint compression  $N_{22}$  combined with in-plane shear  $N_{12}$ . The loading of the unit cell follows the stress path  $N_{22} = N_{12} = -25$  kN/m and  $M_{22} = 1.8$  kNm/m. Numerical results are shown in Figure 4.21 for the final situation in the softening regime. Note that all the joints of the unit cell are damaged except a small part of the head-joint. The negative local maximum of the related acoustic tensor determinant and the deformed shape of the unit cell show that an out-of-plane failure occurs along the bed joint.

As a result, the proposed approach allows to properly detect the occurrence of localisation when both membrane and flexural loadings are considered. This proves again that the localisation and failure orientation analysis has to be based on the averaged or homogenised tangent stiffness taking into account the membrane-flexural coupling.

### 4.6.3 Influence of the RVE size

All computations presented so far are performed on a unit cell of masonry and allow to deal with single period damage patterns as bed joint and stair-case failures. Note that the use of a single period RVE for *localisation detection* is justified in this case by the fact that only material non-linearities are considered. As a result, the loss of uniqueness in the average response cannot be caused by geometrical non-linearities and the detection of localisation and its orientation are therefore independent of the RVE size.

It is also emphasized that the averaged post-peak response is itself RVE size dependent. Larger RVEs would indeed contain several parallel average cracks for a given loading program. If all of these cracks develop, the same average response would be obtained. If on the contrary a bifurcation treatment is used inside the RVE, only one of these cracks will develop, leading to a more brittle averaged response in the post-peak regime. This size dependence of the averaged post-peak response calls for specific ingredients in its exploitation in structural computations (see Section 4.6.4).

Furthermore, note that the damage patterns whose period is not a masonry stacking period cannot be considered using a unit cell of masonry at the mesoscopic scale. This can be illustrated by applying on the unit cell a bending moment  $M_{11}$  where the  $x_1$ -axis

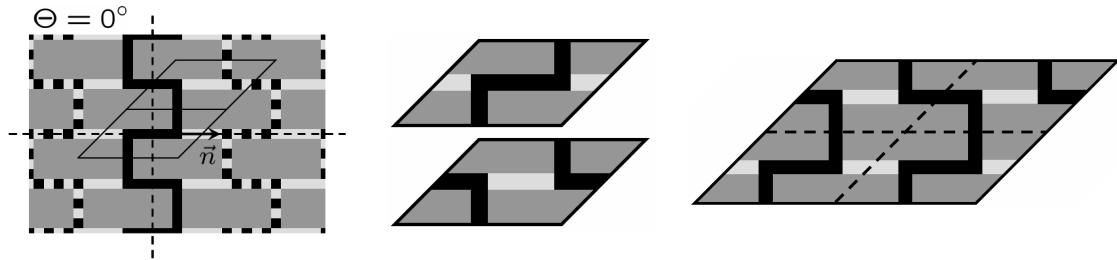


Figure 4.22: Out-of-plane failure pattern and its average orientation defined by the normal  $\vec{n}$  for the loading of a bending moment  $M_{11}$  (left), corresponding failure patterns in a unit cell (centre), and failure pattern in a RVE composed by  $2 \times 2$  unit cells (right).

is parallel to the bed joint. The failure mode corresponding to this loading is depicted in

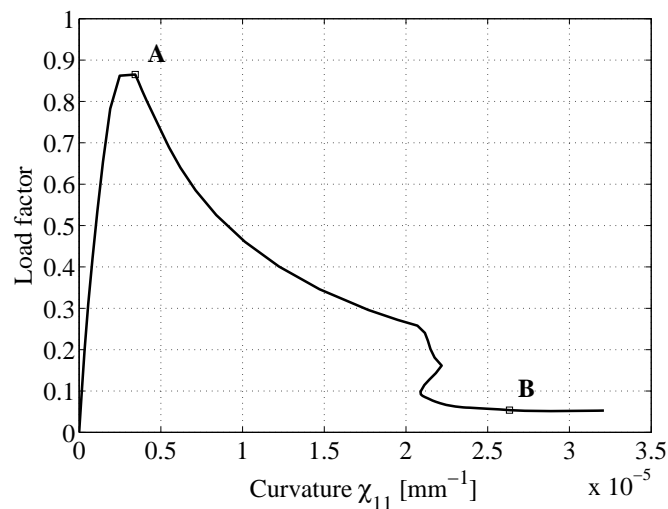


Figure 4.23: Load-curvature response under a bending moment  $M_{11}$ . The unit load factor corresponds to  $M_{11} = 2$  kN.

Figure 4.22 assuming that no failure can occur in the brick. The normal to this average crack orientation is oriented at  $0^\circ$ , and the two corresponding possible damage patterns extracted from a unit cell both match stair-case modes ( $\Theta = \pm 45^\circ$ ). As a result, the unit cell final state cannot correspond to an orientation of  $\Theta = 0^\circ$ . A RVE composed by  $2 \times 2$  unit cells is able to represent properly the crack pattern, see Figure 4.22. To illustrate this, the load-curvature response depicted in Figure 4.23 represents the variation of the load factor as a function of the curvature  $\chi_{11}$ . Note that this response exhibits a snap-back in the softening regime around  $\chi_{11} = 2 \times 10^{-5}$  mm<sup>-1</sup>. The numerical results for this case are shown in Figure 4.24. At the peak of the response (Figure 4.24, state A), a crack with an average normal orientation of  $-0.5^\circ$  is detected from the acoustic tensor determinant negative maximum and it is shown that no normal opening of the bed joint occurs which matches the failure mode depicted in Figure 4.22 (left). During the final phase of the softening regime (Figure 4.24, state B), all the joints of the unit cell are damaged. The orientation corresponding to the negative local maximum has however significantly changed and matches the normal orientation of a stair-case failure mode at  $45^\circ$ . Note that this change of failure orientation occurs just at the snap-back in the softening regime.

It can thus be concluded that the use of the proposed localisation detection with a

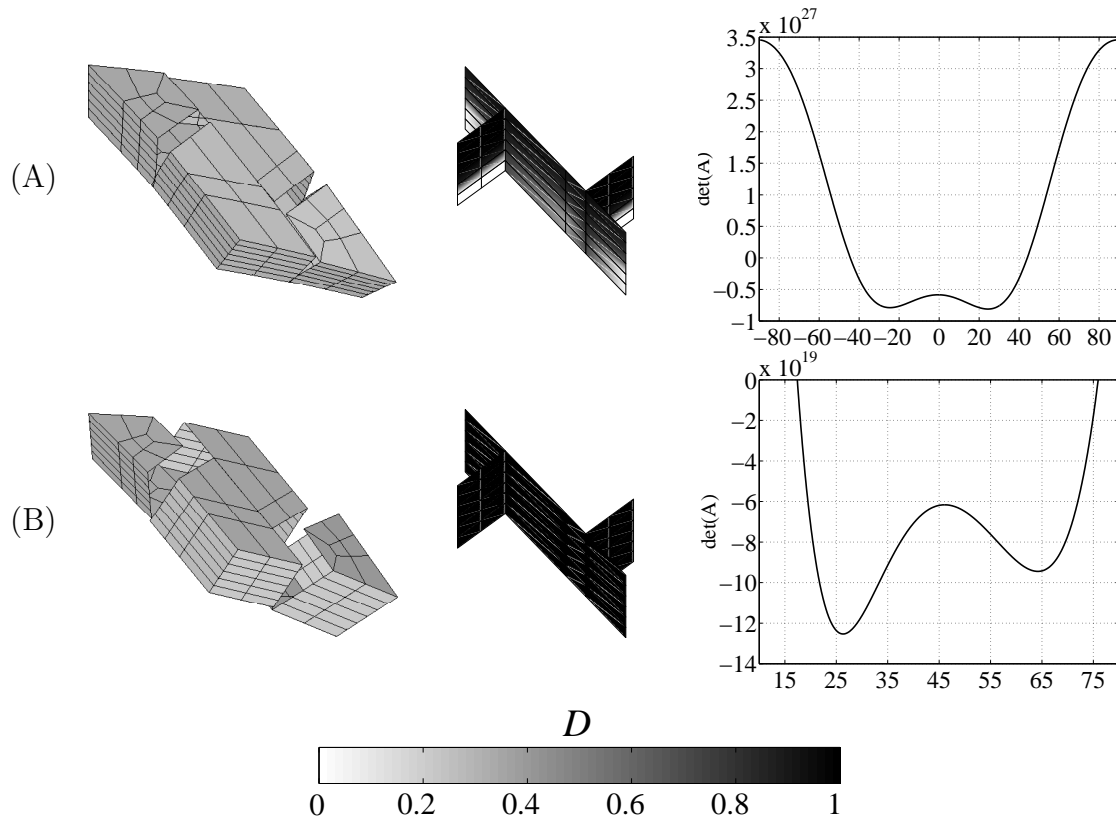


Figure 4.24: Out-of-plane failure under a bending moment  $M_{11}$ : deformed shape of the unit cell (the displacements are magnified by a factor of 500 (A) and 50 (B)) (left), joint damage distribution (centre) and related acoustic tensor determinant spectrum as a function of the normal orientation  $\Theta$  ( $^\circ$ ) (right).

unit cell is able to properly detect localisation orientation for patterns which do match the single period nature of the cell. Larger RVEs matching the periodicity of the damage pattern are needed when their periodicity does not match the stacking of constituents.

#### 4.6.4 Incorporation in structural computations

The results above suggest that unit cell computations could be used in multi-level methods, see Feyel and Chaboche (2000). The localisation information obtained from cell computations can indeed be used to feed a structural scale shell description accounting for localisation in the spirit of Massart et al. (2007a). However, two important observations have to be emphasized in this respect. First, the computations presented in this Chapter are performed on proportionally loaded unit cells. For certain cases, like the out-of-plane stair-case failure, it can be shown that the negative local maximum of the related acoustic tensor determinant which determines the crack normal orientation does not appear immediately after the response peak. The crack normal orientation deduced from the non positive-definiteness of the acoustic tensor evolves during the softening regime and tends progressively towards the mesostructurally motivated average localisation orientation. Should this occur in structural computations, this would call for some technique allowing to account for the variation of the average crack orientation at the structural scale. If not, an evolving localisation orientation at the mesoscale could lead to macroscopic stress locking. Note however that such a variation was observed for proportional

stress loading, while damage localisation can induce stress redistribution in structural computations. Secondly, the potential presence of snap-backs in a cell response in relation with strain-driven scale transition procedures should be treated if they are incorporated in structural computations using advanced path following techniques, see Massart et al. (2005a).

## 4.7 Conclusions

A computational homogenisation-based detection of localisation was proposed for masonry shells. It was shown that the combination of a computational homogenisation scheme for out-of-plane behaviour with an acoustic tensor-based localisation criterion adapted to thin planar shell kinematics allows to determine structural localisation orientations consistent with the preferential fine-scale damage patterns of masonry. This approach was illustrated by an example of out-of-plane bed joint failure and two examples of out-of-plane stair-case failure with different geometrical aspect ratios of the units.

The robustness of the proposed localisation detection procedure was discussed. It was shown that this approach allows the proper localisation tracking when the mesoscopic material properties are modified and when both membrane and flexural loadings are considered. It was also illustrated that the proposed approach should be extended with larger RVEs to properly detect localisation orientation for patterns which do not match the periodicity of the unit cell. Finally, the need to treat potential presence of snap-back in the average response and of macroscopic stress locking due to evolving localisation orientation was emphasized for further incorporation of the proposed approach in structural computations.

As an extension of the present work, the proposed approach could be directly incorporated in a two-scale computational framework. In order to build a consistent framework, the structural localisation treatment should be based on the homogenised response of the RVE with a proper implementation of energetic consistency. Moreover, the presented framework should be extended to the Reissner-Mindlin shell kinematics in order to take into account the transverse shear effects. Finally, as already mentioned, a more physically general description of the various failure modes of masonry shells (incorporating brick cracking or friction related phenomena) would require a more advanced mesoscopic description. Such enhancements can be accommodated without any modification of the scale transition and localisation detection procedures.

# Chapter 5

## Assessment of periodic homogenisation-based multi-scale computational schemes for quasi-brittle structural failure

New methods for the modelling of structural failure by means of multi-scale approaches were recently proposed, in which the structural description involves coarse-scale discontinuities, the behaviour of which is fed by Representative Volume Element (RVE) computations. Their main asset consists in identifying the material response from fine-scale material parameters and computations, including the failure behaviour of the material. One of the distinctions between the available approaches relates to the boundary conditions applied on the RVE. The methods based on classical computational homogenisation usually make use of periodic boundary conditions. This assumption remains a priori debatable for the localised behaviour of quasi-brittle materials. For the particular case of periodic materials (masonry), the level of approximation induced by the periodic assumption is here scrutinised. A new displacement discontinuity-enhanced scale transition is therefore outlined based on energetic consistency requirements. The corresponding multi-scale framework results are compared with complete fine-scale modelling results used as a reference, showing a good agreement in terms of limit load, and in failure mechanisms at both the fine scale and at the overall structural level.

### 5.1 Introduction

The formulation of macroscopic constitutive laws for the behaviour of damaging quasi-brittle materials is a difficult task. Complex closed-form constitutive laws formats are needed to account for effects such as damage-induced anisotropy. In addition, evolution laws have to be used for the additional parameters entering such equations, which leads to cumbersome and costly experimental identification procedures, especially when initial

---

This Chapter is based on: B.C.N. Mercatoris and T.J. Massart, Assessment of periodic homogenization-based multiscale computational schemes for quasi-brittle structural failure, *International Journal for Multiscale Computational Engineering*, 7(2), 153–170, 2009.

anisotropy is considered. The masonry material poses all of these challenges simultaneously, due to its strongly heterogeneous microstructure which considerably influences its overall mechanical behaviour.

The focus will here be set on structural computations for masonry structures. In this context, the formulation of closed-form constitutive laws has been pursued in the last decade, see for instance Lourenço et al. (1997), Berto et al. (2002) for examples of two-dimensional developments. To complement general closed-form constitutive equations, multi-scale techniques have been proposed and applied to non-linear mechanical behaviour with different purposes (material identification vs. structural computations), as well as different range of applicability (periodic or non-periodic materials, quasi-brittle vs. ductile materials). Restricting the overview on textured quasi-brittle materials such as masonry, different approaches were presented recently. A first class of frameworks bears similarities to domain decomposition methods, rather than upscaling fine-scale material behaviour towards coarser scales material response, Brasile et al. (2007a,b), Ibrahimbegovic and Markovic (2003), Markovic and Ibrahimbegovic (2004). In these methods, the structure is decomposed in non-overlapping subdomains. The equilibrium equations are solved on the structure using this domain decomposition, together with compatibility conditions at the interfaces between them. Such an approach allows to incorporate non-linear behaviour features in the computations up to failure. It does not rely on other a priori assumptions, while keeping a significant but distributed computational effort, mainly prescribed by the level of details associated to the chosen microstructural modelling strategy. Another class of frameworks is based on the identification of average (coarse scale) material behaviour features by means of representative volume element (RVE) or unit cell computations. A nested multi-scale computational strategy, known as  $FE^2$ , was proposed in Feyel and Chaboche (2000), Smit et al. (1998), Kouznetsova et al. (2001); and applied to the mechanical behaviour of metallic and polymeric materials, and was later extended to other physical phenomena, Ozdemir et al. (2008a,b). The coarse-scale material behaviour of a classical continuum description is then sampled at each quadrature points by using an auxiliary fine-scale boundary value problem based on periodic homogenisation averaging principles. This allows to derive numerically the average stress and tangent stiffness for an applied average strain. The applicability of such an approach is restricted to situations in which the principle of scale separation applies between the fine and coarse descriptions. The computational effort therefore remains important, but substantially decreases with respect to a full fine-scale modelling of structures.

A simplified adaptation to cracking in quasi-brittle materials was first proposed in Luciano and Sacco (1997, 1998) with off-line periodic homogenisation, but without structural scale localisation treatment. Two different strategies were proposed recently to tackle damage localisation at the coarse scale by introducing displacement or strain discontinuities in multi-scale methods. A first approach consists in feeding the behaviour of coarse-scale equivalent displacement discontinuities with information extracted from the aggregation of all fine-scale material instabilities present in a unit cell, in the spirit of Belytschko et al. (2008). Another methodology making use of the initially periodic microstructure of masonry is explicitly based on periodic homogenisation of unit cells and based on embedded strain discontinuities, as in Massart et al. (2007a). However, periodicity is an assumption which remains strongly debatable in the localised cracking regime, since the principle of scales separation does not apply in that case. Yet, for the initially periodic masonry material, with failure modes clearly dominated by its periodic microstructure, the degree of approximation involved by the local periodicity assumption

remains untested, and will be challenged here.

The main objective of this Chapter is to analyse the effect of this periodicity assumption. This will be achieved by comparing the results obtained from a homogenisation-based multi-scale computation on confined shear wall tests with the results of a full fine-scale model based on the same material parameters value, and taken as a reference result. In order to make this comparison possible, an improvement of the framework proposed in Massart et al. (2007a) will be presented. The coarse (structural) scale localisation will therefore be described by the introduction of strong discontinuities in the kinematical description in the spirit of Armero (1999). Secondly, a cohesive law-based model will be used at the fine scale in order to improve the efficiency of the computations, and allow a complete fine-scale modelling of the confined shearing test.

The Chapter is structured as follows. A simple scalar damage model with interface elements used for the mortar joints at the fine scale is formulated in Section 5.2. The essential ingredients of a localisation-enhanced multi-scale scheme for failure of periodic quasi-brittle materials are presented in Section 5.3. The details of the upscaling towards a coarse-scale displacement discontinuity are presented in this Section with a special emphasis on the aspects differing from Massart et al. (2007a), and on the energy consistency argument. The results obtained from this multi-scale framework for confined shearing tests are discussed and compared with those of complete fine-scale models in Section 5.4. Finally, the conclusions and prospects are given in Section 5.5.

## 5.2 Simplified fine-scale constitutive setting for masonry

Since the aim is to compare multi-scale modelling results with a full fine-scale representation containing all the heterogeneities of the mesostructure, the same fine-scale constitutive laws have to be used in both cases. The choice of a simplified fine-scale constitutive setting may be motivated for both modelling approaches. For multi-scale computation, the constitutive laws of the constituents are kept simple in order to focus on the extraction of coarse-scale averaged behaviour features based on a finer scale description. For full fine-scale computations, this allows to get an affordable discretisation in terms of computational cost. Therefore, the failure behaviour of the bricks is not considered in this study and they are assumed elastic. The combined behaviour of the brick-joint interface and of the mortar is modelled by an initially elastic interface element, for which both the normal and tangential stiffnesses ( $k_n$ ,  $k_t$ ) can be related to the elastic behaviour of mortar, Lourenço and Rots (1997). A classical Mohr-Coulomb type strength criterion is used with a tension cut-off and a linear compression cap, as depicted in Figure 5.1. The parameters  $f_t$  and  $f_c$  are respectively the tensile mode I strength of the mortar or mortar-brick interfaces, and the compressive strength of masonry as a composite.  $c$  is the cohesion,  $\varphi$  is the friction angle, and  $\vartheta$  is the angle which defines the linear compression cap for the mortar joints.

A scalar damage model with an exponential evolution law is considered. The traction-separation law which links the traction vector  $\vec{t}$  across the interface to the relative displacement vector  $\vec{\delta}$  is given by

$$\vec{t} = (1 - D) \mathbf{H} \cdot \vec{\delta} \quad (5.1)$$

where  $D$  is the scalar damage variable growing from zero (virgin material) to one (complete failure) and  $\mathbf{H}$  is an elastic stiffness second order tensor which depends on the elastic

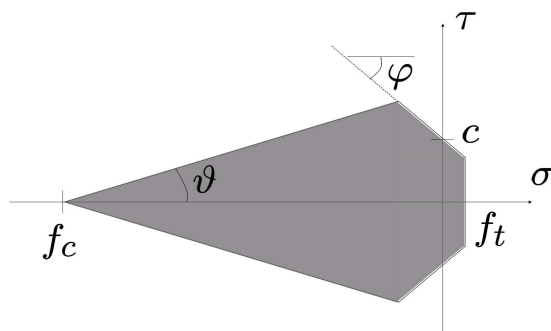


Figure 5.1: Mohr-Coulomb criterion for the mortar joint/mortar-brick interface with tensile cut-off and linear compressive cap.

stiffnesses  $k_n$  and  $k_t$ . Note that (5.1) implies that no stiffness recovery is taken into account upon crack closure.

The damage evolution law of the mortar joint is given by

$$D(\kappa) = 1 - \frac{f_t}{k_n \kappa} e^{-\frac{f_t}{G_f} (\kappa - \frac{f_t}{k_n})} \quad \text{for } \kappa \geq \frac{f_t}{k_n} \quad (5.2)$$

where  $G_f$  is the mode I tensile fracture energy. Since the damage criterion has to take into account the different behaviours in tension and compression, the damage-driving parameter  $\kappa$  is taken as the most critical value of an equivalent relative displacement defined by

$$\delta_{eq} = \max \left\{ \begin{array}{l} \frac{f_t}{c} \tan \varphi \delta_n + \frac{f_t}{c} \frac{k_t}{k_n} |\delta_t| \\ \delta_n \\ -\frac{f_t}{f_c} \delta_n + \frac{f_t}{f_c} \frac{k_t}{k_n} \frac{1}{\tan \vartheta} |\delta_t| \end{array} \right\} \quad (5.3)$$

where  $\delta_n$  and  $\delta_t$  are the normal and tangential relative displacements, respectively. Note that since only one fracture energy parameter is used, the compressive fracture energy of masonry is implicitly defined by the tensile fracture energy  $G_f$  and the relative values of parameters  $f_c$  and  $f_t$ , and cannot be adapted independently. As aforementioned, note that relations (5.1) to (5.3) were postulated for the sake of simplicity and to focus on the subject of the Chapter, i.e. the degree of approximation introduced by the scale transition procedure. More complex mortar formulations including different damage evolutions in mode I and mode II in terms of energy dissipation could be used as well, see Lourenço and Rots (1997). A brick damage model could also be used for instance in order to extend the detection procedure to additional failure modes involving brick failure, see Lourenço and Rots (1997), Massart et al. (2005b) for the case of in-plane problems.

## 5.3 Homogenisation-based upscaling framework for failure

### 5.3.1 Periodic homogenisation of masonry behaviour

To keep this contribution focused, details concerning classical aspects of periodic computational homogenisation will only be sketched, their developments being available in

the literature, see Anthoine (1995), Kouznetsova et al. (2001). The essentials of masonry behaviour can be homogenised from the behaviour of its basic constituents, i.e. bricks and mortar joints. Based on its initially periodic microstructure, a unit cell (i.e. a single period RVE) can be used together with averaging relations, see Figure 5.2. A periodic displacement field of the following form is used, see Anthoine (1995)

$$\vec{u} = \mathbf{E} \cdot \vec{x} + \vec{w} \quad (5.4)$$

where  $\mathbf{E}$  is a coarse-scale strain tensor,  $\vec{x}$  is the position vector of an arbitrary point within the cell and  $\vec{w}$  is a periodic mesoscopic fluctuation field, added to the linear displacement field to account for the heterogeneity of the material. Such a displacement field allows to enforce the averaging relation linking fine and coarse-scale strains

$$\mathbf{E} = \frac{1}{V_{\text{cell}}} \int_{V_{\text{cell}}} \boldsymbol{\varepsilon}(\vec{u}) \, dV \quad (5.5)$$

where  $V_{\text{cell}}$  indicates the cell volume. Practically, the periodicity of the fluctuation field is enforced by linear tying relations involving the displacements of opposite boundaries, see Kouznetsova et al. (2001). The work equivalence principle (Hill-Mandel) is used in order to link the mesoscopic and macroscopic virtual work, see Anthoine (1995)

$$\boldsymbol{\Sigma} : \delta \mathbf{E} = \frac{1}{V_{\text{cell}}} \int_{V_{\text{cell}}} \boldsymbol{\sigma} : \delta \boldsymbol{\varepsilon} \, dV \quad (5.6)$$

which results in the averaging relation between coarse and fine-scale stress tensors

$$\boldsymbol{\Sigma} = \frac{1}{V_{\text{cell}}} \int_{V_{\text{cell}}} \boldsymbol{\sigma} \, dV \quad (5.7)$$

Based on the periodicity assumption, relations (5.4)-(5.7) allow to formulate a boundary value problem on the unit cell, and to control or extract average quantities (strains, stresses, tangent stiffness) from displacements or tying forces at specific controlling points, see Kouznetsova et al. (2001) for details. This methodology was used extensively for material characterisation, i.e. without incorporation within structural computations, initially for elastic behaviour, see Pande et al. (1989), Anthoine (1995). Recent works considered the extension to non-periodic random microstructures using statistically equivalent unit cells, see Zeman and Šejnoha (2007). Their extension to non-linear behaviour showed that physically meaningful results could be obtained in terms of strength and failure patterns, see Pegon and Anthoine (1997), Anthoine (1997), Massart et al. (2004, 2005b).

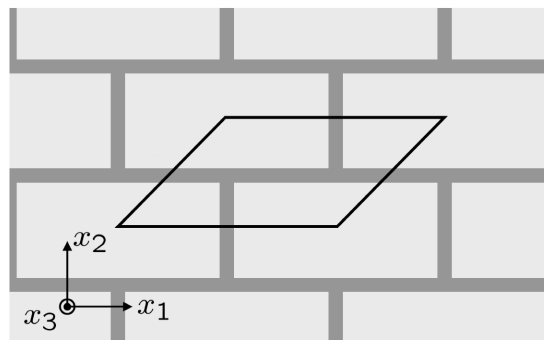


Figure 5.2: In-plane periodicity of running bond masonry, see Anthoine (1995).

### 5.3.2 Principles for upscaling the failure behaviour of periodic materials

As presented in Feyel and Chaboche (2000), Smit et al. (1998), Kouznetsova et al. (2001), the upscaling procedure prior to coarse-scale localisation consists in applying periodic homogenisation in each coarse-scale point of a classical continuum. However, failure at each scale of representation should be carefully treated to obtain meaningful results. At the scale of constituents, classical closed-form constitutive laws can be used, as described in Section 5.2.

At the coarse scale, and since no a priori postulated constitutive relation is readily available, the detection of localisation has to be based on the average quantities resulting from the upscaling procedure. As a result, the onset of structural localisation is detected from the homogenised tangent stiffness and the associated acoustic tensor. The localisation can be associated to a condition for the loss of ellipticity of the coarse-scale equilibrium problem, based on the non positive-definiteness of the homogenised acoustic tensor for some orientation, see Rice (1976), Rice and Rudnicki (1980). Alternatively, it can be associated to a condition for the loss of uniqueness of the discretised fine-scale boundary value problem, i.e. non positive-definite character of the homogenised tangent stiffness, see de Borst et al. (1993). As already identified in Massart (2003), Mercatoris et al. (2009), the latter criterion will be used to detect occurrence of localisation and the former to extract the average orientation of the localisation zone. It is emphasised that when periodic homogenisation is used, this coarse-scale localisation detection procedure actually introduces a periodicity-related approximation with respect to a fine-scale description, since this type of boundary condition may overconstrain the unit cell and overestimate the average tangent stiffness of the material.

An important and debated choice is related to the RVE size. In the present case of quasi-brittle failure, a geometrically linear description is used. The loss of uniqueness can only be associated to material non-linearities, and the localisation detection is not RVE-size dependent, see Massart et al. (2004). As a result, a unit cell will be used here, thereby restricting the model to damage configurations which can be described with such a cell, i.e. single period cracks.

Once structural localisation and its orientation are detected, a discontinuity with this orientation has to be introduced in the coarse-scale description to account for the damage localisation, together with elastically unloading surrounding zones, as sketched in Figure 5.3a. In Massart et al. (2007a), a strain discontinuity with a given width (see Figure 5.3) was used within a relaxed Taylor model to represent the average effect of the localising zone in a coarse-scale quadrature point. The presence of this strain discontinuity was not explicitly incorporated in the coarse-scale discretisation as such, but was rather embedded in the average behaviour of the considered quadrature point. The behaviour of the localising region was directly obtained from the homogenised behaviour of a further damaging unit cell. Here, the discontinuity will be explicitly introduced in the coarse-scale displacement field discretisation in the spirit of Armero (1999), by using a lumped displacement jump. This format requires the extraction of a cohesive response from the average behaviour of a damaging unit cell. This extraction should enforce that the correct amount of dissipated energy is transferred to the coarse scale. Again, it is emphasised that this treatment of structural localisation implicitly carries assumptions if periodic homogenisation is still used to extract this coarse-scale cohesive response, since the scale separation assumption is not satisfied anymore upon coarse-scale localisation.

Furthermore, as an additional choice, the zones surrounding the localising regions are assumed to unload elastically, an assumption which might not be satisfied during the complete loading history of all the concerned points in the structure.

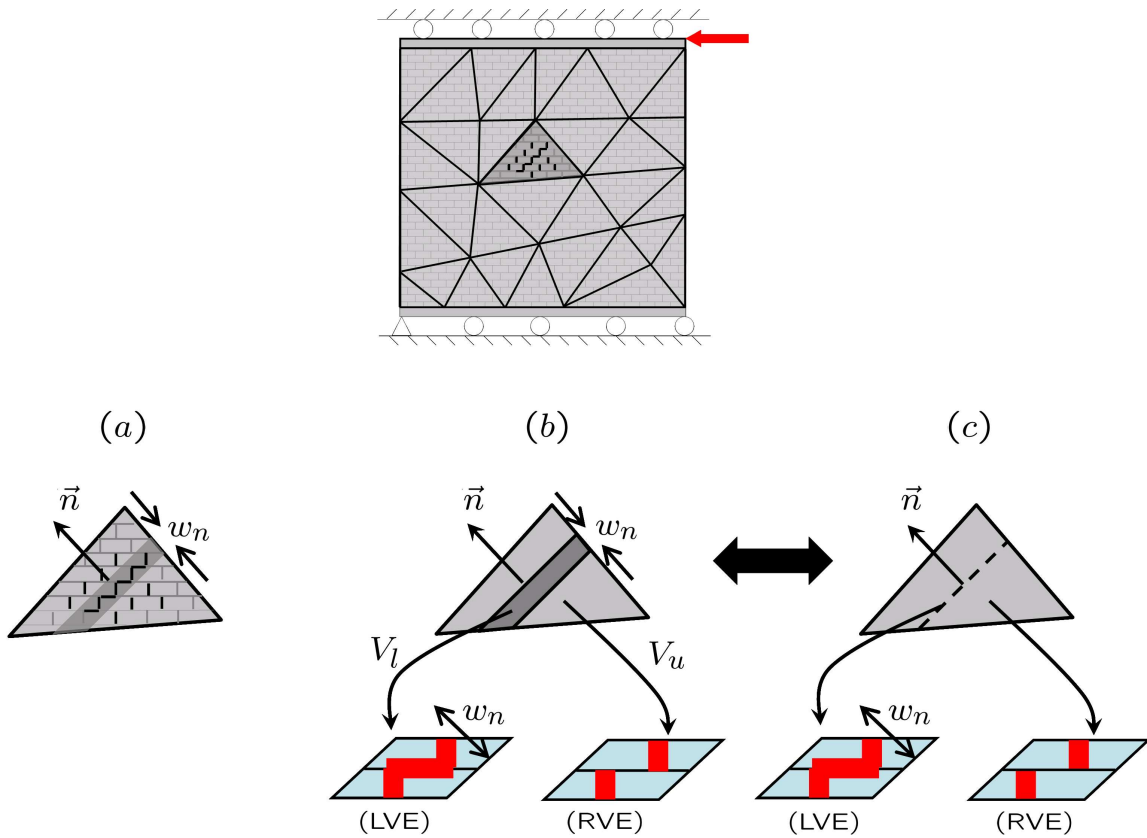


Figure 5.3: Identification of a coarse-scale discontinuity from a fine-scale damage pattern. (a) fine-scale damage pattern, (b) identification of a further damaging and localising band of volume  $V_l$  and of an unloading surrounding regions of volume  $V_u$ , (c) aggregation towards a strong discontinuity at coarse scale. Comparison of (a) and (b) defines the localising volume, while the energetic consistency originates from the equivalence between (b) and (c).

### 5.3.3 Incorporation of a strong discontinuity at coarse scale

The structural scale problem is solved using the finite element method and using an embedded strong discontinuity model in which the behaviour of the discontinuity is obtained from fine-scale computations. Once structural localisation is detected, the coarse-scale displacement field is enriched by a strong discontinuity, as proposed by Armero (1999). A displacement jump  $\vec{\xi}$  is introduced along a discontinuity line  $\Gamma_d$ , the orientation of which is deduced from the acoustic tensor-based criterion. This jump is added to the regular continuous part of the displacement field according to

$$\vec{u}_e = \vec{u} + \Psi \vec{\xi} \quad (5.8)$$

where  $\Psi$  represents a set of functions exhibiting a unit jump along the discontinuity line. The enhanced strain tensor is obtained by differentiating Equation (5.8), which leads to

$$\mathbf{E}_e = (\vec{\nabla} \vec{u}_e)^{\text{sym}} = \mathbf{E}(\vec{u}) + \mathbf{G}(\vec{\xi}) + (\vec{\xi} \vec{n})^{\text{sym}} \delta_{\Gamma_d} \quad (5.9)$$

where  $\mathbf{E}(\vec{u})$  is the strain tensor based on classical kinematics,  $\mathbf{G}(\vec{\xi})$  is the regular part of the enhanced strain tensor  $\mathbf{E}_e$  which depends on the displacement jump and  $\delta_{\Gamma_d}$  is the Dirac function centred on the discontinuity line. This Dirac function is integrated along the discontinuity line and therefore does not need regularisation, see de Borst et al. (2001). The details concerning the discretisation of such an enhanced kinematics, among which the construction of the tensor  $\mathbf{G}$  can be found in Armero (1999) and are sketched in 3, and will be omitted here for brevity.

In order to determine the additional displacement jump field, the weak form of equilibrium is solved together with a weak continuity condition on the stress along the discontinuity line:

$$\int_{\Gamma_d} \left( \vec{T}_d - \boldsymbol{\Sigma} \cdot \vec{n} \right) d\Gamma_d = 0 \quad (5.10)$$

where  $\vec{T}_d$  is the traction vector across the discontinuity,  $\boldsymbol{\Sigma}$  is the stress tensor in the bulk, surrounding the discontinuity, and  $\vec{n}$  is the normal to the discontinuity line  $\Gamma_d$ . A material response which links the traction vector to the displacement jump is required to drive the discontinuity and reads

$$\delta \vec{T}_d = {}^2\mathbf{C}_d \cdot \delta \vec{\xi} \quad (5.11)$$

where  ${}^2\mathbf{C}_d$  is the discontinuity tangent stiffness tensor. Once the embedded discontinuity is introduced, the bulk of the element is assumed to unload elastically from the state reached at that point.

Note that this strong discontinuity approach is an element-based enrichment of the displacement field. This carries the advantage that the additional displacement jump field may be condensed at the element level. As a corresponding drawback, this implies that the crack path continuity and the displacement jump field continuity across the element boundaries are not ensured, which may have consequences in terms of global energy dissipation. Note also that an extension in this respect could be considered with an XFEM-based implementation at the coarse scale as in Belytschko et al. (2008). However, the extraction of an average discontinuity behaviour from the homogenisation of fine-scale computations can lead to the re-orientation of this discontinuity as a result of further fine-scale damage evolutions. This fact is particularly important for the case of strongly textured materials as masonry, and should be accounted for to avoid stress locking phenomena at the coarse scale, which is easier to accommodate with an element-based enrichment.

### 5.3.4 Upscaling localising behaviour towards coarse-scale discontinuities

In this Chapter, contrary to the approach proposed by Armero (1999) where constitutive laws are given by closed-form laws, both the bulk and discontinuity material behaviours are deduced from fine-scale unit cell computations. A material secant stiffness is extracted from the unit cell in which the structural localisation has just been detected. The material behaviour of the discontinuity, described by Equation (5.11) at the coarse scale, must be extracted from the fine-scale description by means of an enhanced upscaling procedure. A further damaging unit cell is used for this purpose, which will be denoted in the sequel as Localising Volume Element (LVE), see Figure 5.3.

The extraction of the coarse-scale discontinuity response requires the definition of an average strain  $\mathbf{E}^{\text{LVE}}$  to be applied on the LVE from the coarse-scale displacement jump;

as well as the evaluation of  $\vec{T}^d$  and  ${}^2\mathbf{C}_d$  from the results of the LVE computation. An approximate energy consistency argument is used as illustrated in Figure 5.3 in order to build a relationship between the displacement jump vector  $\vec{\xi}$  across a zero-thickness zone with an orientation  $\vec{n}$  used at the coarse scale, and the average strain  $\mathbf{E}^{\text{LVE}}$  applied to a localising region with a finite volume detected at the fine scale. The localisation width  $w_n$  defining the volume of the localising region therefore has to enter this relationship to take into account in the coarse-scale description the finite fine-scale volume on which damage localisation occurs. The introduction of the fine-scale localisation width in the scale transition indeed allows to objectively upscale the total energy dissipation independently of the coarse-scale discretisation.

Writing the work variation for the idealised band-surrounding representation (Figure 5.3b), in which the localising region behaviour is identified from the LVE and the unloading region is associated with an unloading RVE yields

$$\delta W_m = \int_{V_u} \boldsymbol{\Sigma}^{\text{RVE}} : \delta \mathbf{E}^{\text{RVE}} dV_u + \int_{V_l} \boldsymbol{\Sigma}^{\text{LVE}} : \delta \mathbf{E}^{\text{LVE}} dV_l \quad (5.12)$$

where  $V_l$  and  $V_u$  represent respectively the volumes of the further loading (damaging) and unloading regions. In the corresponding coarse-scale representation (Figure 5.3c), the localising behaviour is lumped into a zero-thickness cohesive zone and the complete volume of the element is assumed to unload according to the behaviour extracted from the RVE. The corresponding work variation reads

$$\delta W_M = \int_{V_u} \boldsymbol{\Sigma}^{\text{RVE}} : \delta \mathbf{E}^{\text{RVE}} dV_u + \int_{V_l} \boldsymbol{\Sigma}^{\text{RVE}} : \delta \mathbf{E}^{\text{RVE}} dV_l + \int_{\Gamma_d} \vec{T}^d \cdot \delta \vec{\xi} d\Gamma \quad (5.13)$$

The strain jump variation associated with a strain discontinuity mode vector  $\delta \vec{m}$  along a discontinuity line of normal  $\vec{n}$  is given by

$$\delta \mathbf{E}^{\text{LVE}} - \delta \mathbf{E}^{\text{RVE}} = \frac{1}{2} (\vec{n} \delta \vec{m} + \delta \vec{m} \vec{n}) \quad (5.14)$$

Assuming that the variations  $\delta \mathbf{E}^{\text{LVE}}$ ,  $\delta \mathbf{E}^{\text{RVE}}$ , and  $\delta \vec{\xi}$  are constant on the domains on which they are integrated, assuming that the traction continuity is enforced along the boundary between the localising and unloading regions, and defining the traction across the coarse-scale discontinuity from the LVE average stress, one obtains

$$\vec{T}^d = \boldsymbol{\Sigma}^{\text{LVE}} \cdot \vec{n} = \boldsymbol{\Sigma}^{\text{RVE}} \cdot \vec{n} \quad (5.15)$$

Imposing the energy equivalence  $\delta W_m = \delta W_M$  then yields

$$w_n (\delta \mathbf{E}^{\text{LVE}} - \delta \mathbf{E}^{\text{RVE}}) \cdot \vec{n} = \delta \vec{\xi} \quad (5.16)$$

As a result, the average strain on the LVE is related to the coarse-scale displacement jump according to

$$\delta \mathbf{E}^{\text{LVE}} \cdot \vec{n} = \frac{\delta \vec{\xi}}{w_n} + \delta \mathbf{E}^{\text{RVE}} \cdot \vec{n} \quad (5.17)$$

The first term of this relation expresses that the lumped displacement jump along the discontinuity at the coarse scale should incorporate a measure of the fine-scale finite volume on which damage occurs,  $w_n$  in this case. Note that this localisation zone width can vary with the failure mode observed at the fine scale. Here it will be taken equal to the

size of a unit cell in the direction of the normal to the detected localisation orientation. This carries the implicit assumption that the localisation occurs with single period cracks, which might not hold for given cracking modes, such as for instance vertical brick cracking under horizontal tension. The second term of relation (5.17) accounts for the fact that the RVE unloading is attributed to the complete volume of the element at the coarse scale. A part of the material inside the LVE is indeed also unloading upon localisation (namely the brick which behaves elastically), but this effect is already incorporated in the averaging operation on the LVE. This second term allows not to take this contribution twice in the energy consistency argument, under the assumption that the unloading material inside the localising band reacts as the identified surrounding material (i.e. with an secant unloading from the bifurcation point). Since the contribution of this second term is usually small, and for the sake of simplicity, it will be neglected in the sequel. Note that this approximation is theoretically valid for cases in which the localisation width is indeed negligible with respect to the dimensions of the coarse-scale elements.

The complete multi-scale nested procedure with localisation enhancement is depicted in Figure 5.4. Note that orientation of the discontinuities after their introduction is not fixed. Subsequent localisation analysis of the tangent stiffness of the LVE may indeed detect rotations in the detected localisation orientation as a result of further (unstable) damage growth. In such case, the coarse-scale discontinuity is allowed to rotate in order to avoid stress locking. This rotation is however limited at each step, in order to avoid convergence difficulties linked to sudden and strong rotations.

## 5.4 Comparison of multi-scale and fine-scale results on structural computations

In order to compare fine-scale and multi-scale approaches, the same structural computation will be performed using both descriptions. The in-plane confined shearing of a planar masonry wall without and with an opening is considered.

### 5.4.1 Confined shearing of a full masonry wall

In this Section, the multi-scale framework results are compared to fine-scale modeling results for a full masonry wall. The tested geometry is shown in Figure 5.5. It consists of a planar masonry wall of dimensions  $2220 \times 2160 \times 98 \text{ mm}^3$ , with bricks of dimensions  $120 \times 60 \times 98 \text{ mm}^3$  stacked according to a running bond pattern. Note that the size of the wall remains limited by the computational cost of the full fine-scale computation. The aspect ratio of the bricks prescribes a preferential stair-case crack pattern orientation of  $45^\circ$ . A clamping of the top and bottom brick rows in the loading set-up is represented by two bands of elements with elastic behaviour and with a stiffness comparable to concrete. The loading is applied in two phases. In the first phase, the wall is compressed by prescribing a uniform vertical displacement of the top boundary. In the second loading phase, the vertical displacement of the top boundary is kept fixed and a horizontal shearing displacement is prescribed on the top right corner of the wall. For low pre-compression loads, damage is first initiated during the confined shearing phase with the appearance of horizontal tensile cracks at the top left and bottom right corners of the wall. The extension of these tensile damage zones is lower for higher initial compressions. Their appearance is followed by the formation of a compressive strut between the bottom left

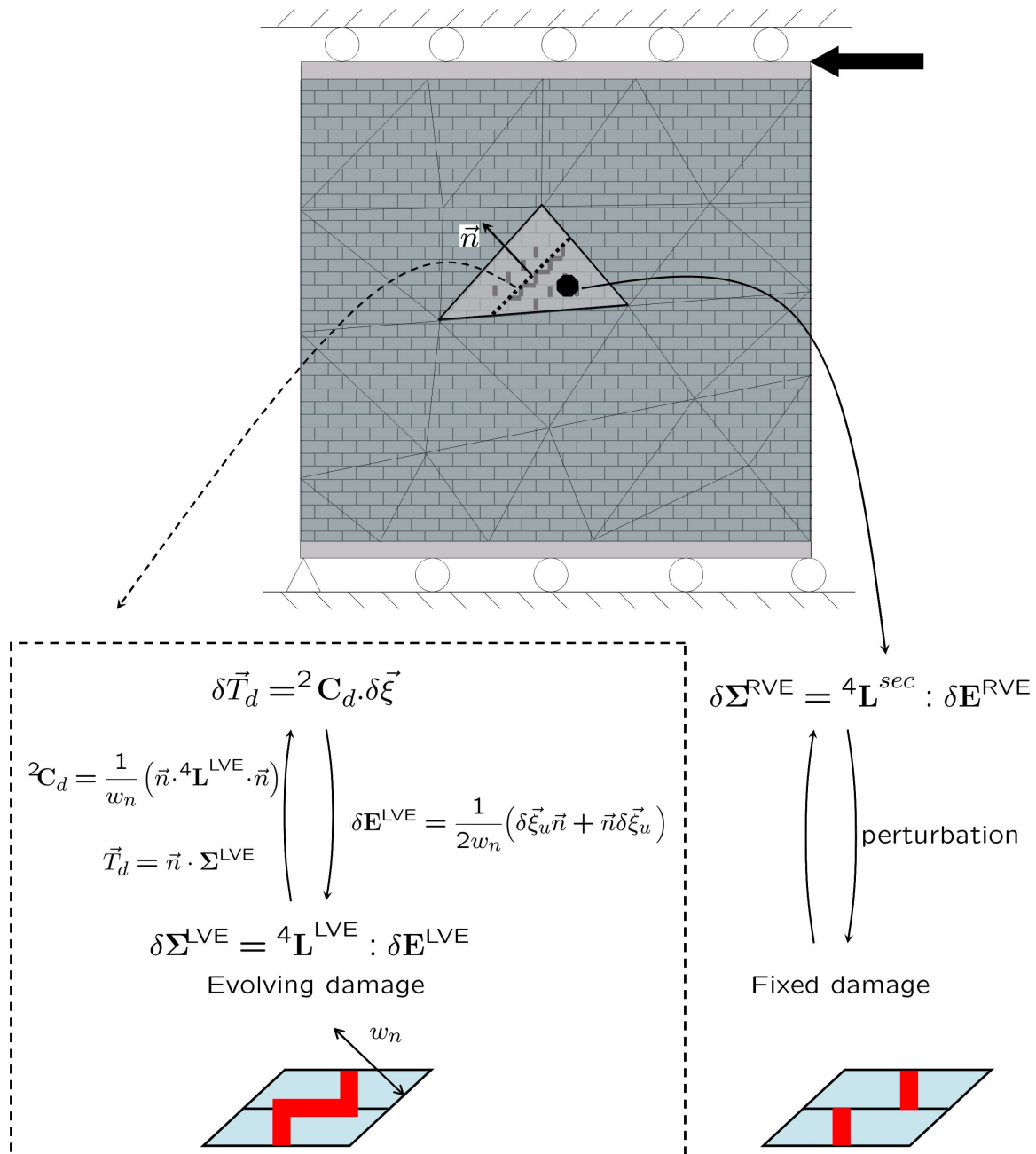


Figure 5.4: Complete localisation-enhanced nested scheme.

and top right corners. Upon further shearing, diagonal cracking appears in the central zone of the specimen in the compressive strut, with a stair-case crack pattern at the fine scale. During this compressive strut cracking phase, a strong interaction occurs between the fine-scale preferential cracking orientation, and the coarse-scale stress distribution prescribed by the confining boundary conditions. The difference between the respective orientation of the strut and of the fine-scale pattern strongly influences the damage-induced energy dissipation. Finally, a structural failure mechanism is formed by the propagation of diagonal cracking towards the compressed corners of the wall. Depending on the compressive strength of the mortar, final failure may occur by compressive crushing at the compressed corners of the wall, associated with brick cracking at the fine scale. Since bricks are assumed elastic, compressive crushing is represented here phenomenologically

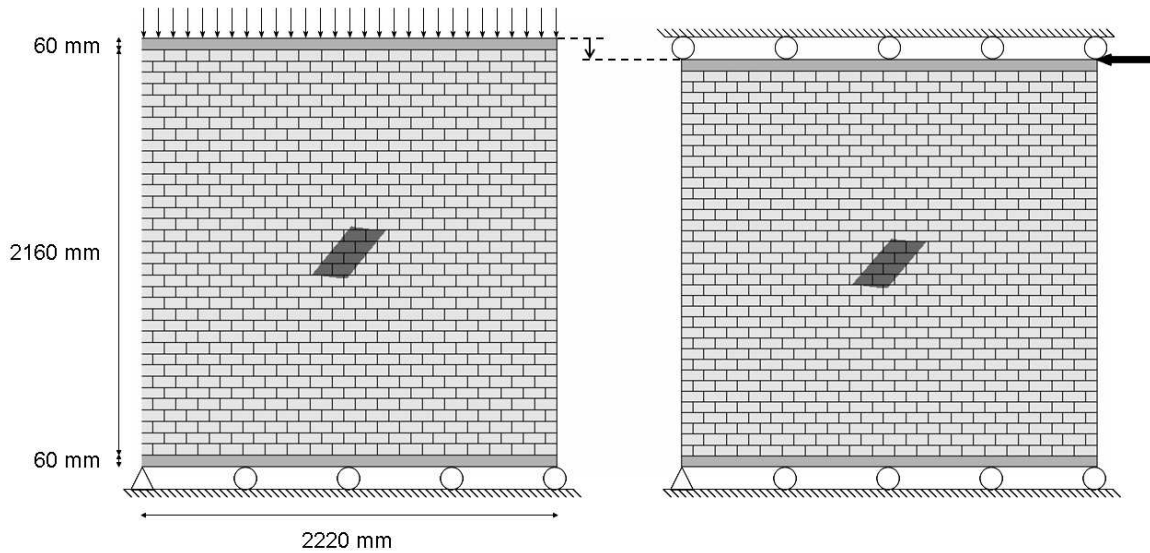


Figure 5.5: Confined shearing wall test description. The loading is applied in two successive phases: (a) compressive load applied on the top boundary layer, (b) horizontal shearing. The dark grey area depicts the stair-case crack defect introduced in the central zone of the wall to initiate localisation of damage in the diagonal compressive strut (decrease of the tensile strength and the cohesion of 50%).

by the compressive cracking of bed joints, see Lourenço and Rots (1997).

Due to the strong confinement present in this test, the stress distribution in the central part of wall remains rather uniform at the early stages of cracking, and the initial shearing damage zone is therefore quite diffuse. This transition from a distributed damage pattern to a localised cracking is difficult to capture computationally, and requires strong step refinements along the computations even for a full fine-scale discretisation. Furthermore, the use of a rather coarse discretisation in multi-scale computations needed at the coarse scale to keep the localisation width smaller than the structural scale element size also induces numerical difficulties, linked to the proper evaluation of stress concentrations for the coarse-scale discontinuity propagation, especially for uniformly distributed stress states. Therefore, a defect is introduced in the central part of the wall to trigger the damage localisation more easily, both in the fine-scale and coarse-scale computations, see Figure 5.5. Finally, since the focus is here set on the assessment of the results obtained with a periodicity-based scale transition, a rather favourable mesh topology is adopted at the coarse scale. A diagonal band of elements with an orientation consistent with the average orientation of the compressive strut is introduced in the coarse discretisation in order to properly capture the stress concentration and to allow the complete separation of two rows of nodes with propagating embedded discontinuities. This allows to avoid numerical crack propagation difficulties. Note that the influence of such a mesh alignment at the coarse scale is the same as if enhanced assumed strain methods were used with closed-form material laws.

For the multi-scale computation, the masonry wall is discretised at the structural scale by using 3-noded plane stress finite elements with one Gauss integration point. The clamped top and bottom brick rows are discretised with 4-noded linear elements with  $2 \times 2$  Gauss integration points. The coarse-scale mesh consists of 388 elements and of 536 displacement degrees of freedom (excluding the displacement jumps condensed at the element level). The unit cell computations use a rather coarse discretisation with quadratic

2D and interface elements. For the complete fine-scale computation, the bricks are discretised using 8-noded quadratic plane stress finite element with  $3 \times 3$  Gauss integration points. The mortar joints are represented by 6-noded quadratic interface finite elements with 3 Lobatto quadrature points. Each brick was discretised using 6 by 5 elements, resulting in a model consisting of 160000 dofs. All meshes used for the different levels of descriptions are sketched in the Figures in the next subsections.

Note that the choice of this test calls for several comments regarding the use of periodic homogenisation. Homogenisation with such boundary conditions is known to overestimate the average stiffness of the material, an approximation which is particularly debatable near free boundaries for instance. In the presented test setup, the strong initial confinement in the central zone of the wall allows to decrease the importance of this issue. As a result, the periodic assumption is not expected to be a too penalising assumptions for the *detection* of localisation in the diagonal strut. Conversely, this assumption may prove quite crude for localisation in the bed joints in the first cracking stages. In the same line, it is recognised that the use of periodically homogenised properties for localised behaviour itself remains untested since the scale separation principle does not apply anymore in this case. This is particularly the case here given the dimensions of the tested wall (which are prescribed by the cost of the full fine-scale computation), as the size of the fine-scale localisation volume is not much smaller than the coarse-scale material points volume. The use of the periodicity assumption for the localised regime will thus be challenged here by using the most critical conditions for its application.

Note that the compressive and shearing loading phases of the wall in both simulations and the cell computations in the multi-scale approach are controlled by displacement. In particular, no path following technique is used at the coarse scale in the multi-scale computation. Therefore, the multi-scale and full fine-scale computations results are quantitatively compared until the limit load of the structural response is reached.

The material parameters used for the computations are defined at the fine scale for both approaches, see Section 5.2, and their values are reported in Table 5.1. The tensile fracture energy of mortar joints is however increased with respect to realistic values (at least for tensile mode I fracture) in order to avoid any snap-back effect in the unit cell average response, see Massart et al. (2005b).

Note that the computation cost is not challenged in this contribution. The size of the structure has been chosen such that a full fine-scale model is feasible. The computation costs of the both multi-scale and full fine-scale approaches are therefore comparable. Practically, a multi-scale method would definitely be used to deal with larger structures. In this case, a multi-scale approach would of course be much more effective in terms of computation cost than a full fine-scale computation.

Finally, due to the nested incremental iterative scheme, the presented multi-scale procedure has a rather high computational cost even with coarse discretisations at both fine and coarse scales. Since all cell responses may be computed independently, the

Table 5.1: Brick (a) and mortar/mortar-brick interface (b) material parameters, see Lourenço (1996).

	$E$ (MPa)	$\nu$	$k_n$ ( $\frac{\text{MPa}}{\text{mm}}$ )	$k_t$ ( $\frac{\text{MPa}}{\text{mm}}$ )	$f_t$ (MPa)	$G_f$ ( $\frac{\text{mJ}}{\text{mm}^2}$ )	$c$ (MPa)	$\varphi$ ( $^\circ$ )	$f_c$ (MPa)	$\vartheta$ ( $^\circ$ )
(a)	16700	0.15	-	-	-	-	-	-	-	-
(b)	-	-	438	182	0.2	0.1	0.28	40	6.0	35

proposed multi-scale method is well suited for parallel computations. The multi-scale computation reported here was performed with such an implementation.

The comparison of the results of both approaches is based both on the overall response of the wall (load-displacement response in the second phase and identification of the failure mechanisms), and on the obtained damage patterns at critical spots.

The load-displacement response of the second loading phase is depicted in Figure 5.6. As can be seen, the multi-scale simulation overestimates the initial stiffness by more than 22% with respect to the full fine-scale modelling. The load bearing capacity of the wall given by the multi-scale computation is however underestimated by only 1.1% with respect to the full fine-scale solution. The multi-scale peak load appears for a shearing displacement smaller by 7% with respect to the full fine-scale solution. This may be associated to the fact that the overestimation of the initial global stiffness leads to stronger stress concentrations and therefore earlier cracking appearance in terms of the imposed shearing displacement.

For each of the three points of the load-displacement curve denoted by a capital letter, a detailed view of the structural state is given in the next Figures. The damage distribution is illustrated on the undeformed structural configuration for the complete fine-scale solution. For the same value of the shearing displacement (point A and B) and for the response peak (point C), the coarse-scale discontinuities are depicted on the undeformed shape of the coarse-scale discretisation of the multi-scale computation. The damage distributions of the unit cells corresponding to typical positions in the structure are also given.

As can be seen in Figure 5.7 representing the damage state at point A in the load-displacement curve, the initial stage of horizontal mode I cracking in bed joints is qualitatively reproduced by the multi-scale computation. The overestimation of the initial

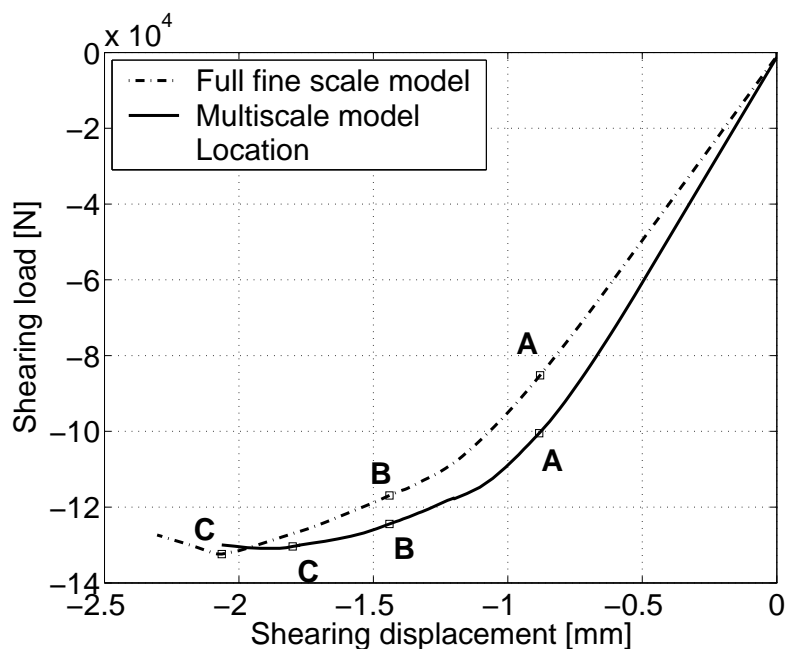


Figure 5.6: Confined shearing wall test. Comparison of the load-displacement responses for full fine-scale modelling (dashed line) and multi-scale simulation (solid line). The capital letters match states for which detailed damage maps are compared in the following Figures.

stiffness of the wall and the rather coarse meshes used in the multi-scale approach may explain the difference in the extension of these cracks. In the complete fine-scale solution, the horizontal mode I cracking is localised in the upper left and lower right tensile bed joints. The multi-scale computation shows a less localised horizontal cracking due to the fact that the stress concentrations are partly smoothed by the rather coarse discretisation in this zone. The fine-scale damage patterns is nevertheless well reproduced, see unit cell (1) in Figure 5.7. A rather localised damage state promoted by the defect appears in the central zone in the complete fine-scale simulation, represented as well in the multi-scale framework by embedded discontinuities. Note that their orientation is consistent with the unit cell stair-case damage patterns and the full fine-scale simulation, see unit cell (2) in Figure 5.7. In the multi-scale solution, the extension of the embedded discontinuities corresponding to the diagonal cracking is larger, probably due to the overestimation of the initial global stiffness. Note that around the stair-case cracking fronts in the full fine-scale solution, the damage distribution is rather diffused and only the head-joints are partially damaged. This damage pattern is also well reproduced by the multi-scale computation in non-localised states (no coarse-scale discontinuity in this zone), see unit cell (3) in Figure 5.7. In the compressed corners, the full fine-scale solution shows a slight initiation of damage in the head-joints while bed joints are partially damaged in the multi-scale solution, see unit cell (4) in Figure 5.7.

The next stage in the cracking process is still located in the rising part of the load-displacement curve (point B). It matches the transition from a diffuse damage pattern in the central zone of the compressive strut towards localisation. Figure 5.8 depicts this

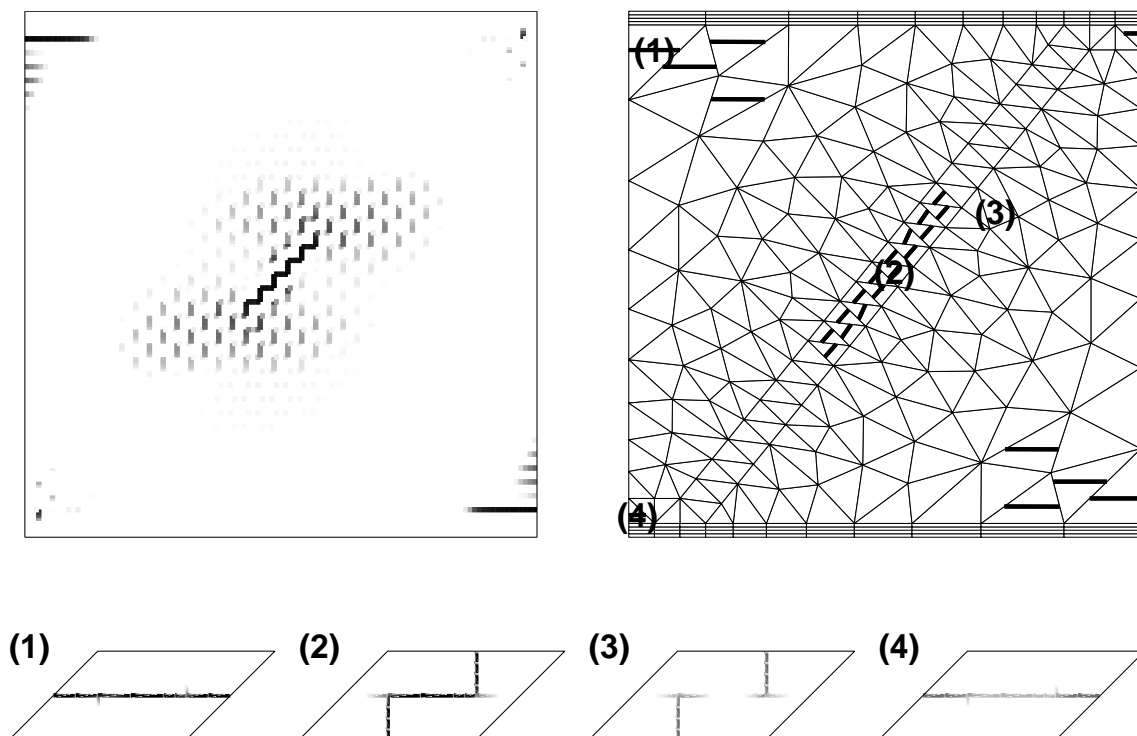


Figure 5.7: Damage maps at point A of the confined shearing load-displacement response of the full wall: (left) damage maps of the complete fine-scale computation (black lines indicate fully damaged joints and gray lines indicate partially damaged joints), (right) coarse-scale discontinuities for the multi-scale computation and (bottom) related damage state of unit cells.

state of the wall for both approaches. Note that the orientation of the slanted embedded discontinuities in the diagonal band of elements is independent of the coarse-scale mesh but consistent with the full fine-scale modelling and the unit cell stair-case damage patterns, see unit cell (1) in Figure 5.8. The orientation of these embedded discontinuities in fact evolves towards the average stair-case orientation given by the brick stacking geometry. Note that the discrepancy between the fine-scale preferential orientation ( $45^\circ$ ) and the compressive strut average direction (about  $50^\circ$ , as illustrated from the fine-scale solution of Figures 5.9 and 5.10), is the cause for the presence of several diagonal cracks and therefore influences the global energy dissipation. These parallel stair-case cracks with respect to the main one are accounted for in the multi-scale approach by non-localised damage zones as illustrated by cell (2) in Figure 5.8. In the top right and bottom left zones, compressive and shearing failure in bed joints appeared in the multi-scale framework, see unit cell (3) in Figure 5.8, which matches rather well with the full fine-scale solution. The multi-scale solution also shows quasi fully damaged head-joints near the compressed corners, see unit cell (4) in Figure 5.8, which matches the damage patterns of the full fine-scale solution.

Upon completion of the propagation in the compressive strut, the compressed corners fail under compressive crushing at the peak load of the wall response (point C in Figure 5.6). This compressive crushing failure (represented here phenomenologically by joints compressive failure) is correctly captured by both the complete fine-scale and the multi-scale descriptions, see unit cells (1) and (2) in Figure 5.9. In each description, this damage pattern occurrence matches the peak load of the curve. As expected, the stress

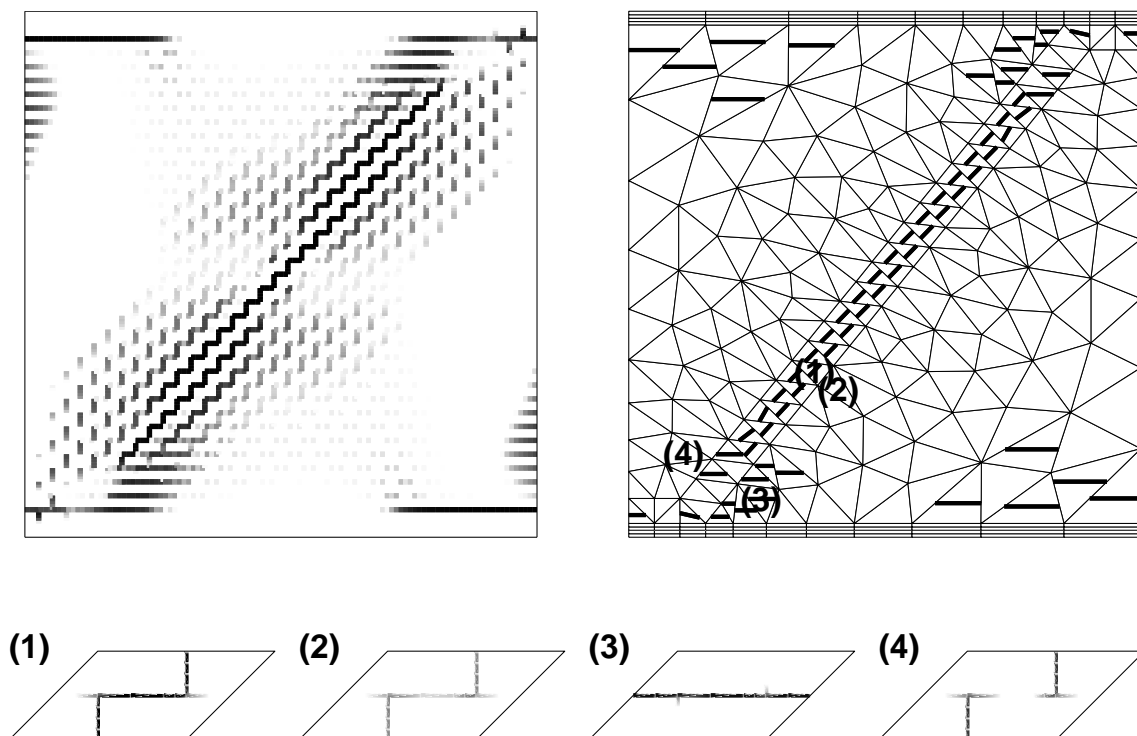


Figure 5.8: Damage maps at point B of the confined shearing load-displacement response of the full wall: (left) damage maps of the complete fine-scale computation (black lines indicate fully damaged joints and gray lines indicate partially damaged joints), (right) coarse-scale discontinuities for the multi-scale computation and (bottom) related damage state of unit cells.

redistribution stops the horizontal cracks propagation in the upper and lower bed joints. For the sake of completeness, Figure 5.9 shows that the multi-scale framework properly detects the appearance of bed joint failure along free edges of the wall as in the full fine-scale solution, see unit cell (3) in Figure 5.9. Finally, unit cell (4) in Figure 5.9 shows that certain joints of the wall remain safe during the loading phase in accordance with the full fine-scale simulation results.

To further illustrate the global failure mechanisms, the deformed configurations at the peak load (point C) are depicted in Figure 5.10 for both the full fine-scale and multi-scale computations. The tensile and compressive failure of the bed joints in the corners are well reproduced by the multi-scale computation, see unit cells (1) and (2) in Figure 5.10. The stair-case opening in the central zone of the compressive strut of the multi-scale solution matches as well the failure mechanism of the full fine-scale solution. In this zone, the head-joints fail with a tensile mode whereas the damaged part of bed joints present a rather shearing failure mode, see unit cell (3) in Figure 5.10. Finally, note that the orientation of embedded discontinuities matches the average orientation of the stair-case opening in the full fine-scale solution, see Figure 5.10. The full fine-scale solution also shows the effect of a different orientation of the fine-scale preferential damage orientation and of the global compressive strut. Three stair-case cracks are indeed recognizable in this simulation, resulting in an average orientation of the damaged compressive strut of  $50^\circ$ .

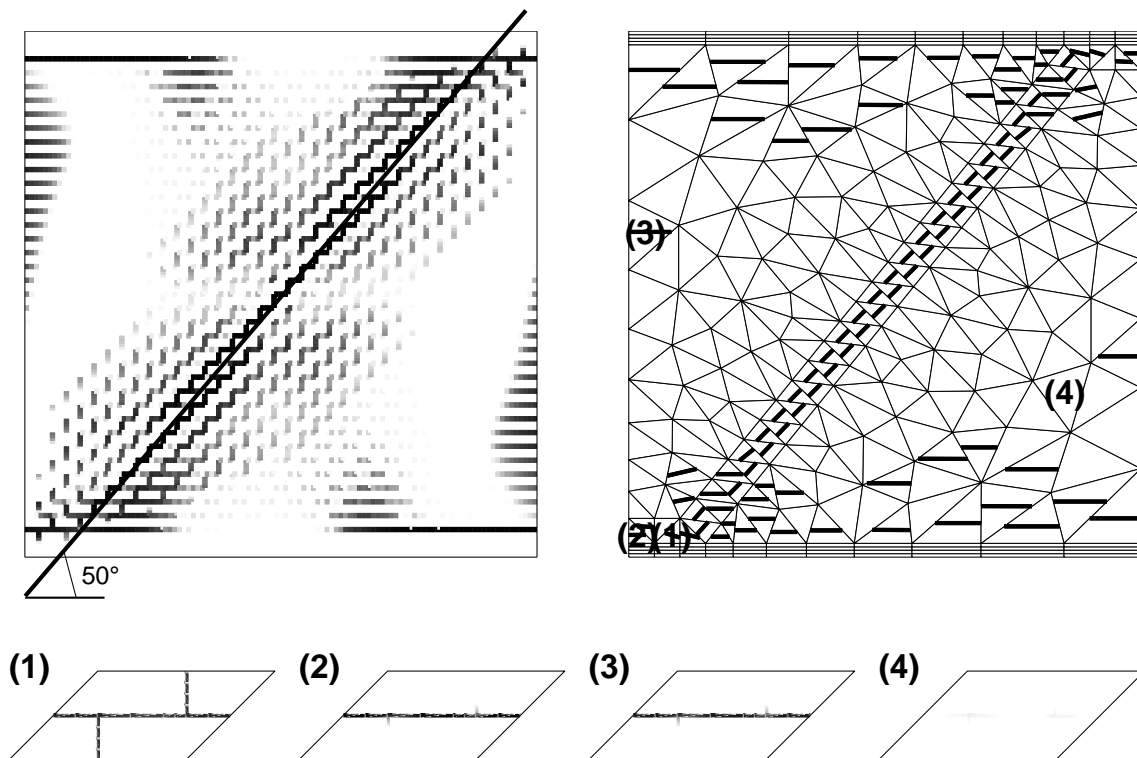


Figure 5.9: Damage maps at point C of the confined shearing load-displacement response of the full wall: (left) damage maps of the complete fine-scale computation (black lines indicate fully damaged joints and gray lines indicate partially damaged joints), (right) coarse-scale discontinuities for the multi-scale computation and (bottom) related damage state of unit cells.

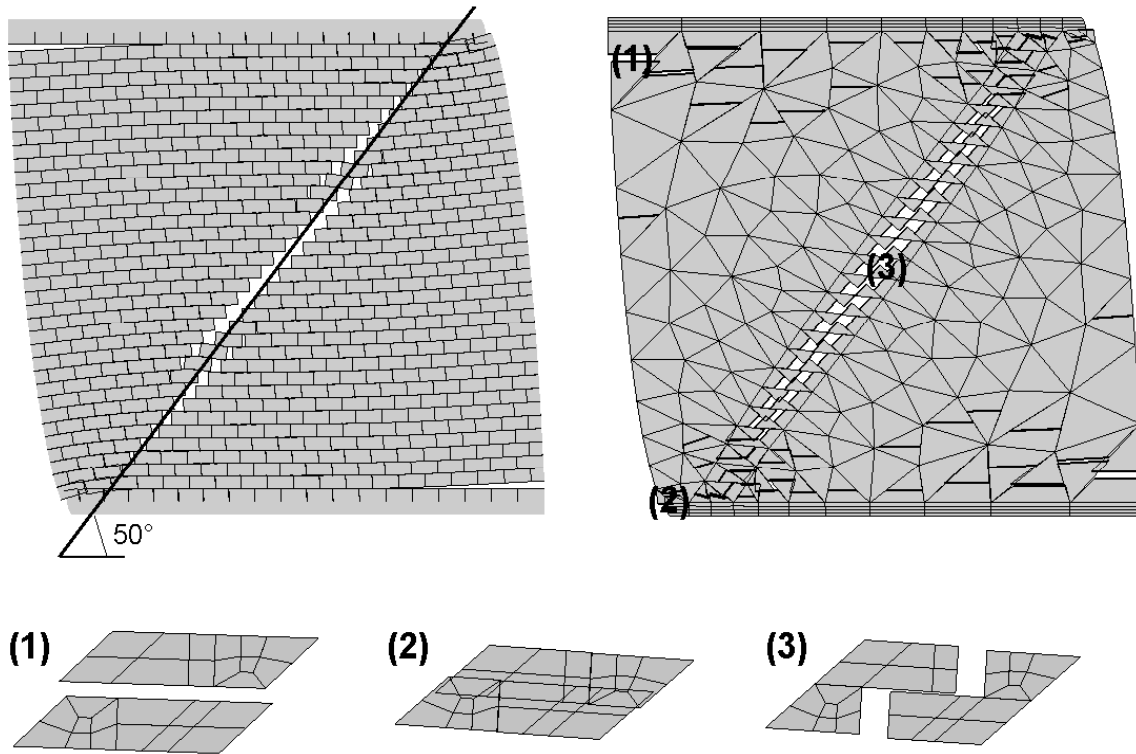


Figure 5.10: Deformed configuration at point C of the confined shearing load-displacement response of the full wall (the displacements of the wall are magnified by a factor of 200): (left) deformed configuration of the complete fine-scale computation, (right) deformed configuration of the multi-scale computation and (bottom) related deformed unit cells (the displacements of the cells are magnified by a factor of 50).

#### 5.4.2 Confined shearing of a masonry wall with an opening

In the same spirit as for the full wall test presented in Section 5.4.1, the multi-scale framework results are compared here to fine-scale modelling results on a planar wall with an opening. The tested geometry is shown in Figure 5.11. The dimensions of the wall and the bricks are the same as for the full wall test. The opening of dimensions  $660 \times 720 \text{ mm}^2$  is not centred in the wall in order to avoid symmetry at the macroscopic scale as shown in Figure 5.11. As for the full wall test, a clamping of the top and bottom brick rows in the loading set-up is represented by two bands of elements with elastic behaviour and with a stiffness comparable to concrete. The same two-phase loading scheme as for the full wall computation is used with compression followed by confined shearing. Early in the confined shearing phase, damage is first initiated with the appearance of diagonal cracks starting at the top right and bottom left corners of the opening due to stress concentrations. Upon further shearing, horizontal tensile cracks appear at the free boundaries of the wall at the level of the horizontal edges of the opening. Finally, a structural failure mechanism is formed by the propagation of diagonal cracking towards the compressed corners of the wall with compressive crushing of two corners of the opening in front of the tensile cracks.

The stress concentrations induced by the opening helps the transition from a distributed damage pattern to a localised cracking and therefore allows to (partially) avoid the numerical difficulties observed with the full wall simulation to initiate cracking. No defect is therefore needed to trigger the damage localisation. However, a rather coarse

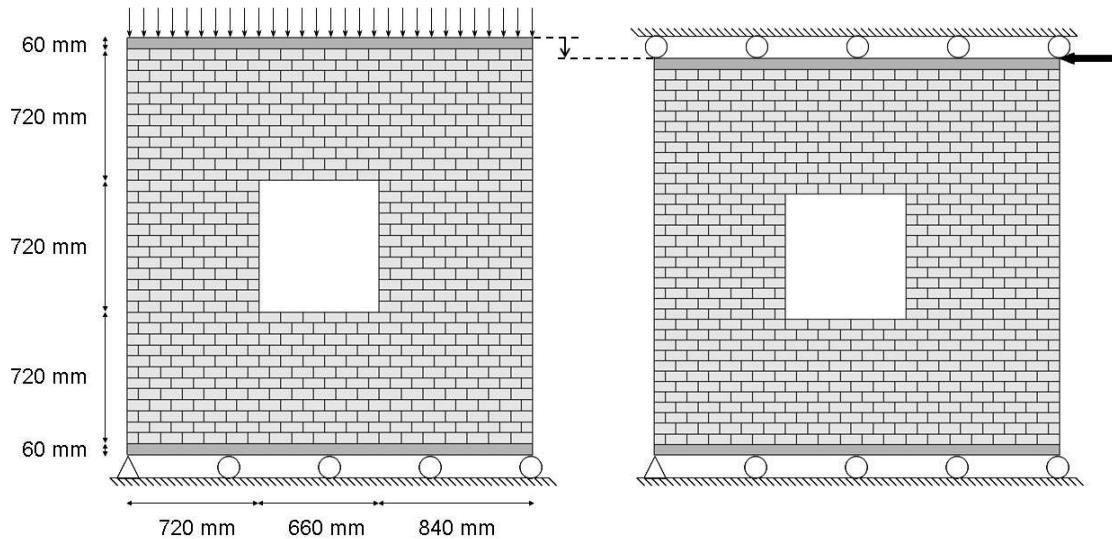


Figure 5.11: Confined shearing test on a wall with an opening. The loading is applied in two successive phases: (a) compressive load applied on the top boundary layer, (b) horizontal shearing.

discretisation is used at the coarse scale for the multi-scale computation in order to keep the localisation width smaller than the structural scale element size. As a consequence, the stress concentrations are smoothed and underestimated at the corners of the opening. Furthermore, a rather favourable mesh topology is still adopted at the coarse scale in order to properly capture the evolving stress concentrations and to allow the complete separation of two rows of nodes with propagating embedded discontinuities.

For the multi-scale computation, the masonry wall is discretised at the structural scale by using 3-noded plane stress finite elements with one Gauss integration point. The clamped top and bottom brick rows are discretised with 4-noded linear elements with  $2 \times 2$  Gauss integration points. The coarse-scale mesh consists of 431 elements and of 612 displacement degrees of freedom (excluding the displacement jumps condensed at the element level). The unit cell computations use a rather coarse discretisation with quadratic 2D and interface elements. For the complete fine-scale computation, the bricks are discretised using 8-noded quadratic plane stress finite element with  $3 \times 3$  Gauss integration points. The mortar joints are represented by 6-noded quadratic interface finite elements with 3 Lobatto quadrature points. Each brick was discretised using 4 by 2 elements, resulting in a model consisting of 47388 dofs. All meshes used for the different levels of descriptions are sketched in the Figures below.

As for the full wall test, this test is chosen to challenge the periodicity assumption of the homogenisation procedure for the localised regime by using the most critical conditions for its application. Therefore, the multi-scale and full fine-scale computations results are quantitatively compared until the limit load of the structural response is reached. Both simulations are controlled by displacement. The values of the fine-scale material parameters used for both approaches and defined in Section 5.2 are given in Table 5.2. Note that the tensile fracture energy of mortar joints is still increased with respect to realistic values in order to avoid any mesostructural snap-back effect, see Massart et al. (2005b).

The comparison of the results of both multi-scale and full fine-scale computations is based on the load-displacement response of the shearing phase, the identification of the

Table 5.2: Brick (a) and mortar/mortar-brick interface (b) material parameters, see Lourenço (1996).

	$E$ (MPa)	$\nu$	$k_n$ ( $\frac{\text{MPa}}{\text{mm}}$ )	$k_t$ ( $\frac{\text{MPa}}{\text{mm}}$ )	$f_t$ (MPa)	$G_f$ ( $\frac{\text{mJ}}{\text{mm}^2}$ )	$c$ (MPa)	$\varphi$ ( $^\circ$ )	$f_c$ (MPa)	$\vartheta$ ( $^\circ$ )
(a)	16700	0.15	-	-	-	-	-	-	-	-
(b)	-	-	438	182	0.18	0.05	0.28	36	6.0	35

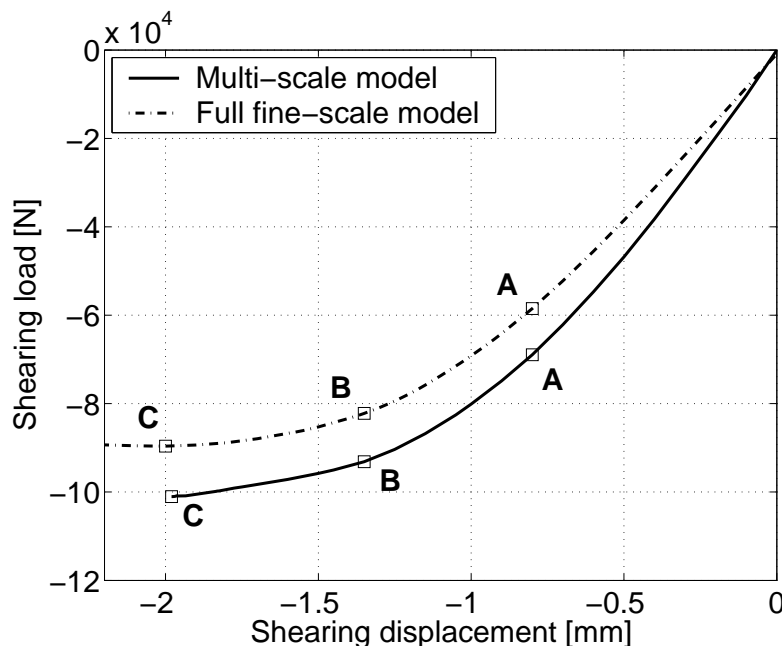


Figure 5.12: Confined shearing test on a wall with an opening. Comparison of the load-displacement responses for full fine-scale modelling (dashed line) and multi-scale simulation (solid line). The capital letters match states for which detailed damage maps are compared in the following Figures.

failure mechanisms, and the obtained damage patterns.

The load-displacement response of the second loading phase of the wall with an opening is depicted in Figure 5.12. As for the full wall test, the multi-scale simulation overestimates the initial stiffness by more than 22% with respect to the full fine-scale modelling. However the load bearing capacity is not predicted as well as for the full wall test since it is overestimated by 12% with respect to the full fine-scale solution (assuming that the load peak is reached for the multi-scale modelling). This overestimation of the peak load can be associated to the underestimation of the stress concentrations at the opening corners in the multi-scale simulation, which are better captured in the full fine-scale modelling due to the fine discretisation.

For each of the three points of the load-displacement curve denoted by a capital letter, a detailed view of the structural state is given in the next Figures. The damage distribution is illustrated on the undeformed structural configuration for the complete fine-scale solution. For the same value of the shearing displacement (points A, B and C), the coarse-scale discontinuities are depicted on the undeformed shape of the coarse-scale discretisation of the multi-scale computation. The damage distributions of the unit cells corresponding to typical positions in the structure are also given.

As can be seen in Figure 5.13 representing the damage state at point A in the load-displacement curve, two parallel stair-case cracks start to propagate from the top right and bottom left corners of the opening in the full fine-scale solution. This cracking mode is qualitatively reproduced by the multi-scale computation and the orientation of the corresponding embedded discontinuities is consistent with the unit cell stair-case damage patterns and the full fine-scale simulation, see unit cell (1) in Figure 5.13. Note that near the stair-case cracking fronts, no structural localisation is detected but a damage state appears at the fine scale in head-joints, see unit cell (2) in Figure 5.13. A rather diffused damage state also appears around the opening. In the parts of the wall below and above the opening, the bed joints are partially damaged in the full fine-scale solution, which is in accordance with the horizontal embedded discontinuities in the multi-scale framework, see unit cell (3) in Figure 5.13. The overestimation of the initial stiffness of the wall and the rather coarse meshes used in the multi-scale approach may explain the difference in the extension of these embedded discontinuities and the presence of horizontal embedded discontinuities on the free boundaries of the wall. In the left-hand and right-hand parts on the wall, only the head-joints are partially damaged. Although no structural localisation is detected in these zones in the multi-scale solution, the unit cell damage patterns are consistent with the full fine-scale solution, see unit cell (4) in Figure 5.13.

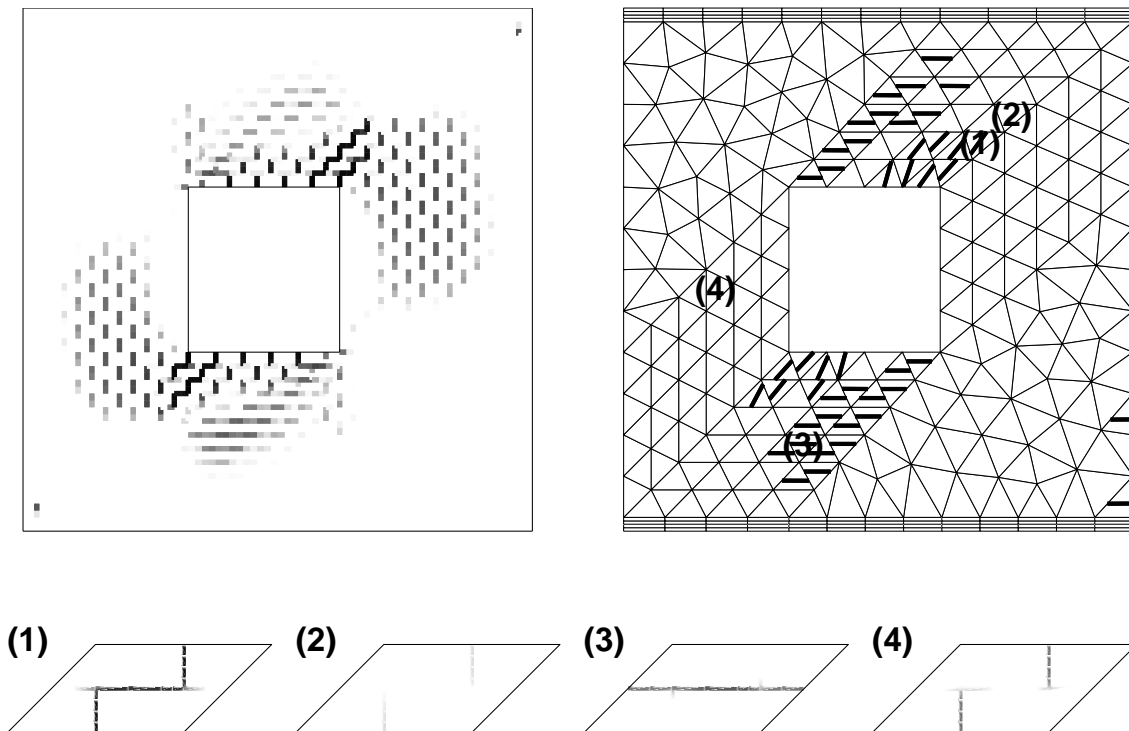


Figure 5.13: Damage maps at point A of the confined shearing load-displacement response of the wall with an opening: (left) damage maps of the complete fine-scale computation (black lines indicate fully damaged joints and gray lines indicate partially damaged joints), (right) coarse-scale discontinuities for the multi-scale computation and (bottom) related damage state of unit cells.

The next stage in the cracking process is still located in the rising part of the load-displacement curve (point B) for which the stair-case cracks almost propagate towards the corners of the wall. Figure 5.14 depicts this state of the wall for both approaches. The damage state and the orientation of the embedded discontinuities at the stair-case cracking fronts are well reproduced by the multi-scale computation, see unit cell (1) in Figure 5.14. Around these cracking fronts, the damage state in the multi-scale framework is in accordance with the full fine-scale solution, see unit cells (2) and (3) in Figure 5.14. Furthermore, unit cell (4) in Figure 5.14 shows that the damage state appearing in the bed joints along the free boundaries of the wall is well reproduced by the multi-scale simulation.

Upon completion of the stair-case cracking propagation, the compressed corners fail under compressive crushing at the peak load of the wall response (point C), similarly to the full wall test. In these compressed corners, the symmetric stair-case damage pattern appears in both the complete fine-scale and the multi-scale descriptions, as shown in unit cell (1) in Figure 5.15. Note that since the stair-case cracks do not completely propagate towards the corners of the wall in the multi-scale simulation, the load bearing capacity may not be reached at the point C of the load-displacement response of the multi-scale computation. For the sake of completeness, Figure 5.15 shows that the multi-scale framework properly detects the evolution of the damage state in the wall with respect to

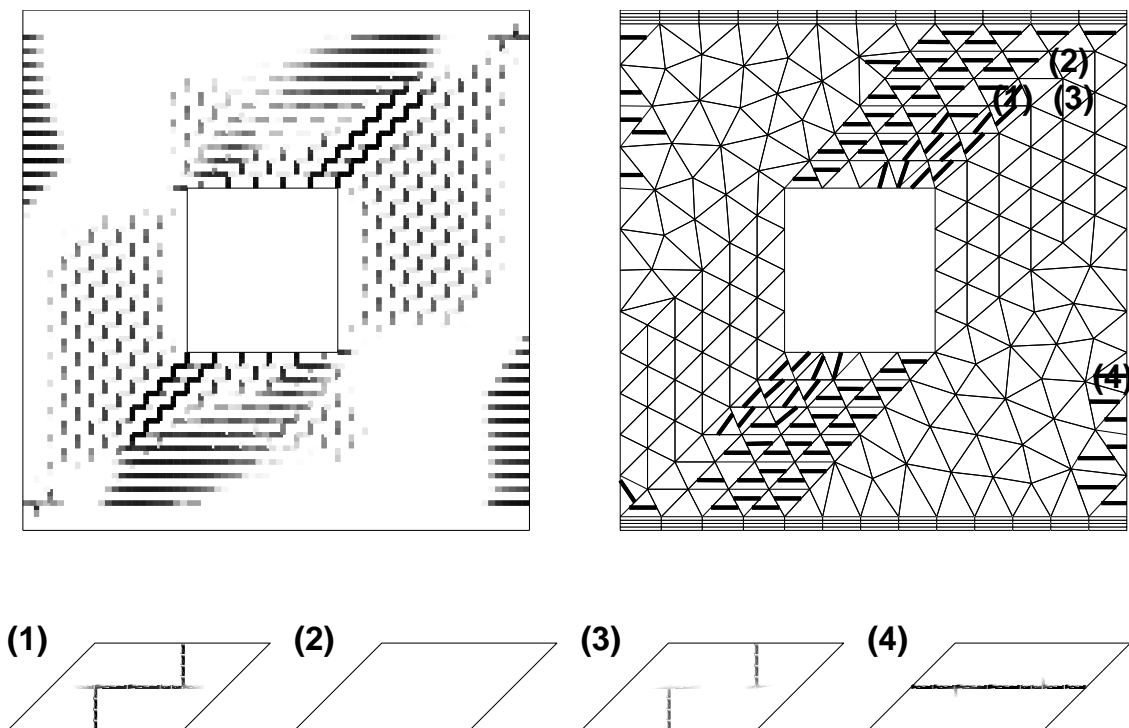


Figure 5.14: Damage maps at point B of the confined shearing load-displacement response of the wall with an opening: (left) damage maps of the complete fine-scale computation (black lines indicate fully damaged joints and gray lines indicate partially damaged joints), (right) coarse-scale discontinuities for the multi-scale computation and (bottom) related damage state of unit cells.

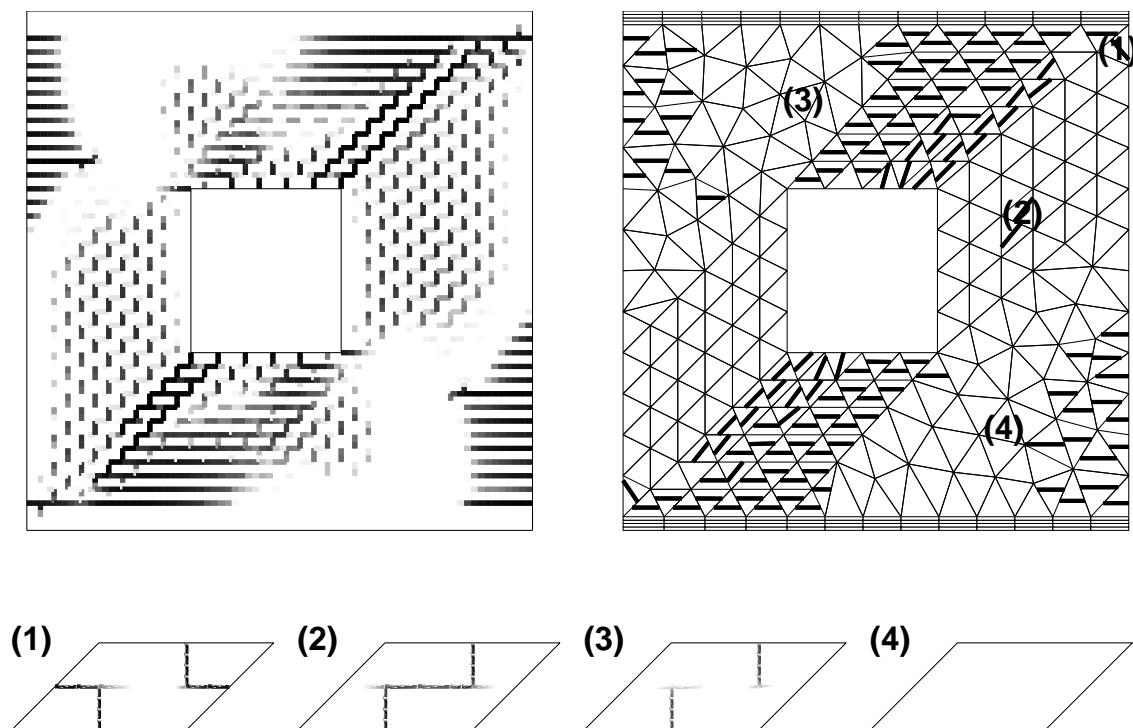


Figure 5.15: Damage maps at point C of the confined shearing load-displacement response of the wall with an opening: (left) damage maps of the complete fine-scale computation (black lines indicate fully damaged joints and gray lines indicate partially damaged joints), (right) coarse-scale discontinuities for the multi-scale computation and (bottom) related damage state of unit cells.

the complete fine-scale solution, see unit cells (2) and (3) in Figure 5.15. Finally, unit cell (4) in Figure 5.15 shows that some zones remain safe during the loading phase in accordance with the full fine-scale simulation results.

In order to illustrate the global failure mechanism, the deformed configurations at the peak load (point C) are depicted in Figure 5.16 for both the full fine-scale and multi-scale computations. The crack openings in the multi-scale solution match the failure mechanism observed in the full fine-scale solution. Near the stair-case cracking fronts, the head-joints fail with a tensile mode whereas the damaged part of bed joints rather present a shearing failure mode, see unit cell (1) in Figure 5.16. Further from the stair-case cracking fronts where the cracks are fully open, both the head-joints and bed joints fail with a mixed tensile and shearing mode, see unit cell (2) in Figure 5.16. Unit cells (3) and (4) in Figure 5.16 respectively show that the tensile opening at the free boundaries of the wall and the failure of the compressive corners are well reproduced by the multi-scale computation.

### 5.4.3 Discussion

The first observation is related to the presence of an overestimation of the stiffness in the initial stage of the second phase loading. This overestimation can be attributed to

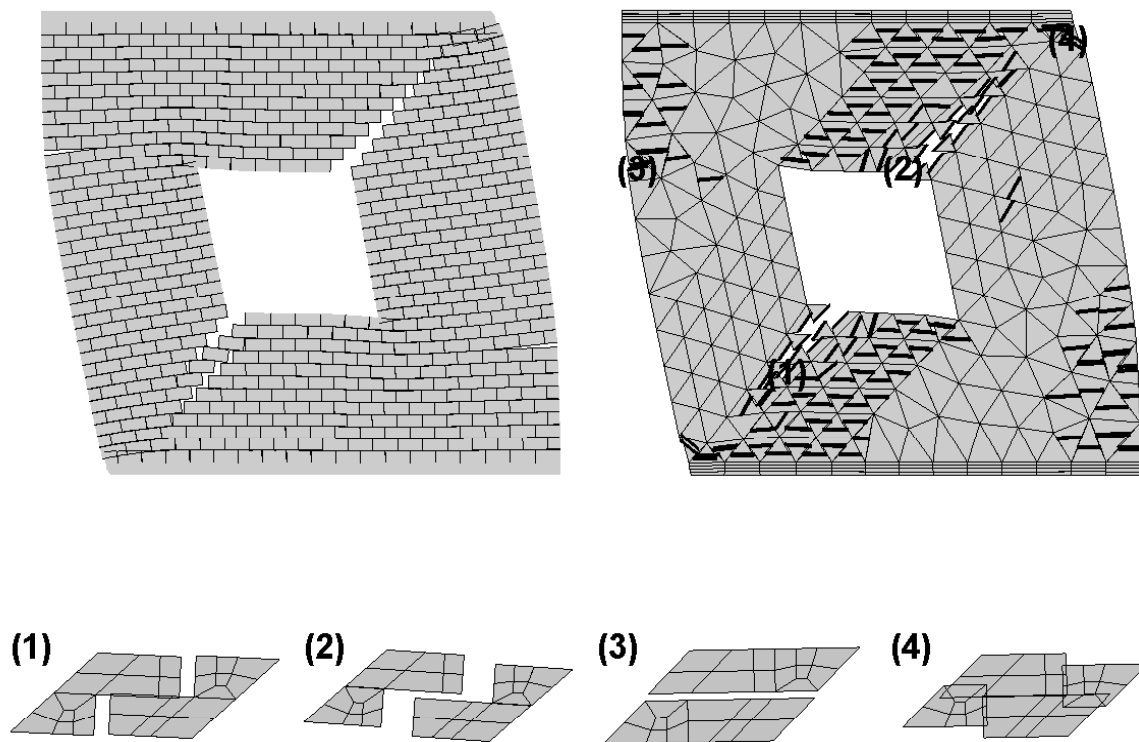


Figure 5.16: Deformed configuration at point C of the confined shearing load-displacement response of the wall with an opening (the displacements of the wall are magnified by a factor of 200): (left) deformed configuration of the complete fine-scale computation, (right) deformed configuration of the multi-scale computation and (bottom) related deformed unit cells (the displacements of the cells are magnified by a factor of 50).

the use of periodic homogenisation, as well as to the use of a rather coarse discretisation in the multi-scale approach, both at the coarse scale and in the unit cell computations. The use of a coarse discretisation at the structural scale was needed here to keep the localisation width smaller than the structural scale element size. Note that in practical applications of the multi-scale framework, larger structures would be considered. A mesh refinement at the structural scale would restrict the stiffness overestimation such that the sole contribution brought by the periodicity assumption would remain.

In the case of the confined shearing full wall test, it is emphasised that the periodicity assumption of the computational homogenisation procedure gets increasingly challenged along the shearing loading phase; even though it may be argued that this assumption keeps its validity before any localisation detection, due to the confined character of the stress distribution. Upon localisation in the bed joints under mode I loading, periodicity is clearly lost as shown in Figure 5.7 (fine scale). Nevertheless, the presence of these cracks is detected in the multi-scale procedure at the correct shearing displacement. This suggests that the overestimation of the initial stiffness does not affect strongly the initiation of the cracking process. Upon localised behaviour, the local periodicity assumption is strongly challenged, especially because the localised bandwidth is comparable to the coarse mesh size. The stress distribution in the centre of the wall remains rather diffuse

when the tensile cracks of bed joints are initiated. As a consequence, the periodicity assumption remains a good approximation for non-localised states in the compressive strut. Further in the shearing loading phase, the crack propagates in the compressive strut until the complete development of the failure mechanism when the compressed corners fail (corresponding to the overall response peak). The cohesive behaviour of the coarse-scale discontinuities is obtained on a periodic unit cell. As a result, the coarse-scale dissipation is directly controlled by the periodicity assumption, even though the cracking in the compressive strut does not consist in many parallel active cracks, as depicted in Figure 5.10. However, the good agreement between the simulations both in the global response and in the obtained damage patterns shows that the periodicity assumption does not prevent from reaching quantitative results for the treated wall. The load bearing capacity seems to be controlled mainly by the global failure mechanism since the peaks of both approaches match, in spite of the difference in the initial global stiffnesses.

This consideration gives a motivation for the limit analysis assumptions where the load bearing capacity is related to the considered failure mode, as for instance in Milani et al. (2006a). The limit analysis approaches focus on the identification of the limit load of structures without considering stable crack situations. The proposed multi-scale framework is therefore considered as a complementary approach, since it allows to capture the crack patterns along the loading path and therefore allows to model cracking for loading levels well below the limit loads. In the case of the confined shearing wall test with an opening, the periodicity assumption of the computational homogenisation procedure is still more challenged even before any localisation detection due to the presence of the opening. Nevertheless, the damage patterns and the global failure mechanism are qualitatively well reproduced by the multi-scale modelling with respect to the full fine-scale solution. The overestimation of the load bearing capacity may result from the coarse discretisation used at the coarse scale.

It is also emphasised that the proposed multi-scale framework is tested here using the most challenging conditions for its application in terms of the scale separation issue. In particular, its use in much larger structures would result in larger scale jump. As a result, the localised behaviour would be modelled with a better estimation of the energy dissipation.

The use here of coarse-scale embedded localisation zones as proposed in Armero (1999) is a major difference with the approach proposed in Belytschko et al. (2008), which makes use of XFEM techniques. The lack of crack path continuity in the approach here could lead to strong approximations in terms of energy dissipation if coarse meshes are used at the structural scale. This is particularly the case for mode I loading when a single crack is to be represented (i.e. a strongly localised failure mode), a case in which an XFEM implementation would yield better results, as illustrated in Belytschko et al. (2008) for a three point bending configuration. As a result, it could be expected that the early bed joint cracking in the full wall would be modelled more accurately in an XFEM-enhanced multi-scale framework. Conversely, the compressive strut cracking is obtained with a fine-scale damage evolution which leads to reorientations of the averaged cracking zone, a feature which can be more easily incorporated in an embedded discontinuity formulation, than in an XFEM-based description. Furthermore, for compression dominated average failure modes, more distributed damage states are obtained as illustrated in the case of the wall with and without an opening, in which case, several embedded zones can appear to account for this fact. Finally, it should be noted that the representation of the compressive failure of the corners by means of a cohesive zone is questionable, since

it consists in a volume-driven dissipation. Here, a proper representation of this failure mechanism and of the associated energy dissipation is obtained because the size of the unit cell is comparable to the coarse-scale element size. If larger structures have to be modelled with compressive failure zones, a proper volume energy dissipation should be accounted for by adapting specifically the localisation size  $w_n$  for the compressive stress states.

## 5.5 Conclusions

A periodic homogenisation-based multi-scale method was proposed for the modelling of quasi-brittle structural failure. In order to upscale failure information, a new displacement discontinuity-enhanced scale transition was developed based on approximate energetic consistency requirements. This framework was assessed by a comparison with a complete fine-scale model on confined shearing wall tests with and without an opening, in order to estimate the impacts of the periodicity and scale separation assumptions.

In the case of the confined shearing wall tests with and without an opening, it was shown that the multi-scale modelling yields results in good agreement with respect to complete fine-scale computations results provided stress distributions are confined. In spite of an overestimation of the initial stiffness by the multi-scale modelling, the cracking patterns are correctly reproduced, with a good estimation of the failure mechanisms at both the structural and fine scales. Furthermore, the multi-scale approach also allows to obtain quantitative information on the limit load, which is obtained with less than 2% error with respect to the full fine-scale simulation in the case of the confined shearing full wall test and with a larger error (about 12%) in the case of the confined shearing wall test with an opening.

The results obtained here suggest that further studies could be useful in order to extend their scope. First, a parametric study should be performed in order to analyse the results obtained for different mesh refinements at the coarse scale, different fine-scale geometrical features (size of the unit cell, aspect ratio of the unit cell), and different material features (fracture energies). Secondly, additional features could be introduced in the fine-scale laws. This would include brick cracking (leading to more localised patterns in the compressive strut), as well as more refined mortar joints laws (independent fracture energies for mode I, mode II and compressive fractures). Finally, the extension of the framework to out-of-plane failure should be performed, based on the results of Mercatoris et al. (2009), see Chapter 4.

# Chapter 6

## A coupled two-scale computational scheme for the failure of periodic quasi-brittle thin shells

This Chapter presents a multi-scale framework for the failure of periodic quasi-brittle thin shells. The macroscopic behaviour of textured or periodic heterogeneous materials is strongly influenced by their mesostructure. Their periodicity and the quasi-brittle nature of their constituents result in complex behaviours such as damage-induced anisotropy properties with localisation of damage, which are difficult to model by means of macroscopic closed-form constitutive laws. A multi-scale approach can therefore offer an attractive and flexible solution for the modelling of such heterogeneous materials. A non-linear periodic computational homogenisation procedure is used for the in-plane and the out-of-plane behaviour of such planar shells, combined to an acoustic tensor-based detection criterion adapted to shell kinematics in order to detect the structural-scale localisation. Based on an assumption of single period failure, the localisation of damage at the structural scale is represented by means of mesostructurally informed embedded strong discontinuities incorporated in the macroscopic shell description. A new enhanced scale transition is outlined for shell failure based on an approximate energy consistency argument in order to objectively upscale the energy dissipation. The corresponding multi-scale framework results are compared for the case of masonry to full fine-scale modelling results used as a reference, showing a good agreement in terms of load bearing capacity, of failure mechanisms and of associated energy dissipation.

### 6.1 Introduction

The structural failure behaviour of quasi-brittle textured heterogeneous materials such as masonry is difficult to capture, because of complex behaviours such as damage-induced anisotropy leading to stress redistributions, as can be observed in experimental tests, see Page (1981, 1983), Dhanasekar et al. (1985), van der Pluijm (1999). Closed-form constitutive laws were proposed to model such a macroscopic behaviour for the case of

---

This Chapter is based on: B.C.N. Mercatoris and T.J. Massart, A coupled two-scale computational scheme for the failure of periodic quasi-brittle thin shells. Submitted for publication.

masonry walls subjected to both in-plane loading, Papa and Nappi (1997), Lourenço et al. (1997), Berto et al. (2002) and out-of-plane loading, Lourenço (2000). As a counterpart to their efficiency, these closed-form relations may be costly to identify due to a large number of material parameters and, can be complex to formulate from a mathematical point of view. A characterisation of the flexural behaviour is even more complex since membrane-flexural couplings have to be taken into consideration. In addition, localisation of damage is observed at the structural scale in narrow zones and is strongly related to the material mesostructure. The characteristic size and the orientation of this localisation phenomenon has to be captured properly to determine the structural failure modes together with the associated energy dissipation.

A multi-scale approach can therefore offer an attractive and flexible solution in the characterisation of such periodic heterogeneous materials. Different multi-scale techniques have been developed in the past decades allowing to postulate closed-form constitutive laws at the scale of the constituents, on which the material parameters are a priori more straightforward to identify. First substructuring methods based on a structural decomposition in non-overlapping subdomains have been proposed for heterogeneous materials, see Ghosh et al. (2001), Ibrahimbegovic and Markovic (2003), Markovic and Ibrahimbegovic (2004) for instance. In these approaches, compatibility conditions are used to connect the discretisation of the subdomains to the macroscopic finite element mesh playing the role of a frame. A similar approach was applied more recently for the in-plane non-linear behaviour of large masonry structures in Brasile et al. (2007a,b). A concept of structural decomposition was also combined to an asymptotic homogenisation procedure with Voronoi cells for damage assessment in two-dimensional random particle-reinforced porous composites, see Ghosh et al. (2001), and recently enhanced for the modelling of damage-induced anisotropy in ductile cast alloys, see Ghosh et al. (2009). Asymptotic homogenisation was initially presented for periodic heterogeneous materials in Bensoussan et al. (1978), Sanchez-Palencia (1980), Suquet (1987), using an asymptotic expansion of the macroscopic variables which allows to define a boundary value problem on a representative volume element (RVE) for each order under consideration, see Peerlings and Fleck (2004). This technique is still widely used for composite materials, see the recent extensive review in Kalamkarov et al. (2009). Based on the scale separation assumption used in periodic homogenisation, a computational homogenisation scheme known as  $FE^2$  was proposed allowing to numerically compute the average non-linear response of a heterogeneous microstructure by means of averaging theorems and a boundary value problem on a RVE mainly for two-dimensional and three-dimensional applications, see Smit et al. (1998), Feyel and Chaboche (2000), Kouznetsova et al. (2001) as well as Geers et al. (2009) for a state of the art of this methodology. In order to reduce the high computational cost of direct computational homogenisation procedures with a certain compromise on the solution accuracy, transformation field analysis was presented in Dvorak (1992) for plastic and damaging composites. It is based on the decomposition of each constituent of the microstructure into subdomains in which uniform inelastic strain fields are assumed, leading to off-line homogenisation, as recently applied for in-plane loaded masonry walls in Sacco (2009).

Since complex heterogeneous materials may appear in shell-like structures (laminated composite, honeycomb-type sandwich, masonry structure), some extensions of multi-scale approaches to shell-like formulations recently appeared. Unit cell asymptotic homogenisation techniques were used to determine the elastic properties of beam-like structures in Cartraud and Messenger (2006), of composite shell structures with orthotropic rein-

forcements in Challagulla et al. (2008), and of periodic running bond masonry walls subjected to out-of-plane loading in Cecchi and Sab (2002b, 2004, 2007). These techniques were further combined with limit analysis concepts and optimisation techniques in order to compute ultimate strength properties of structures and determine their failure mechanism, as in Milani et al. (2006a,b), Cecchi et al. (2007), Cecchi and Milani (2008). A structural limit analysis approach based on a homogenisation procedure accounting for the strength domain of any shell failure mechanism was developed recently in Milani et al. (2008) for the structural analysis of curved shells such as arches, vaults and domes. For structural computations, a twofold multi-scale enrichment methodology using the asymptotic homogenisation theory and a partition of unity method was proposed recently in Oskay (2009) for the inelastic analysis of thin heterogeneous plate structures. This approach was combined with an eigendeformation-based model reduction which generalises transformation field analysis to account for interface debonding within the microstructure, see Oskay and Fish (2007, 2008). Another multi-scale framework based on asymptotic homogenisation was developed for the failure of thin heterogeneous plates, see Oskay and Ghanshyam (2009), where macroscopic inelastic and damage fields are linked to microscopic inelastic and damage fields by means of weighted averaging relations.

The FE<sup>2</sup> computational homogenisation approach was extended recently for structured thin sheets using the homogenisation of a through-thickness RVE based on a second-order strategy, see Geers et al. (2007), Coenen et al. (2008). The thick shell case still raises questions concerning the transverse shear upscaling and is the topic of current research. A more restricted periodic homogenisation procedure was presented in Mistler et al. (2007) for the case of elastic Kirchhoff-Love masonry shells.

These multi-scale methods were recently extended to incorporate the damage and plastic behaviour of heterogeneous materials. Some are based on non-local descriptions at the structural scale, see Ghosh et al. (2009), Oskay and Ghanshyam (2009), allowing to consider structural strain localisation bands with relatively fine mesh combined with remeshing. The substructuring approaches based on a structural decomposition allows to incorporate non-linear behaviour features up to failure in the case where the characteristic length scale of the microstructure is not small enough to satisfy the scale separation principle, see Ibrahimbegovic and Markovic (2003), Markovic and Ibrahimbegovic (2004), Brasile et al. (2007a,b). These methods keep a significant but distributed computational effort, mainly prescribed by the level of details associated with the chosen microstructural modelling strategy. A continuum model coupled with asymptotic homogenisation method and incorporating an internal length deduced from the microstructure was proposed recently in Dascalu et al. (2008) to describe size effects, material softening and damage-induced anisotropy in brittle heterogeneous material, while a second-order computational homogenisation approach was proposed in Kouznetsova et al. (2004) incorporating in the macroscopic continuum a length scale defined by the size of the RVE.

Since it is crucial to properly treat localisation at each scale to keep a well-posed problem for a softening analysis, continuous-discontinuous scale transitions started to emerge recently. A first approach based on this concept was developed in Massart et al. (2007b,a) for damage in in-plane loaded masonry wall, using a twofold first-order computational homogenisation scheme and relying on the definition of a localisation band using strain discontinuities driven by an evolving damaging unit cell. The detection of localisation is based on the homogenised tangent stiffness leading to a physically based description of preferential damage orientations, and a condition of increasing energy dissipation is also used to treat microstructural snap-backs. An improved version of the method in-

incorporating strong embedded discontinuities was proposed recently in Mercatoris and Massart (2009). Another multi-scale approach was recently coupled to the X-FEM approach, and consists in feeding the behaviour of structural scale equivalent displacement discontinuities with information extracted from the aggregation of all microstructural material instabilities present in a unit cell, see Belytschko et al. (2008), Belytschko and Song (2009).

In the present Chapter, a periodic computational homogenisation will be used in order to capture the quasi-brittle structural failure of initially periodic thin heterogeneous shells with an application to out-of-plane loaded masonry walls. The scale transitions therefore have to be adapted to represent structural localisation by means of fine-scale informed discontinuities since the size of the localisation zone can be smaller than the RVE size. To achieve this, different techniques to represent damage localisation by incorporating discontinuities within classical continuum descriptions can be used. Initially, embedded discontinuities were used by introducing jumps either into strain fields, leading to weak discontinuities as in Ortiz et al. (1987), Belytschko et al. (1988); or into displacement fields leading to a strong discontinuity approach, see Simo et al. (1993), Lofti and Shing (1995), Oliver (1996a,b), Armero and Garikipati (1996), Armero (1999), Wells and Sluys (2000). The extended finite element method based on the partition unity concept was next presented in Moës et al. (1999), Belytschko and Black (1999), Belytschko et al. (2001), Wells and Sluys (2001); allowing for continuous crack path and crack kinematics, in contrast with the embedded discontinuity approach, which uses mainly element-based enrichments. A recent extensive review of the X-FEM methodology is available in Belytschko et al. (2009). These two approaches (embedded discontinuity and X-FEM) have been extended for through-thickness cracks of plates and shells in the last decade. In this context, the extended finite element method was adapted to the Reissner-Mindlin formulation in Dolbow et al. (2000), the continuum-based shell formulation in Areias and Belytschko (2005), and the Kirchhoff-Love formulation in Rabczuk et al. (2007). In addition, the X-FEM methodology was used recently for quasi-static crack propagation of thin shells taking into account softening, adhesion and contact behaviour, see Areias and Rabczuk (2008); and for dynamic quasi-brittle fracture of thin shells subjected to impulse loads, see Song and Belytschko (2009). Although the X-FEM methodology prevails in the modelling of crack propagation, the embedded discontinuity method still has drawn interest in the past years. The two-dimensional strong embedded discontinuity approach proposed in Armero (1999) was extended to the Euler-Bernoulli beam kinematics in Armero and Ehrlich (2006b) and the Reissner-Mindlin plate kinematics in Armero and Ehrlich (2006a). This last approach will be used in the sequel to represent the structural localisation.

This Chapter presents the extension to thin shells of a methodology which has been applied for in-plane loaded structures in Mercatoris and Massart (2009). The proposed methodology both allows to predict the load bearing capacity and the associated failure modes as limit analysis methods, as well the evolution of stable cracks, i.e. the service states far below the ultimate load capacity, and therefore provides an estimation of the total energy dissipation.

The Chapter is structured as follows. The embedded strong discontinuity presented in Armero and Ehrlich (2006a) and used at the structural scale to represent the localised shell failure is briefly sketched in Section 6.2. The main ingredients of periodic computational homogenisation scheme for thin shell properties are given in Section 6.3, followed by a homogenisation-based failure detection proposed in Mercatoris et al. (2009) in Sec-

tion 6.4. The details of the upscaling procedure towards a coarse-scale discontinuity for shell failure are presented in Section 6.5. The results obtained with this multi-scale framework are illustrated for the failure of out-of-plane loaded masonry wall, and are discussed and compared with those of complete fine-scale simulations in Section 6.6. Finally, the conclusions and prospects are given in Section 6.7.

## 6.2 Localised shell failure with embedded strong discontinuity

### 6.2.1 Shell formulation

In this Section, the formulation of a shell finite element which will be used in the sequel is presented. The computational homogenisation scheme which will be defined in Section 6.3 for infinitesimal strains is based on the Kirchhoff-Love assumptions. As further motivated, a shear-enhanced element with the Reissner-Mindlin description will however be used in order to properly treat the discontinuity opening even if thin shells are considered. The problem of interest here is a planar shell defined by the reference surface  $\Omega$ , its contour  $\partial\Omega$  both included in the  $x, y$  reference plane and its constant thickness  $h$  along the  $z$  direction. The geometrically linear Reissner-Mindlin kinematics is assumed in such a way that the kinematics of any material point  $P$  in the shell thickness is described by

$$\vec{v}_P = \vec{v}(x, y) + z\vec{\beta}(x, y) \quad \text{and} \quad w_P = w(x, y) \quad (6.1)$$

where  $\vec{v}$  is the in-plane or membrane displacement vector,  $\vec{\beta}$  is the rotation vector, see Figure 6.1 for the sign convention, and  $w$  is the out-of-plane displacement also called the

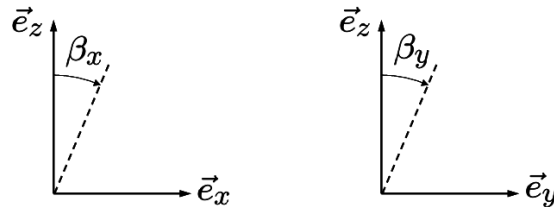


Figure 6.1: Sign convention of rotations in shell kinematics

transverse deflection. The generalised strains, namely the membrane deformation tensor  $\mathbf{E}$ , the curvature tensor  $\boldsymbol{\chi}$ , and the transverse shear strain vector  $\vec{\gamma}$  are given by

$$\mathbf{E} = (\vec{\nabla}\vec{v})^{\text{sym}}, \quad \boldsymbol{\chi} = (\vec{\nabla}\vec{\beta})^{\text{sym}} \quad \text{and} \quad \vec{\gamma} = \vec{\nabla}w + \vec{\beta} \quad (6.2)$$

and are work conjugate to the membrane force tensor  $\mathbf{N}$ , the bending moment  $\mathbf{M}$  and the transverse shear force vector  $\vec{T}$ , respectively. The quasi-static equilibrium of the shell can therefore be expressed in a weak form by the variational statement

$$\int_{\Omega} (\mathbf{N} : \delta\mathbf{E} + \mathbf{M} : \delta\boldsymbol{\chi} + \vec{T} \cdot \delta\vec{\gamma}) \, d\Omega = \int_{\Omega} \delta w_s^{\text{ext}} \, d\Omega + \int_{\partial\Omega} \delta w_c^{\text{ext}} \, d\Gamma \quad (6.3)$$

for all admissible variations  $\delta\vec{v}$ ,  $\delta\vec{\beta}$  and  $\delta w$ , and where  $\delta w_s^{\text{ext}}$  and  $\delta w_c^{\text{ext}}$  represent the external work density variations of applied forces and torques, respectively per unit area and per unit length. To close the formulation, the stress variables are linked to the strain

variables through a constitutive relation. For the sake of simplicity, the couplings between the shearing behaviour and the membrane-flexural behaviour are neglected, which leads to a constitutive relation given in its linearised form by

$$\begin{cases} \delta \mathbf{N} = {}^4\mathbf{L}_{mm} : \delta \mathbf{E} + {}^4\mathbf{L}_{mf} : \delta \boldsymbol{\chi} \\ \delta \mathbf{M} = {}^4\mathbf{L}_{fm} : \delta \mathbf{E} + {}^4\mathbf{L}_{ff} : \delta \boldsymbol{\chi} \\ \delta \vec{T} = {}^2\mathbf{L}_{ss} \cdot \delta \vec{\gamma} \end{cases} \quad (6.4)$$

where the five tensors  $\mathbf{L}_{ab}$  (with  $a, b = [m, f, s]$ ) are the material tangent stiffnesses governing the membrane ( $m$ ), flexural ( $f$ ) and shearing ( $s$ ) behaviours, as well as the membrane-flexural couplings. In the present Chapter, the coarse-scale material response (6.4) will be deduced from the mesostructural behaviour by means of a computational homogenisation procedure. As will be shown in Section 6.3, the homogenisation procedure used here is restricted to a Kirchhoff-Love shell kinematics, and therefore only furnishes the membrane-flexural material response. As a consequence, the uncoupled shearing behaviour will be driven here by a postulated closed-form law. For the sake of simplicity, a linear elastic transverse shear behaviour characterised by a shearing modulus will be assumed for the shell bulk behaviour. The proposed approach is therefore restricted to the cases for which the non-linear transverse shear effects are negligible.

Yet, a Kirchhoff-Love approximation will be avoided at the structural (coarse) scale in order to avoid the use of  $C^1$  interpolation. When using  $C^0$  Reissner-Mindlin kinematics, it is well-known that an independent interpolation of the transverse shear needs to be carefully selected in order to avoid shear locking in the thin structure limit. For this purpose, the assumed transverse shear strain interpolation proposed in Batoz and Lardeur (1989) will be used. This independent interpolation of the transverse shear strain is based on the strong form of the rotation equilibrium which reads  $\vec{T} = \vec{\nabla} \cdot \mathbf{M}$  in the absence of body torques. This approach was initially proposed in Batoz and Lardeur (1989) for the case of linear elastic triangle finite elements, also called discrete shear triangle (DST), and will here be extended to account for the material non-linearities. In this extension, the shear enhancement is assumed to be independent of the membrane effects and the spatial variations of the material tangents are neglected. The development of the assumed shear strain technique is reported in Batoz and Lardeur (1989), and will be omitted here for the sake of brevity. Only the required adaptations needed in the case of a non-linear material response will be reported here.

In the case of non-linear material behaviour, the assumed transverse shear strain approach can be reformulated by considering the aforementioned assumptions and using a first-order development of the total stress values needed in the strong form of rotational equilibrium. Using a classical incremental iterative Newton-Raphson scheme, the bending moment tensor and the transverse shear force vector at the current iteration ( $i$ ) can be approximated by

$$\mathbf{M}^{(i)} \approx \mathbf{M}^{(0)} + {}^4\mathbf{L}_{ff}^{(0)} : \Delta \boldsymbol{\chi}^{(i)} \quad (6.5)$$

$$\vec{T}^{(i)} \approx \vec{T}^{(0)} + {}^2\mathbf{L}_{ss}^{(0)} \cdot \Delta \vec{\gamma}^{(i)} \quad (6.6)$$

where the iteration (0) corresponds to the last converged step and the symbol  $\Delta$  represents the incremental variation of a variable from the last converged state to the current iteration. Substituting the rotation equilibrium with (6.5) into (6.6), and using the constitutive flexural relation (6.4) without the membrane and shearing couplings, an assumed transverse shear strain variation can be related to the incremental variation of rotation

field according to

$$\Delta \vec{\gamma}^{(i)} = ({}^2\mathbf{L}_{ss}^{(0)})^{-1} \cdot \left( {}^4\mathbf{L}_{ff}^{(0)} : \vec{\nabla} \left( \vec{\nabla} \Delta \vec{\beta}^{(i)} \right)^{\text{sym}} \right) \quad (6.7)$$

Note that the interpolation of the assumed transverse shear strain requires at least a quadratic interpolation of the rotation field due to the second derivative present in Equation (6.7). The remainder of the subsequent developments can be found in Batoz and Lardeur (1989). The proposed reformulation of this assumed transverse shear strain approach for the case of non-linear material behaviour allows to avoid numerical difficulties by keeping an asymptotically quadratic convergence of the Newton-Raphson scheme.

## 6.2.2 Embedded strong discontinuity in shell formulation

For the modelling of localised failure resulting from material instabilities, localised energy dissipation has to be carefully treated in order to keep a well-posed problem and avoid significant mesh dependency. One of the techniques used to account for localisation consists in the use of embedded discontinuities see Ortiz et al. (1987), Belytschko et al. (1988), Simo et al. (1993), Lofti and Shing (1995), Armero and Garikipati (1996), Armero (1999), Wells and Sluys (2000), Jirásek (2000). Here, an embedded strong discontinuity approach is considered for the Reissner-Mindlin shell kinematics, in the spirit of Armero (1999), Armero and Ehrlich (2006a). Since this approach uses element-based kinematics enrichments, the crack path continuity and the crack opening continuity across the element boundaries are not ensured (at least in the initial version of the framework), in contrast with the extended finite element method (X-FEM) in which the crack kinematics is interpolated from nodal parameters, see Moës et al. (1999), Dolbow et al. (2000). This element-based character can however be seen as an advantage for the case of multi-scale, homogenisation-driven embedded discontinuities since fine-scale damage evolution may lead to rotating discontinuities, as will be illustrated in Section 6.6, see also Mercatoris et al. (2009).

In the embedded strong discontinuity approach proposed by Armero and Ehrlich (2006a), the kinematics is enriched by discontinuous fields upon localisation. An in-plane displacement jump vector  $\vec{\xi}_v$  and a rotation jump vector  $\vec{\xi}_\beta$  are introduced along a discontinuity line  $\Gamma_d$ . The orientation of the discontinuity has to be determined in the detection procedure, here based on a localisation analysis given in Section 6.4. In the sequel, the discontinuity will be introduced at the geometrical centre of the element. In agreement with the Reissner-Mindlin kinematics, a transverse deflection jump  $\xi_w$  is also introduced at an articulation point with position  $\vec{x}_{\Gamma_d}$ , which corresponds to the centre of the rotation jump, see Figure 6.2. These jumps are added to the regular, continuous part of the engineering displacement fields according to

$$\begin{cases} \vec{v}_e &= \vec{v} + \Psi_v \vec{\xi}_v \\ \vec{\beta}_e &= \vec{\beta} + \Psi_\beta \vec{\xi}_\beta \\ w_e &= w + \Psi_w \left( \xi_w - (\vec{x} - \vec{x}_{\Gamma_d}) \cdot \vec{\xi}_\beta \right) \end{cases} \quad (6.8)$$

where  $\Psi_v$ ,  $\Psi_\beta$  and  $\Psi_w$  represent a set of functions exhibiting a unit jump along the discontinuity line. Note that the enriched transverse deflection field depends on the rotation jump vector as shown in Equation (6.8). The enhanced generalised strains are obtained

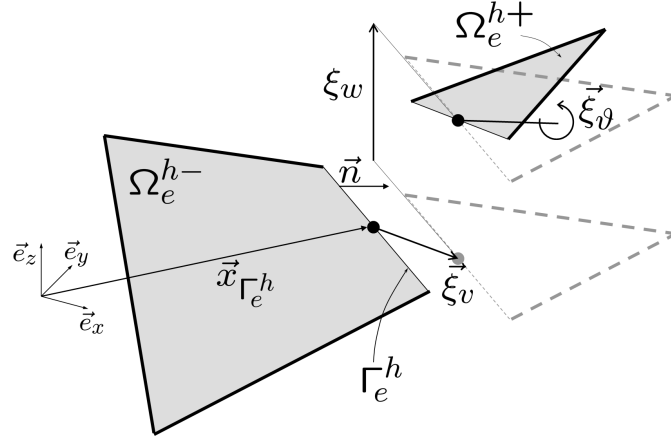


Figure 6.2: Embedded strong discontinuity for the Reissner-Mindlin shell kinematics according to Armero and Ehrlich (2006a).

by differentiating Equations (6.8) in the sense of (6.2)

$$\begin{cases} \mathbf{E}_e &= \mathbf{E}(\vec{v}) + \mathbf{G}_E(\vec{\xi}_v) + (\vec{\xi}_v \vec{n})^{\text{sym}} \delta_{\Gamma_d} \\ \boldsymbol{\chi}_e &= \boldsymbol{\chi}(\vec{\beta}) + \mathbf{G}_\chi(\vec{\xi}_\beta) + (\vec{\xi}_\beta \vec{n})^{\text{sym}} \delta_{\Gamma_d} \\ \vec{\gamma}_e &= \vec{\gamma}(\vec{\beta}, w) + \vec{G}_\gamma(\vec{\xi}_\beta, \xi_w) + \left( \xi_w - (\vec{x} - \vec{x}_{\Gamma_d}) \cdot \vec{\xi}_\beta \right) \vec{n} \delta_{\Gamma_d} \end{cases} \quad (6.9)$$

where the tensors  $\mathbf{G}_E$ ,  $\mathbf{G}_\chi$  and the vector  $\vec{G}_\gamma$  are the regular parts of the enhanced generalised strains which depend on the jumps, and  $\delta_{\Gamma_d}$  is the Dirac function centred on the discontinuity line. Note that in this approach, the Dirac function is integrated along the discontinuity line and therefore does not need regularisation, see de Borst et al. (2001). The details concerning the discretisation of such an enhanced kinematics, among which the construction of  $\mathbf{G}_E$ ,  $\mathbf{G}_\chi$  and  $\vec{G}_\gamma$  can be found in Armero (1999), Armero and Ehrlich (2006a), and will be omitted here for brevity.

In order to determine the additional jump parameters, the weak form of global equilibrium (6.3) is solved together with the weak form of continuity of the generalised tractions along the discontinuity line:

$$\int_{\Gamma_d} \left[ \delta \vec{\xi}_v \cdot \left( \vec{N}_d - \mathbf{N} \cdot \vec{n} \right) + \delta \vec{\xi}_\beta \cdot \left( \vec{M}_d - \mathbf{M} \cdot \vec{n} \right) + \left( \delta \xi_w - (\vec{x} - \vec{x}_{\Gamma_d}) \cdot \delta \vec{\xi}_\beta \right) \left( T_d - \vec{T} \cdot \vec{n} \right) \right] d\Gamma = 0 \quad (6.10)$$

where  $\vec{N}_d$ ,  $\vec{M}_d$  and  $T_d$  are respectively the membrane force vector, the bending moment vector and the transverse shear force scalar across the discontinuity,  $\mathbf{N}$ ,  $\mathbf{M}$  and  $\vec{T}$  are the generalised stresses in the bulk, surrounding the discontinuity, and  $\vec{n}$  is the normal to the discontinuity line  $\Gamma_d$ . A material response which links the generalised stresses across the discontinuity to the engineering displacement jumps is required to drive the discontinuity. As for the constitutive material law of the shell bulk (6.4), it is assumed that no coupling exists between the transverse shear behaviour and the flexural and membrane behaviours, since the scale transitions which will be given in Section 6.3 are restricted to thin shells. The constitutive relation of the discontinuity should therefore have the following format:

$$\begin{cases} \delta \vec{N}_d &= {}^2\mathbf{C}_{\text{mm}}^d \cdot \delta \vec{\xi}_v + {}^2\mathbf{C}_{\text{mf}}^d \cdot \delta \vec{\xi}_\beta \\ \delta \vec{M}_d &= {}^2\mathbf{C}_{\text{fm}}^d \cdot \delta \vec{\xi}_v + {}^2\mathbf{C}_{\text{ff}}^d \cdot \delta \vec{\xi}_\beta \\ \delta T_d &= {}^0\mathbf{C}_{\text{ss}}^d \delta \xi_w \end{cases} \quad (6.11)$$

where the five tensors  $\mathbf{C}_{ab}^d$  with  $a, b = [m, f, s]$  are the discontinuity tangent stiffness tensors. As for (6.4), these tensors can be deduced from closed-form laws like in Armero and Ehrlich (2006a); or alternatively by homogenisation, see Section 6.5. Once the embedded strong discontinuity is introduced, the bulk of the element is assumed to unload elastically from the state reached at that point in order to reflect the assumed quasi-brittle nature of the material.

### 6.3 Non-linear computational homogenisation of thin shell properties

In the context of non-linear material behaviour of thin heterogeneous shell, the meso-structural material behaviour is upscaled towards the non-localised membrane-flexural constitutive relations (6.4) by means of a computational homogenisation scheme. The principles of this upscaling relations were developed in Mistler et al. (2007) and will be briefly recalled here for the sake of clarity (more details are available in Mercatoris et al. (2009)). The purpose of computational homogenisation is to obtain the average macroscopic response of a heterogeneous material from the underlying mesostructure of the material and the behaviour of its constituents. It is based on the solution of a mesostructural boundary value problem on a representative volume element (RVE) relying on averaging theorems. It makes use the principle of scale separation between the two scales of representation, which assumes that the material configuration is macroscopically homogeneous, but microscopically heterogeneous, Kouznetsova et al. (2001).

For a macroscopic shell representation, a three dimensional through-thickness RVE is used to represent the mesostructure. Considering the classical simplifying assumptions in engineering shell descriptions, the scale transitions need to be carefully derived especially for the transverse shear behaviour of thick shells, see Geers et al. (2007), Coenen et al. (2008). For the sake of simplicity, the computational homogenisation procedure proposed in Mistler et al. (2007) for the elastic membrane-flexural behaviour of thin masonry shells is used here to take into account the material non-linearities. The aspects related to transverse shear are detailed in Section 6.5.2.

#### 6.3.1 Averaging relations for Kirchhoff-Love shell kinematics

At the fine scale, a shell is represented by a prismatic through-thickness RVE, defined by its trace  $\mathcal{S}_{\text{RVE}}$  on the reference surface of the shell and its thickness  $h$ , corresponding to the shell thickness, see Geers et al. (2007). The averaging theorems linking the coarse (macro) scale and the fine (meso) scale quantities have to be verified for the strain, the stress and the work variations. For the case of the Kirchhoff-Love shell kinematics, it is postulated that the macroscopic membrane strain tensor  $\mathbf{E}$  is the average of the local membrane strain tensor over the reference surface  $\mathcal{S}_{\text{RVE}}$ . The macroscopic curvature tensor  $\boldsymbol{\chi}$  is assumed to be the surface average of the local curvature tensor over  $\mathcal{S}_{\text{RVE}}$

$$\mathbf{E} = \frac{1}{\mathcal{S}_{\text{RVE}}} \int_{\mathcal{S}_{\text{RVE}}} (\vec{\nabla} \vec{u}_r)^{\text{sym}} \, d\mathcal{S}_{\text{RVE}} \tag{6.12a}$$

$$\boldsymbol{\chi} = \frac{1}{\mathcal{S}_{\text{RVE}}} \int_{\mathcal{S}_{\text{RVE}}} -\vec{\nabla} \vec{\nabla} u_z \, d\mathcal{S}_{\text{RVE}} \tag{6.12b}$$

where  $\vec{u}_r$  and  $u_z$  are the projections of the mesostructural displacement vector, respectively, on the reference surface and in the thickness direction.

In a computational homogenisation technique, the energy consistency is classically assumed, and expressed here by

$$\mathbf{N}:\delta\mathbf{E} + \mathbf{M}:\delta\boldsymbol{\chi} = \frac{1}{\mathcal{S}_{\text{RVE}}} \int_{\mathcal{V}_{\text{RVE}}} \boldsymbol{\sigma}:\delta\boldsymbol{\varepsilon} \, d\mathcal{V}_{\text{RVE}} \quad (6.13)$$

where  $\boldsymbol{\varepsilon}$  is the (local) mesostructural infinitesimal strain tensor work conjugate to the mesoscopic stress field  $\boldsymbol{\sigma}$ , and  $\mathbf{N}$  and  $\mathbf{M}$  are respectively the macroscopic membrane force and bending moment tensors. Combining relations (6.12) and (6.13) with appropriate boundary conditions on the RVE leads to the satisfaction of the averaging theorem for the stress measures and allows to relate the macroscopic membrane force tensor  $\mathbf{N}$  and the macroscopic bending moment tensor  $\mathbf{M}$  to the mesoscopic statically admissible stress field  $\boldsymbol{\sigma}$  at the surface of the RVE.

### 6.3.2 Homogenisation with periodic boundary conditions

Here, the coupled two-scale framework will be defined assuming perfect periodicity of the mesostructure (the consequences of this assumption will be discussed in the sequel of the paper), and will be illustrated for the particular case of a quasi-brittle textured material such as masonry. Note however that other initially periodic materials could be treated with similar assumptions, such as honeycomb panels. Periodic boundary conditions on RVEs are often used Smit et al. (1998), Kouznetsova et al. (2001), and were shown to provide a better estimation of the overall elastic properties than other boundary conditions, see Terada et al. (2000), van der Sluis et al. (2000). Assuming that the rigid body translations and rotations of the RVE vanish, it can be shown, see Anthoine (1995), that the kinematically admissible displacement field is strain-periodic and given by

$$\vec{u}_r = \mathbf{E}\cdot\vec{x} + z\boldsymbol{\chi}\cdot\vec{x} + \vec{u}_r^p \quad (6.14a)$$

$$u_z = -\frac{1}{2}\vec{x}\cdot\boldsymbol{\chi}\cdot\vec{x} + u_z^p \quad (6.14b)$$

where  $\vec{u}_r^p$  and  $u_z^p$  are in-plane and out-of-plane periodic displacement fluctuation fields, added to the average displacement field to account for the heterogeneity of the material. Such a displacement field satisfies the averaging relations (6.12). Both fluctuation fields can be eliminated, and the periodic boundary conditions can be prescribed on the RVE using tying relations, see Anthoine (1995), Mistler et al. (2007) for detailed developments.

### 6.3.3 Control system of the mesoscopic boundary value problem

In a general case, the proper size and geometry of a RVE should be deduced from statistical considerations as shown in Zeman and Šejnoha (2007) or defined by the periodicity of a given mesostructure. In the case of a small strain description, the Kirchhoff-Love generalised strains (membrane and curvature) are given by six independent scalar quantities. The average deformed state of a RVE can therefore be fully prescribed using six controlling degrees of freedom if the periodicity conditions are enforced. The macroscopic membrane deformations are prescribed using three reference plane displacement components, while the macroscopic curvatures are fixed by three out-of-plane displacement components. Using Equations (6.14) and the periodicity conditions, the relations linking the controlling

displacements to the average coarse-scale strains can be written in a matrix form

$$\{u_{\text{ctl}}\} = [D_u]^{-1}\{E_{\text{KL}}\} \tag{6.15}$$

where  $\{u_{\text{ctl}}\}$  is a column vector of the six controlling degrees of freedom,  $\{E_{\text{KL}}\}$  is a column vector of the Kirchhoff-Love generalised strains, and  $[D_u]$  is a matrix which depends on the in-plane dimensions of the RVE, see Mistler et al. (2007). Considering the strain-periodic displacement field (6.14) and the energy consistency (6.13), the average Kirchhoff-Love generalised stresses can be obtained from the controlling forces conjugated to the controlling degrees of freedom, and which represent the action of the neighbouring cells, see Mercatoris et al. (2009). In a matrix form, this relation is noted

$$\{\Sigma_{\text{KL}}\} = [D_f]\{f_{\text{ctl}}\} \tag{6.16}$$

where  $\{f_{\text{ctl}}\}$  is a column vector of the six controlling forces,  $\{\Sigma_{\text{KL}}\}$  is a column vector of the Kirchhoff-Love generalised stresses, and  $[D_f]$  is a matrix which depends on the in-plane dimensions of the RVE. The coarse-scale material tangent stiffness can be extracted from the mesostructural response and is given by

$$[L] = [D_f][K^*][D_u]^{-1} \tag{6.17}$$

where  $[L]$  is the matrix form of the homogenised membrane-flexural material tangent stiffness, and  $[K^*]$  is the fine-scale (discrete) tangent stiffness matrix condensed at the controlling degrees of freedom ( $\{\delta f_{\text{ctl}}\} = [K^*]\{\delta u_{\text{ctl}}\}$ ), see Mercatoris et al. (2009).

The case of running bond masonry is considered as an illustration of the proposed approach. This composite material initially exhibits a two-dimensional orthotropic heterogeneous structure with a periodic stacking of constituents along two directions in its own plane. For the non-linear behaviour of such a material within a geometrically linear setting, a unit cell, i.e. a single period RVE, can be used as in Pegon and Anthoine (1997), Massart et al. (2004, 2005b) since the failure is then not size dependent as long as single period failure is considered. For the sake of simplicity, a parallelepipedic through-thickness portion of masonry sketched in Figure 6.3 will be used as in Mistler et al. (2007). Note again that similar assumptions could be made for other initially periodic materials. Knowing the geometry of the RVE, the scale transition operators  $[D_u]$  and  $[D_f]$  can be expressed as a function of the in-plane dimensions of the cell, Mistler et al. (2007), Mercatoris et al. (2009).

Based on Equations (6.15), any average deformation path can be prescribed. The related mesostructural boundary value problem is completely defined from the prescribed controlling degrees of freedom and the periodicity boundary conditions, and can be solved

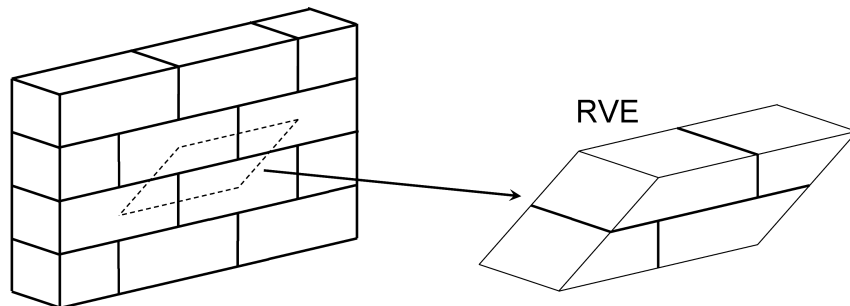


Figure 6.3: Parallelepipedic through-thickness RVE for running bond masonry.

using a classical finite element scheme, provided mesostructural constitutive laws are postulated. This type of control is classically used in multi-scale nested scheme using displacement-based finite element schemes, Kouznetsova et al. (2001), Massart et al. (2007a). Note that this Kirchhoff-Love shell computational homogenisation scheme can be connected to the general second-order solid-solid computational homogenisation framework developed in Kouznetsova et al. (2002). Such a link was established for the Reissner-Mindlin case by introducing the shell kinematical assumptions in the macroscopic second-gradient continuum, see Geers et al. (2007) for more details.

## 6.4 Homogenisation-based failure detection in thin shells

For the embedded discontinuity modelling of the localised behaviour of thin shells, a criterion to detect localisation and its orientation is required. In the context of computational homogenisation, the detection and orientation of coarse-scale localisation has to be deduced from the response of mesostructural RVE computations since no closed-form material law is postulated a priori at the structural scale. Since the computational homogenisation framework presented in Section 6.3 is restricted to thin shells neglecting the transverse shear effects, a homogenisation-based criterion is used for the Kirchhoff-Love description to detect the onset of localisation and its orientation. Note that the transverse shear effects should be taken into account to detect more complex failure mechanism such as tearing. The two-scale approach proposed here will be restricted to membrane-flexural failure mode in which the transverse shear effects are negligible.

The criterion proposed in Makowski and Stumpf (1998) and used in Mercatoris et al. (2009) to detect localisation in the context of two-scale computations will be used here. This procedure is based on the homogenised material tangent stiffness governing the membrane and flexural constitutive relations (6.4), which can be deduced from the condensed stiffness of the RVE. The conditions for the appearance of a localisation zone in which material degradation grows and localises can be treated as a material bifurcation, similarly to Rice (1976), Rice and Rudnicki (1980). Across the interface between the localising zone ( $l$ ) and its surrounding material ( $s$ ), the displacement and rotation fields can be assumed to be continuous and the generalised strain jumps have the form

$$\begin{cases} \delta \mathbf{E}^{(l)} - \delta \mathbf{E}^{(s)} &= \frac{1}{2} (\delta \vec{m}_E \vec{n} + \vec{n} \delta \vec{m}_E) \\ \delta \boldsymbol{\chi}^{(l)} - \delta \boldsymbol{\chi}^{(s)} &= \frac{1}{2} (\delta \vec{m}_\chi \vec{n} + \vec{n} \delta \vec{m}_\chi) \end{cases} \quad (6.18)$$

where  $\vec{n}$  is the normal to the localising zone, and  $\vec{m}_E$  and  $\vec{m}_\chi$  are the strain jump modes, which vanish in the initial, homogeneous situation, and must become nonzero for a bifurcated state to exist. Note that in Equation (6.18), the generalised strain jumps are obtained from a strain jump mode vector of only two components, i.e. the longitudinal deformation tangent to the discontinuity is not taken into account. Equilibrium requires the continuity of the projected stress quantities at the interface of the localising zone, which reads

$$\begin{cases} \vec{n} \cdot (\delta \mathbf{N}^{(l)} - \delta \mathbf{N}^{(s)}) &= 0 \\ \vec{n} \cdot (\delta \mathbf{M}^{(l)} - \delta \mathbf{M}^{(s)}) &= 0 \end{cases} \quad (6.19)$$

Introducing Equations (6.4) and (6.18) in Equation (6.19) and using the classical linear comparison solid assumption using the same material stiffness tangents on both sides of

the localising zone interface, the stress continuity requirement reads

$$\begin{bmatrix} (\vec{n} \cdot \mathbf{4}\mathbf{L}_{mm} \cdot \vec{n}) & (\vec{n} \cdot \mathbf{4}\mathbf{L}_{mf} \cdot \vec{n}) \\ (\vec{n} \cdot \mathbf{4}\mathbf{L}_{fm} \cdot \vec{n}) & (\vec{n} \cdot \mathbf{4}\mathbf{L}_{ff} \cdot \vec{n}) \end{bmatrix} \begin{Bmatrix} \vec{m}_E \\ \vec{m}_\chi \end{Bmatrix} = 0 \quad (6.20)$$

This system of equations admits a non-trivial solution (i.e. a bifurcated state exists) only if

$$\det(\mathbf{A}(\vec{n})) = \det \left( \begin{bmatrix} (\vec{n} \cdot \mathbf{4}\mathbf{L}_{mm} \cdot \vec{n}) & (\vec{n} \cdot \mathbf{4}\mathbf{L}_{mf} \cdot \vec{n}) \\ (\vec{n} \cdot \mathbf{4}\mathbf{L}_{fm} \cdot \vec{n}) & (\vec{n} \cdot \mathbf{4}\mathbf{L}_{ff} \cdot \vec{n}) \end{bmatrix} \right) = 0 \quad (6.21)$$

for some direction  $\vec{n}$ , where  $\mathbf{A}(\vec{n})$  is the acoustic tensor generalised to the Kirchhoff-Love shell theory, see Makowski and Stumpf (1998).

A localisation analysis using this acoustic tensor-based criterion was used in Mercatoris et al. (2009) for thin masonry shells in the context of computational homogenisation. It was shown that a negative local maximum of the acoustic tensor determinant spectrum derived from the homogenised material tangent stiffness allows to determine average orientations of coarse-scale localisation consistent with fine-scale damage patterns. In addition, it was shown that this orientation can rotate due to the evolving damage process at the fine scale. The localisation orientation therefore needs to be updated during the damaging process in order to avoid potential stress locking resulting from a fixed orientation.

In the proposed two-scale approach, this criterion will be used in combination with the criterion for the loss of uniqueness of the discretised fine-scale boundary value problem, based on the nonpositive-definite character of its discretised tangent stiffness, see de Borst et al. (1993). The latter criterion will be used to detect the onset of localisation, while the former acoustic tensor-based criterion will be used to extract the average orientation of the embedded discontinuities as in Massart (2003).

## 6.5 Homogenisation-based upscaling framework for shell localisation

### 6.5.1 Localisation-enhanced two-scaled scheme for thin shells

In the present Chapter, contrary to the approach proposed in Armero (1999) and Armero and Ehrlich (2006a), where constitutive laws are given by closed-form laws, both the bulk and discontinuity material behaviours are deduced from fine-scale unit cell computations. Since the bulk is assumed to unload elastically, a material secant stiffness is extracted from the unit cell in which structural localisation has just been detected by applying an elastic unloading perturbation. The membrane-flexural material behaviour of the embedded discontinuity, described by Equation (6.11) at the coarse scale, must be extracted from the fine-scale description by means of an enhanced upscaling procedure. A further damaging unit cell is used for this purpose, which will be denoted in the sequel as Localising Volume Element (LVE), as shown in Figure 6.4.

The extraction of the coarse-scale embedded discontinuity material response requires the definition of average Kirchhoff-Love generalised strains,  $\mathbf{E}^{\text{LVE}}$  and  $\boldsymbol{\chi}^{\text{LVE}}$ , to be applied on the LVE from both the coarse-scale displacement and rotation jumps; as well as the evaluation of the generalised stresses and the material tangent stiffness of the discontinuity from the results of the LVE computation. To this end, an approximate energy consistency argument is used as illustrated in Figure 6.4 in order to build a relationship between the in-plane displacement and rotation jump vectors across the coarse-scale zero-thickness

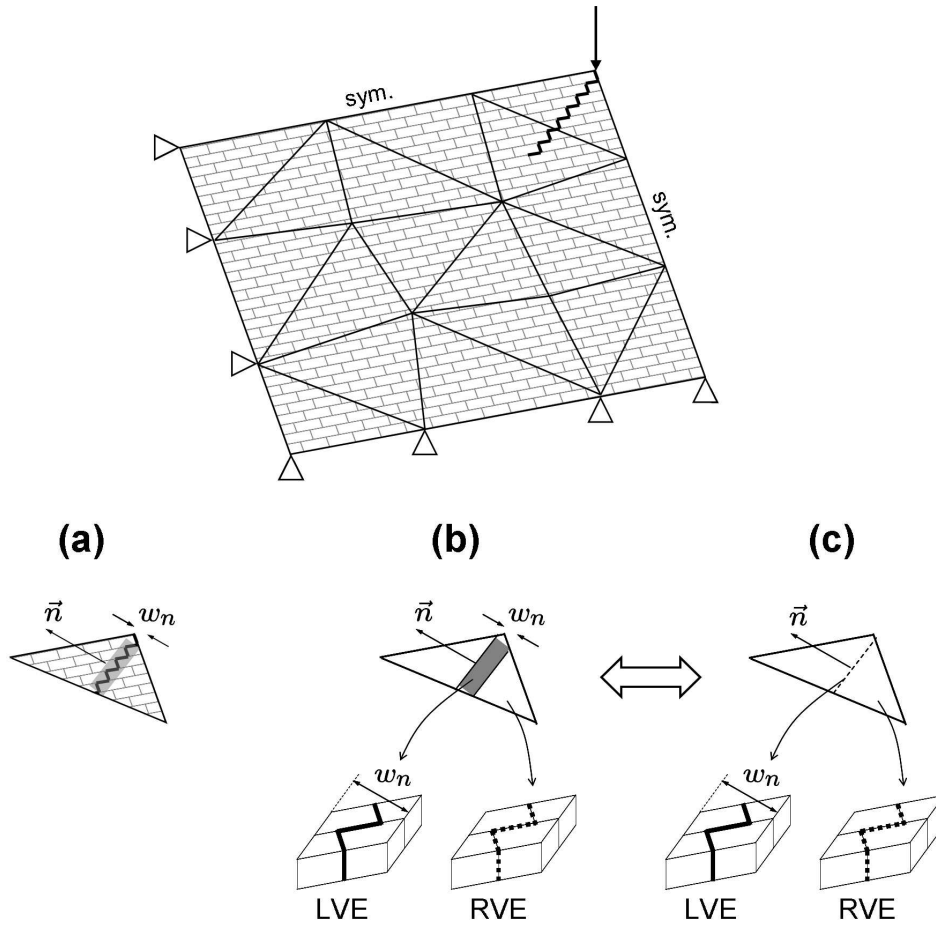


Figure 6.4: Identification of a coarse-scale discontinuity from fine-scale material instabilities. (a) fine-scale damage pattern, (b) identification of a further damaging and localising band and of an unloading surrounding regions, and (c) aggregation toward a strong discontinuity at coarse scale. Comparison of (a) and (b) defines the localising volume, while the energetic consistency originates from the equivalence between (b) and (c)

cohesive zone with an orientation  $\vec{n}$ , and the average Kirchhoff-Love generalised strains applied to a localising region with a finite volume  $w_n$  detected at the fine scale. The localisation width  $w_n$  defining the volume of the localising region has to enter this relationship to take into account in the coarse-scale description the finite fine-scale volume on which the material degradation occurs all other quantities representing energies per unit volume. This introduction of the fine-scale localisation width in the scale transition then allows to objectively upscale the total energy dissipation independently of the coarse-scale discretisation.

The work variation for the idealised band-surrounding representation (Figure 6.4b), in which the localising region behaviour is identified from the LVE and the unloading region behaviour is associated with an unloading RVE, is written as

$$\begin{aligned} \delta W_m = & \int_{\Omega_u} (\mathbf{N}^{\text{RVE}} : \delta \mathbf{E}^{\text{RVE}} + \mathbf{M}^{\text{RVE}} : \delta \boldsymbol{\chi}^{\text{RVE}}) d\Omega_u \\ & + \int_{\Omega_l} (\mathbf{N}^{\text{LVE}} : \delta \mathbf{E}^{\text{LVE}} + \mathbf{M}^{\text{LVE}} : \delta \boldsymbol{\chi}^{\text{LVE}}) d\Omega_l \end{aligned} \quad (6.22)$$

where  $\Omega_l$  and  $\Omega_u$  represent respectively the further loading (damaging) and the unloading

domains ( $\Omega = \Omega_u \cup \Omega_l$  and  $\Omega_u \cap \Omega_l = \emptyset$ ). In the corresponding coarse-scale representation (Figure 6.4c), the localising behaviour is lumped into a zero-thickness cohesive zone and the complete domain  $\Omega$  of the element is assumed to unload according to the behaviour extracted from the RVE. The corresponding work variation reads

$$\begin{aligned} \delta W_M = \int_{\Omega} (\mathbf{N}^{\text{RVE}} : \delta \mathbf{E}^{\text{RVE}} + \mathbf{M}^{\text{RVE}} : \delta \boldsymbol{\chi}^{\text{RVE}}) \, d\Omega \\ + \int_{\Gamma_d} \left( \vec{N}_d \cdot \delta \vec{\xi}_v + \vec{M}_d \cdot \delta \vec{\xi}_\beta \right) \, d\Gamma \end{aligned} \quad (6.23)$$

The prescription of the energy equivalence  $\delta W_m = \delta W_M$  gives

$$\begin{aligned} \int_{\Omega_l} (\mathbf{N}^{\text{LVE}} : \delta \mathbf{E}^{\text{LVE}} + \mathbf{M}^{\text{LVE}} : \delta \boldsymbol{\chi}^{\text{LVE}}) \, d\Omega_l \\ = \int_{\Omega_l} (\mathbf{N}^{\text{RVE}} : \delta \mathbf{E}^{\text{RVE}} + \mathbf{M}^{\text{RVE}} : \delta \boldsymbol{\chi}^{\text{RVE}}) \, d\Omega_l + \int_{\Gamma_d} \left( \vec{N}_d \cdot \delta \vec{\xi}_v + \vec{M}_d \cdot \delta \vec{\xi}_\beta \right) \, d\Gamma \end{aligned} \quad (6.24)$$

Assuming that all the strain and displacement jump variations and stresses present in Equation (6.24) are constant on the domains on which they are integrated (which allows to extract them from the integral sign), the energy equivalence then reads

$$\begin{aligned} (\mathbf{N}^{\text{LVE}} : \delta \mathbf{E}^{\text{LVE}} + \mathbf{M}^{\text{LVE}} : \delta \boldsymbol{\chi}^{\text{LVE}}) \, l \, w_n \\ = (\mathbf{N}^{\text{RVE}} : \delta \mathbf{E}^{\text{RVE}} + \mathbf{M}^{\text{RVE}} : \delta \boldsymbol{\chi}^{\text{RVE}}) \, l \, w_n + \left( \vec{N}_d \cdot \delta \vec{\xi}_v + \vec{M}_d \cdot \delta \vec{\xi}_\beta \right) \, l \end{aligned} \quad (6.25)$$

where  $l$  and  $w_n$  are the length and the width of the localisation band, respectively. Assuming (in an approximate way) that the stress continuity is strongly enforced along the boundary between the localising and unloading domains, and defining the stresses across the coarse-scale discontinuity from the LVE average stresses, one obtains

$$\begin{cases} \vec{N}_d = \mathbf{N}^{\text{LVE}} \cdot \vec{n} = \mathbf{N}^{\text{RVE}} \cdot \vec{n} \\ \vec{M}_d = \mathbf{M}^{\text{LVE}} \cdot \vec{n} = \mathbf{M}^{\text{RVE}} \cdot \vec{n} \end{cases} \quad (6.26)$$

Note that these assumptions lead to an approximate equivalence since the stress continuity is actually enforced in a weak form in the framework. Under these assumptions, the energy equivalence (6.25) may be satisfied by imposing

$$\begin{cases} w_n (\delta \mathbf{E}^{\text{LVE}} - \delta \mathbf{E}^{\text{RVE}}) : \mathbf{N}^{\text{LVE}} = \delta \vec{\xi}_v \cdot (\mathbf{N}^{\text{LVE}} \cdot \vec{n}) \\ w_n (\delta \boldsymbol{\chi}^{\text{LVE}} - \delta \boldsymbol{\chi}^{\text{RVE}}) : \mathbf{M}^{\text{LVE}} = \delta \vec{\xi}_\beta \cdot (\mathbf{M}^{\text{LVE}} \cdot \vec{n}) \end{cases} \quad (6.27)$$

As from the detection criterion presented in Section 6.4, the membrane and curvature strain jump variations associated with the strain discontinuity vectors  $\delta \vec{m}_E$  and  $\delta \vec{m}_\chi$  along a discontinuity line of normal  $\vec{n}$ , see Equation (6.18), is given by

$$\begin{cases} \delta \mathbf{E}^{\text{LVE}} - \delta \mathbf{E}^{\text{RVE}} = \frac{1}{2} (\vec{n} \delta \vec{m}_E + \delta \vec{m}_E \vec{n}) \\ \delta \boldsymbol{\chi}^{\text{LVE}} - \delta \boldsymbol{\chi}^{\text{RVE}} = \frac{1}{2} (\vec{n} \delta \vec{m}_\chi + \delta \vec{m}_\chi \vec{n}) \end{cases} \quad (6.28)$$

Substituting (6.28) into (6.27), the average generalised strains to be applied on the LVE can be related to the coarse-scale displacement and rotation jumps according to

$$\begin{cases} \delta \mathbf{E}^{\text{LVE}} \cdot \vec{n} = \frac{\delta \vec{\xi}_v}{w_n} + \delta \mathbf{E}^{\text{RVE}} \cdot \vec{n} \\ \delta \boldsymbol{\chi}^{\text{LVE}} \cdot \vec{n} = \frac{\delta \vec{\xi}_\beta}{w_n} + \delta \boldsymbol{\chi}^{\text{RVE}} \cdot \vec{n} \end{cases} \quad (6.29)$$

The first term of these relations expresses that the lumped displacement and rotation jumps along the discontinuity at the coarse scale should incorporate a measure of the fine-scale finite volume on which damage occurs,  $w_n$  in this case (the length of localisation enters the framework with the integration along the discontinuity in (6.25)). Note that this localisation bandwidth can vary with the failure mode observed at the fine scale depending on the fine-scale texture of the material. Here it will be taken equal to the size of a unit cell in the direction of the normal to the detected localisation orientation. This carries the implicit assumption that localisation occurs with single period cracks, which might not hold for more complex cracking modes spreading over several periods of the fine-scale structure of the material. The second term of relation (6.29) accounts for the fact that the RVE unloading is attributed to the complete volume of the element at the coarse scale. A part of the material inside the LVE is indeed also unloading upon localisation, but this effect is already incorporated in the averaging operation on the LVE. This second term allows not to take this contribution twice in the energy consistency argument, under the assumption that the unloading material inside the localising band reacts as the identified surrounding material (i.e. with a secant unloading from the bifurcation point). Since the contribution of this second term is usually small, and for the sake of simplicity, it will be neglected in the sequel. As a result, using Equation (6.28), the generalised strains to be applied on the LVE can be expressed by

$$\begin{cases} \delta \mathbf{E}^{\text{LVE}} = \frac{1}{2w_n} \left( \vec{n} \delta \vec{\xi}_v + \delta \vec{\xi}_v \vec{n} \right) \\ \delta \boldsymbol{\chi}^{\text{LVE}} = \frac{1}{2w_n} \left( \vec{n} \delta \vec{\xi}_\beta + \delta \vec{\xi}_\beta \vec{n} \right) \end{cases} \quad (6.30)$$

Note that this approximation is theoretically valid for cases in which the localisation bandwidth is indeed negligible with respect to the dimensions of the coarse-scale elements.

The material response of the coarse-scale embedded discontinuity is obtained by the projection of the homogenised material response of the LVE. The membrane force vector  $\vec{N}_d$  and the bending moment vector  $\vec{M}_d$  across the discontinuity are given by the first equalities of Equation (6.26). Introducing Equation (6.30) in the homogenised membrane and flexural constitutive relations (6.4) for the LVE and using Equation (6.26), the four discontinuity tangent stiffness tensors  $\mathbf{C}_{ab}^d$  (with  $a, b = [m, f]$ ) are deduced from the four homogenised tangent stiffness tensors of the LVE,  $\mathbf{L}_{ab}$  (with  $a, b = [m, f]$ ), and read

$$\begin{bmatrix} \mathfrak{C}_{mm}^d & \mathfrak{C}_{mf}^d \\ \mathfrak{C}_{fm}^d & \mathfrak{C}_{ff}^d \end{bmatrix} = \frac{1}{w_n} \begin{bmatrix} (\vec{n} \cdot \mathbf{L}_{mm}^{\text{LVE}} \cdot \vec{n}) & (\vec{n} \cdot \mathbf{L}_{mf}^{\text{LVE}} \cdot \vec{n}) \\ (\vec{n} \cdot \mathbf{L}_{fm}^{\text{LVE}} \cdot \vec{n}) & (\vec{n} \cdot \mathbf{L}_{ff}^{\text{LVE}} \cdot \vec{n}) \end{bmatrix} \quad (6.31)$$

where the localisation bandwidth  $w_n$  allows to keep the energy consistency.

The complete two-scale nested procedure with localisation enhancement is depicted in Figure 6.5. The orientation of the discontinuities after their introduction is not fixed and can be updated in order to avoid stress locking, as mentioned in Section 6.2.2 and motivated in Section 6.4. This rotation is however limited to a fixed maximum value at each step, in order to avoid convergence difficulties linked to sudden and strong rotations which may occur as a result of locally non proportional loading and of fine-scale preferential degradation orientation.

### 6.5.2 Computational aspect

Since the use of embedded discontinuities does not ensure the crack path continuity across the element boundaries, shell discontinuity modes such as the transverse deflection

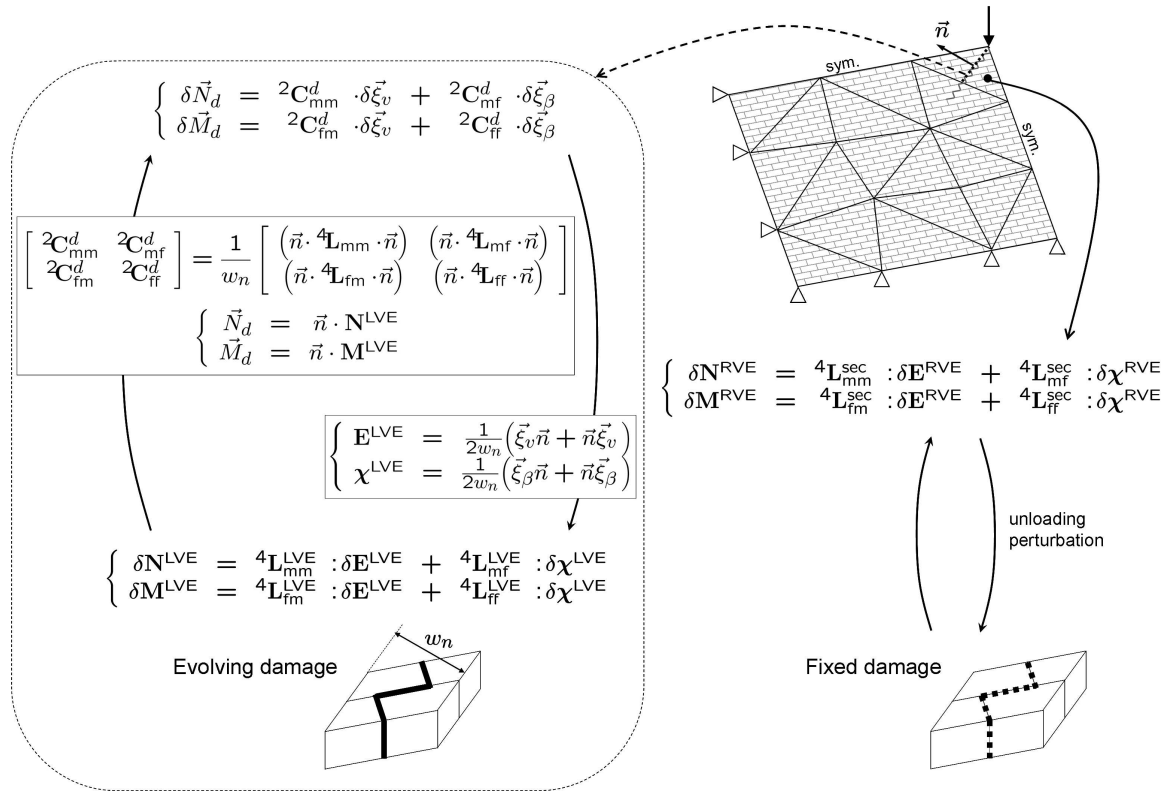


Figure 6.5: Complete localisation-enhanced nested scheme.

opening may be needed locally to avoid stress locking whereas they do not occur globally. For instance, a pure flexural crack may require non-physical transverse deflection openings to be properly open if the embedded discontinuities are misaligned with the global crack, as shown in Figure 6.6. The latter situation can occur since the crack path is not continuous and the discontinuities are introduced at the geometrical centre of the elements. Due to this misalignment, transverse forces temporarily occur during the global opening and vanish in a fully softened state by allowing transverse deflection openings. This further motivates the use of the Reissner-Mindlin kinematics as a generality even if only pure flexural failure is considered.

A multi-scale approach is proposed here to deduce the structural material law of both the embedded discontinuity (6.11) and the bulk (before and after localisation) from the fine-scale behaviour by means of a computational homogenisation procedure, while the proposed homogenisation approach is restricted to the case of thin shells neglecting non-linear transverse shear effects, see Mistler et al. (2007), Mercatoris et al. (2009). Since no

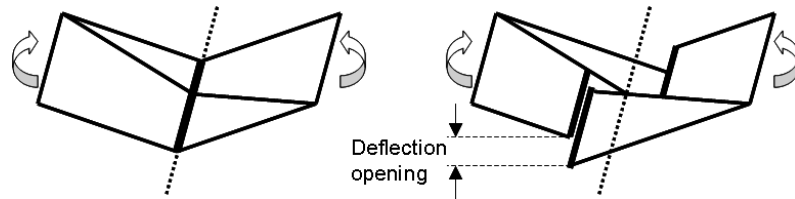


Figure 6.6: Pure flexural crack in two triangle elements: (left) embedded strong discontinuities aligned with the global crack and (right) embedded strong discontinuities misaligned with the global crack requiring transverse deflection openings.

transverse shear behaviour can be obtained from this upscaling procedure, a closed-form assumption should be introduced at the structural scale for this part of the behaviour. To avoid any locking due to a transverse deflection discontinuity, inconsistent with the thin shell upscaling assumption, an exponential decay of the shear force is assumed as a function of the deflection discontinuity. The initial behaviour of the discontinuity is assumed initially rigid with respect to shear, with a dummy stiffness  $d_w$ . The decreasing exponential relation used to properly reduce the spurious transverse shear force appearing due to the flexural failure mechanism reads

$$T_d = \frac{T_d^0}{\kappa} \left( \alpha + (1 - \alpha) e^{-\frac{|T_d^0|\kappa}{h_w}} \right) |\xi_w| \quad \text{for } \kappa \geq \frac{|T_d^0|}{d_w} \quad (6.32)$$

where  $T_d^0$  is the value of the transverse shear force projected on the discontinuity at the onset of localisation (i.e. at the discontinuity introduction), and  $\kappa$  is a history parameter equal to the highest value of  $|\xi_w|$  reached. The parameter  $\alpha$  is introduced in order to keep a minimal level of stress across the transverse discontinuity to avoid singularities and the parameter  $h_w$  determines how rapidly the transverse shear stiffness decays with the transverse deflection opening. Note that the parameter  $h_w$  could be interpreted as a fracture energy, the value of which should be significantly small in order that the total energy dissipated in the transverse deflection opening is negligible with respect to the physical energy dissipation of flexural failure. Note also that the parameters  $d_w$ ,  $\alpha$  and  $h_w$  will be calibrated in the sequel to obtain a proper convergence of the structural resolution scheme.

## 6.6 Comparison of the coupled two-scale scheme results with direct fine-scale simulations

In order to assess the capabilities of the proposed approach, the two-scale framework results are compared to three-dimensional fine-scale modelling results used as a reference for the case of quasi-brittle textured materials such as masonry. This comparison is performed here for two cases of out-of-plane loading of masonry shells leading to propagating flexural failure. A non-uniform four-point bending loading of a planar masonry shell resulting in bed joint flexural failure, and a benchmark presenting stair-case flexural failure are considered. The multi-scale results are compared to complete fine-scale simulation results based on the failure mechanisms and on the overall structural response, focusing on the load bearing capacity and the energy dissipation (area under the softening curve). In order to scrutinise the degree of approximation induced by the assumptions of the homogenisation procedure, namely the periodicity and the scale separation principle, the same three-dimensional fine-scale constitutive laws are used for both the full fine-scale and multi-scale computations. These constitutive laws will be presented briefly in the first part of this section for the case of masonry constituents.

In these illustrations of flexural failure, both the use of periodic homogenisation of the LVE and the scale separation assumption are strongly challenged in order to estimate their impact on the structural behaviour. It is recognised that the periodicity assumption remains strongly debatable in the cracking regime. However, the initial periodic texture of the material can be assumed to limit the consequences of this assumption on the energy dissipation because of the preferential weak orientations fixed by the material structure.

Secondly, the scale separation principle does not apply strictly anymore since the size of the tested structures is limited by the cost of the full fine-scale computations and since a relatively refined coarse-scale mesh is necessary to track the cracking propagation. The coarse-scale element size has therefore to be chosen similar to the characteristic length of the unit cell, which is inconsistent with the scale separation principle. Note that the coarse-scale localisation modelling is a priori independent of coarse-scale mesh due to the use of embedded strong discontinuity, see Armero (1999) and Armero and Ehrlich (2006a). However, a band of elements is introduced in the coarse-scale discretisation in order to properly capture the stress concentration and to allow the complete separation of two rows of nodes with propagating embedded discontinuities. This choice is motivated by the fact that the coarse-scale element size can not be smaller than the RVE size preventing from using a finer unstructured discretisation at the coarse scale.

The choice of applying this two-scale framework to the masonry material can be motivated by the fact that the damaging behaviour observed at the fine scale is straightforward to model phenomenologically, see Section 6.6.1, since the cracking zones are a priori known and coarse meshes are sufficient to discretise the RVE. In addition, the masonry shell failure can be detected by using homogenisation as shown in Mercatoris et al. (2009). The use of a multi-scale approach for masonry can also be motivated by the complexity of formulating macroscopic closed-form constitutive laws for such a composite.

Note that the results obtained for an in-plane case in Mercatoris and Massart (2009) can be reproduced with this framework by modifying the membrane-flexural couplings in order to represent a plane stress state.

Finally, it is noted that the proposed two-scale approach is well suited for parallel computations since all the cell responses may be computed independently at each iteration of the structural incremental iterative scheme. Such an implementation was used here using MATLAB MPI to overcome the high computational cost encountered for such non-linear multi-scale computations, see Kepner and Ahalt (2004).

### 6.6.1 Three-dimensional fine-scale constitutive model for masonry cracking

The choice of a simplified fine-scale constitutive setting is motivated here for both modelling approaches in order to focus on the homogenisation procedure, and as this allows one to get an affordable computational cost. The proposed two-scale approach is compared to a complete fine-scale model for the case of masonry composed of bricks and mortar joints. Since the mortar joints are much weaker than the bricks, the failure behaviour of the latter is not considered and the bricks are assumed elastic in this study for the sake of simplicity. The combined behaviour of the brick-joint interface and of the mortar is modelled by an initially elastic interface element, for which both the normal and tangential stiffnesses ( $k_n$ ,  $k_t$ ,  $k_s$ ) can be related to the elastic behaviour of mortar, see Lourenço and Rots (1997). The tangential stiffnesses are assumed here to be equal ( $k_t = k_s$ ) but could be considered different as well. Depending on the loading mode, either a classical Mohr-Coulomb-type strength criterion or a tension cutoff is used, see Figure 6.7. The parameter  $f_t$  is the tensile mode I strength of the mortar or mortar-brick interfaces, while  $c$  is the cohesion and  $\varphi$  is the friction angle of the mortar joints. For the sake of simplicity and in order to facilitate the computational convergence, an infinite compression strength is assumed.

A three-dimensional scalar damage model with an exponential evolution law is consid-

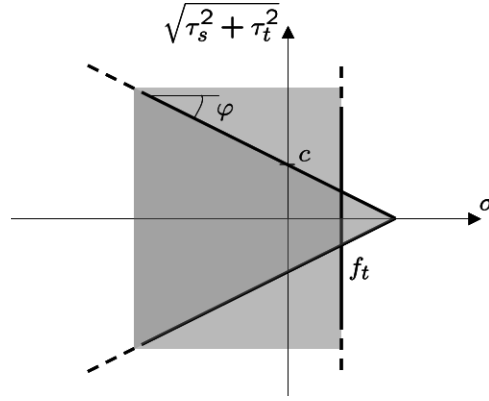


Figure 6.7: Mohr-Coulomb criterion and tensile cutoff for the mortar joint/mortar-brick interface at the fine scale.

ered. The traction-separation law, which links the traction vector  $\vec{t}$  across the interface to the relative displacement vector  $\vec{\delta}$ , is given by

$$\vec{t} = (1 - D) \mathbf{H} \cdot \vec{\delta} \tag{6.33}$$

where  $D$  is the scalar damage variable growing from zero (virgin material) to one (complete failure) and  $\mathbf{H}$  is a three-dimensional elastic stiffness (second order tensor) which depends on the elastic stiffnesses  $k_n$  and  $k_t$ . Note that (6.33) implies that no stiffness recovery is taken into account upon crack closure.

The damage evolution law of the mortar joint is given by

$$D(\kappa) = 1 - \frac{f_t}{k_n \kappa} e^{-\frac{f_t}{G_f} (\kappa - \frac{f_t}{k_n})} \quad \text{for } \kappa \geq \frac{f_t}{k_n} \tag{6.34}$$

where  $G_f$  is the mode I tensile fracture energy. Since the considered interface is three-dimensional and since the damage criterion has to take into account the different behaviours in tension and compression, the damage-driving parameter  $\kappa$  is taken as the most critical value of an equivalent relative displacement defined by

$$\delta_{eq} = \max \left\{ \begin{array}{l} \frac{f_t}{c} \tan \varphi \delta_n + \frac{f_t}{c} \frac{k_t}{k_n} \sqrt{\delta_s^2 + \delta_t^2} \\ \delta_n \end{array} \right\} \tag{6.35}$$

where  $\delta_n$  and  $\sqrt{\delta_s^2 + \delta_t^2}$  are the normal and tangential relative displacements, respectively. Note that relations (6.33) to (6.35) were postulated for the sake of simplicity and to focus on the subject of the Chapter, i.e. the formulation and assessment of the shell type scale transition procedure. More complex mortar formulations including different damage evolutions in mode I and mode II in terms of energy dissipation, see Lourenço and Rots (1997), or incorporating plastic dilatancy, see van Zijl (2004), could be used as well. A brick damage model could also be used for instance in order to extend the detection procedure to additional failure modes involving brick failure, see Lourenço and Rots (1997), Massart et al. (2005b) for the case of in-plane problems.

### 6.6.2 Bed joint flexural failure in out-of-plane loaded masonry shell

For the first illustration, a rectangular planar masonry shell in which the bed joints and head-joints are parallel to the shell edges is subjected to a non-uniform four-point bending loading, as shown in Figure 6.8. The masonry shell of dimensions  $480 \times 960 \times 98 \text{ mm}^3$  is simply supported in the out-of-plane direction along the two small edges parallel to the bed joints, and a transverse deflection is prescribed at two points of one of the free edges in order to allow cracking to propagate along the bed joints from one free edge to the other, see Figure 6.8. The in-plane rigid body displacements are precluded by the boundary conditions. The loading is non uniformly distributed on the width of the shell to test the proper crack propagation by the method. The bricks dimensions are  $120 \times 60 \times 98 \text{ mm}^3$ .

For the multi-scale computation, the masonry wall is discretised at the coarse scale by using three-noded Reissner-Mindlin shell finite elements with one Gauss integration point. The DST formulation adapted to material non-linearities as presented in Section 6.2.1 is used in order to avoid transverse shear locking. The coarse-scale mesh consists of 70 shell elements and of 240 degrees of freedom (excluding the jump parameters condensed at the element level). The unit cell computations use a rather coarse discretisation made of volume and interface elements with quadratic interpolation. For the complete fine-scale computation, the bricks are discretised using twenty-noded quadratic volume finite elements with  $3 \times 3 \times 3$  Gauss integration points. The mortar joints are represented by sixteen-noded quadratic interface finite elements with  $3 \times 3$  Lobatto quadrature points. Each brick is discretised using  $4 \times 2$  elements in the in-plane direction and 6 elements in the thickness direction, resulting in a full fine-scale model consisting of 68,280 dofs. A view of meshes used for the different levels of descriptions are sketched in Figures 6.10 and 6.11 for the mortar interfaces.

The material parameters used for this loading case are defined at the fine scale for both approaches, see Section 6.6.1. Since the mortar joints are not loaded in mode II in this case, only the tensile cutoff is activated in the damage criterion. The values considered for the material parameters are reported in Table 6.1.

The load-displacement response of the masonry shell is depicted in Figure 6.9 for both the multi-scale and the complete fine-scale model. The multi-scale simulation approximates correctly the overall response as could be expected for this simple loading case. The load bearing capacity of the wall obtained by the multi-scale simulation overestimates by only 0.5% the complete fine-scale solution. The most significant difference between both results, which however remains acceptable, is the slightly more brittle behaviour of the

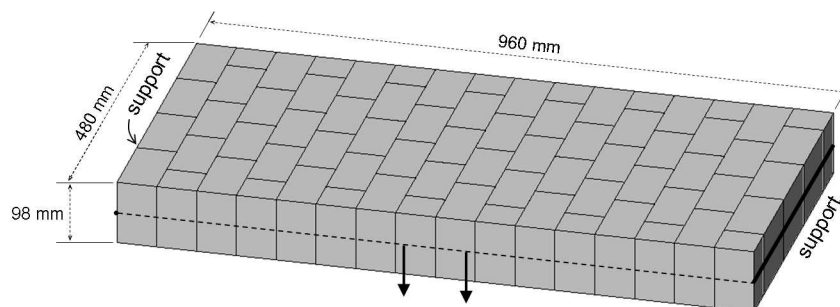


Figure 6.8: Non-uniform four-point bending loading leading to bed joint flexural failure of masonry shell.

Table 6.1: Out-of-plane loaded masonry wall leading to bed joint flexural failure. Brick (a) and mortar/mortar-brick interface (b) material parameters, see Lourenço (1996).

	$E$ (MPa)	$\nu$	$k_n$ ( $\frac{\text{MPa}}{\text{mm}}$ )	$k_t$ ( $\frac{\text{MPa}}{\text{mm}}$ )	$f_t$ (MPa)	$G_f$ ( $\frac{\text{mJ}}{\text{mm}^2}$ )	$c$ (MPa)	$\varphi$ ( $^\circ$ )
(a)	16700	0.15	-	-	-	-	-	-
(b)	-	-	438	182	0.2	0.005	-	-

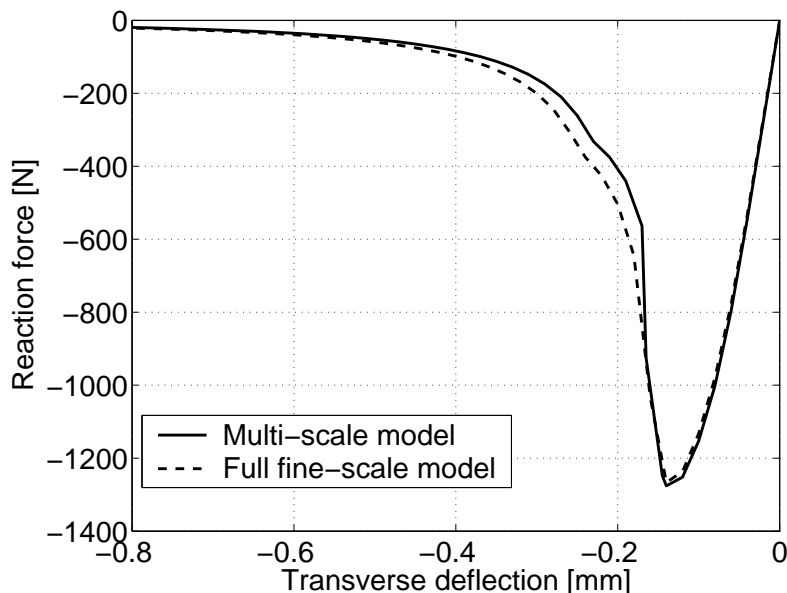


Figure 6.9: Non-uniform four-point bending loading of masonry wall leading to bed joint flexural failure. Comparison of the load-displacement responses for full fine-scale modelling (dashed line) and multi-scale simulation (solid line).

multi-scale response in the softening regime.

Figure 6.10 depicts the deformed configuration and the damage state at the structural response peak. The propagation of the bed joint crack up to the half width of the shell is well reproduced by the multi-scale simulation with an orientation of the coarse-scale discontinuities consistent with the bed joint damage pattern. Note that material bifurcation and coarse-scale discontinuity are detected once damage spreads over half of the bed joint, i.e. the level of crack propagation in the coarse-scale description (up right) is consistent with the full fine-scale damage map (bottom left), see also Mercatoris et al. (2009) for a further discussion about the detection criterion. A good agreement is observed between both solutions for the propagating crack in terms of bed joint opening and damage state, see unit cells 1, 2 and 3 in Figure 6.10. Particularly, the membrane opening at the free edge is equal to 0.00454 mm in the LVE cell of the multi-scale solution and to 0.00554 mm in the full fine-scale solution.

At the end of the softening regime, a fully opened traction-free crack can be observed in Figure 6.11. Both the multi-scale and the complete fine-scale solutions are again in good agreement. The bed joint opening and the fully damaged bed joint pattern are well reproduced by the structural crack in the multi-scale simulation, see unit cell (1) in Figure 6.11. Although the bulk is completely unloaded, the non-localised damage state of bed joints in the bulk region near the crack also reproduces well the fine-scale simulation results, see unit cell (2) in Figure 6.11. Further from the localisation zone, the mortar

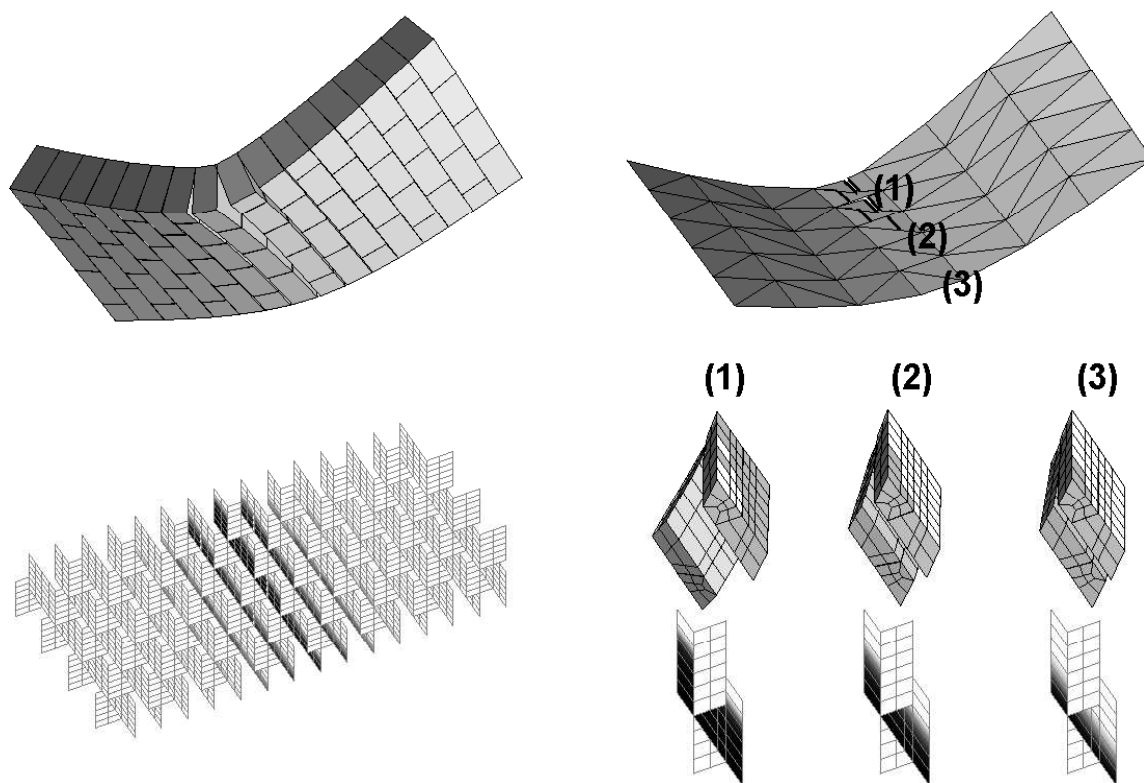


Figure 6.10: Deformed configuration and damage maps at the structural peak load of the non-uniform four-point bending response: (upper left) deformed configuration of the complete fine-scale simulation, (lower left) damage maps of the complete fine-scale simulation (black patches indicate fully damaged joints and gray patches indicate partially damaged joints), (upper right) deformed configuration of the multi-scale simulation with the coarse-scale discontinuities and (lower right) related deformed configuration and damage state of unit cells. The displacements of the deformed configurations are magnified by a factor 2000.

joints remain undamaged and the mesostructure is completely unloaded, see unit cell (3) in Figure 6.11. In addition to coarse-scale rotation jumps in the multi-scale solution, in-plane displacement jumps are obtained along the crack path. These membrane openings result from membrane-flexural couplings which are present for masonry flexural behaviour due to the different tensile and compressive behaviour of mortar joint. The membrane opening at the free edge is equal to 0.182 mm in the multi-scale solution and to 0.179 mm in the full fine-scale solution, which still shows a good agreement between the both models.

Note that, because the crack path is discontinuous across the element boundaries and the coarse-scale discontinuities are not aligned with the global crack, see Figure 6.6, transverse deflection openings need to occur in order to avoid stress locking as aforementioned in Section 6.5.2. The behaviour of this transverse discontinuity is modelled with an exponentially decreasing shearing force and allows one to properly decrease the transverse shear force and open the flexural failure mechanism, since the energy dissipated in this transverse opening has to be negligible with respect to the flexural energy dissipation.

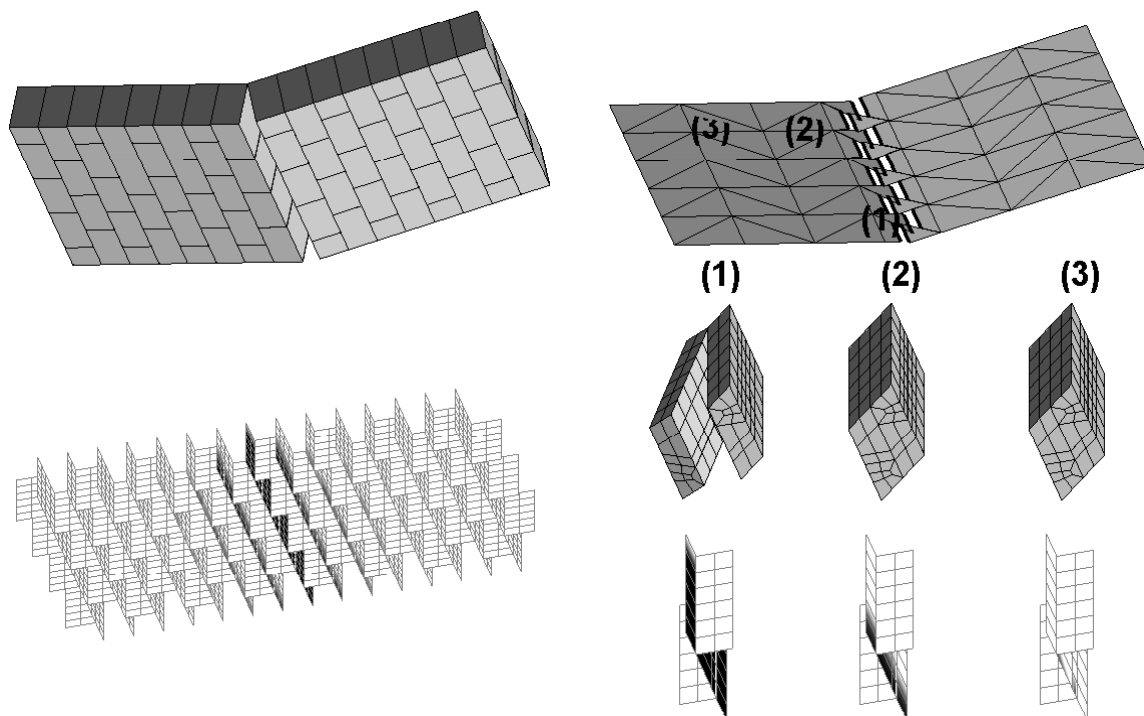


Figure 6.11: Deformed configuration and damage maps at the end of the softening tail of the non-uniform four-point bending response: (upper left) deformed configuration of the complete fine-scale simulation, (lower left) damage maps of the complete fine-scale simulation (black patches indicate fully damaged joints and gray patches indicate partially damaged joints), (upper right) deformed configuration of the multi-scale simulation with the coarse-scale discontinuities and (lower right) related deformed configuration and damage state of unit cells. The displacements of the deformed configurations are magnified by a factor 100.

### 6.6.3 Stair-case flexural failure in out-of-plane loaded masonry shell

As a second illustrative application, the analysis of an out-of-plane loaded planar masonry shell presenting a stair-case flexural failure mode is considered. The tested geometry is depicted in Figure 6.12. It consists of a square shell of dimensions  $1920 \times 1920 \text{ mm}^2$  with a thickness of 98 mm and with bricks of dimensions  $120 \times 60 \times 98 \text{ mm}^3$  stacked according to a running bond pattern. The aspect ratio of the bricks therefore prescribes a fine-scale preferential stair-case crack pattern orientation of 45 degrees corresponding to the orientation of the shell diagonal. The square shell is simply supported on its four edges in the thickness direction and subjected to a transverse deflection at its centre. The edges are not constrained in the in-plane directions leading to membrane openings occurring due to the membrane-flexural couplings. According to experimental results obtained elsewhere, this benchmark leads to four stair-case bending cracks initiating at the shell centre and propagating towards the shell corners along the diagonals of the wall, see Dallot et al. (2008) for the case of masonry-like structures. Note that, this failure mechanism only occurs when the orientations of both the stair-case pattern and the diagonal are consistent, which is the case in the present benchmark. Due to symmetry of the masonry shell, the loading and the crack pattern of only a quarter of the shell is considered. Furthermore,

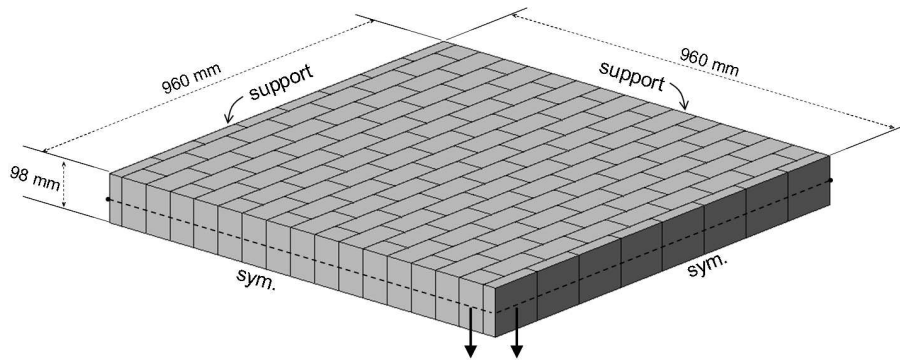


Figure 6.12: Out-of-plane loading of masonry wall leading to stair-case flexural failure. Due to the symmetry, a quarter of the wall is considered.

Table 6.2: Out-of-plane loaded masonry wall leading to stair-case flexural failure. Brick (a) and mortar/mortar-brick interface (b) material parameters, see Lourenço (1996). The tensile strength  $f_t$  is deduced from the Mohr-Coulomb criterion.

	$E$ (MPa)	$\nu$	$k_n$ ( $\frac{\text{MPa}}{\text{mm}}$ )	$k_t$ ( $\frac{\text{MPa}}{\text{mm}}$ )	$f_t$ (MPa)	$G_f$ ( $\frac{\text{mJ}}{\text{mm}^2}$ )	$c$ (MPa)	$\varphi$ ( $^\circ$ )
(a)	16700	0.15	-	-	-	-	-	-
(b)	-	-	438	182	-	0.02	0.28	36

the prescribed centred transverse deflection is not localised at one point but is applied at the two nodes close to the centre, see Figure 6.12. This ‘smeared’ loading allows to avoid too high stress concentrations at the shell centre leading potentially to non-expected failure modes in the corner element as the centre node is kept free to properly represent the discontinuity.

The shell discretisation contains 186 DST shell elements with 112 nodal degrees of freedom. An element band is still introduced along the expected localisation zone at the coarse scale for a better tracking of the cracking front propagation (even though this band does not consist in a finer mesh). The fine-scale wall and the unit cells are discretised in the same way as in the previous studied case, see Section 6.6.2, except that 4 volume elements are used in the thickness direction for both the fine-scale and unit cell discretisations. The full fine-scale model then consists of 97443 dofs.

The values of the material parameters used at the fine scale for both approaches are reported in Table 6.2. Note that only the Mohr-Coulomb criterion is activated in this case in order to facilitate the computations. Furthermore, the fracture energy of mortar joints is increased with respect to realistic values in order to avoid any mesostructural snap-backs, see Massart et al. (2005b).

The overall load-displacement response of the multi-scale computation is compared to the complete fine-scale solution in Figure 6.13. It is shown that the multi-scale model gives a good estimation of the loading part of the response curve as well as of the load bearing capacity of the wall. The energy dissipation is however underestimated by the multi-scale model leading to a more brittle behaviour in the softening regime with respect to the complete fine-scale simulation. Part of this discrepancy might originate from the periodicity conditions applied on the LVE, leading to an over stiff and more brittle response. This could also be partially attributed to the fact that the structural dimensions are not sufficiently large with respect to the cell dimensions (scale separation), combined to the

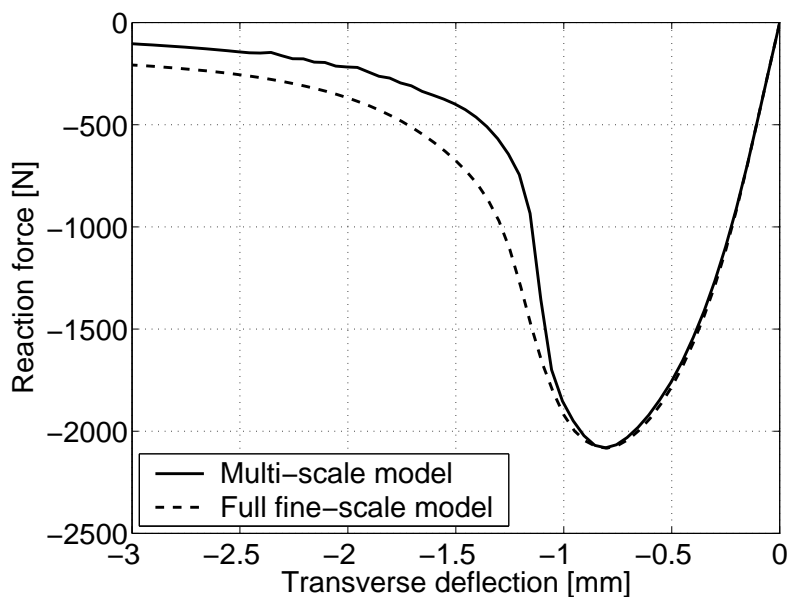


Figure 6.13: Out-of-plane loading of masonry wall leading to stair-case flexural failure. Comparison of the load-displacement responses for full fine-scale modelling (dashed line) and multi-scale simulation (solid line).

neglected second term in relation (6.29). This last effect would in any case decrease in computations related to larger structures. Nevertheless, a fair agreement is found between both approaches.

The deformed configuration and the damage state at the response peak are presented in Figure 6.14 for both the multi-scale and the complete fine-scale models. The coarse-scale discontinuities propagation in the multi-scale solution is in good agreement with the stair-case crack propagation predicted by the full fine-scale computation (top figures in Figure 6.14). As in the previous case of bed joint flexural failure, the structural response peak corresponds to a propagated crack up to the half of the diagonal at the coarse scale. The damage state of mortar joints is well reproduced by the multi-scale computation with respect to the full fine-scale solution. At the centre of the wall ahead of the cracking front, all the joints are partially damaged but the stair-case pattern is clearly more damaged than the bed joint pattern, see unit cell (1) in Figure 6.14. The deformed configuration of the unit cell (1) also shows the corresponding stair-case opening. At the cracking front, half of the stair-case joint is damaged, corresponding to the level at which structural localisation is detected, and the corresponding stair-case mode starts to open, see unit cell (2) in Figure 6.14. At the corner of the wall, the damage state is still diffuse and starts in the upper and lower parts of the bed joint as shown in unit cell (3) in Figure 6.14. Furthermore, the mesostructure-informed orientation of each embedded discontinuity evolves during propagation due to evolving damage, but tends to the average orientation of the stair-case pattern, see Mercatoris et al. (2009). As can be seen in Figure 6.14, the discontinuities near the cracking front are indeed not parallel to the diagonal, while the orientation of the previously triggered discontinuities is consistent with the unit cell stair-case damage patterns and the full fine-scale simulation, which motivates the use of rotating embedded discontinuities.

Figure 6.15 presents the deformed configuration and the damage state at the end of the softening tail for both multi-scale and complete fine-scale solutions. A fully open stair-case

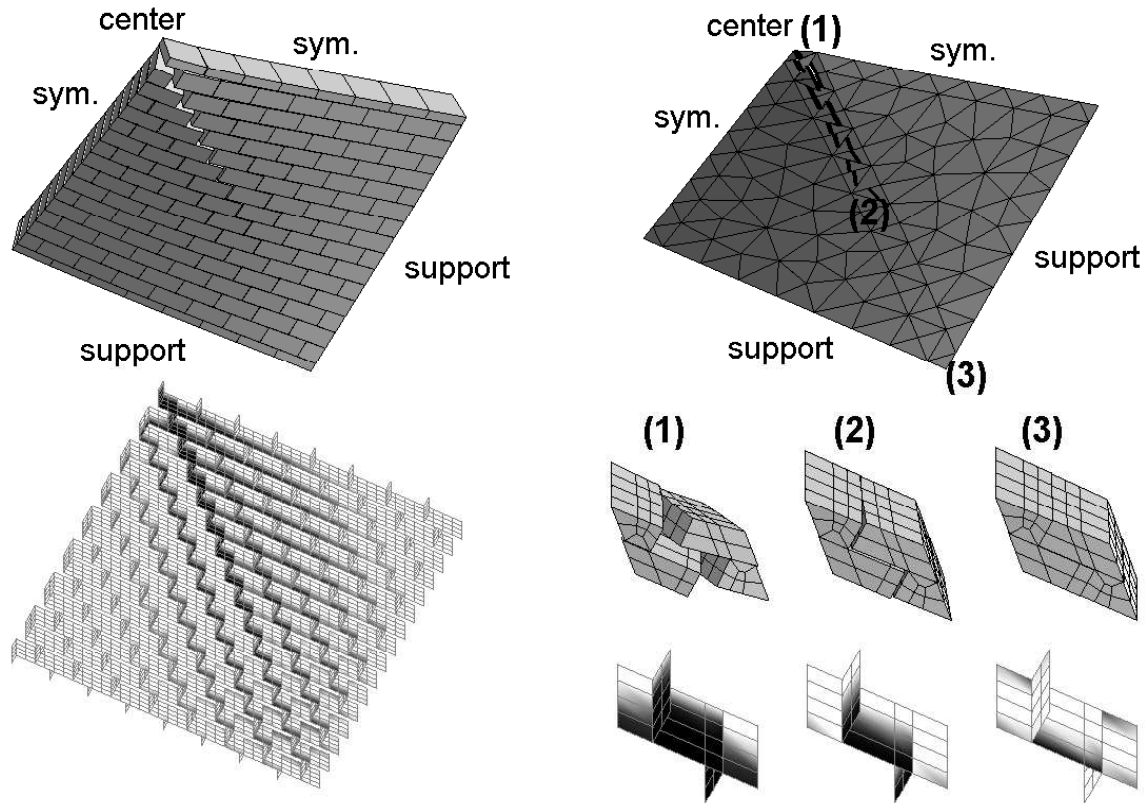


Figure 6.14: Deformed configuration and damage maps at the peak load of the out-of-plane loading of the diagonally stair-case cracked masonry wall: (upper left) deformed configuration of the complete fine-scale simulation, (lower left) damage maps of the complete fine-scale simulation (black patches indicate fully damaged joints and gray patches indicate partially damaged joints), (upper right) deformed configuration of the multi-scale simulation with the coarse-scale discontinuities and (lower right) related deformed configuration and damage state of unit cells. The displacements of the deformed configurations are magnified by a factor 500.

flexural crack is obtained between the centre and the corner of the wall. The orientation of all the discontinuities is consistent with the unit cell stair-case damage pattern and the full fine-scale solution, see unit cell (1) in Figure 6.15. The deformed configuration of a quarter of the fully softened wall geometrically corresponds to two planar triangles linked by a hinge line. Although the bulk is completely unloaded, mortar joints are partially damaged due to the degradation preceding the localisation phenomenon, see the damage map of the fine-scale solution in Figure 6.15. This damage state is also well reproduced by the multi-scale model as shown by unit cells (2) and (3) in Figure 6.15 where, respectively, the bed joint pattern and the stair-case pattern are partially damaged. The bed joint pattern damage is more pronounced in the right part - cell (2) - since the bed joints are continuous while the left part - cell (3) - is less damaged as a result of the non continuity of the head-joints at the fine scale. This non-symmetric non-localised damage pattern is thus clearly consistent between both simulations. A membrane opening is again observed due to the membrane-flexural couplings, and transverse discontinuities are again necessary to avoid the appearance of stress locking since the embedded discontinuity lines are not exactly aligned with the theoretical hinge due to the discretisation.

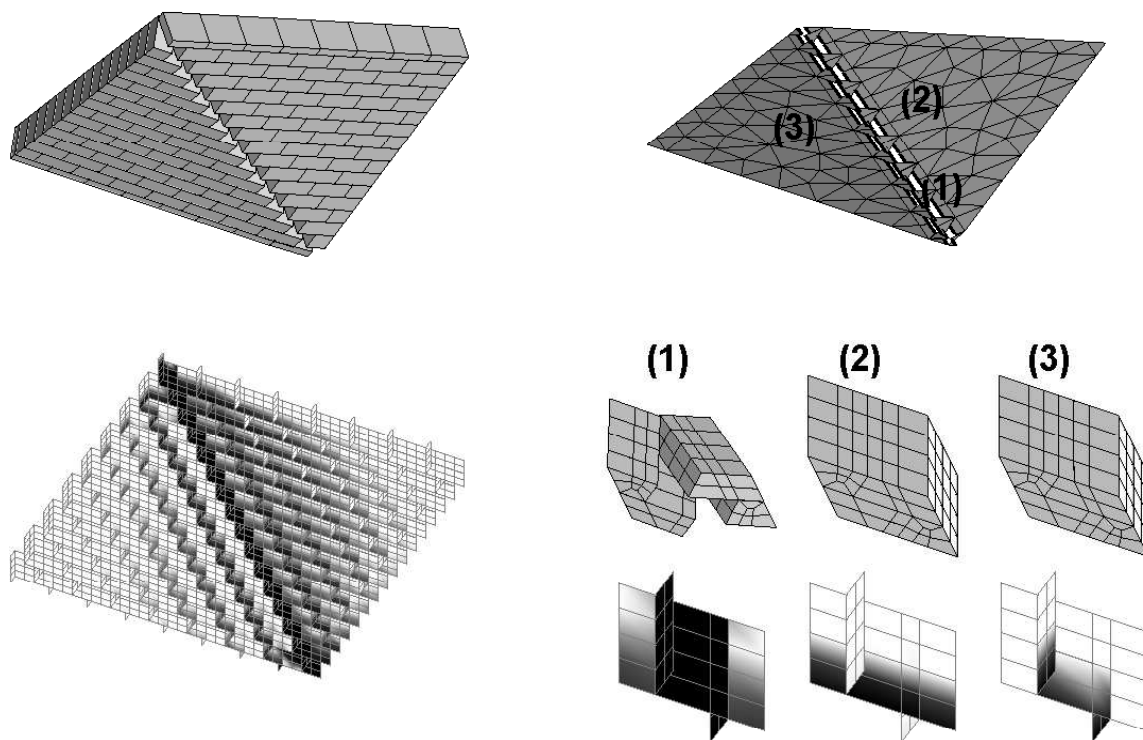


Figure 6.15: Deformed configuration and damage maps at the end of the softening tail of the out-of-plane loading of the diagonally cracked masonry wall: (upper left) deformed configuration of the complete fine-scale simulation, (lower left) damage maps of the complete fine-scale simulation (black patches indicate fully damaged joints and gray patches indicate partially damaged joints), (upper right) deformed configuration of the multi-scale simulation with the coarse-scale discontinuities and (lower right) related deformed configuration and damage state of unit cells. The displacements of all the deformed configurations are magnified by a factor of 100.

### 6.6.4 Discussion

In this Section, some additional computational results are used in order to discuss the limits of applicability and the robustness of the proposed two-scale computational procedure for shell failure. The assumption of single period cracks is first discussed for the case of bed joint flexural failure. The influence of the mesostructural material properties on the structural response, which can easily be accommodated by the proposed framework, is then emphasised.

#### Single period crack assumption

An important limitation of the proposed approach is the fact that only single period cracks can be correctly represented by the multi-scale model from the point of view of energy dissipation since single period unit cells are used at the fine scale. More complex failure mechanisms such as cracks parallel to the head-joints involving brick failure can not therefore be accurately modelled in terms of energy dissipation, even if such situations are less likely to occur in out-of-plane loading. To illustrate this limit of applicability, the previous multi-scale solution discussed in Section 6.6.2 for the case of bed joint flexural failure is compared to a full fine-scale simulation presenting two bed joint cracks instead of one. For this purpose, the same non-uniform four-point bending loading case is considered

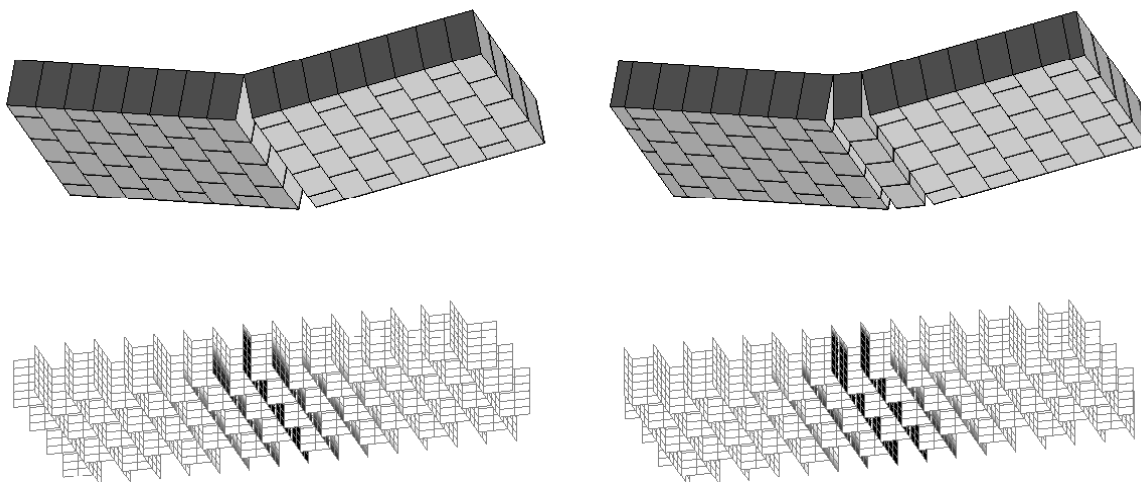


Figure 6.16: Deformed configuration and damage maps of complete fine-scale solution for bed joint flexural failure mechanism: (left) one bed joint cracks and (right) two bed joint cracks.

for a complete fine-scale computation with a shifted brick stacking configuration in order to have two bed joint patterns between the loading points, see Figure 6.16.

The overall response of the full fine-scale computation with two bed joint cracks is depicted in Figure 6.17 and compared to the previous results discussed in Section 6.6.2. Although the load bearing capacity and the fine-scale failure pattern involved in the failure mechanism remain unchanged, the behaviour of the wall incorporating two cracks in the full fine-scale solution is significantly more ductile in the softening regime. This results from the presence of a double bed joint crack which dissipates more energy than the single bed joint crack, a situation which cannot be accommodated by the multi-scale framework proposed here. In order to treat more complex multi-period failure mode, larger RVE could be taken into account but with the added complexity that bifurcation at the fine scale (i.e. within the solution of the mesostructural unit cell boundary value problem) should then be considered to reproduce single crack modes with periodic boundary conditions on the LVE.

### Influence of mesostructural material properties

In order to emphasise the flexibility of the proposed approach, a variation of a material parameter such as the mortar joint fracture energy is considered next. The aim of this illustration is to show that the localised coarse-scale flexural behaviour is correctly upscaled from an energy point of view and driven by the material behaviour of the mesostructure at the scale of which closed-form constitutive laws are postulated. For this purpose, the multi-scale and complete fine-scale computations of the stair-case flexural failure mechanism presented in Section 6.6.3 are performed with higher fracture energy value for the mortar joints. The structural responses of these simulations are depicted in Figure 6.18 and compared with the results discussed in Section 6.6.3. It is shown that the wall with a higher fracture energy ( $G_f = 0.1 \text{ mJ/mm}^2$ ) presents a significantly more ductile behaviour than the wall with a lower fracture energy ( $G_f = 0.02 \text{ mJ/mm}^2$ ). This results in higher energy dissipation and therefore a less localised behaviour at the fine scale, i.e. more diffuse damage zones as shown in Figure 6.19. Figure 6.18 also compares the structural responses of both the multi-scale and full fine-scale models for the higher

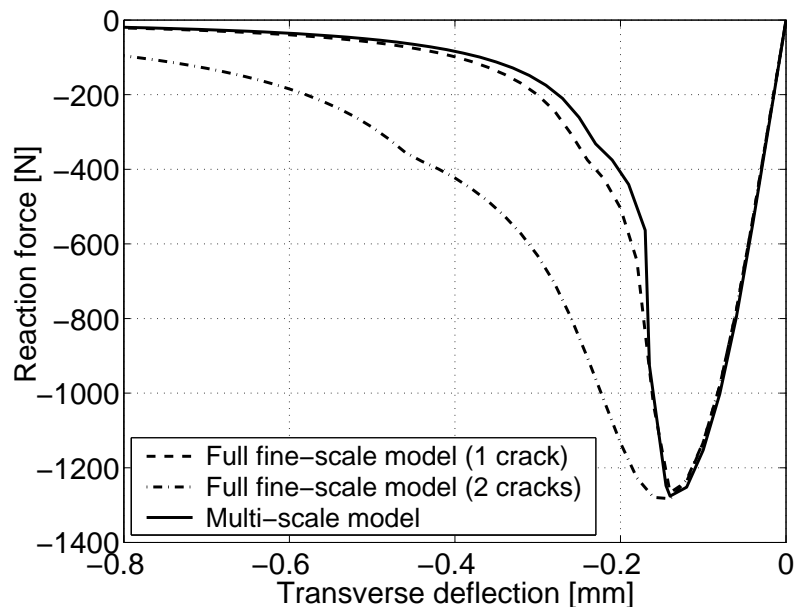


Figure 6.17: Non-uniform four-point bending of masonry wall leading to bed joint flexural failure. Comparison of the load-displacement responses for full fine-scale modelling with one bed joint crack (dashed line), full fine-scale modelling with two bed joint cracks (dash-dot line) and multi-scale simulation (solid line).

mortar fracture energy value. As for the previous case, the loading part of the response and the load bearing capacity are well estimated by the multi-scale approach. The softening behaviour of the multi-scale solution is still more brittle with respect to the complete fine-scale simulation and the deviation seems proportional to the energy dissipation. As already mentioned, this gap is expected to decrease for larger structures for which the scale separation principle is satisfied.

The deformed configuration and the damage state at the end of the softening tail are depicted in Figure 6.19 for the higher fracture energy value. It is shown that the damage zone is more diffuse than for the case of lower mortar fracture energy, see Figure 6.15. Nevertheless, the damage pattern and the stair-case openings are still well reproduced by the multi-scale model, see unit cells (1), (2) and (3) in Figure 6.19.

## 6.7 Conclusions

A new periodic homogenisation-based multi-scale method was proposed for the modelling of quasi-brittle thin shell failure. This method allows to take into account the localised behaviour of a textured material by correctly upscaling the energy dissipation associated to the failure mechanism. This framework was assessed by a comparison to a complete fine-scale model on out-of-plane loaded masonry wall tests including bed joint and stair-case bending cracks. It was shown that the multi-scale solutions were in good agreement with respect to the full fine-scale computation results. Particularly, the failure modes are correctly reproduced by the multi-scale approach in localised and non-localised zones. The limits of applicability and the robustness of the proposed method was discussed. The assumption of single period failure was discussed for a particular case. The influence of the mesostructure, which can easily be accommodated by the proposed frame-

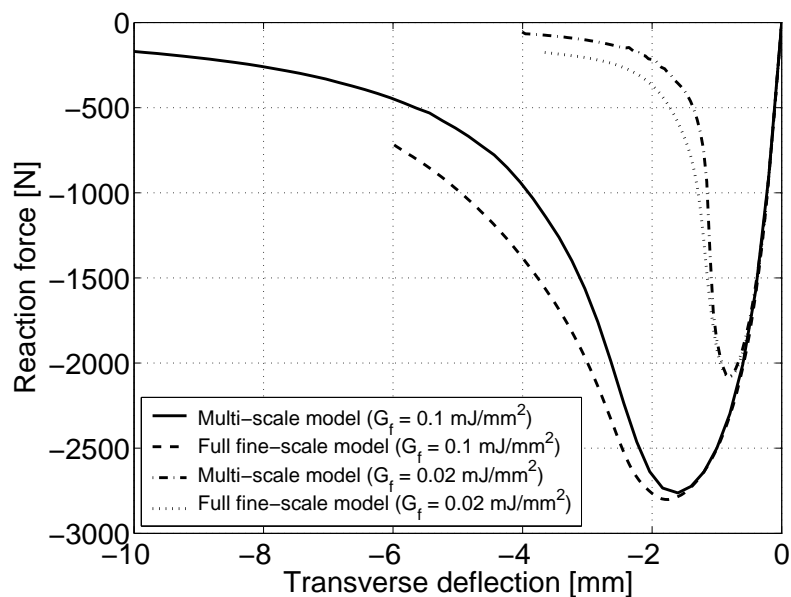


Figure 6.18: Out-of-plane loading of masonry wall leading to stair-case flexural failure. Comparison of the load-displacement responses for full fine-scale modelling (dashed line) and multi-scale simulation (solid line) with a mortar fracture energy value of  $G_f = 0.1 \text{ mJ/mm}^2$ . The load-displacement responses for full fine-scale modelling (dotted line) and multi-scale simulation (dash-dot line) with a mortar fracture energy value of  $G_f = 0.02 \text{ mJ/mm}^2$  are recalled, see Figure 6.13.

work, was emphasised for the case of a material property of a constituent.

The results obtained here suggest that further developments could be useful in order to extend their scope. The proposed multi-scale approach should be extended to the case of thick shells allowing to introduce the transversal shear and the deflection opening in the scale transitions. The concept of crack branching could be incorporated, see Linder and Armero (2009), in order to perform the proposed framework on more complex masonry benchmarks. In order to reduce the computational cost, the multi-scale approach could also be combined with semi-analytical homogenisation (TFA) for shell behaviour, see Sacco (2009) for an in-plane case. Finally, the proposed multi-scale framework could be applied to geometrically more complex masonry structures such as arches, domes and vaults. It could also be interesting to apply this method to other types of heterogeneous shell such as honeycomb-type sandwiches.

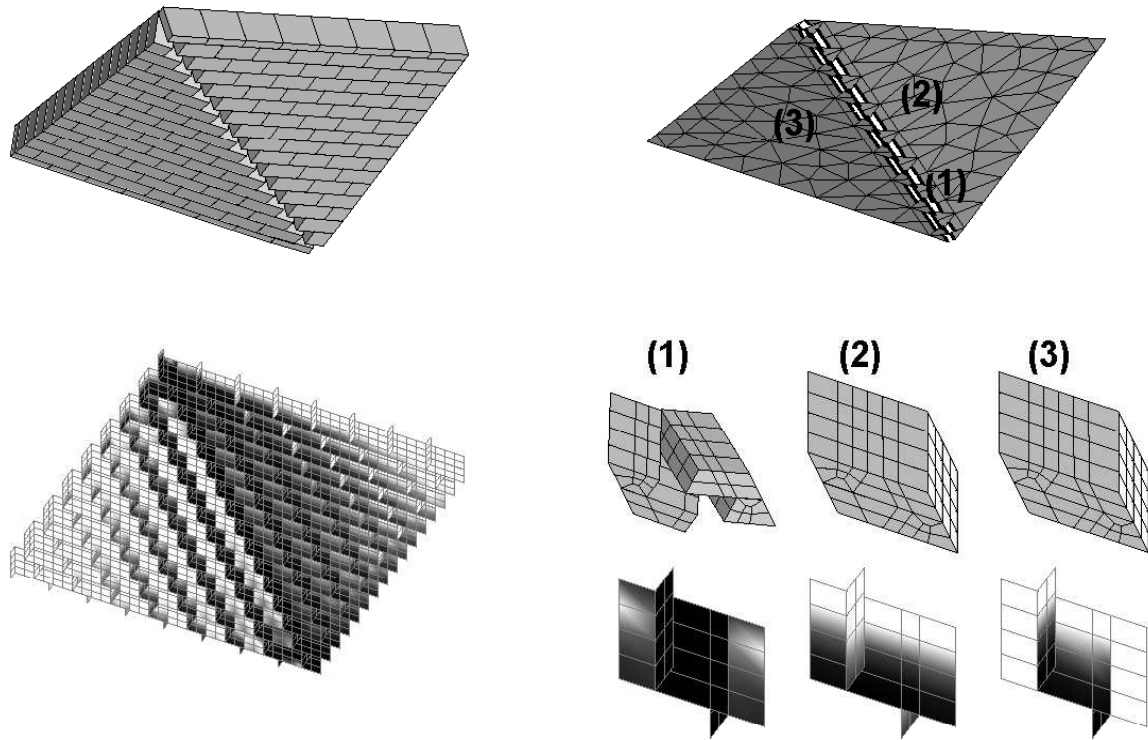


Figure 6.19: Deformed configuration and damage maps at the end of the softening tail of the out-of-plane loading of the diagonally stair-case cracked masonry wall: (upper left) deformed configuration of the complete fine-scale simulation, (lower left) damage maps of the complete fine-scale simulation (black patches indicate fully damaged joints and gray patches indicate partially damaged joints), (upper right) deformed configuration of the multi-scale simulation with the coarse-scale discontinuities and (lower right) related deformed configuration and damage state of unit cells. The displacements of all the deformed configurations are magnified by a factor of 50.

# Chapter 7

## Conclusions and perspectives

The objective of the research reported in this dissertation was the development of a mesostructurally informed computational tool for the representation of structural localised behaviour of planar masonry thin shells. Masonry is a textured periodic heterogeneous material which presents a quasi-brittle behaviour. The typical ordered mesostructure of masonry leads to preferential cracking orientations which are complex to incorporate within closed-form structural descriptions. The appearance of damage-induced anisotropy indeed results in stress redistributions and loading path dependency. As a result, damage localisation can be observed at both the mesoscopic and macroscopic scales. The representation of such a behaviour in structural planar applications is a considerable challenge, not only due to the complexity of formulating macroscopic closed-form constitutive laws, but also due to the difficulty to identify their numerous parameters through costly experimental procedures, to be reproduced for every new mesostructure. In addition, the representation of the flexural behaviour requires even more complex closed-form laws since other aspects of the behaviour such as membrane-flexural couplings have to be taken into consideration.

Multi-scale approaches allow to deal with this complexity by postulating closed-form constitutive laws at the scale of the constituents, for which the parameters are a priori more straightforward to identify. In the context of non-linear behaviour, computational homogenisation furnishes a versatile approach to link fine and structural scales. Based on the periodicity of the mesostructure, a representative volume element (RVE) is defined and modelled using mesoscopic closed-form material laws. The macroscopic material response is extracted in an average sense from the solution of a deformation-driven mesostructural boundary value problem. The complex formulation of closed-form macroscopic constitutive laws are avoided, which allows one to consider complex mesostructures, which may evolve during the loading process. Furthermore, any method may be used to resolve this mesoscopic problem and any closed-form constitutive laws may be postulated for the constituents. This flexibility renders the multi-scale approach particularly attractive for the characterisation of heterogeneous materials.

For the modelling of localised behaviour using a multi-scale approach, the localisation of damage needs to be computationally treated at each scale under consideration. For the case of masonry, a damaging cohesive zone model is used at the mesoscopic scale to represent the behaviour of mortar joints. At the structural scale, displacement discontinuities offer an attractive way to capture localisation since the size of the localisation zone is usually smaller than the RVE size. An embedded strong discontinuity approach adapted for an engineering shell description available from the literature and recalled in

Chapter 3 was selected here for this purpose. This approach allows to represent the collective behaviour of fine-scale cracks using average cohesive zones including mixed cracking modes and incorporating evolving orientations needed to accommodate fine-scale damage evolutions. In the context of multi-scale modelling, both the appearance and the material behaviour of these cohesive zones have to be driven by the mesostructural response. An acoustic tensor-based localisation criterion adapted to thin shell kinematics, combined with a computational homogenisation scheme for out-of-plane behaviour was proposed for the localisation detection of masonry shells in Chapter 4. A localisation analysis was performed on unit cells to show that the structural localisation orientations determined by this criterion are consistent with the preferential fine-scale damage patterns of masonry observed in mesoscopic computations. The robustness of the proposed localisation detection procedure was discussed focusing on the influence of the mesoscopic material properties, the loading modes and the RVE size.

Next, a continuous-discontinuous homogenisation scheme has been developed for quasi-brittle thin shell failure. A periodic non-linear computational homogenisation method is used to capture the local quasi-brittle material behaviour of masonry thin shells. An enhanced upscaling procedure based on an approximate energy consistency has been formulated to extract the material behaviour of the discontinuity, in which the structural localisation behaviour is extracted from a further damaging sample, denoted as Localising Volume Element (LVE). This new methodology was firstly proposed for the case of in-plane loaded structures in Chapter 5. The proposed multi-scale framework was assessed by a comparison with a complete fine-scale model for the case of the confined shearing of a masonry wall with and without an opening in order to estimate the impact of the challenged periodicity and scale separation assumptions. It was shown that the multi-scale solutions are in good agreement with respect to the full fine-scale computation results, provided stress distributions are confined. In spite of an overestimation of the initial stiffness by the periodicity assumption used in the multi-scale modelling, the load bearing capacity and the cracking patterns are correctly reproduced, with a good estimation of the failure mechanisms at both the structural and fine scales. The proposed methodology was then extended to a shell description in order to model the localised behaviour of out-of-plane loaded structures in Chapter 6. The complete multi-scale scheme was again assessed by a comparison against three-dimensional direct fine-scale simulations on out-of-plane loaded masonry wall tests, including bed joint and stair-case bending cracks. It was shown that the failure modes are correctly reproduced by the multi-scale approach in localised and non-localised zones, with a good prediction of the energy dissipation associated to the failure mechanism. The limits of applicability and the robustness of the proposed method was discussed focusing on the assumption of single period failure and the influence of the mesoscopic properties, which can easily be accommodated by the proposed framework.

One of the drawbacks associated with the computational homogenisation procedure is its typical high computational cost compared with purely phenomenological descriptions. This procedure is however well suited for parallel computations since all the cell responses may be computed independently at each iteration of the structural incremental iterative scheme. Such an implementation was therefore used in this study. In order to even more reduce the computational effort, additional strategies could be incorporated in the future in the proposed framework with a certain compromise on the solution accuracy. First, an adaptative scale transition criterion could be defined to determine when the extraction of the material information from the mesostructural sample is really required. Secondly, the multi-scale approach proposed here could be also combined with semi-

analytical homogenisation such as the concept of transformation field analysis. Sacco (2009) proposed recently such an approach for in-plane cases but the out-of-plane case remains to be explored.

In order to model quasi-brittle behaviour, convergence difficulties of the incremental-iterative resolution scheme are often observed, thereby increasing the computational cost. These difficulties are mainly caused by the occurrence of snap-back phenomena at the structural scale, as well as at the mesostructural level, which is a peculiar feature of strain-driven multi-scale schemes. In addition to classical path-following techniques, see Geers (1999a,b), and energy dissipation-based techniques, see Gutiérrez (2004), Massart et al. (2005a), a procedure should be defined allowing both the mesoscopic and macroscopic computations to communicate in terms of resolution scheme. For instance, a strongly local mesostructural snap-back occurring in the loading path followed by another increase of stress can lead to convergence difficulties of the structural resolution scheme. For such a case, enlarging the structural step can help the mesoscopic computation to converge whereas a classical strategy consisting in reducing the structural step may be inappropriate. Enlarging the structural step however has to be used carefully since a large step can lead to other types of convergence difficulties related to crack propagation and softening analysis. The choice of reducing or enlarging the structural step should be related to the crack propagation state and the structural stiffness. In addition to upscaling dissipation information as in Massart et al. (2005a), the solution procedures could therefore exchange additional information between the scales such as for instance the iteration number, the convergence norms, and the step reduction or increase decisions. The adaptivity of the scale transition and the treatment of the mesostructural snap-back could also be investigated by keeping an intrinsically discrete description at the structural scale, linking forces and displacements at discrete points delivered by the computational homogenisation procedure.

The results obtained in this dissertation suggest that further developments could be useful in order to extend their scope. The proposed multi-scale approach could be extended to the case of thick shells, allowing to introduce transversal shear and deflection openings in the scale transitions. For this purpose, the acoustic tensor-based localisation detection and the continuous-discontinuous homogenisation scheme should be adapted to the Reissner-Mindlin description. The extension of the computational homogenisation procedure to the thick shell case still raises questions concerning the transverse shear upscaling, and is the subject of current research work, see Coenen et al. (2008).

The concept of crack branching could be incorporated for the macroscopic scale description, see Linder and Armero (2009), in order to apply the proposed framework on more complex masonry benchmarks where for instance a bed joint bending crack splits into two stair-case bending cracks. A criterion should however be defined to determine when crack branching is required. This criterion could require the material behaviour of the crack branching to be driven by several LVEs, one for each branch for instance, or by a larger cell accounting for more than one mesostructural period.

The proposed multi-scale framework should also be extended to non-planar shell descriptions in order to be applied to geometrically more complex masonry structures such as arches, domes and vaults. A more physically general description of the various failure modes of masonry shells incorporating for instance brick cracking or friction related phenomena could also be achieved but would require a more advanced mesoscopic description. These last two enhancements can be accommodated without any modification of the scale transition and localisation detection procedures. Finally, the proposed methodology could

---

be extended to the domain of large displacement by means of a co-rotational approach and in a more general way to the concept of finite deformation. It could also be interesting to apply this method to other types of heterogeneous shell such as honeycomb-type sandwiches.

# Bibliography

- Anthoine, A. (1995). Derivation of the in-plane elastic characteristics of masonry through homogenization theory. *International Journal of Solids and Structures*, 32(2):137–163.
- Anthoine, A. (1997). Homogenization of periodic masonry: plane stress, generalized plane strain or 3D modelling ? *Communications in Numerical Methods in Engineering*, 13(5):319–326.
- Areias, P. M. A. and Belytschko, T. (2005). Non-linear analysis of shells with arbitrary evolving cracks using XFEM. *International Journal for Numerical Methods in Engineering*, 62(3):384–415.
- Areias, P. M. A. and Rabczuk, T. (2008). Quasi-static crack propagation in plane and plate structures using set-valued traction-separation laws. *International Journal for Numerical Methods in Engineering*, 74(3):475–505.
- Areias, P. M. A., Song, J. H., and Belytschko, T. (2006). Analysis of fracture in thin shells by overlapping paired elements. *Computer Methods in Applied Mechanics and Engineering*, 195(41–43):5343–5360.
- Armero, F. (1999). Large-scale modeling of localized dissipative mechanisms in a local continuum: applications to the numerical simulation of strain localization in rate-dependent inelastic solids. *Mechanics of Cohesive-Frictional Materials*, 4(2):101–131.
- Armero, F. (2001). On the characterization of localized solutions in inelastic solids: an analysis of wave propagation in a softening bar. *Computer Methods in Applied Mechanics and Engineering*, 191(3–5):181–213.
- Armero, F. and Ehrlich, D. (2006a). Finite element methods for the multi-scale modeling of softening hinge lines in plates at failure. *Computer Methods in Applied Mechanics and Engineering*, 195(13–16):1283–1324.
- Armero, F. and Ehrlich, D. (2006b). Numerical modeling of softening hinges in thin euler-bernoulli beams. *Computers & Structures*, 84(10–11):641–656.
- Armero, F. and Garikipati, K. (1996). An analysis of strong discontinuities in multiplicative finite strain plasticity and their relation with the numerical simulation of strain localization in solids. *International Journal of Solids and Structures*, 33(20–22):2863–2885.
- Batoz, J. L. and Dhett, G. (1990). *Modélisation des structures par éléments finis, vol. 2 poutres et plaques*. Herms, Paris. (in French).

- Batoz, J. L. and Lardeur, P. (1989). A discrete shear triangular nine d.o.f. element for the analysis of thick to very thin plates. *International Journal for Numerical Methods in Engineering*, 28(3):533–560.
- Belytschko, T. and Black, T. (1999). Elastic crack growth in finite elements with minimal remeshing. *International Journal for Numerical Methods in Engineering*, 45(5):601–620.
- Belytschko, T., Fish, J., and Engelmann, B. E. (1988). A finite element with embedded localization zones. *Computer Methods in Applied Mechanics and Engineering*, 70(1):59–89.
- Belytschko, T., Gracie, R., and Ventura, G. (2009). A review of extended/generalized finite element methods for material modeling. *Modelling and Simulation in Materials Science and Engineering*, 17(4). Article Number: 043001.
- Belytschko, T., Loehnert, S., and Song, J. H. (2008). Multiscale aggregating discontinuities: A method for circumventing loss of material stability. *International Journal for Numerical Methods in Engineering*, 73(6):869–894.
- Belytschko, T., Moës, N., Usui, S., and Parimi, C. (2001). Arbitrary discontinuities in finite elements. *International Journal for Numerical Methods in Engineering*, 50(4):993–1013.
- Belytschko, T. and Song, J. H. (2009). Coarse-graining of multiscale crack propagation. *International Journal for Numerical Methods in Engineering*. (in-press).
- Bensoussan, A., Lions, J. L., and Papanicolaou, G. (1978). *Asymptotic analysis for periodic structures*. North-Holland Publishing Company.
- Berto, L., Sabetta, A., Scotta, R., and Vitaliani, R. (2002). An orthotropic damage model for masonry structures. *International Journal for Numerical Methods in Engineering*, 55(2):127–157.
- Bottauscio, O., Chiampì, M., Manzin, A., Roccatò, P. E., and Zucca, M. (2007). A multiscale approach to the analysis of magnetic grid shields and its validation. *Journal of Computational Physics*, 227(2):1470–1482.
- Bottauscio, O., Piat, V. C., Chiampì, M., Codegone, M., and Manzin, A. (2008). Extension of thin-shell formulation to ferromagnetic heterogeneous shield modeling. *Journal of Magnetism and Magnetic Materials*, 320(20):E1020–E1023.
- Brasile, S., Casciaro, R., and Formica, G. (2007a). Multilevel approach for brick masonry walls - Part I: A numerical strategy for the nonlinear analysis. *Computer Methods in Applied Mechanics and Engineering*, 196:4934–4951.
- Brasile, S., Casciaro, R., and Formica, G. (2007b). Multilevel approach for brick masonry walls - Part II: On the use of equivalent continua. *Computer Methods in Applied Mechanics and Engineering*, 196:4801–4810.
- Cartraud, P. and Messenger, T. (2006). Computational homogenization of periodic beam-like structures. *International Journal of Solids and Structures*, 43(3–4):686–696.

- Cecchi, A. and Di Marco, R. (2000). Homogenization of masonry walls with a computational oriented procedure. Rigid or elastic block? *European Journal of Mechanics A/Solids*, 19(3):535–546.
- Cecchi, A. and Milani, G. (2008). A kinematic FE limit analysis model for thick English bond masonry walls. *International Journal of Solids and Structures*, 45(5):1302–1331.
- Cecchi, A., Milani, G., and Tralli, A. (2007). A Reissner-Mindlin limit analysis model for out-of-plane loaded running bond masonry walls. *International Journal of Solids and Structures*, 44(5):1438–1460.
- Cecchi, A. and Rizzi, N. L. (2001). Heterogeneous elastic solids: a mixed homogenization-rigidification technique. *International Journal of Solids and Structures*, 38(1):29–36.
- Cecchi, A. and Sab, K. (2002a). A multi-parameter homogenization study for modeling elastic masonry. *European Journal of Mechanics A/Solids*, 21(2):249–268.
- Cecchi, A. and Sab, K. (2002b). Out of plane for heterogeneous periodic materials: the case of masonry. *European Journal of Mechanics A/Solids*, 21(5):715–746.
- Cecchi, A. and Sab, K. (2004). A comparison between a 3D discrete model and two homogenised plate models for periodic elastic brickwork. *International Journal of Solids and Structures*, 41(9–10):2259–2276.
- Cecchi, A. and Sab, K. (2007). A homogenized Reissner-Mindlin model for orthotropic periodic plates: Application to brickwork panels. *International Journal of Solids and Structures*, 44(18–19):6055–6079.
- Challagulla, K. S., Georgiades, A., Saha, G. C., and Kalamkarov, A. L. (2008). Micromechanical analysis of grid-reinforced thin composite generally orthotropic shells. *Composites Part B-Engineering*, 39(4):627–644.
- Cirak, F., Ortiz, M., and Pandolfi, A. (2005). A cohesive approach to thin-shell fracture and fragmentation. *Computer Methods in Applied Mechanics and Engineering*, 194(21–24):2604–2618.
- Coenen, E. W. C., Kouznetsova, V. G., and Geers, M. G. D. (2008). A multi-scale computational strategy for structured thin sheets. *International Journal of Material Forming*, 1(Suppl.):61–64.
- Cuomo, M. and Ventura, G. (2000). A complementary energy formulation of no tension masonry-like solids. *Computer Methods in Applied Mechanics and Engineering*, 189(1):313–339.
- Dallot, J. and Sab, K. (2008a). Limit analysis of multi-layered plates. Part I: The homogenized Love-Kirchhoff model. *Journal of the Mechanics and Physics of Solids*, 56(2):561–580.
- Dallot, J. and Sab, K. (2008b). Limit analysis of multi-layered plates. Part II: Shear effects. *Journal of the Mechanics and Physics of Solids*, 56(2):581–612.
- Dallot, J., Sab, K., and Godet, O. (2008). Experimental validation of a homogenized plate model for the yield design of masonry walls. *Comptes Rendus Mécanique*, 336(6):487–492.

- Dascalu, C., Bilbie, G., and Agiasofitou, E. K. (2008). Damage and size effects in elastic solids: A homogenization approach. *International Journal of Solids and Structures*, 45(2):409–430.
- de Borst, R. (2003). Numerical aspects of cohesive-zone models. *Engineering Fracture Mechanics*, 70(14):1743–1757.
- de Borst, R., Sluys, L. J., Muhlhaus, H. B., and Pamin, J. (1993). Fundamental issues in finite element analyses of localization of deformation. *Engineering Computations*, 10(2):99–121.
- de Borst, R., Wells, G. N., and Sluys, L. J. (2001). Some observations on embedded discontinuity models. *Engineering Computations*, 18(1–2):241–254.
- De Buhan, P. and De Felice, G. (1997). A homogenization approach to the ultimate strength of brick masonry. *Journal of the Mechanics and Physics of Solids*, 45(7):1085–1104.
- Dhanasekar, M., Page, A. W., and Kleeman, P. W. (1985). The failure of brick masonry under biaxial stresses. *Proceedings of the Institution of Civil Engineers, Part 2*, 79(2):295–313.
- Dolbow, J., Moës, N., and Belytschko, T. (2000). Modeling fracture in Mindlin-Reissner plates with the extended finite element method. *International Journal of Solids and Structures*, 37(48–50):7161–7183.
- Dvorak, G. J. (1992). Transformation field analysis of inelastic composite materials. *Proceedings of the Royal Society of London. Series A, Mathematical Physical and Engineering Sciences*, 437(1900):311–327.
- Feyel, F. and Chaboche, J. L. (2000). FE<sup>2</sup> multiscale approach for modelling the elasto-viscoplastic behaviour of long fiber SiC/Ti composite materials. *Computer Methods in Applied Mechanics and Engineering*, 183(3–4):309–330.
- Fish, J. and Fan, R. (2008). Mathematical homogenization of nonperiodic heterogeneous media subjected to large deformation transient loading. *International Journal for Numerical Methods in Engineering*, 76(7):1044–1064.
- Fish, J. and Yuan, Z. (2005). Multiscale enrichment based on partition of unity. *International Journal for Numerical Methods in Engineering*, 62(10):1341–1359.
- Geers, M. G. D. (1999a). Enhanced solution control for physically and geometrically non-linear problems. Part I - The subplane control approach. *International Journal for Numerical Methods in Engineering*, 46(2):177–204.
- Geers, M. G. D. (1999b). Enhanced solution control for physically and geometrically non-linear problems. Part II - Comparative performance analysis. *International Journal for Numerical Methods in Engineering*, 46(2):205–230.
- Geers, M. G. D. (2005). Multiscale modelling and design of new materials (course notes). *International Center for Mechanical Sciences*. Udine.

- Geers, M. G. D., Coenen, E. W. C., and Kouznetsova, V. G. (2007). Multi-scale computational homogenization of structured thin sheets. *Modelling and Simulation in Materials Science and Engineering*, 15(4):S393–S404.
- Geers, M. G. D., Kouznetsova, V. G., and Brekelmans, W. A. M. (2009). Multi-scale computational homogenization: Trends and challenges. *Journal of Computational and Applied Mathematics*. (in-press).
- Ghergu, M., Griso, G., Mechkour, H., and Miara, B. (2005). Homogenization of thin piezoelectric perforated shells. *Comptes Rendus Mécanique*, 333(3):249–255.
- Ghosh, S., Bai, J., and Paquet, D. (2009). Homogenization-based continuum plasticity-damage model for ductile failure of materials containing heterogeneities. *Journal of the Mechanics and Physics of Solids*, 57(7):1017–1044.
- Ghosh, S., Lee, K., and Raghavan, P. (2001). A multi-level computational model for multi-scale damage analysis in composite and porous materials. *International Journal of Solids and Structures*, 38(14):2335–2385.
- Gitman, I. M., Askes, H., and Sluys, L. J. (2008). Coupled-volume multi-scale modelling of quasi-brittle material. *European Journal of Mechanics A/Solids*, 27:302–327.
- Grytz, R. and Meschke, G. (2008). Consistent micro-macro transitions at large objective strains in curvilinear convective coordinates. *International Journal for Numerical Methods in Engineering*, 73(6):805–824.
- Gutiérrez, M. A. (2004). Energy release control for numerical simulations of failure in quasi-brittle solids. *Communications in Numerical Methods in Engineering*, 20(1):19–29.
- Hansbo, A. and Hansbo, P. (2004). A finite element method for the simulation of strong and weak discontinuities in solid mechanics. *Computer Methods in Applied Mechanics and Engineering*, 193(33–35):3523–3540.
- Ibrahimbegovic, A. and Markovic, D. (2003). Strong coupling methods in multi-phase and multi-scale modeling of inelastic behavior of heterogeneous structures. *Computer Methods in Applied Mechanics and Engineering*, 192(28–30):3089–3107.
- Jirásek, M. (2000). Comparative study on finite elements with embedded discontinuities. *Computer Methods in Applied Mechanics and Engineering*, 188(1–3):307–330.
- Kalamkarov, A. L., Andrianov, I. V., and Danishevs'kyi, V. V. (2009). Asymptotic homogenization of composite materials and structures. *Applied Mechanics Reviews*, 62(3). Article Number: 030802.
- Kalamkarov, A. L., Saha, G. C., and Georgiades, A. V. (2007). General micromechanical modeling of smart composite shells with application to smart honeycomb sandwich structures. *Composite Structures*, 79(1):18–33.
- Kepner, J. and Ahalt, S. (2004). Matlabmpi. *Journal of Parallel and Distributed Computing*, 64:997–1005.

- Kouznetsova, V. G., Brekelmans, W. A. M., and Baaijens, F. P. T. (2001). An approach to micro-macro modeling of heterogeneous materials. *Computational Mechanics*, 27(1):37–48.
- Kouznetsova, V. G., Geers, M. G. D., and Brekelmans, W. A. M. (2002). Multi-scale constitutive modelling of heterogeneous materials with a gradient-enhanced computational homogenization scheme. *International Journal for Numerical Methods in Engineering*, 54(8):1235–1260.
- Kouznetsova, V. G., Geers, M. G. D., and Brekelmans, W. A. M. (2004). Multi-scale second-order computational homogenization of multi-phase materials: a nested finite element solution strategy. *Computer Methods in Applied Mechanics and Engineering*, 193(48–51):5525–5550.
- Larsson, R. (2004). A discontinuous shell-interface element for delamination analysis of laminated composite structures. *Computer Methods in Applied Mechanics and Engineering*, 193(30–32):3173–3194.
- Linder, C. and Armero, F. (2007). Finite elements with embedded strong discontinuities for the modeling of failure in solids. *International Journal for Numerical Methods in Engineering*, 72(12):1391–1433.
- Linder, C. and Armero, F. (2009). Finite elements with embedded branching. *Finite Elements in Analysis and Design*, 45(4):280–293.
- Lofti, H. R. and Shing, P. B. (1995). Embedded representation of fracture in concrete with mixed finite elements. *International Journal for Numerical Methods in Engineering*, 38(8):1307–1325.
- Lourenço, P. B. (1996). *Computational strategies for masonry structures*. PhD thesis, Delft University of Technology.
- Lourenço, P. B. (2000). Anisotropic softening model for masonry plates and shells. *Journal of Structural Engineering - ASCE*, 126(9):1008–1016.
- Lourenço, P. B., de Borst, R., and Rots, J. G. (1997). A plane stress softening plasticity model for orthotropic materials. *International Journal for Numerical Methods in Engineering*, 40(21):4033–4057.
- Lourenço, P. B. and Rots, J. G. (1997). Multisurface interface model for analysis of masonry structures. *Journal of Engineering Mechanics - ASCE*, 123(7):660–668.
- Luciano, R. and Sacco, E. (1997). Homogenization technique and damage model for old masonry material. *International Journal of Solids and Structures*, 34(24):3191–3208.
- Luciano, R. and Sacco, E. (1998). A damage model for masonry structures. *European Journal of Mechanics A/Solids*, 17(2):285–303.
- Makowski, J. and Stumpf, H. (1998). Strain localization in stress-resultant theory of shells. *Mechanics Research Communications*, 25(4):455–465.
- Markovic, D. and Ibrahimbegovic, A. (2004). On micro-macro interface conditions for micro scale based FEM for inelastic behavior of heterogeneous materials. *Computer Methods in Applied Mechanics and Engineering*, 193(48–51):5503–5523.

- Massart, T. J. (2003). *Multi-scale modeling of damage in masonry structures*. PhD thesis, Eindhoven University of Technology & Université Libre de Bruxelles (ULB).
- Massart, T. J., Peerlings, R. H. J., and Geers, M. G. D. (2004). Mesoscopic modeling of failure and damage-induced anisotropy in brick masonry. *European Journal of Mechanics A/Solids*, 23(5):719–735.
- Massart, T. J., Peerlings, R. H. J., and Geers, M. G. D. (2005a). A dissipation-based control method for the multi-scale modelling of quasi-brittle materials. *Comptes Rendus Mécanique*, 333(7):521–527.
- Massart, T. J., Peerlings, R. H. J., and Geers, M. G. D. (2007a). An enhanced multi-scale approach for masonry wall computations with localization of damage. *International Journal for Numerical Methods in Engineering*, 69(5):1022–1059.
- Massart, T. J., Peerlings, R. H. J., and Geers, M. G. D. (2007b). Structural damage analysis of masonry walls using computational homogenization. *International Journal of Damage Mechanics*, 16(2):199–226.
- Massart, T. J., Peerlings, R. H. J., Geers, M. G. D., and Gottcheiner, S. (2005b). Mesoscopic modeling of failure in brick masonry accounting for three-dimensional effects. *Engineering Fracture Mechanics*, 72(8):1238–1253.
- Mercatoris, B. C. N., Bouillard, P., and Massart, T. J. (2009). Multi-scale detection of failure in planar masonry thin shells using computational homogenisation. *Engineering Fracture Mechanics*, 76(4):479–499.
- Mercatoris, B. C. N. and Massart, T. J. (2009). Assessment of periodic homogenization-based multiscale computational schemes for quasi-brittle structural failure. *International Journal for Multiscale Computational Engineering*, 7(2):153–170.
- Mergheim, J., Kuhl, E., and Steinmann, P. (2005). A finite element method for the computational modelling of cohesive cracks. *International Journal for Numerical Methods in Engineering*, 63(2):276–289.
- Milani, E., Milani, G., and Tralli, A. (2008). Limit analysis of masonry vaults by means of curved shell finite elements and homogenization. *International Journal of Solids and Structures*, 45(20):5258–5288.
- Milani, G., Lourenço, P. B., and Tralli, A. (2006a). Homogenised limit analysis of masonry walls, Part I: Failure surfaces. *Computers & Structures*, 84(3–4):166–180.
- Milani, G., Lourenço, P. B., and Tralli, A. (2006b). Homogenised limit analysis of masonry walls, Part II: Structural examples. *Computers & Structures*, 84(3–4):181–195.
- Milani, G., Lourenço, P. B., and Tralli, A. (2006c). Homogenization approach for the limit analysis of out-of-plane loaded masonry walls. *Journal of Structural Engineering - ASCE*, 132(10):1650–1663.
- Mistler, M., Anthoine, A., and Butenweg, C. (2007). In-plane and out-of-plane homogenization of masonry. *Computers & Structures*, 85(17–18):1321–1330.

- Moës, N., Dolbow, J., and Belytschko, T. (1999). A finite element method for crack growth without remeshing. *International Journal for Numerical Methods in Engineering*, 46(1):131–150.
- Moorthy, S. and Ghosh, S. (1998). A voronoi cell finite element model for particle cracking in elastic-plastic composite materials. *Computer Methods in Applied Mechanics and Engineering*, 151(3–4):377–400.
- Oliver, J. (1996a). Modelling strong discontinuities in solid mechanics via strain softening constitutive equations, part 1: fundamentals. *International Journal for Numerical Methods in Engineering*, 39(21):3575–3600.
- Oliver, J. (1996b). Modelling strong discontinuities in solid mechanics via strain softening constitutive equations, part 2: numerical simulation. *International Journal for Numerical Methods in Engineering*, 39(21):3601–3623.
- Ortiz, M., Leroy, Y., and Needleman, A. (1987). A finite element method for localized failure analysis. *Computer Methods in Applied Mechanics and Engineering*, 61(2):189–214.
- Oskay, C. (2009). Two-level multiscale enrichment methodology for modeling of heterogeneous plates. *International Journal for Numerical Methods in Engineering*. (in-press).
- Oskay, C. and Fish, J. (2007). Eigendefor-mation-based reduced order homogenization for failure analysis of heterogeneous materials. *Computer Methods in Applied Mechanics and Engineering*, 196(7):1216–1243.
- Oskay, C. and Fish, J. (2008). On calibration and validation of eigendefor-mation-based multiscale models for failure analysis of heterogeneous systems. *Computational Mechanics*, 42(2):181–195.
- Oskay, C. and Ghanshyam, P. (2009). A multiscale failure model for analysis of thin heterogeneous plates. *International Journal of Damage Mechanics*. (in-press).
- Ozdemir, I., Brekelmans, W. A. M., and Geers, M. G. D. (2008a). Computational homogenization for heat conduction in heterogeneous solids. *International Journal for Numerical Methods in Engineering*, 73(2):185–204.
- Ozdemir, I., Brekelmans, W. A. M., and Geers, M. G. D. (2008b). FE<sup>2</sup> computational homogenization for the thermo-mechanical analysis of heterogeneous solids. *Computer Methods in Applied Mechanics and Engineering*, 198(3–4):602–613.
- Page, A. W. (1981). The biaxial compressive strength of brick masonry. *Proceedings of the Institution of Civil Engineers, Part2*, 71:893–906.
- Page, A. W. (1983). The strength of brick masonry under biaxial tension-compression. *International Journal of Masonry Constructions*, 3(1):26–31.
- Pande, G. N., Liang, J. X., and Middleton, J. (1989). Equivalent elastic moduli for brick masonry. *Computers and Geotechnics*, 8(3):243–265.
- Papa, E. and Nappi, A. (1997). Numerical modelling of masonry: A material model accounting for damage effects and plastic strains. *Applied Mathematical Modelling*, 21(6):319–335.

- Peerlings, R. H. J., de Borst, R., Brekelmans, W. A. M., and de Vree, J. H. P. (1996). Gradient-enhanced damage for quasi-brittle materials. *International Journal for Numerical Methods in Engineering*, 39(19):3391–3403.
- Peerlings, R. H. J. and Fleck, N. A. (2004). Computational evaluation of strain gradient elasticity constants. *International Journal for Multiscale Computational Engineering*, 2(4):599–619.
- Pegon, P. and Anthoine, A. (1997). Numerical strategies for solving continuum damage problems with softening: Application to the homogenization of masonry. *Computers & Structures*, 64(1–4):623–642.
- Pietruszczak, S. and Ushaksaraei, R. (2003). Description of inelastic behaviour of structural masonry. *International Journal of Solids and Structures*, 40(15):4003–4019.
- Pijaudier-Cabot, G. and Bažant, Z. P. (1988). Dynamic stability analysis with nonlocal damage. *Computers & Structures*, 29(3):503–507.
- Rabczuk, T., Areias, P. M. A., and Belytschko, T. (2007). A meshfree thin shell method for non-linear dynamic fracture. *International Journal for Numerical Methods in Engineering*, 72:524–548.
- Remmers, J. J. C., Wells, G. N., and de Borst, R. (2003). A solid-like shell element allowing for arbitrary delaminations. *International Journal for Numerical Methods in Engineering*, 58(13):2013–2040.
- Rice, J. R. (1976). *The localization of plastic deformations*. In: Koiter W.T., editor, *Theoretical and Applied Mechanics*. North-Holland Publishing Company.
- Rice, J. R. and Rudnicki, J. W. (1980). A note on some features of the theory of localization of deformation. *International Journal of Solids and Structures*, 16:597–605.
- Sacco, E. (2009). A nonlinear homogenization procedure for periodic masonry. *European Journal of Mechanics A/Solids*, 28(2):209–222.
- Sanchez-Palencia, E. (1980). *Non-homogeneous media and vibration theory*, volume 127. Springer-Verlag, Berlin.
- Simo, J. C., Oliver, J., and Armero, F. (1993). An analysis of strong discontinuities induced by strain-softening in rate-independent inelastic solids. *Computational Mechanics*, 12(5):277–296.
- Sluys, L. J. and Berends, A. H. (1998). Discontinuous failure analysis for mode-I and mode-II localization problems. *International Journal of Solids and Structures*, 35(31–32):4257–4274.
- Smit, R. J. M., Brekelmans, W. A. M., and Meijer, H. E. H. (1998). Prediction of the mechanical behavior of nonlinear heterogeneous systems by multi-level finite element modeling. *Computer Methods in Applied Mechanics and Engineering*, 155(1–2):181–192.
- Song, J. H. and Belytschko, T. (2009). Dynamic fracture of shells subjected to impulsive loads. *Journal of Applied Mechanics - Transactions of the ASME*, 76(5). Article Number: 051301.

- Suquet, P. (1987). *Elements of homogenization for inelastic solid mechanics*. In: *Homogenization techniques for composite media.*, volume 272. Springer-Verlag, Berlin.
- Terada, K., Hori, M., Kyoya, T., and Kikuchi, N. (2000). Simulation of the multi-scale convergence in computational homogenization approach. *International Journal of Solids and Structures*, 37:2285–2311.
- van der Pluijm, R. (1999). *Out-of-plane bending of masonry - behaviour and strength*. PhD thesis, Eindhoven University of Technology.
- van der Sluis, O., Schreurs, P. J. G., Brekelmans, W. A. M., and Meijer, H. E. H. (2000). Overall behaviour of heterogeneous elastoviscoplastic materials: effect of microstructural modelling. *Mech. Mater.*, 32:449–462.
- van Zijl, G. P. A. G. (2000). *Computational modelling of masonry creep and shrinkage*. PhD thesis, Delft University of Technology.
- van Zijl, G. P. A. G. (2004). Modeling masonry shear-compression: Role of dilatancy highlighted. *Journal of Engineering Mechanics - ASCE*, 130(11):1289–1296.
- van Zijl, G. P. A. G., de Borst, R., and Rots, J. G. (2001). A numerical model for the time-dependent cracking of cementitious materials. *International Journal for Numerical Methods in Engineering*, 52(7):637–654.
- Wells, G. N. and Sluys, L. J. (2000). Application of embedded discontinuities for softening solids. *Engineering Fracture Mechanics*, 65(2–3):263–281.
- Wells, G. N. and Sluys, L. J. (2001). A new method for modelling cohesive cracks using finite elements. *International Journal for Numerical Methods in Engineering*, 50(12):2667–2682.
- Xu, X. P. and Needleman, A. (1994). Numerical simulations of fast crack growth in brittle solids. *Journal of the Mechanics and Physics of Solids*, 42(9):1397–1434.
- Zeman, J. and Šejnoha, M. (2007). From random microstructures to representative volume elements. *Modelling and Simulation in Materials Science and Engineering*, 15(4):S325–S335.
- Zucchini, A. and Lourenço, P. B. (2002). A micro-mechanical model for the homogenisation of masonry. *International Journal of Solids and Structures*, 39:3233–3255.

# Summary

In a context of restoration of historical masonry structures, it is crucial to properly estimate the residual strength and the potential structural failure modes in order to assess the safety of buildings. Due to its mesostructure and the quasi-brittle nature of its constituents, masonry presents preferential damage orientations, strongly localised failure modes and damage-induced anisotropy, which are complex to incorporate in structural computations. Furthermore, masonry structures are generally subjected to complex loading processes including both in-plane and out-of-plane loads which considerably influence the potential failure mechanisms. As a consequence, both the membrane and the flexural behaviours of masonry walls have to be taken into account for a proper estimation of the structural stability.

Macroscopic models used in structural computations are based on phenomenological laws including a set of parameters which characterises the average behaviour of the material. These parameters need to be identified through experimental tests, which can become costly due to the complexity of the behaviour particularly when cracks appear. The existing macroscopic models are consequently restricted to particular assumptions. Other models based on a detailed mesoscopic description are used to estimate the strength of masonry and its behaviour with failure. This is motivated by the fact that the behaviour of each constituent is a priori easier to identify than the global structural response. These mesoscopic models can however rapidly become unaffordable in terms of computational cost for the case of large-scale three-dimensional structures.

In order to keep the accuracy of the mesoscopic modelling with a more affordable computational effort for large-scale structures, a multi-scale framework using computational homogenisation is developed to extract the macroscopic constitutive material response from computations performed on a sample of the mesostructure, thereby allowing to bridge the gap between macroscopic and mesoscopic representations. Coarse graining methodologies for the failure of quasi-brittle heterogeneous materials have started to emerge for in-plane problems but remain largely unexplored for shell descriptions. The purpose of this study is to propose a new periodic homogenisation-based multi-scale approach for quasi-brittle thin shell failure.

For the numerical treatment of damage localisation at the structural scale, an embedded strong discontinuity approach is used to represent the collective behaviour of fine-scale cracks using average cohesive zones including mixed cracking modes and presenting evolving orientation related to fine-scale damage evolutions.

A first originality of this research work is the definition and analysis of a criterion based on the homogenisation of a fine-scale modelling to detect localisation in a shell description and determine its evolving orientation. Secondly, an enhanced continuous-discontinuous scale transition incorporating strong embedded discontinuities driven by the damaging mesostructure is proposed for the case of in-plane loaded structures. Finally, this continuous-discontinuous homogenisation scheme is extended to a shell description

in order to model the localised behaviour of out-of-plane loaded structures. These multi-scale approaches for failure are applied on typical masonry wall tests and verified against three-dimensional full fine-scale computations in which all the bricks and the joints are discretised.

# Acknowledgements - Remerciements

I would like to express my sincere gratitude to Thierry Massart, my PhD director, for his guidance, help and support throughout these four years. I have particularly appreciated his availability and all the pleasant and relaxed discussions we have had together. I am also infinitely grateful for his meticulous corrections of this manuscript. This close collaboration has allowed me to learn enormously not only from a professional point of view, but also from a human point of view. I have truly enjoyed all these moments we have shared in commuting and travelling together.

I would also like to sincerely thank Philippe Bouillard, my PhD co-director, for giving me the opportunity to carry out this PhD project, and for his help, advice, and energy invested in the starting of this adventure.

Next, I would like to address special thanks to Marc Geers for his precious and pertinent comments, and to Varvara Kouznetsova for her help and explanation about ‘straight-forward but somewhat lengthy’ mathematical manipulations. I also want to thank Guy Warzée for his confidence in me.

For its financial support, the F.R.S.-FNRS is gratefully acknowledged.

I owe many thanks to Guy Paulus for his help in ‘minor’ computer-related issues, especially with his ‘favourite’ operating system. I would also like to warmly thank all my colleagues for the perfect working and social atmosphere, but also for their support in the final round. I have truly enjoyed your company during all these years.

Je souhaiterais également remercier ma famille proche pour m’avoir tant soutenu et encouragé dans la dernière ligne droite.

Pour finir, je tiens à remercier du fond du coeur Audrey, mon petit Ange. Ton amour et ton soutien m’ont permis de tenir. Je suis conscient de ne pas avoir été très présent cette dernière année mais sache que je n’ai jamais cessé de penser à toi. Il est temps pour moi maintenant de te rendre au double tout l’amour que tu m’as donné.

Benoît Mercatoris,  
Novembre 2009